upna Universidad Pública de Navarra
Nafarroako Unibertsitate Publikoa

METAMATERIALS AND PLASMONICS APPLIED TO DEVICES BASED ON PERIODIC STRUCTURES AT HIGH FREQUENCIES: MICROWAVES, TERAHERTZ AND OPTICAL RANGE

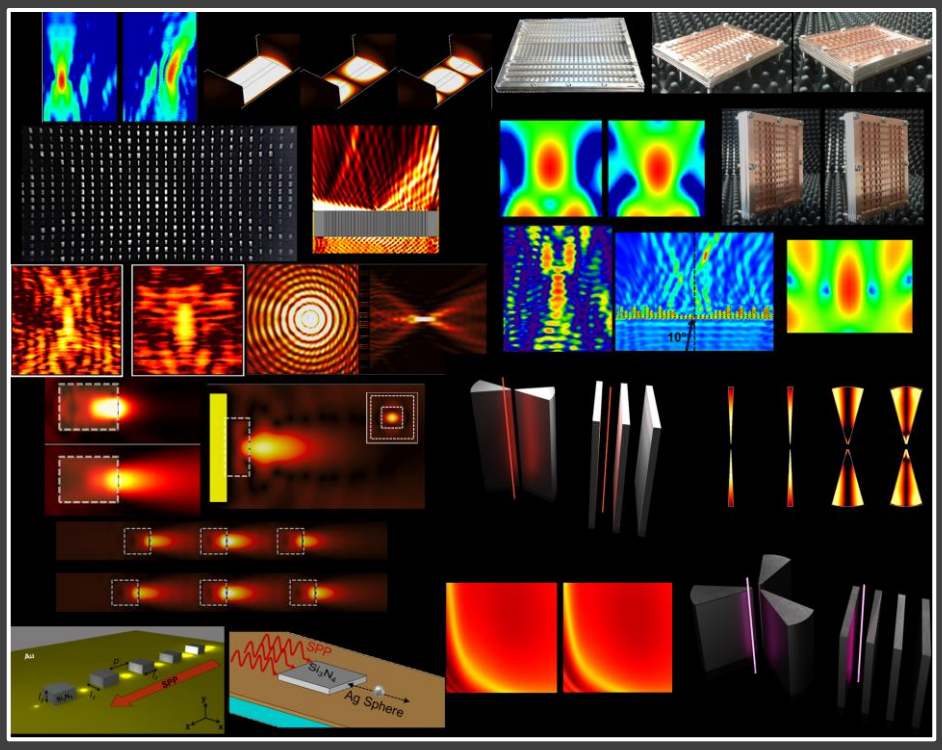

DOCTORAL THESIS

POSTGRADUADE PROGRAMME: COMMUNICATION TECHNOLOGY

VÍCTOR PACHECO-PEÑA

SUPERVISED BY: DR. MIGUEL BERUETE DÍAZ

upna Universidad Pública de Navarra Nafarroako Unibertsitate Publikoa

PAMPLONA, 2016

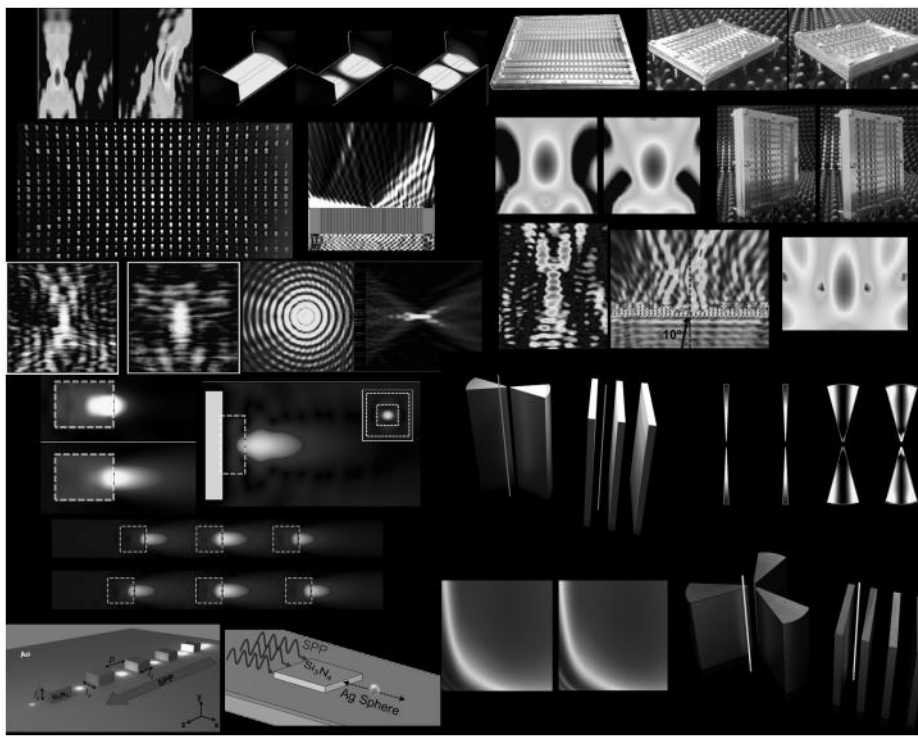

upna Universidad Pública de Navarra
Nafarroako Unibertsitate Publikoa

Doctoral thesis submitted for the degree of Doctor of Philosophy in Telecommunication Engineering

Postgraduade programme: Communication Technology

Metamaterials and Plasmonics Applied to Devices Based on Periodic Structures at High Frequencies: Microwaves, Terahertz and Optical Range

Presented by:

Víctor Manuel Pacheco Peña

Supervised by:

Dr. Miguel Beruete Díaz

Pamplona, 2016

upna Universidad Pública de Navarra Nafarroako Unibertsitate Publikoa

ACKNOWLEDGEMENTS

I would like to give my grateful acknowledgement for the financial support from the Spanish Ministerio de Educación, Cultura y Deporte under grant FPU AP-2012-3796, for the invaluable opportunity to undertake the research for this thesis at the Public University of Navarra.

I wish to give my gratitude to Prof. Mario Sorolla who unfortunately is not longer with us. Prof. Sorolla supported my work in science from the very beginning and convinced me to apply for the FPU grant. I will always be grateful to him. To Dr. Miguel Beruete Díaz, who supervised this thesis, I wish to express my sincere and deep gratitude. Many thanks for the constant and unconditional support. Also, thank you to my colleagues and friends from UPNA, Unai, Baha, Pablo, Víctor, Alicia and Jose. Thank you all for making me feel at home.

I would like to thank Prof. Nader Engheta from the University of Pennsylvania and Dr. Miguel Navarro-Cia from the University of Birmingham for the opportunity of being part of their research teams for a few months.

Finally, I want to give a special thank to my family in El Salvador (my mother, sisters, brother and father). Many thanks for their unconditional support all these years that I have been far from home. Special thanks to my grand mother who passed away this year. Thank you for being my second mother, I will always love her, she will always be in my heart. Special thanks to someone who has played an important role in my life and to whom this work is dedicated, David Hall, thanks for being with me everyday and supporting me during all these years. Many, many thanks.

AGRADECIMIENTOS

Quisiera dar un agradecido reconocimiento a la ayuda financier por parte del Ministerio de Educación, Cultura y Deporte de España por la ayuda FPU AP-2012-3796, por la invaluable oportunidad de emprender la investigación para ésta tesis en la Universidad Pública de Navarra.

Deseo dar my agradecimiento al Prof. Mario Sorolla quien desafortunadamente no está con nosotros. Prof. Sorolla apoyó mi trabajo en la ciencia desde el principio y me convenció para aplicar a la ayuda FPU. Siempre estaré agradecido con él. A Dr. Miguel Beruete Díaz, with supervisó ésta tesis, deseo expresar mi sincere y profundo agradecimiento. Muchas gracias por el apoyo constante e incondicional. También, gracias a mis colegas y amigos de la UPNA, Unai, Baha, Pablo, Víctor, Alicia y José. Muchas gracias a todos por hacerme sentir como en casa.

Quisiera agradecer a Prof. Nader Engheta de la Universidad de Pennsylvania y Dr. Miguel Navarro-Cía de la Universidad de Birmingham por la oportunidad de ser parte de su grupo de investigación por unos meses.

Finalmente, quiero dar especiales gracias a mi familia en El Salvador (mi madre, hermana, hermano y padre) y a mi pareja. Muchas gracias por su apoyo incondicional todos estos años que he estado fuera de casa. Yo se que ellos siempre han estado conmigo. Especiales gracias a mi abuelita quien murió este año. Gracias por ser mi segunda mamá, siempre la amaré, ella estará en mi corazón siempre. Especial agradecimiento a quien ha jugado un fuerte papel en mi vida y a quien está dedicado este trabajo, David Hall, gracias por estar conmigo cada día y apoyarme durante todos estos años.

ABSTRACT

(English)

This thesis shows the research work performed under the doctorate program "Communication Technology" from Universidad Pública de Navarra (UPNA), for the degree of Doctor of Philosophy (PhD) in Telecommunications Engineering. The guidance, supervision and direction of this doctoral thesis has been developed by Dr. Miguel Beruete Díaz from UPNA. During the PhD program, two stays have been completed by this doctoral student in the following institutions: University of Pennsylvania under the supervision of Prof. Nader Engheta (3 months) and Imperial College London under the guidance of Dr. Miguel Navarro-Cía (2 months).

The topics treated in this thesis are developed within the millimeter, terahertz and optical frequencies. Mainly metamaterials and periodic structures are used in the design of different devices such as lenses, steerers, waveguides etc. The structure of the thesis is as follows:

In Chapter 1, the background of metamaterials and the extraordinary transmission phenomenon is described. It starts with a definition and clasification of metamaterials, showing how they can be studied from the effective medium approach. Then, the implications of the metal modeling in the terahertz band are described. Surface plasmons polaritons and localized surface plasmons are presented which are the two main fields of study of plasmonics. Finally, a brief introduction of refractive elements is given in order to put the thesis in context.

Chapter 2 shows the design of different practical devices from millimeter to visible frequencies using epsilon-near-zero metamaterials. First, it describes how to emulate this type of artificial material using narrow hollow rectangular waveguides. Then, this structure is applied to the design of lenses, power splitters, beam steerers and sensors.

In Chapter 3, the fishnet metamaterial is used in the design of zoned metalenses. The operation principle of the zoning technique is described and applied in the design of plano-concave zoned lenses. Then, the reference phase and phase reversal techniques are used along with the zoning technique to improve the performance of the fishnet metalenses. The focusing and radiation pattern performances are numerically and experimentally evaluated.

Chapter 4 discusses how dielectric cuboids can be used to produce terajets at terahertz frequencies under plane wave illumination. These structures are evaluated at different frequency harmonics within the terahertz band and also in reflection mode. A mechanism to produce jets at optical frequencies is provided by exciting the cuboids

with surface plasmons. The dielectric cuboids are then applied to different practical devices such as waveguides and sensors.

In Chapter 5, a full analytical description of bowtie and tripod nanoantennas illuminated with a localized emitter is provided using conformal transformation. The non-radiative and radiative Purcell enhancement is evaluated depending of the geometry and materials of the nanoantennas. All the analytical results are validated numerically.

Finally, chapter 6 shows the main conclusions derived from this thesis and gives a list of work that will be studied in the near future.

(Español)

Esta tesis muestra el trabajo de investigación desarollado bajo el programa de doctorado "tecnología de las comunicaciones" de la Universidad Pública de Navarra (UPNA), para el grado de Doctor (PhD) en Ingenieria de Telecomunicaciones. La guía, supervisión y dirección de esta tesis doctoral ha sido desarrollada por Dr. Miguel Beruete Díaz de la UPNA. Durante el programa de PhD, dos estancias internacionales han sido completadas por este estudiante doctoral en las siguientes instituciones: Universidad de Pennsylvania bajo la supervisión de Prof. Nader Engheta (3 meses) y Imperial College London bajo la guía de Dr. Miguel Navarro-Cía (2 meses).

Los temas tratados en esta tesis son desarrollados en milimétricas, terahercios y frecuencias ópticas. Se usan principalmente metamateriales y estructuras periódicas en el diseño de diferentes dispositivos como lentes, direccionadores de haz, guías de onda etc. La estructura de la tesis es como sigue:

En el Capítulo 1, se describen los principios básicos de los metamateriales y las estructuras de transmisión extraordinaria. Comienza con una definición y clasificación de los metamamteriales, mostrando como éstos pueden ser estudiados desde el enfoque de medio efectivo. Se presentan a continuación los plasmones de superficie y plasmones localizados, los cuales son los dos principales campos de estudio de la plasmónica. Finalmente, se realiza una breve introducción sobre los elementos refractivos con el fin de ubicar la tesis en contexto.

El Capítulo 2 muestra el diseño de diferentes dispositivos prácticos desde milimétricas a frecuencias ópticas usando metamateriales con permitividad cercana a cero. Primero, se describe cómo emular éste tipo de material artificial usando guias de onda rectangulares estrechas. Luego, esta estructura es aplicada al diseño de lentes, divisores de potencia, direccionadores de haz y sensores.

En el capítulo 3, se usa el metamaterial de tipo red de pesca *"fishnet"* en el diseño de metalentes zonadas. Se describe el principio de operación de la técnica de zonado y se aplica al diseño de lentes plano-cóncavas. Más adelante, se propone el uso de las técnicas de referencia de fase y fase inversa junto con el concepto de zonado para

mejorar la respuesta de las metalentes tipo *fishnet*. Se evalúan numérica y experimentalmente las respuestas del foco y patrón de radiación.

El Capítulo 4 discute cómo producir terajets a frecuencias del terahercio con cuboides dieléctricos iluminados con onda plana. Estas estructuras se evalúan a diferentes harmónicos dentro del terahercio y también en modo de reflexión. Se presenta un mecanismo para producir jets a frecuencias ópticas excitando los cuboides a través de plasmones de superficie. Éstos cuboides dieléctricos se aplican luego a diferentes dispositivos prácticos como guías de onda y sensores.

En el Capítulo 5 se presenta una descripción analítica completa de nanoantenas de tipo pajarita y trípode haciendo uso de la transformación conformada. Se evalúa la mejora del parámetro de Purcell no-radiativo y radiativo en función de la geometría y materiales de las nanoantenas. Todos los resultados analíticos son validados numéricamente.

Finalmente, el Capítulo 6 muestra las principales conclusiones derivadas de ésta tesis y una lista de trabajos que serán estudiados en el futuro cercano

Table of Contents

Chapter 1

Introduction

Most of materials that can be found in nature have values of permittivity (ε) and permeability (μ) larger than the free-space values (ε_o,μ_o). For example, common dielectrics (widely used from microwave to optical frequencies) have only electric response, exhibiting a finite value of relative electric permittivity larger than one and a relative magnetic permeability equal to one. With the aim to surpass the barrier naturally imposed by natural materials, the scientific community has devised engineered artificial materials with electromagnetic (EM) properties unavailable in nature. The first step towards these synthetic materials was the artificial dielectrics reported some decades ago. In them, the magnetic permeability remains constant while the electric permittivity can be modified at will. Even though they only have control over the electric response of the new material, they are considered the precursors of the wider field of man-made materials called metamaterials (MTM). With this new group of artificial materials, the constitutive parameters (ε,μ) can be tailored and controlled at will, achieving extreme parameters values such as close to zero or even negative.

This initial chapter provides a background of MTMs and the extraordinary transmission (ET) phenomenon which are widely used to design artificial media. It also gives an overview of plasmonics with the aim to put the thesis in context. First, the definition and the classification of MTMs are shown and it is also described how these artificial materials can be studied from the effective medium approach. Secondly, we will study the terahertz band and the implications of metal modeling within this region. Then, the two main fields of study of plasmonics are presented: surface plasmons polaritons and localized surface plasmons. Finally we will present a brief introduction of refractive elements, such as lenses and beam steerers which will be designed in further chapters using MTMs.

1.1 Metamaterials

Due to the different contexts where *metamaterials* can be applied, it is not easy to provide a general definition. From a semantic point of view, it is derived from the Greek prefix *μεσα* (= *meta*) which means *beyond*. Hence, it is usually understood that the term MTM describes something well beyond ordinary materials [SOLY 09], [SIHV 07a]. In 1999, Rodger M. Walser defined MTMs as [WEIG 03]:

> *"Macroscopic composites having a synthetic, three-dimensional, periodic cellular architecture designed to produce an optimized combination, not available in nature, of two or more responses to specific excitation"*

From this definition, we may consider a MTM as an artificial material whose EM parameters can be controlled so that it can have values not available in natural materials. The main idea of them is to emulate the response of natural materials when they interact with an EM field. As it is known, the response of natural materials is determined by their atomic composition; i.e., depending on how the atoms and bonds are structured, the response of the material will be different. This response is governed by the macroscopic Maxwell's equations in the frequency range where quantum effects can be neglected; i.e., for frequencies of the electromagnetic waves below 3×10^{16} Hz (wavelengths larger than ~10 nm). They are as follows [JACK 98]:

$$\nabla \times \boldsymbol{E} + \frac{\partial \boldsymbol{B}}{\partial t} = 0 \tag{1.1}$$

$$\nabla \times \boldsymbol{H} - \frac{\partial \boldsymbol{D}}{\partial t} = \boldsymbol{J} \tag{1.2}$$

$$\nabla \cdot \boldsymbol{B} = 0 \tag{1.3}$$

$$\nabla \cdot \boldsymbol{D} = \rho \tag{1.4}$$

where the vectors $\boldsymbol{E}$ and $\boldsymbol{H}$ are the electric and magnetic field, respectively, $\boldsymbol{D}$ is the electric field displacement, $\boldsymbol{B}$ is the magnetic field density and $\boldsymbol{J}$ and ρ are the free current and charge densities, respectively. When an external source interacts with a material, it generates new sources via the magnetization $\boldsymbol{M}$ and polarization $\boldsymbol{P}$ vectors of the material. Hence, the field vectors $\boldsymbol{D}$ and $\boldsymbol{B}$ in Eqs. (1.1-1.4) can be defined as:

$$\boldsymbol{D} = \varepsilon_0 \boldsymbol{E} + \boldsymbol{P} \tag{1.5}$$

$$\boldsymbol{B} = \mu_0 \boldsymbol{H} + \boldsymbol{M} \tag{1.6}$$

with $\varepsilon_0 = 8.854\times10^{-12}$ F/m and $\mu_0 = 4\pi\times10^{-7}$ H/m as the permittivity and permeability in free-space, respectively. From these equations, for a linear material, the electric field displacement and magnetic field density can be rewritten as follows:

$$\boldsymbol{D} = \varepsilon_0 \varepsilon_r \boldsymbol{E} = \varepsilon \boldsymbol{E} \tag{1.7}$$

$$\boldsymbol{B} = \mu_0 \mu_r \boldsymbol{H} = \mu \boldsymbol{H} \tag{1.8}$$

where ε_r and μ_r are respectively the relative permittivity and permeability of the material. These equations show that the EM properties are characterized by these two parameters. Of course, depending on the values of ε and μ we can differentiate between isotropic and anisotropic materials. In the former case, the constitutive parameters do not depend on any direction, hence both are scalars. On the other hand, for anisotropic media, ε and μ depend on the direction; therefore they should be treated as tensors. Moreover, as it will be explained later, most natural materials have a dispersive behavior depending on the operational frequency. For instance, a metal at microwaves behaves nearly as a perfect electric conductor whereas at optical wavelengths it is modelled by a complex permittivity.

As mentioned above, the EM response of a material to an incident wave depends on its atomic structure. For example, if we observe a piece of wood, we see a homogeneous material instead of their constituting atoms, due to the fact that the atoms and the distance between them are smaller than the wavelengths at visible frequencies. This is in fact the main idea of MTMs: they are designed with meta-atoms (called unit cells) much smaller than the operational wavelength. By ensuring this condition, it is possible to homogenize the structure and apply the same macroscopic considerations as for common materials, see Fig. 1.1 for a schematic representation. Hence, similar to natural materials, when an EM wave interacts with a MTM, the incident wave sees a homogeneous medium instead of an array of particles. They are designed with periodical or quasi-periodical arrays of unit cells made of natural materials. However, the arrangement of the unit cells as well as their properties, determine the response of the new MTM which can be considered as a medium with an effective permittivity (ε_{eff}) and permeability (μ_{eff}). In summary, its performance does not depend only on the composition of the material, but also on the geometry and/or spatial distribution of the elementary particles. Hence, they can exhibit negative or close to zero EM parameters without affecting their chemical constitution.

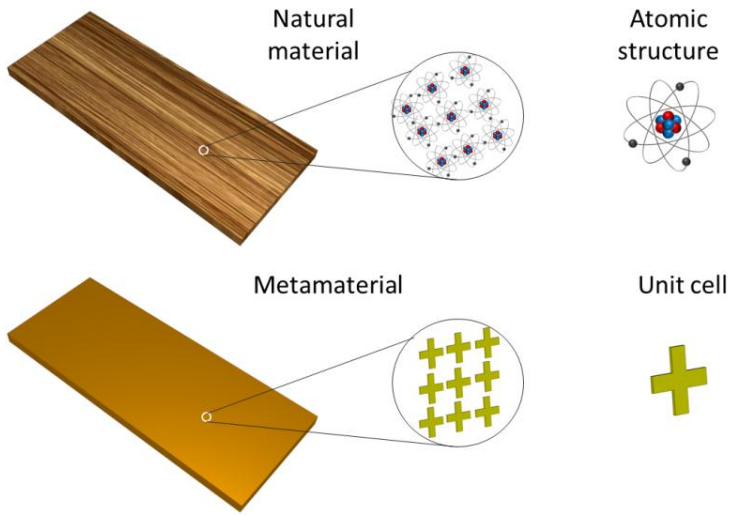

Figure 1.1 Schematic representations of a natural material whose electromagnetic response depends on its atomic structure (top) and the equivalent principle applied with MTMs where the response depends on the geometry, materials and arrangement of the unit cell used (bottom).

The precursors of MTMs are the artificial dielectric materials which trace back to the last century (1940s) where they were mainly used for antennas applications. The seminal work reported by Kock in 1946 [KOCK 46] can be considered as the beginning of the field of artificial dielectrics [BROW 53], [COLL 69], [ROTM 62] and also of MTMs. Generally speaking, artificial dielectrics are formed by an arrangement of conducting obstacles that allow modifying the effective permittivity, while the effective magnetic permeability is considered constant and equal to the free-space value. MTMs extend the concept of artificial dielectrics by providing control on both constitutive EM parameters with extreme (close to zero) and negative values.

It is important to mention that before the MTM, an evolution of artificial dielectrics was the widely known photonic band gap structures (PBG) or photonic crystals (PhC) [YABL 87], [YABL 91], [JOAN 95]. These structures were also proposed to control the response of a medium by forbidding the propagation of EM waves at certain frequencies and/or space regions and also to achieve confinement of light [JOHN 97]. The main characteristic of these artificial media is that the size of the unit cell is comparable to the operational wavelength. Therefore, the macroscopic approach for these structures is no longer valid due to the size of the unit cell, even when it has been demonstrated that a good control of the EM parameters can be achieved. Despite there is a clear difference between these structures and MTMs in terms of the size of the unit cell, they are usually included within the term “metamaterials” due to the evolution of the latter concept and the different contexts where they can be applied.

In 1968, V. G. Veselago [VESE 68] proposed the possibility of doubly-negative materials, i.e. materials with permittivity (ε) and permeability (μ) simultaneously negative. He concluded that the index of refraction (n) of such media should also be negative ($n = -\sqrt{\varepsilon\mu}$) and that a wave is refracted at negative angles at the interface between a material with both positive parameters and a material with both simultaneous negative parameters. This work was considered unrealizable due to the difficulty to get an effective negative permeability. However, J. B. Pendry [PEND 99] in 1999 designed a nonmagnetic particle with special behavior on its effective magnetic permeability (μ_{eff}) showing its strong magnetic response. This particle is the so-called Split-Ring Resonator (SRR) with dimensions smaller than the operation wavelength. The main feature of the SRR is that, for a range of frequencies, the particle exhibits a negative effective permeability value, i.e., it can be considered as a negative permeability material or, as it is usually called, a mu-negative (MNG) material. Following this discovery, the first double negative (DNG) material ever was demonstrated by D. R. Smith in 2000 [SMIT 00]. It was constructed by the combination of SRRs and a wire medium that provides an effective negative dielectric permittivity, achieving simultaneously negative values of permeability and permittivity within a certain bandwidth. Soon after, the negative refraction predicted by Veselago was experimentally demonstrated in 2001 by Shelby [SHEL 01] using a two-dimensional array of strips and SRRs on a circuit board substrate.

A provoking concept that launched definitively the research on MTMs was proposed by the end of 2000 by J. B. Pendry [PEND 00]. He argued that a slab with refractive index $n = -1$ was capable of generating an image at the output with perfect resolution, not only focusing propagating components but also amplifying the evanescent field. In this sense, a simple slab with $n = -1$ and parallel interfaces could be considered as a *perfect lens*. Although in practice losses limit the performance, this opened the path towards "superlenses" with "super resolution" using MTMs [FANG 05], [ZHAN 08].

All these studies show that MTMs can be used to generate artificial media with one or both negative values on their EM parameters. A general classification of materials, including natural and artificial materials, is presented in Fig. 1.2 [ALÙ 07a], [SIHV 07b]. There are basically four different classes of materials: a) Double Positive (DPS) or Right-Handed Media (RHM), b) Double Negative (DNG) or Left-Handed Media (LHM), c) negative permeability (MNG) media and d) negative permittivity (ENG) media. The MNG and ENG materials are commonly called as Single Negative (SNG) materials because only one constitutive parameter is negative.

Note that this classification of materials considers only the sign of the constitutive parameters. As it is shown in Fig. 1.2, an interesting subgroup are those materials with permeability near zero (mu near zero, MNZ), permittivity near zero (epsilon near zero, ENZ) or both parameters near zero (n near zero, NNZ; also called zero index

materials, ZIM) which are placed near (or exactly at) the coordinate axes. Each group has special properties which will be described in this section.

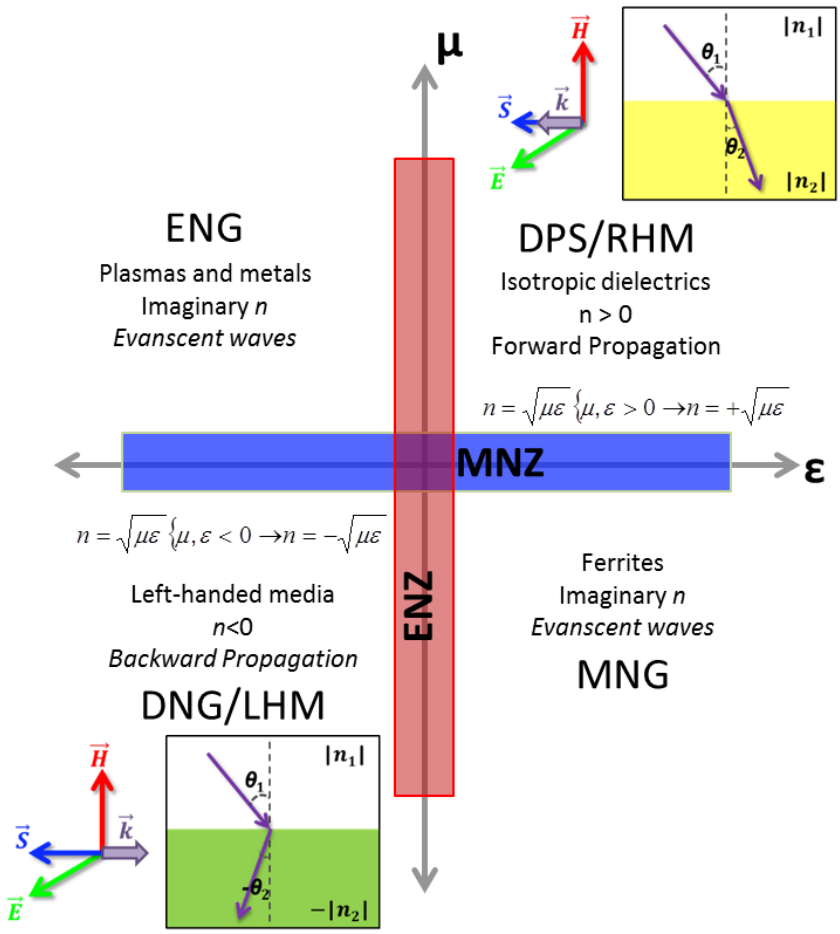

Figure 1.2 Classification of materials depending of the values of the constitutive parameters. Schematic representation of: (top-right inset) DPS/RHM where the energy (***S***) and the wave vector (***k***) propagates in the same direction; (bottom-left inset) DNG/LHM where the energy (***S***) and the wave vector (***k***) are in opposite directions. A schematic representation of the propagation based in the Snell's law is shown in the right panel of each inset.

1.1.1 Double positive (DPS) and Double Negative (DNG) Media

The DPS (or natural materials) media are located in the first quadrant of Fig. 1.2, with $\varepsilon,\mu > 1$ and positive index of refraction $n > 1$. In these materials, the energy (defined with the pointing vector $\boldsymbol{S}$) propagates in the same direction as the wave vector ($\boldsymbol{k}$). This performance is depicted in the top-right inset of Fig. 1.2, where it is shown that the electric ($\boldsymbol{E}$) and magnetic field ($\boldsymbol{H}$) vectors and $\boldsymbol{k}$ form a right-handed triplet.

In practice, a wave propagates through two or more media with different values of n. Hence, it is important to understand the behavior at the interface of different materials with different, but positive, refractive indexes. This can be explained by invoking the widely known Snell's law [WOLF 95], [SOLY 09] as follows:

$$n_1 \sin(\theta_1) = n_2 \sin(\theta_2) \tag{1.9}$$

where the pairs (n_1,θ_1) and (n_2,θ_2) are the refractive indexes and angles of the waves in the media 1 and 2, respectively. When a wave propagates from a medium 1 with $n_1 < n_2$ [see the right panel of top-right inset of Fig. 1.2], it impinges at the interface with an angle (θ_1) and is refracted with angle θ_2 when it enters medium 2 due to the different refractive index. Note that $0 < \theta_2 < \theta_1$. This is because the wavelength inside a medium with a higher refractive index is smaller than the free space wavelength; i.e., the waves will propagate with a lower phase velocity (defined as the measure of the rate at which the phase of a monochromatic EM wave changes which can be defined in both guided and unguided waves) than free-space.

For the case when $n_1 > n_2$ a similar behavior will be obtained. The only difference is that $\theta_2 > \theta_1$. This behavior has been widely applied in the design of lenses using natural dielectrics [FILI 93], [RAMA 98],[YURD 14]. This is due to the fact that natural dielectrics have a magnetic relative permeability value of unity, while the electric relative permittivity is larger than free-space.

Double negative (DNG) materials are located in the third quadrant of Fig. 1.2, where $\varepsilon < 0$ and $\mu < 0$. The DNG materials are also known as Left-Handed media (LHM) or Negative Refractive Index media (NRI). They fall almost entirely within the realm of MTMs [PADI 06], with some rare realizations in nature [PIME 07]. These materials have attracted the attention of the scientific community due to their unconventional EM parameters, as it was explained before. Here, the electric field ($\boldsymbol{E}$), magnetic field ($\boldsymbol{H}$) and $\boldsymbol{k}$ form a left-handed triplet. With this behavior, the phase and group velocities are antiparallel. This performance is schematically shown in the bottom-left inset of Fig. 1.2. Note that this behavior is opposite to DPS media (with a right-handed triplet). Furthermore, the same bottom-left inset of Fig. 1.2 shows the

refraction of a wave when it travels from a medium 1 with a positive refractive index (n_1) to a medium 2 with negative refractive index (n_2). It can be observed that the wave is refracted with a negative angle in medium 2 because of the negative index of refraction that arises directly from its double negative nature ($\varepsilon, \mu < 0$).

1.1.2 Negative permeability (MNG) and negative permittivity (ENG) media

As it can be observed in Fig. 1.2, the MNG media are located in the fourth quadrant of the material classification. These materials have $\mu < 0$ and $\varepsilon > 0$, represent magnetic plasmas and support evanescent waves. One can find in the literature several examples of such materials. However, one of the most representatives is the Split-Ring Resonator (SRR) designed by J. B. Pendry [PEND 99] which is shown in Fig. 1.3(a). This particle exhibits a strong magnetic response for a range of frequency depending on its dimensions, material and arrangement. Below resonance μ_{eff} takes positive values ($\mu_{eff} > 0$); however, for a certain narrow range of frequencies above the resonant frequency, μ_{eff} presents negative values ($\mu_{eff} < 0$). This is because when an external magnetic field parallel to the axis of the particle is applied, circulating currents are induced on the SRR and generate a strong local magnetic dipole moment which can neutralize the incoming magnetic field, producing a negative magnetic response, i.e. a negative resonant permeability. From an equivalent circuit point of view, this particle can be modeled as an *LC* circuit [BAEN 05], [MARQ 08], as is shown in Fig. 1.3(a). Here, ϕ_m is the external magnetic field, C_s is the equivalent capacitance of the upper and lower halves of the particle and C_0 is the total capacitance of the rings.

On the other hand, ENG materials are located in the second quadrant of Fig. 1.2 and they have values of $\varepsilon < 0$ and $\mu > 0$. Similarly to the previous case, these materials represent electric plasmas and also support evanescent waves. They can be synthesized using Complementary Split-Ring Resonators (CSRRs) and also a wire medium, as two of the most highlighted structures.

As observed in Fig. 1.3(a,b) the CSRRs have a complementary behavior to SRRs and they were deeply studied using the Babinet's principle demonstrating that they have $\varepsilon < 0$ [FALC 04]. The CSRR is made by replacing metal/apertures with apertures/metals from the SRR structure, as it is presented in Fig. 1.3(b). In the same way as SRR particles, the CSRR can be modeled as an *LC* circuit whose resonant frequency can be tuned by varying the dimensions of the structure. The *LC*-equivalent model for the CSRR structure [BAEN 05] is presented in Fig. 1.3(b). Note that the dimensions of the rings are the same as for the SRR structures.

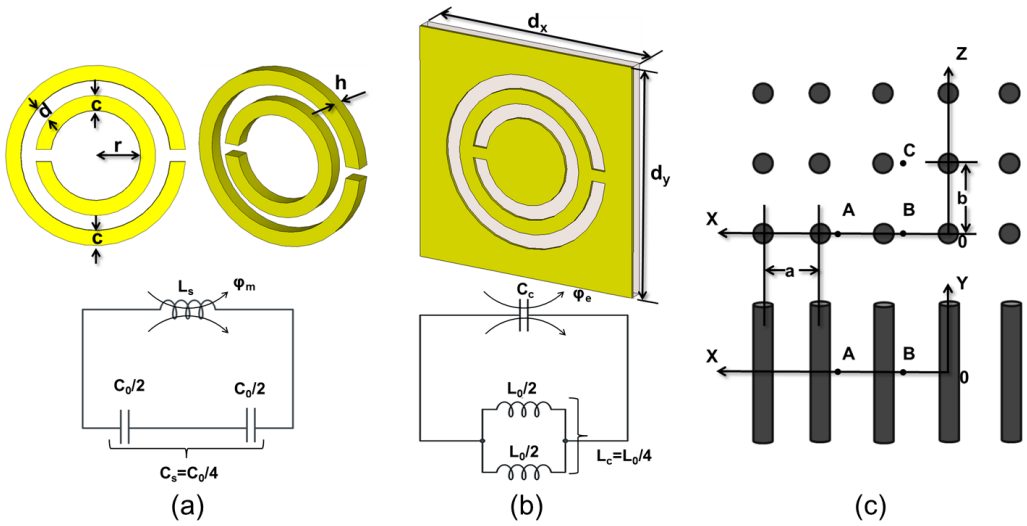

Figure 1.3 Schematic representation of: (a) the Split-Ring Resonator (SRR) and (b) the Complementary Split-Ring Resonator (CSRR) along with the equivalent *LC* circuit. (c) Schematic representation of a 2D wire medium proposed in [BROW 53], [ROTM 62].

For the case of the wire medium, it consists on a 2D or 3D rectangular lattice of metallic rods. It was reported in 1962 by W. Rotman [ROTM 62] using a 2D array of lossy metallic rods based on [BROW 53], see Fig. 1.3(c). It was shown that when an EM wave propagates perpendicularly to the direction of the wires (considering that the electric field component is in the direction of wires), the effective relative permittivity of the structure is less than unity. The analysis was made to model a plasma medium and it was represented as an isotropic lossy dielectric whose magnetic permeability is unity, considering that dc magnetic fields are not present.

1.1.3 Refractive index near zero (NNZ/ZIM) media: the case of ENZ materials

These type of materials might be considered as one of the most complex in terms of the different kinds that can be included: materials with one of their constitutive parameters near zero (MNZ and ENZ) and also those materials placed in or close to the center of Fig. 1.2 (with both constitutive parameters values equal or near zero).

The implications of having a material with $n = 0$ (ZIM) was reported by Ziolkowski in 2004 [ZIOL 04]. In this case, both $\varepsilon = \mu = 0$. It was theoretically demonstrated that in a ZIM, the EM fields are static in the space domain.

Even though an exact ZIM is difficult to realize in practice [SOLY 09], it is possible to design a material with a very low index of refraction; i.e., with a small (but not exactly zero) phase variation inside the material (NNZ). The refraction of a wave that travels inside such low refractive index medium can be described by invoking the Snell's Law (Eq. 1.9). Consider a wave that propagates from a medium 1 to a medium 2. Furthermore, consider that the refractive index in medium 2 is unity ($n_2 = 1$) and that medium 1 has a refractive index close to zero, say $n_1 = 0.01$. Based on this, we can calculate the refracted angle in medium 2 (θ_2) in terms of the incidence angle in medium 1 (θ_1) using Eq. 1.9. The representation of θ_2 with respect to the θ_1 is plotted in Fig. 1.4(a). As it can be observed, the variation of θ_2 is very small with a maximum value below 2º while θ_1 changes from 0º to 90º.

This feature of a NNZ medium was exploited by Enoch in 2002 to improve the emission of a source embedded in a MTM of this type [ENOC 02]. It was considered a source embedded in a NNZ slab surrounded with air. When rays pass through the slab to air, they are refracted but with a direction almost perpendicular to the surface. Therefore, a medium of these characteristics shows a very good directional radiation pattern given that the refracted rays will travel almost perfectly parallel. Some examples of this performance are shown in Fig. 1.4(b-c), where a dipole source is placed inside of a medium with different shapes with $n = 0.01$ surrounded by air. As it is shown, the electric field outside the structures is perpendicular to the surface, producing a shaping of the output field.

This enhancement of the directional radiation patterns has been an interesting research field because it can have many practical applications such as, for example, more directive antennas. Indeed, the first attempt to elaborate a material with low refractive index at microwave frequencies was proposed many decades ago [BROW 53], as mentioned in the previous section. Two structures were analyzed: an array of conducting rods and a set of parallel conducting plates with circular perforated holes. It was demonstrated that both structures could be modelled as effective media due to their equivalent behavior as a continuous dielectric. A low refractive index, less than unity, was obtained with such structures at a certain frequency. Furthermore, the refractive index could be changed by varying the dimensions and positions of rods or the distances between the conducting plates.

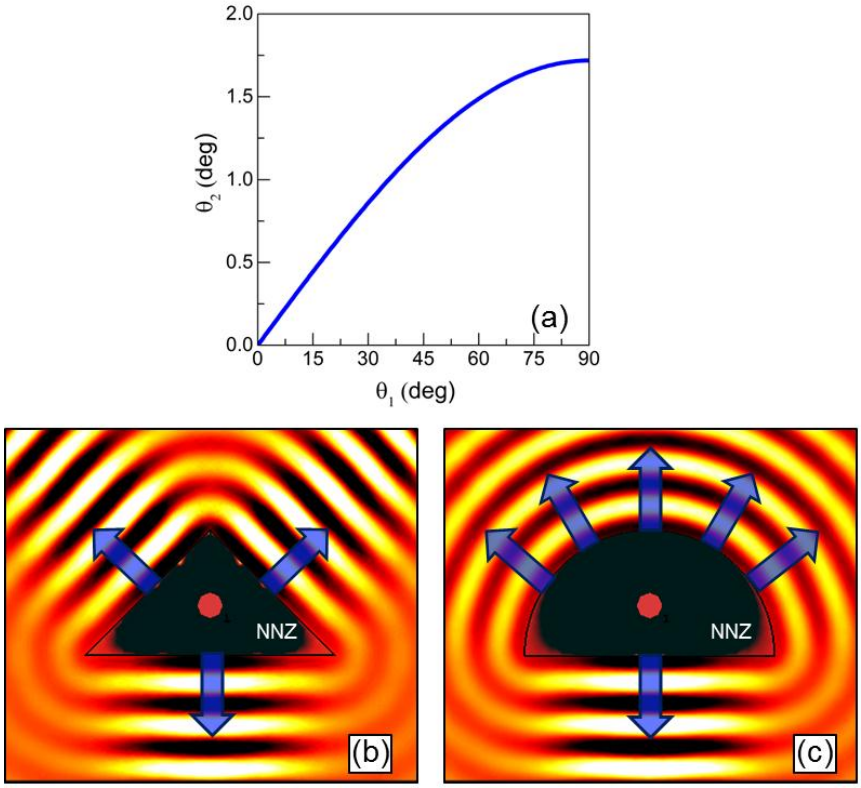

Figure 1.4. (a) θ_2 vs. θ_1 when an EM travels from medium 1 to medium 2 with n_2= 1 and n_1 = 0.01, respectively. Numerical results of the electric field distribution for two different structures demonstrating the idea shown in panel (a): a prism (b) and a hemi-circle (c) with n_1 = 0.01 surrounded by air

Within the realm of the NNZ MTMs, ENZ MTMs are becoming by their own merits a prominent subfield since last decade due to their extreme EM parameters and features. The small refractive index of ENZ materials has been thoroughly analyzed and it was reported that the relative effective permeability (μ_{reff}) may be greater than unity. However, the refractive index remains small, since the effective relative permittivity (ε_{reff}) is close to zero [BAHL 70]. Moreover, the very small phase variation inside ENZ materials results in a low propagation constant (β) and, consequently, a very large wavelength. It is worth saying that extreme parameters of permittivity (as ENZ) may be found in natural materials such as in polar dielectrics [RIVA 05] and highly doped semiconductors at mid infrared frequencies and also in noble metals when they are near the plasma frequency (at visible/ultraviolet) [JOHN 72].

These features have been exploited since the last century and the scientific community has reported several devices for different applications using ENZ materials. For instance, a narrow beam antenna was designed in 1971 by using a single slab with permittivity less than one [GUPT 71]. Moreover, several different unconventional features for the implementation of ENZ artificial materials have been proposed [SILV 06], [LOVA 06], [LOVA 07], [SILV 07a], [SILV 07b], [ENGH 07], [ALÙ 07b], [LIU 08], [EDWA 08], [ALÙ 08a], [ALÙ 08b], [POWE 09], [NAVA 12], [TORR 12a]. In 2006, M. Silveirinha and N. Engheta reported the "tunneling effect" of these materials [SILV 06], which was experimentally demonstrated afterwards [LIU 08]. This phenomenon occurs when an EM wave propagates inside a narrow channel filled with an ENZ material. It is based on the larger wavelength inside ENZ materials which allows wave propagation with low reflection loss (high transmission). Also, it was further reported that if at least one dimension of the ENZ-narrow-channel is electrically small the wave is able to tunnel through it [SILV 06], [LIU 08]. Based on this, this structure can be used to improve the efficiency of some waveguide junctions or bends. In order to illustrate the "tunneling effect", Fig. 1.5(a) shows one of the structures proposed by the authors.

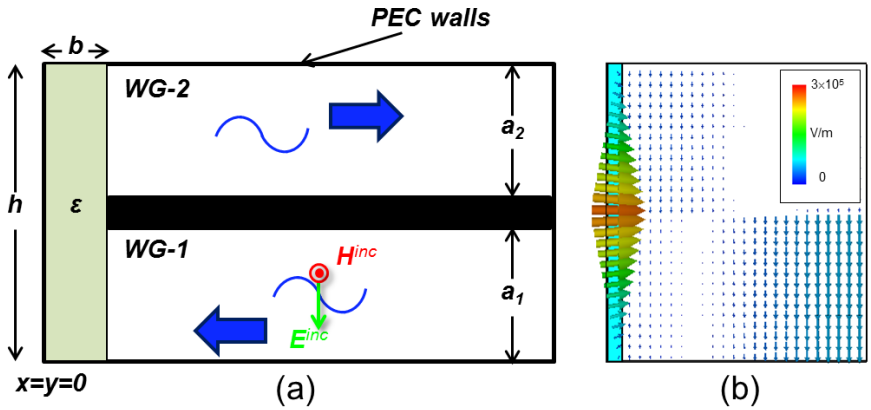

Figure 1.5. (a) Schematic representation of the structure proposed in [SILV 06] to demonstrate the tunneling effect: Two parallel-plate waveguides connected with an ENZ medium forming a bend of 180º. (b) Snapshot of the electric field distribution for the proposed structure.

The structure consists of two parallel-plates waveguides which are connected by an ENZ narrow channel. Both waveguides are placed one on top of the other to obtain a bend of 180˚. Also, it was considered that the distance between each waveguide is very small (black horizontal rectangle in the figure, $h = a_1 + a_2 \sim 2a$). Moreover, both

waveguides have the same dimensions and the EM wave propagates from waveguide 1 (WG-1) to waveguide 2 (WG-2). It was demonstrated that, effectively, the wave was able to tunnel through the ENZ material with very low reflection losses, as it can be observed in Fig. 1.5(b) where a snapshot of the electric field distribution is shown. This tunneling effect in narrow channels filled with ENZ materials is related with two features: squeezing and supercoupling effects which were also experimentally demonstrated [EDWA 08]. Based on these unconventional features of ENZ artificial materials, many applications have been proposed in different fields, such as: impedance matching [SILV 07b], [ALÙ 10], control of the tunneling effect [POWE 09], beam shaping [ALÙ 07b], sensing [ALÙ 08b] and nanocircuits [ENGH 07]. In Chapter 2, different ENZ MTMs are used in the design of lenses, beam steerers, power splitters and a sensor from microwaves up to optical frequencies.

1.2 Terahertz (THz), Plasmonics and Surface Plasmons

In this section it is shown an overview of two important aspects treated in this thesis: the THz-band and Plasmonics. First, the importance of the THz-band is presented along with the EM implications of this frequency regime in terms of the modeling of metals. Secondly, we will move to higher frequencies, such as the optical band, with the aim to describe the main features of surface waves supported by metals (known as Surface Plasmons) and the interaction between electromagnetic radiation and conduction electrons in them.

1.2.1 The THz band

The THz band comprises the region of the electromagnetic spectrum between 0.1 THz and 10 THz (wavelengths from 3 mm to 30 μm). In Fig. 1.6 it is shown the EM spectrum and the location of the THz band. As it can be observed, this band falls just in between two widely known and developed spectral bands: microwaves and optics. However, the THz band has not been as thoroughly studied as the other spectral bands due to the lack of appropriate testing technologies and fabrication. The most important limitation has been the lack of efficient generators and detectors which has historically hindered this band. Moreover, the material losses at these frequencies and the typical fabrication constraints of the order of hundreds of microns (quite small for conventional microwave techniques and too large for the standard photonic nanofabrication technology) have limited the development of new technology in the

THz [LEE 09], [SIEG 02]. In fact, these are mainly the reasons why this spectral range has been known as the "THz gap".

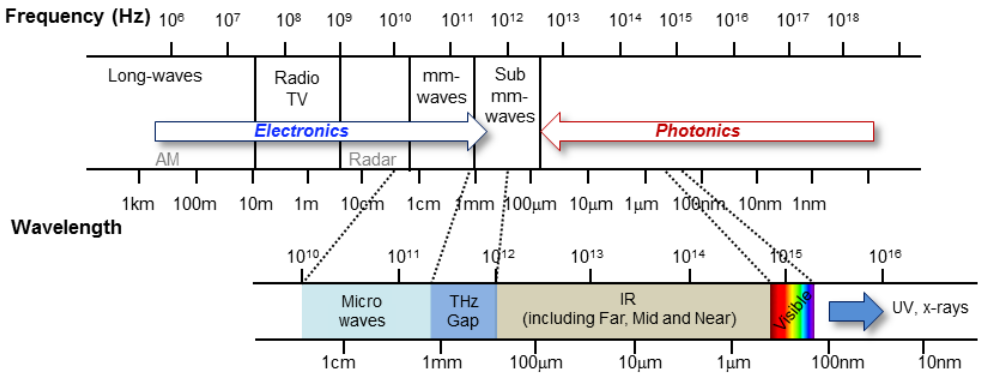

Figure 1.6. Summary of the spectral range from-long waves to UV and x-rays.

Recently, this spectral range has attracted the interest from both researchers and technologist [FERG 02]. This is due to the fact that it offers a great number of exciting applications in several sectors like medicine, sensing, security and biology, to name a few [CHEN 06], [HO 08], [CHEN 09], [RODR 16]. A summary of some applications and features of this spectral band are [DRAG 04], [REDO 13]:

- Many organic molecules have unique absorption features that are precisely in the THz range. Hence, THz spectroscopy is an excellent technique to study them. For example, DNA signature, DNA manipulation, gene diagnostics have been experimentally demonstrated using THz techniques.
- The capability of THz waves to penetrate most materials with a better spatial resolution than microwaves makes this spectral band more suitable for imaging applications.
- The THz radiation is non-ionizing which makes them safe for human operators and living tissue.
- Due to the smaller wavelengths of the THz waves (compared to microwave and millimeter waves), the design of miniaturized antenna array and circuits is an important advantage in the design of imaging devices such as THz cameras.

The interest in this spectral band started in the last century (1960s-1970s) with some studies about the response of materials under the excitation of ultrafast pulse

lasers [REDO 13]. However, it was in the present century (beginning of 2000s) where this band started to gain a great attention. Nowadays, the rapid development of THz technology has been possible thanks to the translation of revolutionary ideas and concepts taken from other regions of the EM spectrum. Therefore, even though there are still several technological improvements to be fulfilled, a great progress has been achieved to the extent that THz modulators [CHEN 09] and multiplexers [KARL 15] have been recently demonstrated. Thanks to these achievements and the growing interest in this spectral range, the "gap" has become an opportunity to fulfil the lack of devices within this range in order to improve the actual technology.

An important aspect that should be taken into account in the design of THz devices is the properties of the materials in this spectral range. By looking at Fig. 1.6, we can observe that the THz band is within two spectral bans where metals are differently modeled. For instance, metals are considered as materials with finite conductivity (σ) in microwaves while they behave as dispersive materials at optical wavelengths. Hence, it is interesting to show how metals may be modeled at different spectral bands.

The EM response of a material excited by an external EM field is commonly modeled using the well-known Drude model [DRUD 00] in honor to Paul Drude who proposed the model in 1900. This model takes into account the intra-band transitions considering a medium with a density of electrons per unit of volume (n_e) with mass m and charge e inside of a background of positive ions at fixed positions with the same density. It is assumed that, when collisions occur, the interaction of an electron with other electrons and with ions is negligible. These approximations are known as "the independent electron approximation" and "free electron approximation", respectively. In the presence of an external field, electrons move according to the three Newton's laws of motion. Moreover, collisions can be considered as instantaneous events which modify the velocity of a given electron. At difference with ordinary gases where collisions are considered between electrons, this model considers only collisions between the electrons and the fixed stationary ions. With this model, it can be found a relation between the current density $\boldsymbol{J}$ and the electric field ($\boldsymbol{E}$) which, after some algebraic operations using Maxwell's equations, results in the following complex relative permittivity (ε_r) of the medium:

$$\varepsilon_r = \varepsilon_\infty + \frac{\omega_p^2}{\omega\left(j\gamma - \omega\right)} \tag{1.10}$$

where ε_∞ is the permittivity at infinite frequency, $\omega_p = (n_e e^2/\varepsilon_0 m)^{1/2}$ is the plasma frequency and represents the frequency at which the permittivity becomes zero, ω is the operational frequency and γ is the collision frequency.

This model can be applied to conductors, semiconductors or plasmas. However, for a better approximation of the model of metals, the Lorentz model can be used together with the Drude model. The Lorentz model describes a dispersive material with multiple resonant frequencies taking into account the electronic inter-band transitions. The combination of both models gives rise to the well-known Drude-Lorentz model of materials [ALAB 13]. The relative permittivity of a material using this approach can be expressed as follows:

$$\varepsilon_r = \varepsilon_\infty + \frac{\omega_p^2}{\omega(j\gamma - \omega)} - \sum_{m=1}^{N} \frac{\varepsilon_{l(m)}\omega_{l(m)}^2}{\omega_{l(m)}^2 - \omega^2 - 2j\gamma_{l(m)}\omega} \tag{1.11}$$

where ε_l, ω_l and γ_l are the permittivity, plasma frequency and collision frequency of the Lorentz model, respectively, and m =1,2…N is an integer number representing the contribution of each Lorentzian oscillations.

Following with the different models of metals, an additional case is when metals are considered as perfect conductors. This is widely used in EM theory since they reduce the computational time of EM simulations and also simplifies the mathematics in different scenarios [RAMO 94]. Here, perfect conductors (also known as perfect electric conductors, PEC) are those with a high conductivity (approaching to infinity). This model is a good approximation at frequencies well below the plasma frequency.

In between the previous models, we can also find the case of "finite conductivity". This is commonly used at microwave and millimeter waves and the relative permittivity is described as follows:

$$\varepsilon_r = 1 - \boldsymbol{j}\frac{\sigma}{\omega\varepsilon_0} \tag{1.12}$$

with $\sigma = (n_e e^2/m\gamma)$. Note that this expression can be obtained directly from the Drude model described in Eq.1.10 when $\omega^2 << \gamma^2$.

The complex permittivity as a function of frequency for the case of silver and gold using both the Drude-Lorentz and the finite conductivity model (Eqs. 1.11-1.12) are shown in Fig. 1.7. The parameters used for both metals are shown in Table 1.1. By comparing these results, it can be observed that the real part of the complex permittivity for the finite conductivity models is quite different compared to the Drude-Lorentz cases for frequencies below to ~10 THz. However, the imaginary part agrees well with both models in the same spectral region. Also, the imaginary part dominates the response in both materials, compared to the real part which is smaller. Hence, the relative permittivity for frequencies < 10 THz can be approximated to the

values obtained with the finite conductivity model. However, above 10 THz, the differences in the imaginary part between the two models are higher.

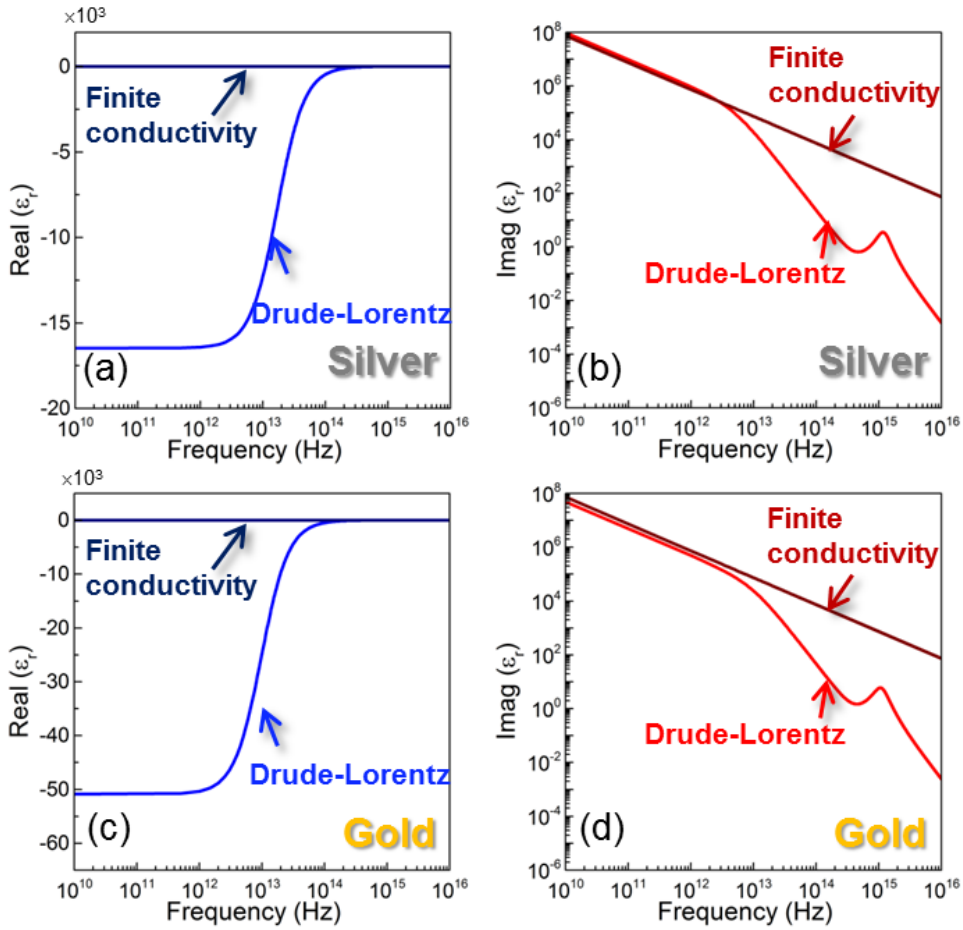

Figure 1.7. Real (left column) and imaginary (right column) part of the relative permittivity of silver (a-b) and gold (c-d) using the Drude-Lorentz model of metals (light curves) and the finite conductivity model (dark curves).

Drude-Lorentz		
Parameter	GOLD	SILVER
ε_∞	9.1	1.174
ω_p (rad/s)	1.3799×10^{16}	13.6973×10^{15}
γ (rad/s)	6.116×10^{13}	30.58×10^{12}
ε_l	3.2	1.69
ω_l (rad/s)	6.9115×10^{15}	7.5398×10^{15}
γ_l (rad/s)	1900×10^{12}	1839×10^{12}
Finite conductivity		
σ (S/m)	4.5×10^{7}	6.3×10^{7}

Table 1.1. Parameters of the Drude-Lorentz and finite conductivity models of Gold and Silver

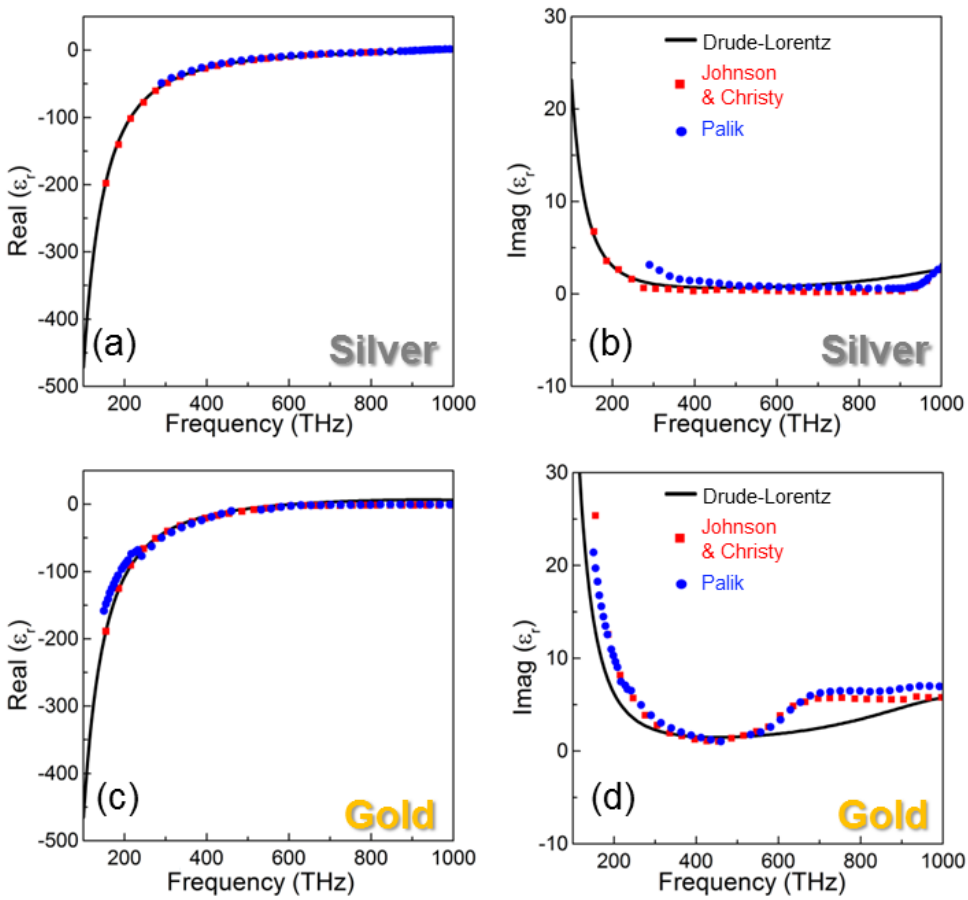

Figure 1.8. Real (left column) and imaginary (right column) part of the relative permittivity of silver (a-b) and gold (c-d) using the Drude-Lorentz model of metals (black curves) along with Johnson & Christy (red squares) and Palik's experimental data (blue circles).

Finally, we can evaluate the Drude-Lorentz model by comparing the complex permittivity with the experimental data. The analytical results are shown in Fig. 1.8 along with Johnson & Christy [JOHN 72] and Palik's experimental results [PALI 85]. As it can be observed, the models agree well for the case of silver. When gold is used, it can still be considered valid but a small deviation between 600-900THz is observed. This is due to the fact that gold is difficult to model within a wide spectral range as shown in Fig. 1.8 considering a single oscillation in the Lorentzian component of the model. Other approximations have been recently reported [VIAL 05], [ETCH 06] to overcome this issue. Therefore, for an efficient modeling of gold, an analytical fitting to the experimental data is preferable. It is important to note that the results at frequencies > 10 THz are better described for this model (in comparison with the finite conductivity case shown in Fig. 1.7). Therefore, the finite σ case is no longer valid for this frequency range and the Drude-Lorentz model should be used.

1.2.2 Plasmonics: Surface plasmons polaritons (SPP) and Localized surface plasmons (LSP)

The field of nanophotonics is dedicated to the study of the behavior of light on the nanometer scale. It can be considered as a branch of optical engineering which deals with optics. As we have studied previously, the response of metals varies depending on the frequency range. The particular features of the metals at optical wavelengths have become an exciting research topic, aimed to efficiently control the light interaction with metal particles or films. Within this realm we can find the subfield of Plasmonics which is mainly focused on the interaction process between the EM radiation and conduction electrons in metals. This process is explained by considering metals as dispersive materials with a permittivity following the Drude or Drude-Lorentz models. This allows accurately modeling the metals and to evaluate its performance at high frequencies where free electrons can be excited to have collective oscillations. Here, we will describe two important aspects of Plasmonics: surface plasmons polaritons (SPPs) and localized surface plasmons (LSPs).

SPPs consist of EM excitations at the interface between a dielectric and a conductor which are evanescently confined in the perpendicular direction [MAIE 04], [PITA 07]. They are TM waves with, i.e, $H_z = H_y = E_x = 0$, considering the propagation along the *z* axis (as it will be described in the following discussion). This phenomenon is a direct consequence of the dispersive permittivity of metals at higher frequencies. Therefore, at this spectral range, the field can slightly penetrate into the metals and can induce self-sustained excitations which may propagate closely confined to the metal near the interface between the dielectric-metal. The study of this phenomenon traces back to the end of the 19th century when Sommerfield analyzed the propagation of waves along the surface of conductors exhibiting a finite conductivity

while studying the problem of radio waves propagating over the surface of the Earth [SOMM 99]. In the 20th century, Ritchie predicted that self-sustained collective excitations of electrons on metal surfaces may exist evaluating the characteristic energy loss of fast electrons traveling in thin metal films [RITC 57]. Then, Powell and Swan demonstrated the existence of these collective excitation [POWE 59a], [POWE 59b] which were then called surface plasmons [STER 60].

To qualitative study the features of SPPs, we can consider the simplest geometry which consists of a flat interface between a dielectric with a positive permittivity and a metal. Both media are considered as semi-infinite. A schematic representation of the geometry is shown in Fig. 1.9(a,b). As shown, the SPPs are supported by this structure and they propagate along the *z* axis with an evanescent electric field at the interface of both materials.

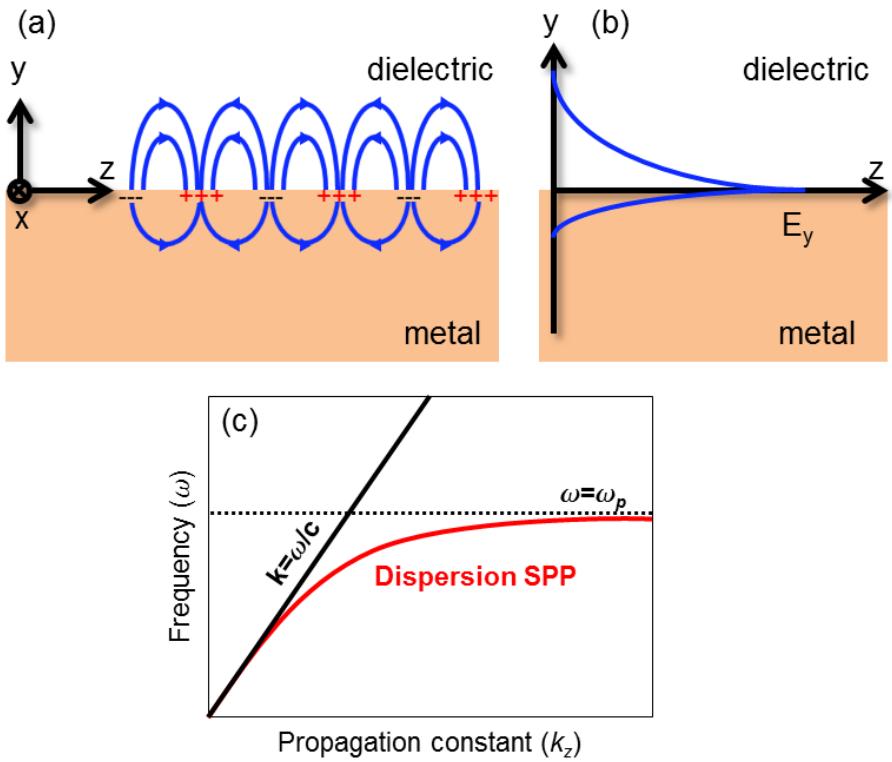

Figure 1.9. (a) Schematic representation of the SPPs along the surface of two semi-infinite media: dielectric (top) and metal (bottom). (b) Amplitude of the electric field, E_y, in a dielectric-metal interface.

In order to calculate the dispersion relation of the SPPs supported by this geometry, the Maxwell's equations should be applied to obtain the required wave equation. A complete explanation of this process can be found in [ISHI 90]. After applying the

correct boundary conditions, we obtain the following dispersion relation of SPPs (for a complete deduction see Appendix A):

$$k_z = k_0 \sqrt{\frac{\varepsilon_d \varepsilon_m}{\varepsilon_d + \varepsilon_m}} \tag{1.13}$$

where k_z is the propagation constant of the SPPs along the direction of propagation, k_0 is the wave vector of the wave in vacuum and ε_d and ε_m are the permittivities of the dielectric and metal, respectively. The results using Eq. 1.13 are shown in Fig. 1.9(c). As it can be observed, the propagation constant of SPPs is closer to the light line for lower angular frequencies. As the operational frequency increases, β_z moves to higher values compared to the light line. Therefore, since $k_z > k_0$, the dispersion curve is located at the right hand side of the dielectric's line cone which produces that the field decays evanescently in both media, as it can be observed in Fig. 1.9(b). An important aspect to be taken into account is the excitation of SPPs in practice. Due to the condition of SPPs $k_z > k_0$, an impinging EM wave under oblique incidence is not sufficient to excite SPPs. This is due to the fact that the projection of the wave number will be smaller than k_z. Therefore, different techniques should be applied such as grating and prisms [MAIE 04] and also dipoles with different polarizations [BALT 13], [RODR 13].

In addition to SPPs, localized surface plasmons (LSPs) are also an important aspect studied by plasmonics. LSPs are non-propagating excitations of conduction electrons in metallic nanoparticles. In order to excite LSPs, the size of the metallic nanoparticle should be smaller than the wavelength in the surrounding medium [MAIE 04]. This is due to the fact that with this condition the phase change of the EM field exciting the nanoparticle can be considered negligible. This idea is depicted in Fig. 1.10(a). Here, a metal sphere is excited with an EM wave with a wavelength longer than its size which allows the incident field be trapped within the metallic nanoparticle. It is important to note that LSPs are geometry dependent and depend on both the metal and shape of the nanoparticle. This feature has become an important field of research for biomedical, spectroscopy and sensing applications because of the strong field concentration achieved with different shapes [ANKE 08], [WILL 07], [PETR 11], [MAYE 11].

The capability of a nanoparticle to confine the incident wave on its geometry via LSPs can be evaluated using the absorption (P_{abs}), scattering (P_{scat}) and extinction concepts (P_{ext}). The first parameter describes the density of the flux of power that is trapped or absorbed by the particle. The second one is related to the total power scattered or reradiated when the incoming field interacts with the particle. The third one represents the total losses due to the power absorbed and scattered.

To better understand these parameters, we can study the response of the nanoparticle in the presence of the external field in terms of a superposition of incident and scattered fields. Let us consider a nanoparticle smaller than the incident

wavelength excited by an external field [as shown in Fig.1.10(a)] where the fields are defined as follows [GIAN 11]:

$$\boldsymbol{H}_{total} = \boldsymbol{H}_{inc} + \boldsymbol{H}_{scat} \tag{1.14}$$

$$\boldsymbol{E}_{total} = \boldsymbol{E}_{inc} + \boldsymbol{E}_{scat} \tag{1.15}$$

were $\boldsymbol{E}$ and $\boldsymbol{H}$ are the vectors of the electric and magnetic field, respectively and the the subindex *inc* and *scat* represents the incident and scattered fields. If we now apply the conservation of energy we arrive to the following expression:

$$\boldsymbol{S}_{total} = \boldsymbol{S}_{inc} + \boldsymbol{S}_{scat} + \boldsymbol{S}_{ext} \tag{1.16}$$

with $\boldsymbol{S}_{inc}$ and $\boldsymbol{S}_{scat}$ as the time-averaged Pointing vectors for the incident and scattered fields, respectively. The third term, $\boldsymbol{S}_{ext}$ accounts for the total energy that is present in the system due to the interference of the incident and scattered field. Finally, the absorbed and scattered power can be calculated by simply integrating Eq. 1.16 along a closed surface (Ω) around the nanoparticle. If a planewave is used to excite the nanoparticle, the integration of $\boldsymbol{S}_{inc}$ is zero and then $\boldsymbol{P}_{abs}$, $\boldsymbol{P}_{scat}$ and $\boldsymbol{P}_{ext}$ are defined as follows:

$$P_{abs} = -\frac{1}{2}\int_{\Omega} \mathrm{Re}\left\{\boldsymbol{E}_{total} \times \boldsymbol{H}^{*}_{total}\right\} \tag{1.17}$$

$$P_{scat} = \frac{1}{2}\int_{\Omega} \mathrm{Re}\left\{\boldsymbol{E}_{scat} \times \boldsymbol{H}^{*}_{scat}\right\} \tag{1.18}$$

$$P_{ext} = P_{abs} + P_{scat} \tag{1.19}$$

Finally the normalized powers are defined as the ratio between each value of P_i and the incident power ($\boldsymbol{S}_{inc}$). In Fig. 10(b), it is shown the normalized absorption for two different nanoparticles: a single cylinder and two cylinders with a gap between them. Silver is used for both structures with a permittivity modeled as in Fig. 1.8. The different spectral distributions of the absorption for both structures is because they are geometrically different. Therefore, a frequency shift in the LSP resonance for both structures is expected. Also, note that the absorption is higher for the case of the two cylinders due to the high field concentration within the gap, producing a higher absorption. For the sake of completeness, the magnitude of the electric field for both structures at each LSP is shown in Fig. 1.10(c,d).

The concepts discussed in this section will be used in chapters 2, 4 and 5 in the design of plasmonic structures and to evaluate the response of plasmonic nanoantennas in the quasi-static limit.

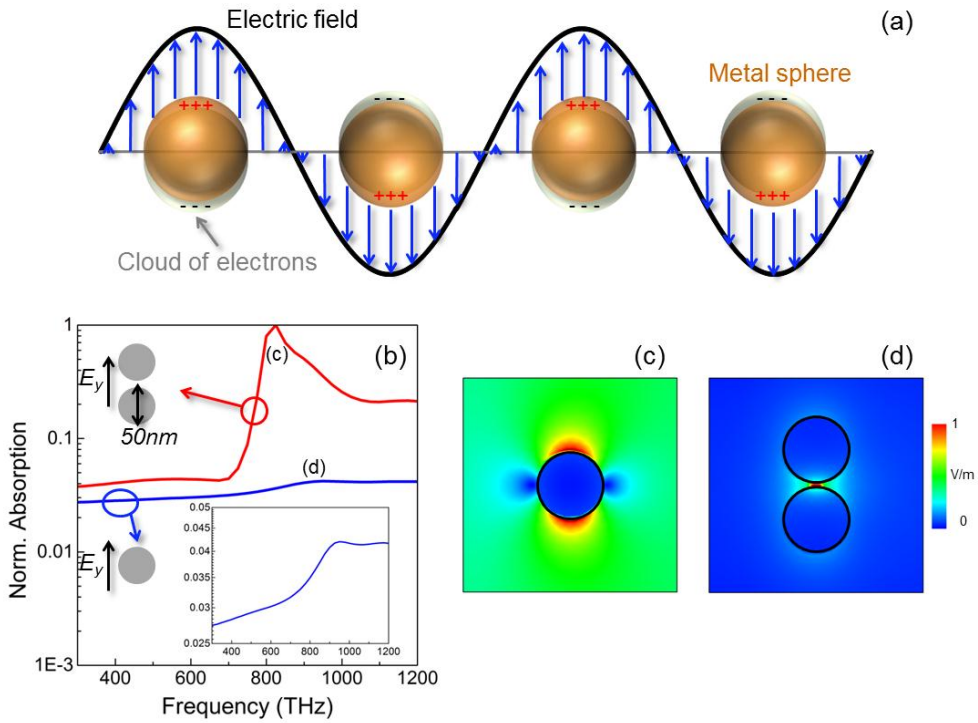

Figure 1.10. (a) Schematic representation of the LSP produced when an EM wave excites a metal nanoparticle with dimensions smaller than the incident wavelength. (b) Normalized absorption for a 2D cylinder with diameter 50 nm (blue line) and two 2D cylinders of diameter 50 nm with a gap of 2 nm between them (red line). The metal used for both structures is silver and they are excited with a vertically polarized plane wave. Magnitude of the field distribution at the peaks shown in (b) for the 2D cylinder (c) and the two cylinders with a gap (d).

1.3 Extraordinary transmission

The term extraordinary transmission (ET) refers to the high transmission peaks that can be observed in the cut-off region of subwavelength hole arrays (SHAs) or slit arrays (SSAs) or in a single aperture surrounded by a periodic groove pattern [BETZ 88], [EBBE 98], [TREA 99], [PORT 99], [MART 01], [TREA 02], [LEZE 02],

[GARC 03], [GARC 05]. It is called extraordinary transmission due to the fact that a single subwavelength hole with radius r in a metal screen of PEC under normal incidence with a wavelength λ should have a transmission proportional to $(r/\lambda)^4$. Hence, it is expected to obtain a very low transmission (opaque screen) when the hole is in cut-off due to the low coupling between the aperture and the radiative EM modes. However, in the end of the last century (1998), Ebbessen *et.al.*, experimentally demonstrated that a silver screen with perforated subwavelength holes can exhibit high transmission peaks within the cut-off region [EBBE 98]. This phenomenon was then called extraordinary optical transmission (EOT) because it was demonstrated at optical frequencies. This seminal work has inspired the scientific community and the physical explanation of this phenomenon is known, not only in the field of optics but also at microwaves millimeter waves [BERU 04a], [BERU 04b], [AKAR 04], [LOMA 04], [LOMA 05] [BERU 05b], [BERU 05c].

1.3.1 Dichroic filters and subwavelength hole arrays (SHAs)

The analysis of the transmission of light through subwavelength holes or gratings can be traced back to the beginning of the last century when Lord Rayleigh studied the transmission of light through these structures [RAYL 07] which were also studied by Wood and Synge [WOOD 02], [SYNG 28]. Almost 40 years after Lord Rayleigh's work, several studies analyzing the scattering by a single aperture were reported [BETH 44], [BOUW 54]. However, perforated plates gained more interest in the 50s, 60s and 70s in the field of microwave engineering [BROW 53], [ROBI 60], [CHEN 71], [CHEN 73] and infrared [ULRI 67] for their use as frequency selective surfaces (FSSs) demonstrating that a transmittance of 100% can be reached when working at wavelengths slightly above the period of the structure. The sizes of the holes for all the FSSs considered at that time were considerable larger for the frequencies of high transmittance. A complete analysis of these FSSs (also known as dichroic filters) is described in [GOLD 97].

Dichroic filters consist of periodically drilled closed-packed waveguides in a metallic plate. They are considered as FSSs because of their bandpass response [HESS 65], [MUNK 00] where the lower cut-off frequency is related to the cut-off frequency of the propagating modes in the waveguide while the higher cut-off is related to the redistribution of energy due to the periodic structure when a new diffraction order becomes propagating.

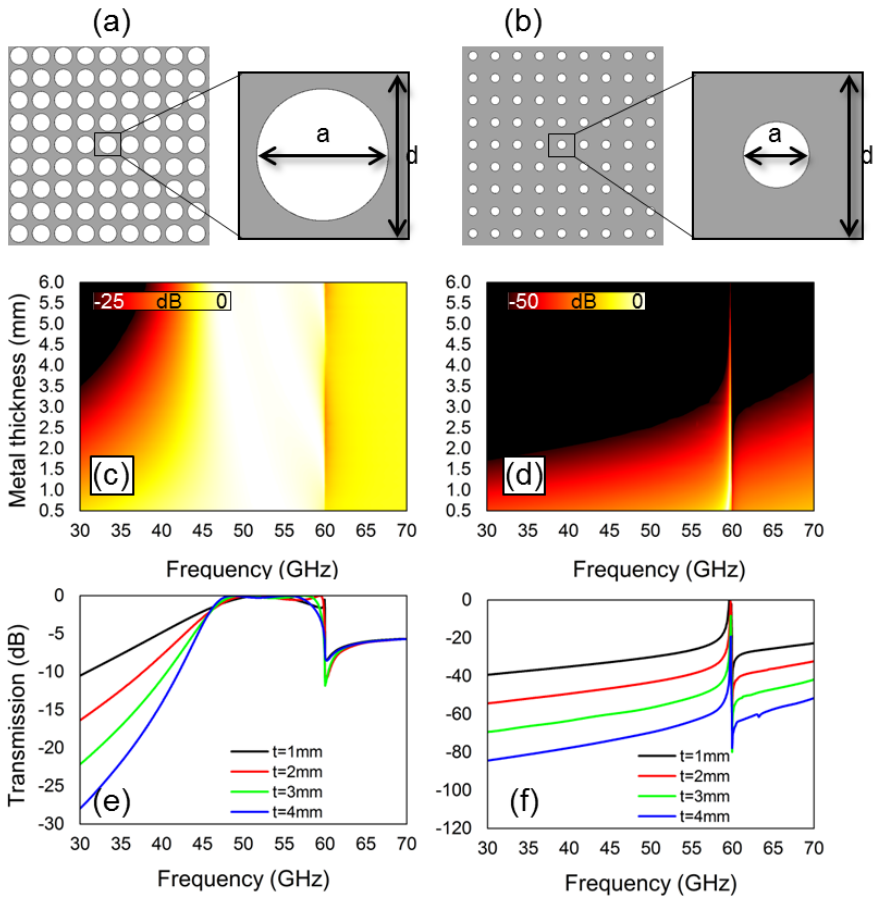

Figure 1.11. Schematic representation of a dichroic filter (a) and a SHA (b). Transmission coefficient as a function of the metal thickness (t) and frequency for the case of: (c) a dichroic filter with hole diameter a = 4 mm and periodicity d = 5 mm and (d) a SHA with hole diameter a = 2 mm and periodicity d = 5 mm. Transmission coefficient extracted from (c,d) for a dichroic filter (e) and SHA (f) with different t.

The main difference between Dichroic filters and SHAs is the density of the holes (the fraction of the unit cell occupied by the holes) [BERU 05a]: the periodicity of a dichroic filter is designed to be lower than the cut-off wavelength of the packed waveguides. On the other hand, SHAs are designed with a periodicity larger than the cut-off wavelength of the holes, i.e., since the size of the holes is smaller than the wavelengths of high transmission, the modes inside the holes are evanescent. For instance, in Fig. 1.11(a,b) it is shown a schematic representation of a dichroic filter

and a SHA, respectively. Here, it is clearly observed how the dimensions of the holes are smaller for the latter structure. Hence, SHAs are more sensitive to the thickness of the metal due to the evanescent decay of the fields inside the hole. This single metallic layer with SHAs has been deeply studied by several groups in order to derive a physical explanation of the ET. It has been demonstrated that an incident wave is able to excite surface waves due to the periodic configuration of the SHA which are then scattered into an infinite number of diffraction modes. Then, the energy tunnels through the holes evanescently to the other interface where the process is inverted, giving rise to the high transmittance peaks [GARC 07], [GARC 10]. Moreover, the SHAs have been further studied in terms of circuit models, providing an improved control of the EM response and design of these structures [BERU 07a], [MEDI 08], [MARQ 09a], [MEDI 10], [YANG 11], [RODR 10].

To better compare the performance of both structures, Fig. 1.11(c,d) shows the transmission coefficient as a function of the metal thickness and frequency for a dichroic filter with a hole diameter of a = 4 mm and a SHA with a = 2 mm. From these results, one can notice that the dichroic filter is working above the cut-off of the holes (f_c = 43.95 GHz) while the SHA works in the cut-off region (f_c = 87.91 GHz). Moreover, note that for the SHA, the transmission coefficient decreases when increasing the metal thickness, as expected, while this parameter is not very important for the performance of dichroic filters. For the sake of completeness, Fig. 1.11(e,f) shows the transmission coefficient for several metal thicknesses extracted form Fig. 1.11(c,d) where the it is more clear the influence of the thickness in the performance of both structures.

1.3.2 Stacked subwavelength hole arrays (SSHAs) and negative refraction

In addition to single layer SHA, a configuration based on multiple stacked metallic layers of SHAs has gained attention of several research groups [BERU 06], [BERU 07a], [ZHAN 05], [MARQ 09b]. This is due to the fact that it is able to support left-handed propagation (i.e., negative refraction index) with very low loss. This structure was first studied by Zhang [ZHAN 05] using a metal-dielectric-metal double layer SSHA.

Nowadays, this structure is known as *fishnet* MTM. It has become one of the most popular candidates to be used as negative refraction material due to the lower losses [BERU 06], [BERU 07a], [BERU 07b], [BERU 07c], [BERU 13] compared to other structures (such as the combination of SRRs and wires [SMIT 00]). With the aim to further improve its performance, the fishnet MTM with double in-plane periodicity was also proposed [NAVA 08], [BERU 09]. From a practical point of view, the main

features of this structure are: i) more compact devices can be designed and also ii) an EM wave with the electric field parallel to the smaller dimension of the unit cell will not propagate within the fishnet MTM; i.e., this structure actually filters the cross-polarization.

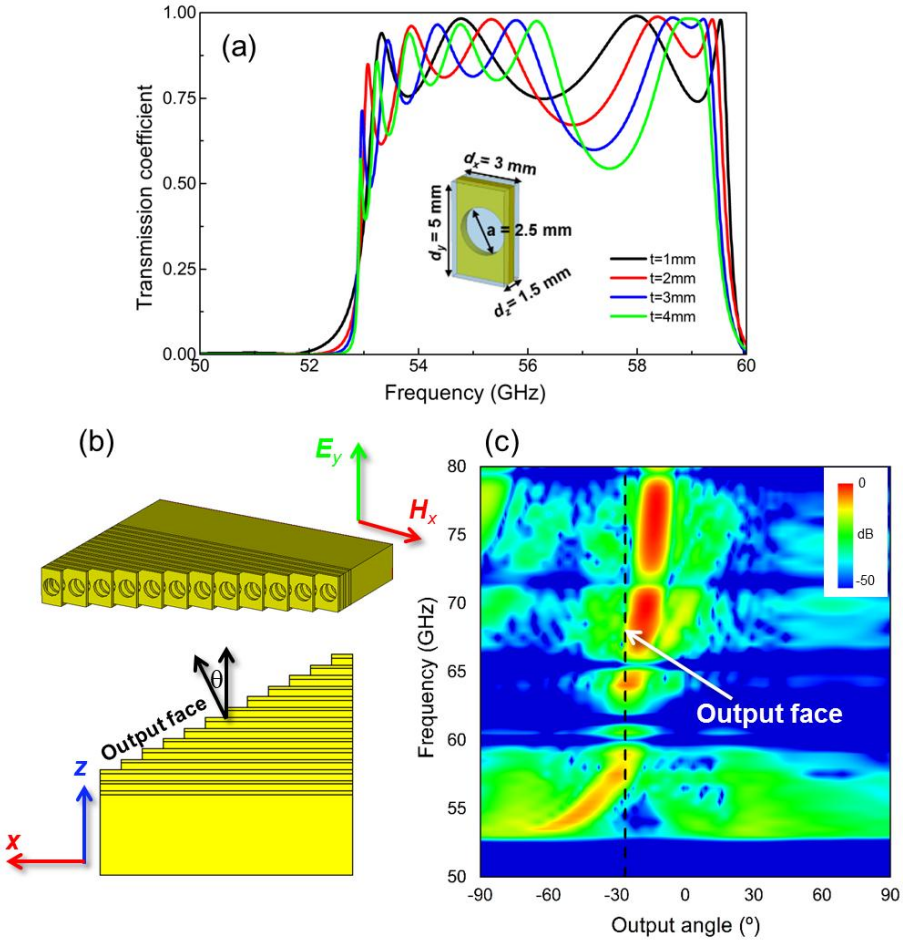

Figure 1.12. (a) Transmission coefficient for several number of perforated plates of a fishnet MTM with dimensions d_x = 3 mm, d_y = 5 mm, d_z = 1.5 mm, metal thickness w = 0.5 mm and hole diameter a = 2.5 mm. (b) Perspective and top views of a prism made of SSHAs. (c) Normalized radiation pattern as a function of frequency and angle for the fishnet MTM prism in (b).

To better understand the performance of this structure, Fig. 12(a) shows the transmission coefficient of an infinite fishnet MTM with double in-plane periodicity for several stacked plates. As it can be observed the number of peaks increase as more

metallic plates are stacked while the transmission coefficient is slightly reduced, as expected due to losses in the metal.

In 2008 and 2009, it was demonstrated that negative refraction can be achieved using this type of unit cell [NAVA 08], [BERU 09]. For this purpose, a prism made of SSHAs illuminated with a plane wave was proposed, see the schematic representation of the structure in Fig. 1.12(b) along with the results of the radiation pattern as a function of frequency and output angle θ in Fig. 1.12(c). Note that the main lobe of radiation changes to different angles when the frequency is modified. This is an expected result because of the dispersive behavior of the fishnet MTM which produces different refraction of the waves traveling through it at different frequencies. Moreover, note that for frequencies between 52 and 58 GHz, negative output angles are obtained while they are positive in the band of 65-80 GHz. The first band of transmission is related to the ET transmission (below cut-off) while the second one is related to the zeroth order diffracted beam for the case of propagating holes. Therefore, with this structure the output beam can be tuned from negative to positive angles by simply changing the operational frequency.

The fishnet MTM has been also studied in terms of the equivalent circuit theory [KAFE 07], [BERU 07a], [MARQ 09b], [KAIP 10], [CARB 10], [BERU 11a], [BERU 11b], [BERU 11c], [TORR 12b] and different practical devices have been reported such as prisms [NAVA 08], lenses [BERU 08], [NAVA 09b], [NAVA 10a] [NAVA 10b], [ORAZ 15a], [ORAZ 15b] demultiplexers, [NAVA 09a], absorbers [NAVA 11a] and unidirectional structures [RODR 16], to name a few.

Other important aspect of the fishnet MTM is that an ideally perfect free-space matching can be achieved because of the manipulation of both constitutive parameters (ε,μ). This performance is required in the design of lenses in order to reduce reflection losses. Therefore, several plano-concave lenses have been recently reported using the fishnet MTM [BERU 08], [NAVA 10a]. This structure will be used in chapter 3 in the design of more compact lenses.

1.4 Refractive elements: Focusing and steering waves

Now that we have presented an overview of MTMs, the THz band, plasmonics and ET, it is time to discuss about two refractive elements that will be used in this thesis: lenses and beam steerers. These two types of devices have become an interesting field of research due to their capability, when correctly designed, to control the direction of propagation of EM waves. They have been applied at microwaves [KOCK 46], millimeter-waves [NAVA 11b], THz [NEU 10], [SAVI 12], [NEU 13] and also in the

field of plasmonics [RADK 07], [ZENT 11], [LEE 15]. Therefore, it is important to show an overview and their operation principle since they will be shown in different chapters of this thesis applied at different spectral bands and materials.

Traditionally, a lens is considered as a transparent structure limited by two surfaces (commonly curves), which are able to refract an incident EM wave. The deviation that experiments a wave is directly related to the shape of these surfaces and the constitutive parameters of the lens material and the surrounding medium. These parameters are taken into account in the so-called Fermat's Principle of least time [SOLY 09] which is important in the lens design.

Conventional dielectric lenses can be classified as *converging* and *diverging lenses* according to the deviation that suffer the rays that travel through them (see Fig. 1.13).

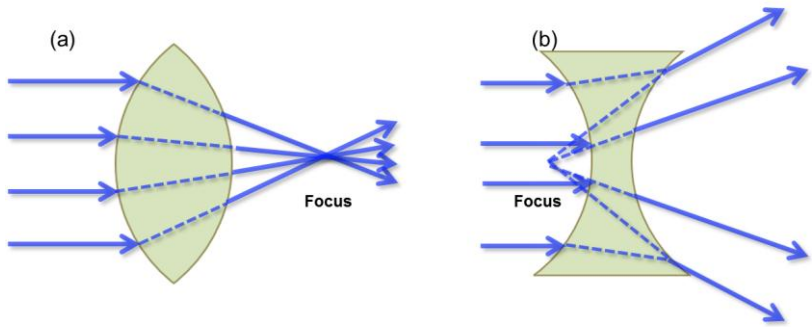

Figure 1.13. Schematic representation of a converging lens (a) and a diverging lens (b).

The *converging lenses* have their center thicker than the edges. This is the reason why they are traditionally named as convex lenses or positive lenses. When a set of parallel rays travels through a lens of this kind the rays converge in a point called "focus" [see Fig. 1.13(a)]. A magnifying glass is an example of these lenses.

On the other hand, *diverging lenses* have a center thinner than the edges. They are commonly called concave lenses or negative lenses. Their performance is also opposite to convex case: when a set of parallel rays travels through a lens with concave surfaces, the rays are "deflected" and "deviated" from the central ray [see Fig. 1.13(b)]. They generate a "virtual image" and the images are reduced from the original size.

Nowadays, the lens design with natural dielectrics has improved and many types of them have been fabricated for different applications [THOR]. Within this realm, artificial dielectrics have been also proposed for this purpose. For instance, the metal-lens antenna developed by Kock in 1946 [KOCK 46] was able to focus EM waves using conducting plates. Its operation principle depends mainly on the different phase velocity between the guided mode and the free-space propagation. By profiling the

arrangement of waveguides (rectangular or parallel plates) Kock showed that it is possible to achieve the required phase difference between adjacent waveguides that results in a focus. Therefore, the curvature of the metal-lens antenna is the opposite of an equivalent optical or dielectric lens, i.e., the lenses interchange their roles: a metal converging lens is made with concave surfaces and vice versa. This is because its refractive index can be lower than unity while the common dielectric lenses have refractive index higher than unity. This can be observed in Fig. 1.14, where a dielectric converging lens and a metal converging lens are represented. Note that both structures are able to focus an incoming plane wave but with different profiles. Also note in the same figure that the wavelength inside the dielectric lens (λ_d) is smaller than in free-space (λ_0). On the other hand, the metal-plate lens [Fig. 1.14(b)] has an opposite behavior to the dielectric lens. It can be observed that the wavelength inside the lens (λ_g) is greater than free-space value, as explained due to the phase velocity inside of the metal-plate/dielectric lens. For the case of the dominant mode of a transverse electric wave between conducting plates, which are parallel to the electric vector [KOCK 46], [RAMO 94], [POZA 04], this parameter can be expressed as follows:

$$v_p = \frac{c}{\sqrt{1-\left(\lambda_0/2a\right)^2}} \tag{1.20}$$

where c is the free-space velocity and a is the distance between the parallel metallic plates. Furthermore, the equivalent refractive index (n) can be expressed in terms of Eq. 1.20, as follows:

$$n = \frac{c}{v_p} = \sqrt{1-\left(\lambda_0/2a\right)^2} \tag{1.21}$$

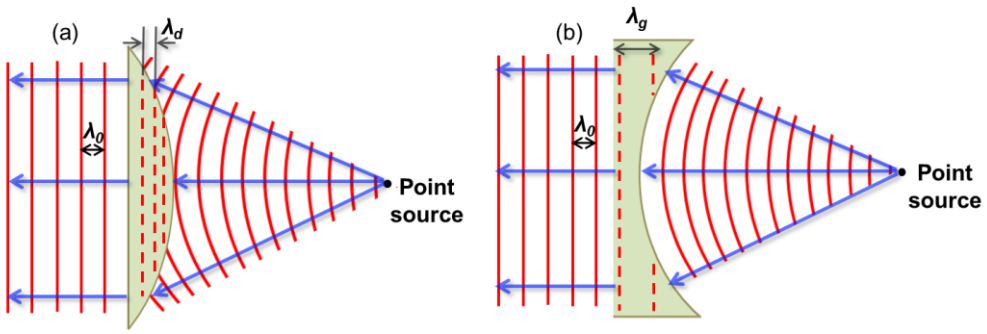

Figure 1.14. Schematic representation of: (a) convex dielectric and (b) concave metal-lens.

As it can be deduced from Eq. 1.21, n can be less than unity when $\lambda_0 < 2a$. Nowadays, the field of lenses [BORN 99] has benefited from the introduction of MTMs. Many types of artificial lenses have recently developed such as immersion lenses [CHAN 10a], [CHAN 10B], [CHAN 10C], novel lenses improving microwave and optical devices in term of high resolution [PEND 00], reduced reflection losses and impedance matching with free space [ALIT 08], or even classical metallic lenses revisited to improve their performance [BERU 08], [NAVA 09b], [NAVA 11b], [NAVA 11c]. Also, graded index lenses been proposed to make them more compact [PAUL 10], [NEU 10], [TORR 12a].

In addition to lenses, beam steerers are other type of refractive elements widely used in radio frequency (RF) and optics. They are used to change the direction of the waves. In optical applications, prisms and mirrors are commonly applied for this purpose. In RF, it is commonly achieved by changing the phase of the signals that feed the elements forming the system or by changing the position of the transmitter in a metal-lens antenna system (also known as mechanical beam steering).

Depending on the required direction or behavior of the beam, a specific type of beam steering should be used. There are different ways to steer EM waves. Fig. 1.15 shows some of them. MTMs have also been studied in order to design devices which can achieve Beam Steering and several structures have been recently reported [DEME 11], [LIN 08], [LIU 09], [OURI 09], [KWON 09].

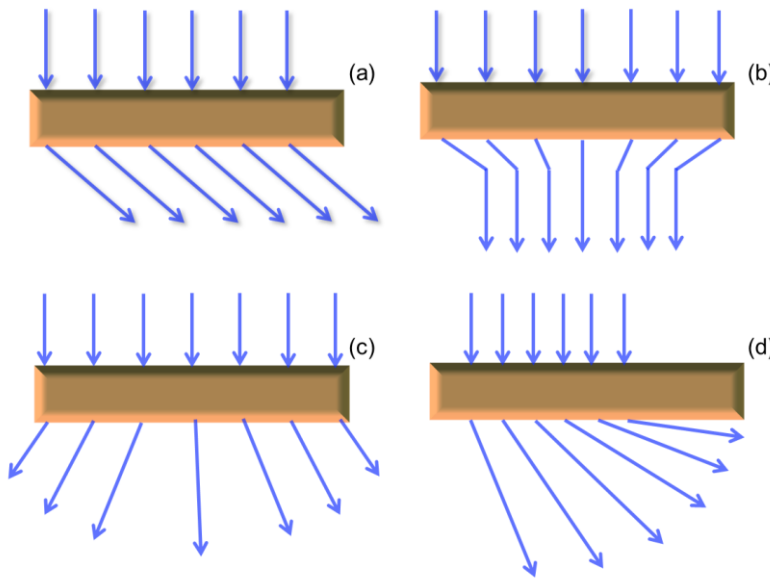

Figure 1.15. Schematic representation of different beam steerers depending on the direction of the output beam: (a) linear angle, (b) linear at 0º, (c) sectorial and (d) sectorial angle.

Chapter 2

Epsilon-Near-Zero metamaterial based devices

Since V. G. Veselago in 1968, proposed the possibility to construct materials with simultaneous negative permittivity (ε) and permeability (μ) values [VESE 68] and after the experimental demonstration more than 30 years later [SMIT 00], many studies have been made to tailor the EM response of artificial materials, so called MTM. The remarkable properties of these media have been applied in the design of novel devices for different applications such as in the field of lenses [PEND 00], antennas [GRBI 02a], [GRBI 02b] and recently invisibility cloaking devices [ALÙ 05], [LEON 06], [ALÙ 07c], [PEND 06], [LIU 11], [MONT 13], [ORAZ 15c]. Even though many researches and applications have been made using different types of MTMs, those with a near-zero permittivity, referred to as Epsilon Near-Zero (ENZ) MTMs have attracted the attention of the scientific community and are becoming, by their own merits, a prominent subfield due to their outstanding features such as fast-wave propagation and small phase delay [ALÙ 07b], [ALÙ 08a], [EDWA 08], [NAVA 12], [TORR 12a], as described in Chapter 1.

In this chapter, ENZ MTMs are used in the design of several practical devices. The chapter starts with an introduction about the theoretical principles of how to emulate an ENZ MTM by simply using a narrow hollow rectangular waveguide [ALÙ 08a]. Then, this structure is applied in the design of several devices: i) ENZ plano-concave lens with the capability to mechanically steer the radiation pattern, ii) a prism made to deflect an incoming plane wave to a fixed output angle, iii) ENZ-GRIN structures: beam steerers, power splitters and a plano-concave lens, iv) an ENZ based sensors for subwavelength dielectrics and v) ENZ lenses at optical frequencies.

2.1 Narrow hollow rectangular waveguides as an ENZ medium

In this section, it is shown how a rectangular narrow hollow waveguide can be used to emulate the response of an ENZ artificial material. The theoretical approach considering the waveguide as an effective medium is performed. Also its respose is numerically evaluated demonstrating that they can mimic the performance of an artificial ENZ medium.

2.1.1 How to synthesize an ENZ medium? The narrow hollow waveguide case

Recently, it has been reported that narrow hollow waveguides can be used as a realization of ENZ MTMs allowing the squeezing and tunneling of EM waves [SILV 06], [EDWA 08], [ALÙ07b], [SILV 07b]. Furthermore, it has been demonstrated that a channel with arbitrary cross-section filled with an ENZ MTM can be used to connect and match two larger waveguide sections [SILV 06], [ALÙ 08c], [POWE 09], [FLEU 13] as it can be observed in Fig. 2.1 [ALÙ 08a].

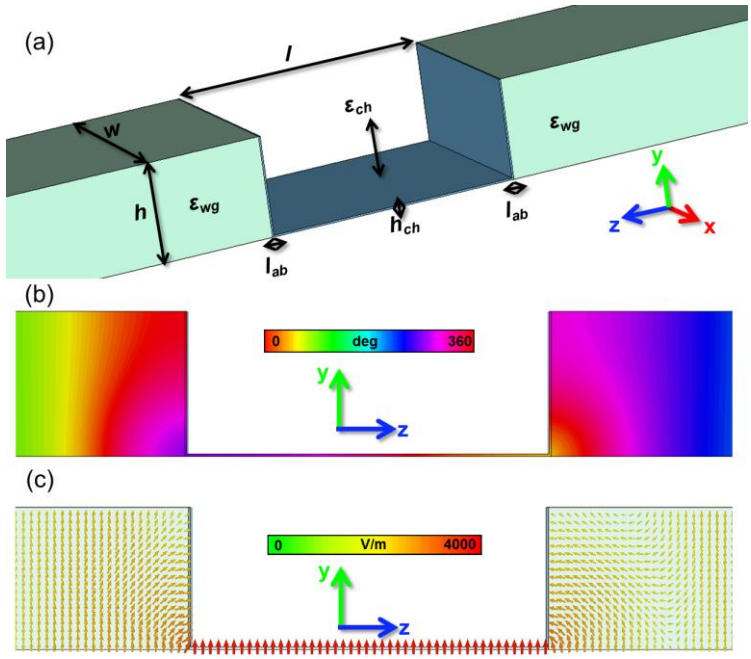

Figure 2.1. Demonstration of the supercoupling effect [ALÙ 08a]. (a) Geometrical representation of the structure and results obtained of (b) the phase of the magnetic field and (c) the electric field distribution.

The structure shown in Fig. 2.1(a) consists of two identical waveguides with uniform width (w = 10.16 cm) and height ($h = w/2$ =5.8 cm), filled with Teflon with effective permittivity ($\varepsilon_{wg}= 2\varepsilon_0$). Also, two waveguides (of length $l_{ab} = h/64$) filled with air (with permittivity $\varepsilon_{ch}= \varepsilon_0$) are used in order to tunnel the incoming wave into the narrow channel with length (l = 12.7 cm) and height ($h_{ch} = h/64$). Fig. 2.1(b) shows the results of the phase of the magnetic field at the tunneling frequency of 1.46 GHz and Fig. 2.1(c) shows a snapshot of the geometrical distribution of electric field at the same tunneling frequency. Note that a uniform phase distribution and amplitude can be observed along the narrow channel [see Fig. 2.1(b,c)] due to the supercoupling effect. Furthermore, it can be observed that the electric field inside the narrow channel is higher than outside due to the field "squeezing".

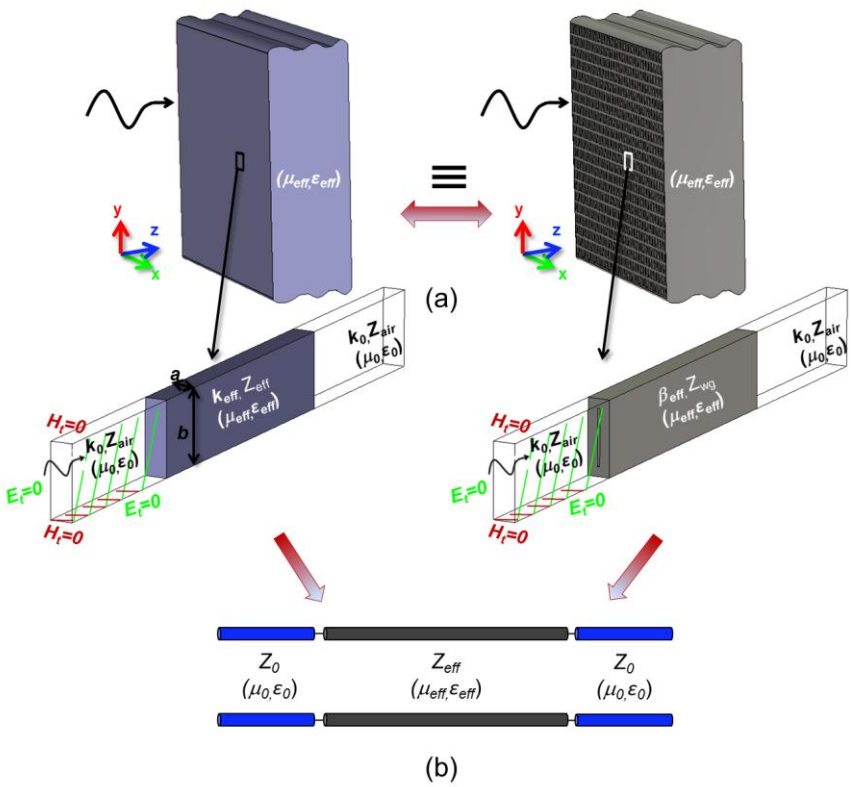

Figure 2.2. (a) Schematic representation of the equivalent problem considering an effective medium modeled as an array of waveguides. (b) Equivalent problem of an effective medium (left) and a waveguide (right) surrounded by air modeled as a transmission line (bottom).

But, how can a narrow hollow waveguide emulate an ENZ MTM? The key is to exploit the intrinsic dispersion of a waveguide. As it is known, a wave propagating in a material has a wavenumber k that is related to the intrinsic properties of the material (ε,μ), as:

$$k = \frac{\omega}{c} = \omega\sqrt{\mu\varepsilon} \tag{2.1}$$

where $\omega = 2\pi f$ is the angular frequency and c is the velocity of light in the medium ($c = 1/(\sqrt{\mu\varepsilon})$. Inside a waveguide, a similar parameter called the propagation constant (β) can be defined. It accounts for the wave propagation in the effective direction, which is usually parallel to the guide axis. In general, the modes in waveguides have a cut-off frequency (f_c) that delimit the propagation and cut-off regimes. For each mode, β depends directly on the cut-off frequency, as follows:

$$\beta = k\sqrt{1-\left(\frac{f_c}{f}\right)^2} \tag{2.2}$$

where k is the wavenumber in the medium filling the waveguide at the working frequency (f). The keypoint to model an effective medium using a waveguide, consists simply in identifying the effective wave propagation inside the waveguide with the propagation in a fictitious medium with effective constitutive parameters ε_{eff} and μ_{eff}, as is schematically shown in Fig. 2.2(a). Mathematically, this means enforcing equality in Eqs. 2.1 and 2.2:

$$\mu_{eff}\varepsilon_{eff} = \left[1-\left(\frac{f_c}{f}\right)^2\right](\mu\varepsilon) \tag{2.3}$$

The exact expression for ε_{eff} and μ_{eff} depends on the waveguide geometry and the operation mode. In the particular case of rectangular waveguides, the dominant mode has a TE nature with the electric field perpendicular to the largest hollow dimension. TE modes have a wave impedance that can be expressed as:

$$Z_{TE} = \sqrt{\frac{\mu}{\varepsilon}} \left(\frac{1}{\sqrt{1 - \left(\frac{f_c}{f} \right)^2}} \right) = \sqrt{\frac{\mu_{eff}}{\varepsilon_{eff}}} \tag{2.4}$$

From that expression we can find the values of ε_{eff} and μ_{eff}:

$$\mu_{eff} = \mu \tag{2.5a}$$

$$\varepsilon_{eff} = \varepsilon \left(1 - \left(\frac{f_c}{f} \right)^2 \right) \tag{2.5b}$$

Note that Eq. 2.5 is consistent with Eq. 2.3 because if we insert the values for μ_{eff} and ε_{eff} derived above, the equality of Eq. 2.3 still holds. From the previous Eq. 2.5a we find that μ_{eff} is equal to the permeability of the medium filling the waveguide which usually does not have magnetic response, so that $\mu_{eff} = \mu_0$. Additionally, Eq. 2.5b shows that the effective dielectric permittivity is dispersive. In particular, near cut-off ($f \to f_c$) ε_{eff} approaches zero. This is exactly the characteristic of ENZ MTMs.

We can establish a further interesting analogy to simplify the calculations. Consider the scheme of Fig. 2.2(a) with the electric field lying along the *x*-axis. With this polarization and assuming normal incidence, this scenario is totally equivalent to an artificial rectangular waveguide of mutually orthogonal electric and magnetic along the *x* and *y* axis, respectively (as shown in the same figure), where the plane wave is modelled by the fundamental transverse electromagnetic (TEM) mode supported by the artificial waveguide. As is well known, a waveguide operating with a TEM mode is equivalent to a transmission line, so the original setup can be reduced to a simple transmission line problem, as shown at the bottom of Fig. 2.2(b). Note that each part corresponds the input/output regions of air and the effective medium with wavenumber and normalized characteristic impedance (k_0,$Z_{air,}$) and (k_{eff},$Z_{eff,}$) in each region. The characteristic impedance is obtained as [COLL 00]:

$$Z_m = \frac{a}{b} \sqrt{\frac{\mu_m}{\varepsilon_m}} \tag{2.6}$$

where (μ_m,ε_m) represent (μ_0,ε_0) and (μ_{eff},ε_{eff}) depending on the transmission line section.

Similarly, we can study a uniform and infinite waveguide array [Fig. 2.2(a)] from a single unit cell (artificial waveguide) and analyze it from the transmission line perspective [COLL 00], [ALÙ 08a]. By taking the largest hollow dimension approximately equal to the metal ($h_y \approx d_y$) [ALÙ 08a], it can be considered that the effective medium with μ_{eff}, ε_{eff} fills the central transmission line, as shown in the bottom panel of Fig. 2.2(b). The normalized characteristic line impedance of the air Z_{air} and waveguide Z_{wg} regions are calculated using Eq. 2.6 and are presented in Eq. 2.7 and Eq. 2.8, respectively [ALÙ 08a],[EDWA 08], [TORR 12a].

$$Z_{air} = \frac{d_x}{d_y}\sqrt{\frac{\mu_0}{\varepsilon_0}} \tag{2.7}$$

$$Z_{wg} = \frac{h_x}{h_y}\sqrt{\frac{\mu_{eff}}{\varepsilon_{eff}}} \tag{2.8}$$

To have impedance matching both impedances must be equal ($Z_{air} = Z_{wg}$). This is achieved if:

$$\frac{h_x}{d_x} = \left(\frac{h_y}{d_y}\right)\left(\frac{\beta}{k_0}\right) \tag{2.9}$$

In the previous expression we have that $\beta << k_0$ when working in the ENZ region (near cut-off) and we have enforced $d_y \approx h_y$. This means that $h_x << d_x$. With this condiction we can simultaneously work under the ENZ MTM approximation and have impedance matching with free-space. This feature leads to the squeezing and supercoupling effects obtained with narrow hollow rectangular waveguides [SILV 06], [SILV 07], [TORR 12a].

It is important to highlight that this study has been performed assuming that all waveguides are identical. If waveguides are slightly different a deviation from the ideal response is inevitable. However, as it will be shown in the following sections, the local periodicity approximation (i.e. designing each waveguide of a non-uniform array assuming that it is a unit cell of an infinite array of identical waveguides) is sufficiently robust for the design of ENZ-based devices.

2.1.2 Performance as an ENZ medium

To further evaluate its response, the results of the normalized electric field (E_x) at the output of a narrow hollow waveguide with different lengths are shown in Fig. 2.3(b) (the dimensions of the waveguide are shown in the caption of the same figure). As it can be observed, peaks of high transmission are obtained close to the cut-off frequency of the dominant TE_{01} mode which are the frequencies related to the ENZ performance. Note that these peaks are close, but not exactly at the cut-off frequency due to the finite size of the waveguide along the propagation axis. Therefore, the exact condition $\varepsilon_{reff} = 0$ is not possible in practical devices. From the same figure, it is interesting to observe that several peaks are also observed above the ENZ frequency in all the cases. These peaks are related to the Fabry-Perot (FP) resonances which show a spectral response strongly dependent on the length of the waveguide (the longer the waveguide the higher the number of FP resonances within a specific spectral range).

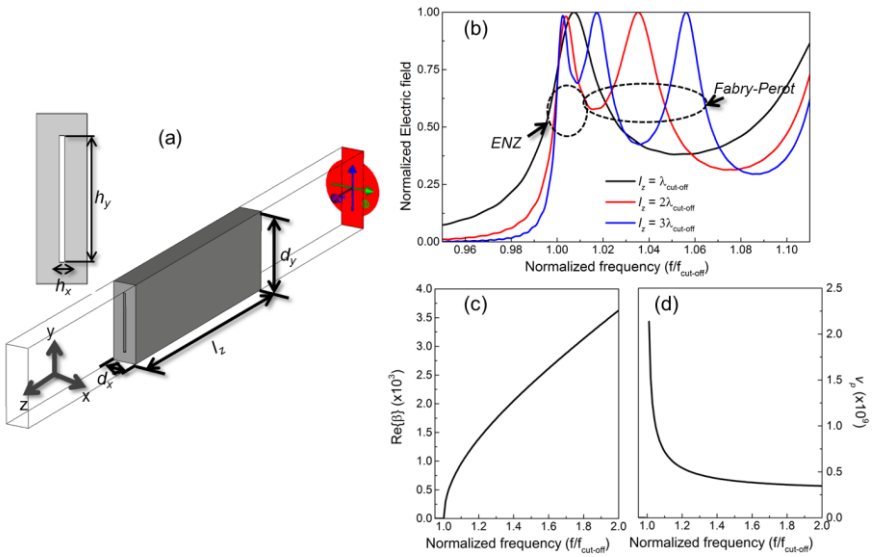

Figure 2.3. (a) Schematic representation of the narrow hollow waveguide. (b) Numerical simulations of the normalized electric field versus the normalized frequency at the output of a rectangular narrow hollow waveguide with dimensions: $d_x = 0.2\lambda_{cut\text{-}off}$, $d_y = (2/3)\lambda_{cut\text{-}off}$, $h_x = (1/50)\lambda_{cut\text{-}off}$, $h_y = (1/2)\lambda_{cut\text{-}off}$ and variable length l_z. Calculated propagation constant (c) and phase velocity (d) for the case of a waveguide with $h_y = (1/2)\lambda_{cut\text{-}off}$ using Eq. 2.10 and Eq. 2.11, respectively.

To better observe this performance, the magnitude of the electric field distribution and phase along the propagation z axis at each ENZ frequency for each length of the waveguide are shown in Fig. 2.4(a,c), respectively. From these figures, it can be clearly observed that the electric field is "squeezed" within the waveguide at the ENZ frequency [see Fig. 2.4(a)]. Moreover, note that almost the same phase as the input is obtained outside of the waveguide [see Fig. 2.4(c)]. This phenomenon corresponds to the mentioned "tunneling effect" which allows the waves to propagate inside an ENZ medium with an almost negligible phase variation [SILV 06], [SILV 07a].

Fig. 2.4(b,d) also shows the results of the magnitude and phase of the electric field along the propagation axis at each FP frequency for each length of the waveguide, respectively. Here, it is evident that the field distribution corresponds to the case of a FP resonance. As it is shown, the electric field inside of the structure is not uniform (compared with the ENZ frequency). Also, note that the phase changes inside the waveguide for all the lengths (l_z). Hence, the tunneling effect is not achieved at this frequency. For the sake of completeness, the results of the electric field distribution on the yz plane for both, ENZ and FP frequencies, are shown in Fig. 2.4(e,g,i) and Fig. 2.4(f,h,j), respectively, where the described features can be better appreciated.

Finally, let us evaluate the features of the narrow hollow rectangular waveguide in terms of the phase velocity ($v_p = \omega/\beta$). For a rectangular waveguide, in addition to Eq. 2.2, β can be expressed as follows:

$$\beta = k_0 \sqrt{1 - \left(\frac{\pi}{k_0 h_y} \right)^2} = \frac{2\pi}{\lambda_w} \tag{2.10}$$

where λ_w is the wavelength of the wave which propagates in the waveguide. Then v_p is:

$$v_p = \frac{\omega}{k_0 \sqrt{1 - \left(\frac{\pi}{k_0 h_y} \right)^2}} \tag{2.11}$$

As observed in Eq. 2.10, β does not vary linearly with frequency. Therefore, the phase velocity represented in Eq. 2.11 is not constant in frequency.

Fig. 2.3(c) shows the values of β and v_p for the case of a rectangular waveguide with normalized hollow dimension $h_y = (1/2)\lambda_{cut\text{-}off}$. Here it is more evident the intrinsic dispersion of the waveguide with both β and v_p having a non-constant response. This property permits to have a high variety of EM responses when they are used to synthesize a medium using an array of waveguides. Also, note that, when

working within the ENZ condition, $\beta \approx 0$ and then $\lambda_w \approx \infty$ (see Eq. 2.10), which is another characteristic of ENZ media (as explained in Chapter 1)

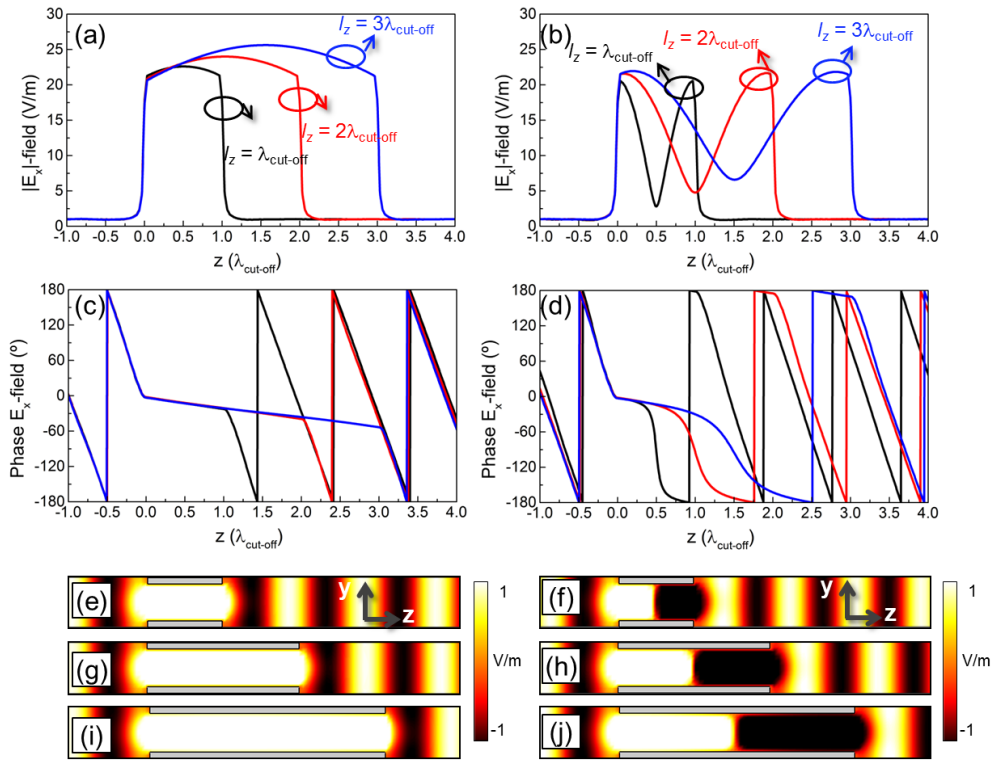

Figure 2.4. Magnitude (first row) and phase (second row) of the electric field at the ENZ (a,c) and FP (b,d) frequencies for the case of the narrow hollow waveguide shown in Fig. 2.3(a) with length $l_z = \lambda_{cut\text{-}off}$ (black), $l_z = 2\lambda_{cut\text{-}off}$ (red) and $l_z = 3\lambda_{cut\text{-}off}$ (blue). Electric field distribution on the *yz*-plane for each length l_z under study at each ENZ (e,g,i) and FP (f,h,i) frequency, respectively.

2.2 Profiled ENZ devices

Now that we have described how narrow hollow rectangular waveguides can emulate ENZ media, we can apply them in the design of practical devices. As it has been discussed in Chapter 1, an interesting feature of an NNZ material (and thus an ENZ medium) is that the EM waves at the output will be perpendicular to the surface of the material. This beam shaping capability is exploited here in the design of a

plano-concave lens and a prism using stacked narrow hollow rectangular waveguides. The mechanical beam steering of EM waves is demonstrated with the former case by changing the position of the source on the focal plane of the lens. Also, the performance of a prism made of an ENZ material is evaluated both analytically and numerically, demonstrating the capability to deflect an incoming EM plane wave at a fixed output angle.

2.2.1 Mechanical beam steering with an ENZ plano-concave metalens

The first structure that we will study is an ENZ plano-concave lens in a lens-antenna configuration. In [TORR 15], it can be found the numerical and experimental results of the focusing performance and radiation pattern of the lens which in fact was the first experimental demonstration of an ENZ lens based on the EM wave squeezing principle at millimeter waves. Here, the efforts will be centered in the evaluation of the mechanical beam steering capabilities [PACH 14a].

The fabricated plano-concave ENZ lens is shown in Fig. 2.5(a). It is designed with an array of narrow hollow rectangular waveguides with a periodicity of d_x = 1.4 mm and d_y = 0.5 mm, along x and y axes, respectively. The hollow aperture along the x axis of each single waveguide is $h_x = 1.1 \pm 0.025$ mm. With this dimension, the cut-off frequency of the dominant mode TE_{10} is 136.36 GHz. As explained in the previous section, to achieve impedance matching with free-space, a very small value of the dimension h_y must be chosen. Therefore, it is designed with $h_y = h_x/42 = 0.05 \pm 0.02$ mm (i.e., $h_y << h_x$), for a detailed illustration of the unit cell please refer to [TORR 15]. The whole lens is fabricated with total dimensions L_x = 76.2 mm, L_y = 86.2 mm and L_z = 40 mm, with a total number of 33 × 144 narrow hollow waveguides along x and y axes, respectively. As it has been described previously, metallic waveguides working near cut-off, can emulate an ENZ medium with near zero values of propagation constant and phase advance inside the medium. Therefore, since the EM waves emerging from the lens will be perpendicular to the surface, if one face of the lens is planar, the other one should be designed with a concave hemi-spherical profile [NAVA 11c], [NAVA 12] in order to convert a spherical phase front into a planar phase front or vice versa. Here, the concave profiled face is designed with a diameter d = 55.5 mm [TORR 15]. Notice that the inner surface of this face represents an ideal case for proper illumination by an antenna in comparison to convex lenses. The latter suffer from worse/lower illumination of the most distant edges of the lens as well as diffraction from them leading to undesirable side-lobes in the radiation pattern. The more effective illumination of the concave lenses yields to more homogeneous output phase fronts, and thus, higher antenna gain may be reached.

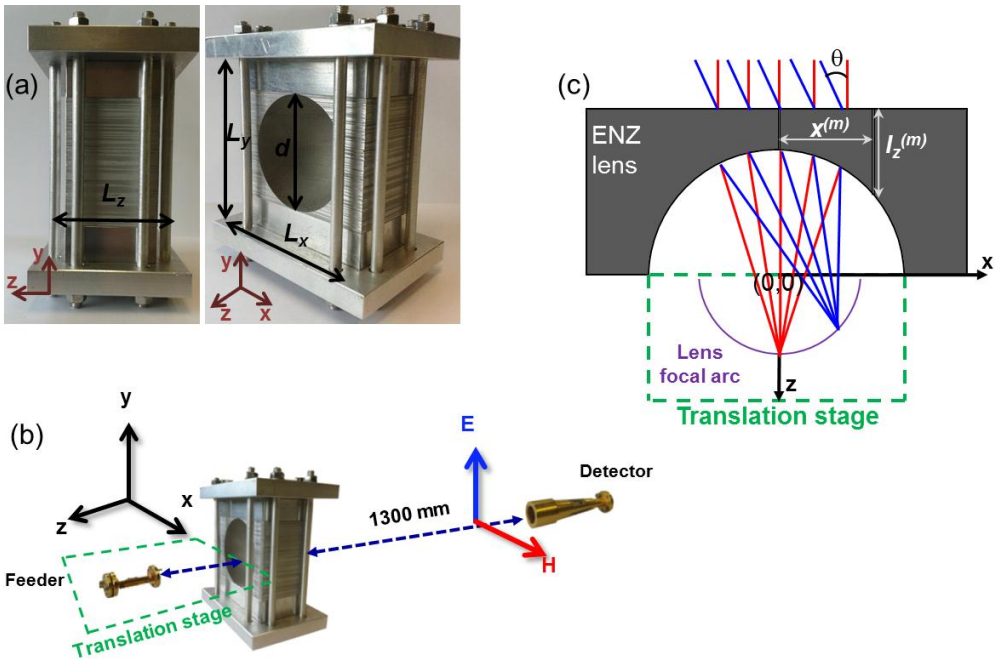

Figure 2.5. (a) Lateral (left) and perspective (right) view of the fabricated ENZ-lens at the D-band of the millimeter waves with total dimensions: L_x = 76.2 mm, L_y = 86.2 mm, L_z = 40 mm and d = 55.5 mm. (b) Experimental configuration used to characterize the radiation pattern of the lens. (c) Top view of the setup shown in (b) along with the lens focal arc (purple curve).

To evaluate the performance of the ENZ-lens under oblique incidence from the flat side of the lens, an equivalent effective isotropic 2D lens is studied analytically. We apply the Huygens-Fresnel approximation considering an array of isotropic dipoles emitting cylindrical waves and placed at the output of each waveguide. Moreover, each dipole emits with unit amplitude and phase (ϕ) calculated as:

$$\phi^{(m)} = k_0\left[\sqrt{\varepsilon_{reff}}\,l_z^{(m)} + \sin(\theta)md_x\right] \tag{2.12}$$

where, md_x is the position of each waveguide along the x-axis with m = 0,1,2,3..., as the waveguide number [see Fig. 2.5(c)], k_0 is the wave number in free-space calculated as $2\pi f/c$, θ is the angle of incidence of the incoming plane wave, ε_{reff} is the relative effective permittivity of the lens and $l_z^{(m)}$ is the length of the m^{th} waveguide calculated as:

$$l_z^{(m)} = \left(\frac{d}{2}\right) - \sqrt{\left(\frac{d}{2}\right)^2 - \left[md_x\right]^2} \tag{2.13}$$

In our case, the experimental ENZ frequency is 144 GHz (λ_0 = 2.083mm) which is above the cut-off frequency of the waveguides and is used as the operating frequency. At this frequency the effective permittivity value of the ENZ lens is ε_{reff} = 0.103 [TORR 15]. Based on this, the analytical results of the normalized power distribution on the *xz*-plane (in front of the concave face of the lens) are shown in Fig. 2.6 (a-g) when a plane wave impinges on the flat surface with the next input angles: θ = 0º, 3º, 6º, 9º, 12º, 15º and 18º, respectively. It is clearly observed that the focal spot is deflected on the *xz* plane.

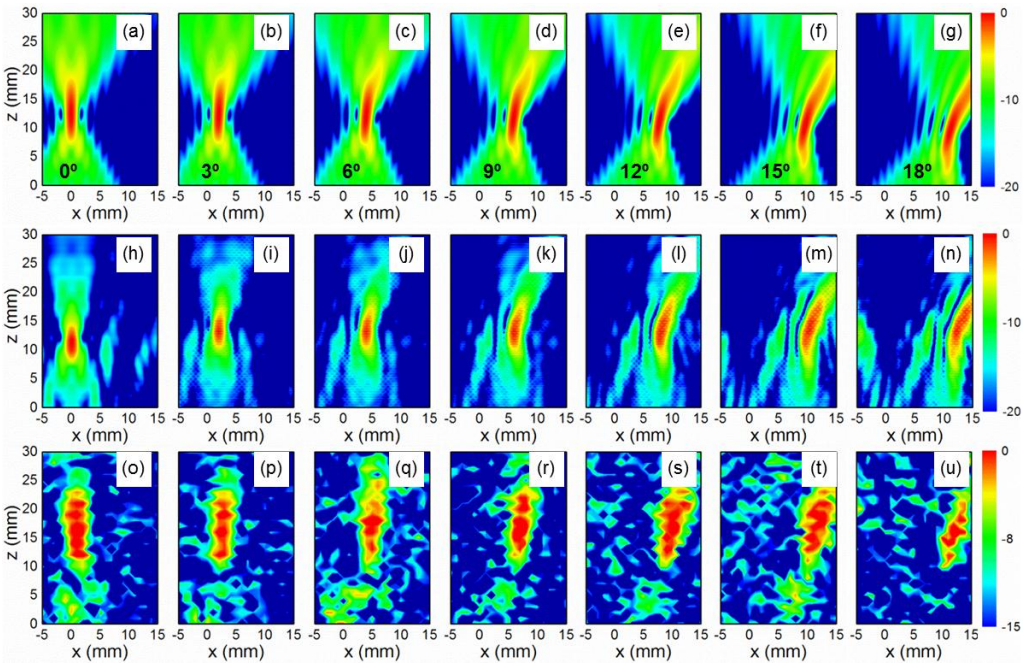

Figure 2.6. Normalized spatial distribution of power on the *xz*-plane for angles from 0º to 18º with a step of 3º: 2D analytical results using the Huygens-Fresnel approximation (a-g), 3D simulation results using the commercial software CST Microwave Studio® (h-n) and experimental results (o-u). The scale bar is in dB.

In order to validate the analytical model and extend the theoretical analysis, the fabricated 3D lens is modeled using the finite-integration software CST Microwave Studio®. To this end, the transient solver is used along with an extremely fine

hexahedral mesh with a minimum mesh size along the x axis of 0.0125 mm ($0.006\lambda_0$) and a total number of ~370×10^6 mesh cells. Aluminum ($\sigma_{Al} = 3.56 \times 10^7$ S/m) is chosen for the metallization and the lens is illuminated from its planar face with a vertically polarized (E_y) plane wave varying the angle of incidence. With this configuration, the simulation results of the normalized power distribution on the xz plane are presented in Fig. 2.6(h-n) for the input angles $\theta = 0^o$, 3^o, 6^o, 9^o, 12^o, 15^o and 18^o, respectively. As it is shown, these results confirm the deflection of focal spot demonstrating a good agreement with the analytical calculations using Huygens-Fresnel approximation.

The experimental characterization is performed using an ABmm™ Millimeter-Wave Vector Network Analyzer [see schematic in Fig. 2.5(b-c)] and the procedure is as follows: the lens is rotated at the desired output angle (θ = 0^o, 3^o, 6^o, 9^o, 12^o, 15^o and 18^o) with respect to a D-band horn antenna placed at 1300 mm (~$624\lambda_0$) from the planar face of the lens. After this, a 2D scan is performed on the xz-plane by moving a flange ended rectangular waveguide (WR-7) from –5 to 15 mm and from 0 to 30 mm along x and z axes respectively with a step of 1 mm. This is done for every illumination angle. This experiment allows us to reproduce the aforementioned simulation and thus to find experimentally the lens focal arc [see Fig. 2.5(c)].

The experimental results of the normalized spatial power distribution on the xz-plane are presented in Fig. 2.6(o-u) for the angles $\theta = 0^o$, 3^o, 6^o, 9^o, 12^o, 15^o and 18^o, respectively. By inspecting Fig. 2.6, it is clear that the analytical, simulation and experimental results follow similar trends. For a quantitative comparison, the positions of the maximum (i.e., focus) on the xz-plane for each study are summarized in Table 2.1. Note that for all the experimental cases, the positions along x are in good agreement with analytical and numerical results. However, there is some disagreement in the z position. This can arguably be due to the effect of the flange ended WR-7 and its phase center uncertainty, which is not considered in the theoretical study. Finally, the maximum deflection experienced by the focus happens as expected for $\theta = 18^o$ and is (x = 11.5, z = 9.9) mm, (x = 12.4, z = 12.8) mm and (x = 14.5, z = 16) mm for the analytical, simulation and experimental results, respectively.

Once the experimental lens focal arc is found, the flange ended rectangular waveguide is placed at each position of Table 2.1, and the angular distribution of the lens antenna radiation from the planar side is measured from -25^o to 10^o with a step of 0.5^o. The experimental results of the normalized radiation pattern are presented in Fig. 2.7 as blue curves (each plot is normalized to the maximum obtained at 0^o). Moreover, by using the Huygens-Fresnel approximation, the angular power distribution at the same distance as for experimental measurements (1300 mm ~ $624\lambda_0$) is calculated for each output angle and shown in Fig. 2.7 at the right of each experimental result as red plots. It can be observed that both results are in good agreement with the experimental output angles close to the values calculated analytically.

Results	Coord.	θ=0º	θ=3º	θ=6º	θ=9 º	θ=12	θ=15º	θ=18º
Analy.	x	0	2	3.9	5.9	7.8	9.6	11.5
	z	12.3	12.3	11.9	11.7	11.2	10.4	9.9
Sim	x	0	1.8	4	5.8	8	10.2	12.4
	z	11.6	13.2	13.2	13.2	13.2	13.2	12.8
Exp	x	1	2	4	6	10	11	14.5
	z	17	17	18	16	16	15	16

Table 2.1. Experimental and analytical results of the beam steering performance using the ENZ-lens. All the results are in mm.

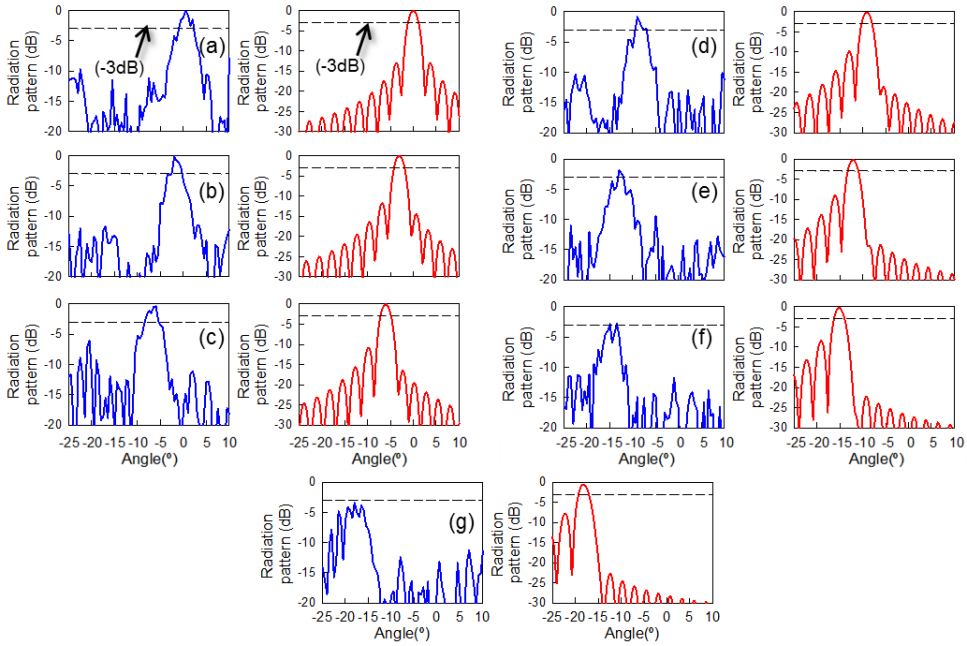

Figure 2.7. Experimental (blue curves) and 2D analytical (red curves) results of the normalized radiation pattern for the output angles: (a) 0º, (b) 3º, (c) 6º, (d) 9º, (e) 12º, (f) 15º and (g) 18º when the feeder is placed at the (*x*,*z*) coordinates of Table 2.1. The black dashed line on each plot corresponds to −3dB which is a standard of the maximum scan loss allowed for a suitable beam steering.

The analytical and experimental results of the beam steering performance of the ENZ-lens are also compared quantitatively in Table 2.2 in terms of the output angle, maximum normalized radiation power at the output angle (*MNRP*), half power beam width (*HPBW*) and side lobe level (*SLL*). It can be observed that the output angles are close to the original angle. Moreover, it is shown that the experimental values of the

HPBW are between 2.5-4.5º with the minimum for the output angle of 0º and maximum for the higher angle (18º) as expected. The same analytical *HPBW* is obtained for all the output angles because of the ideal conditions. The higher *SLL* is observed for an output angle of 18º in the experiment with a value of −4.85 dB, which is closer to the main lobe compared with the other angles. The experimental gain (defined as the ratio of the radiated power density in the direction of maximum emission and the power density radiated by an ideal lossless isotropic radiation that emits all the power fed by the source [NAVA 11b]) at the working frequency (144 GHz) has a maximum of 11 dB at 0º, which is obtained comparing the ENZ-lens with a horn antenna using the comparison method [IEEE 79]. Moreover, it is shown that the maximum normalized radiation power at 18º is below −3dB, which is used as a standard of the maximum scan loss allowed for a suitable beam steering. Based on this, the ENZ-lens here proposed has a suitable beam steering up to ±15º.

OA[a] (º)			MNRP[b] (dB)		HPBW [c] (º)		SLL[d](dB)	
Original	Exp.	Analy.	Exp.	Analy.	Exp.	Analy.	Exp.	Analy.
0	0.5	0	0	0	2.5	2.2	-10.57	-12.8
3	2	3	-0.05	-0.093	3.75	2.2	-11.58	-11.45
6	6	6	-0.36	-0.06	4	2.2	-5.3	-10.9
9	9	9.2	-0.84	-0.37	3	2.2	-10.5	-10
12	13	12.2	-1.88	-0.57	3	2.2	-9.5	-9.81
15	15	15	-2.87	-0.78	2.5	2.2	-11.3	-8.52
18	18	18	-3.45	-1.29	4.5	2.2	-4.85	-7.65

Table 2.2. Experimental and analytical results of the beam steering performance using the ENZ-lens.

[a] OA is the output angle
[b] MNRP is the maximum normalized radiation power at the output angle.
[c] HPBW is the half power beam width.
[d] SLL is the side lobe level.

2.2.2 Beam steering using an ENZ metamaterial Prism

One of the features of a narrow hollow rectangular waveguide as an ENZ medium is that it can be scaled up to higher frequencies such as THz frequencies. Therefore, the aim of this section is to briefly discuss a recently proposed structure made of such artificial material with the ability to change the direction of propagation of an incoming plane wave at THz frequencies [PACH 14b].

In the previous section it has been shown the performance of an ENZ plano-concave lens at millimeter waves and how in fact the narrow hollow waveguides work as an effective ENZ medium. In order to show that this can be also applied to the THz band, the unit cell used in this section is shown in Fig. 2.8(a). The hollow dimension

along the y axis is h_y =150 μm in order to have the cut-off frequency of the fundamental TE_{01} mode at 1 THz. Moreover, the hollow dimension along the x axis is chosen following the ratio h_x/h_y = 0.04.

With these considerations, the waveguide is simulated using the transient solver of the commercial software CST Microwave Studio®. The incident wave is polarized along x, E_x, and propagates along z-axis. Accordingly, top and bottom magnetic walls are used along with left and right electric walls to imitate an infinite waveguide array along both transversal directions (as in section 2.1). An electric field probe is placed at ($x = y = 0$ μm, z = 1500 μm), i.e., just at the output of the rectangular waveguide, in order to record the waveforms at this position and obtain the corresponding spectra by Fourier transformation (FT).

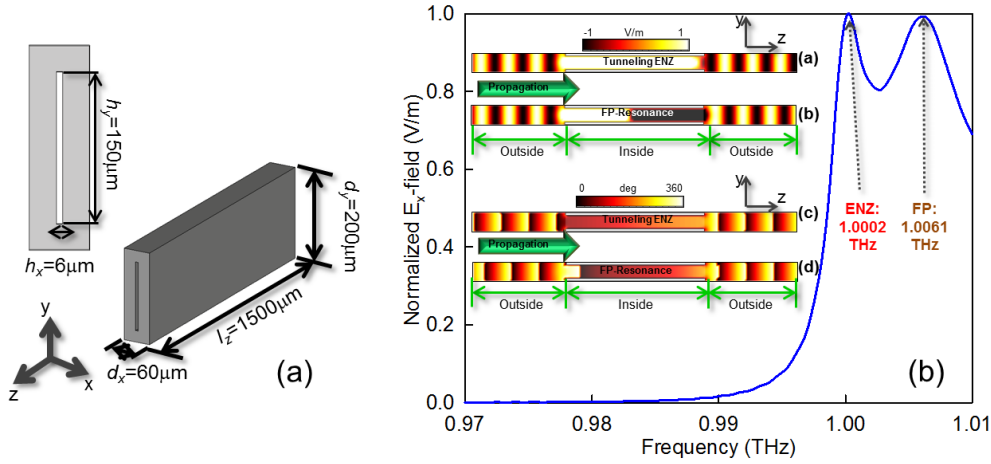

Figure 2.8. (a) Schematic representation, perspective and front view, of the narrow hollow rectangular waveguide used to emulate an ENZ medium at THz frequencies. (b) Simulation results of the normalized E_x-field magnitude (blue line) for the frequency range 0.97-1.01 THz. Insets from top to bottom: simulation results of the E_x-field magnitude for the tunneling frequency (1.0002 THz) and FP resonance (1.0061 THz), and simulation results of the H_y-phase distribution for the ENZ frequency and FP resonance.

The simulation results of the normalized E_x-field magnitude for the frequency range 0.97-1.01 THz are presented in Fig. 2.8(b). The maximum transmission appears at f_0 = 1.0002 THz (above and near cut-off). At this frequency, the propagation constant for the narrow hollow waveguide is $\beta_0 = \psi/l_z$ = 1.22 rad/1500 μm = 813.33 rad/m, much smaller than the wavenumber in free-space (k_0 = 20948.14 rad/m). With this value of β_0 and using Eq. 2.5, the relative effective permittivity obtained is ε_{reff} =

0.0015, confirming that is actually near zero (ENZ) and the waveguide mimics an ENZ medium at the fundamental band [SILV 06] working in the THz spectral range. The tunneling effect at this frequency can be observed in the inset of Fig. 2.8(b) where simulation results of the E_x -magnitude and H_y -phase are presented [inset (a) and (c), respectively]. The uniform E-field distribution along with the small phase variation observed for the H-field corroborates the ENZ behavior, in agreement with the results discussed in Fig. 2.4. As explained before, the other peak that appears at 1.0061 THz corresponds to a half-wavelength FP resonance [ALÙ 08a]. For the sake of completeness, the E_x -magnitude and H_y -phase are shown as insets (b) and (d) in Fig. 2.8(b) where the nature of this resonance can be clearly observed.

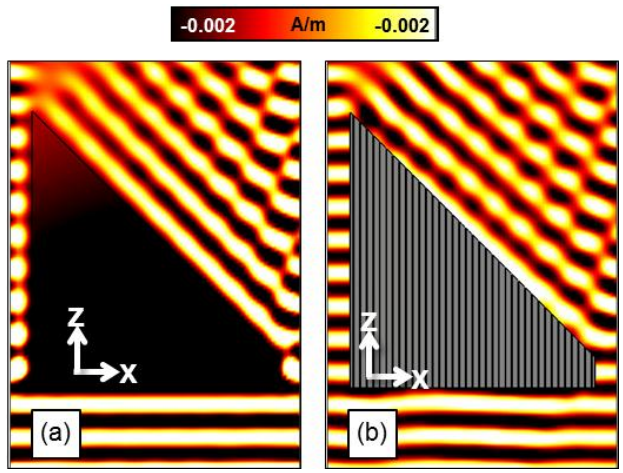

Figure 2.9. Simulation results of the H_y-field distribution of: (a) an isotropic homogenous zero refractive index (impedance-matched) prism with its output face cut at 45º, and (b) an ENZ prism made with stacked narrow hollow rectangular waveguides with a cut of 45º at its output.

Now that we have shown that this structure can be also used at THz frequencies, we can follow the same idea as the plano-concave lens and design a structure with a profiled output face in order to deflect an incoming plane wave (at 45º in our design). Hence, we can design a beam steerer (i.e., a prism) by simply stacking several narrow hollow rectangular waveguides.

The structure is shown in Fig. 2.9(b) and consists of 37 waveguides with the same transversal dimensions as the unit cell described before [see Fig. 2.8(a)] and a length l_z which varies from 280 μm to 2500 μm. Since the electric field lies on the xz-plane, the structure is infinitely replicated along the y-axis by imposing top and bottom magnetic walls in the numerical analysis. Moreover, open boundaries (i.e. perfectly matched

layers) are selected for the other planes. Simulation results of the H_y -field at the ENZ frequency (f =1.0002 THz) are presented in Fig. 2.9(b). It can be observed that the wavefront actually follows the inclination of the output face. In order to compare this structure with the ideal case, simulation results of the H_y-field distribution of an isotropic homogeneous zero refractive index slab ($\varepsilon = \mu = n \sim 0$) is shown in Fig. 2.9(a). The performance of both structures is almost identical, demonstrating that the prism emulates an ENZ medium.

2.3 ENZ graded index (GRIN) structures

A major drawback of the designs shown in the previous section is their relatively large volume given that one surface must be profiled depending on the application. This problem can be reduced by applying the graded index technique (GRIN) [SMIT 05a], [TORR 12a] so that both faces of the structure are planar instead of profiled, reducing highly the volume of the structure. In this section, several ENZ-GRIN structures are designed and discussed: beam steerers, power splitters and a plano-concave lens working at THz frequencies.

2.3.1 Beam steers and power splitters

Here we will discuss different ENZ-GRIN structures with the ability to deflect an incoming plane wave at a desired angle. We start the study with the design of a beam steerer with parallel faces or uniform length (l_z) using stacked narrow hollow rectangular waveguides [PACH 14b].

The refractive index of each waveguide is changed by simply tuning their hollow dimensions so that the phase at the output is gradually modulated. Thus, each waveguide must be tuned to give a particular phase delay at the output. This phase delay depends on the operational frequency, waveguide location and the phase delay inside of a reference waveguide. The behavior of the beam steerer can be easily obtained from ray tracing assuming that the slab is discretized in m+1 waveguides with a periodicity d_x. This is schematically shown in Fig. 2.10(a). Here md_x is the distance between the reference waveguide (rightmost waveguide) and each one of the array elements, and d_i is the excess distance travelled by the wave emitted by each waveguide with respect to the reference. The dimensions of the reference waveguide are the same as those shown in Fig. 2.8(a). With these considerations, we end up with the following equation:

$$\Delta\Phi^{(m)} = \beta^{(m)} l_z = \beta_0 l_z - k_0 (m d_x) \sin(\theta) + 2\pi\alpha \tag{2.14}$$

where β_0 is the propagation constant of the guided mode of the rightmost waveguide used as reference, $\Delta\Phi^{(m)}$ is the phase delay difference between the m^{th} waveguide and the reference one, $\beta^{(m)}$ is the propagation constant at the position md_x, and α is an integer number α = 1,2,3,… which represents a phase change of $2\pi\alpha$. Moreover, by using Eq. 2.10 it is straightforward to fulfill Eq. 2.14 by tuning the height of each hollow $h_y^{(m)}$. So far, the design enforces certain $h_y^{(m)}$ for each waveguide. However, $h_x^{(m)}$, the width of each hollow, is still a free parameter that can be used to impedance match each waveguide to free-space and minimize Fresnel reflection losses of the overall GRIN structure, as detailed before. The free-space matching is then achieved using Eq. 2.9 for each waveguide in the array.

The ENZ-GRIN beam steerer is designed to work at f ~ 1 THz (λ_0 ~ 300 μm) with the following dimensions: thickness $l_z = 5\lambda_0$ = 1500 μm, total width $10\lambda_0$ (which means m+1 = 50 waveguides) and θ = 45º. The $h_y^{(m)}$and $h_x^{(m)}$ dimensions of each waveguide are straightforwardly computed using Eqs. 2.9, 2.10 and 2.14. For the numerical analysis, the finite-integration software CST Microwave Studio® is used applying the same boundary conditions as the previous prism, i.e., top and bottom magnetic walls and open boundary conditions on the right- and left-hand side of the simulation box. Also perfect electric conductor (PEC) is chosen for the steerer. The designed structure is shown in Fig. 2.10(b).

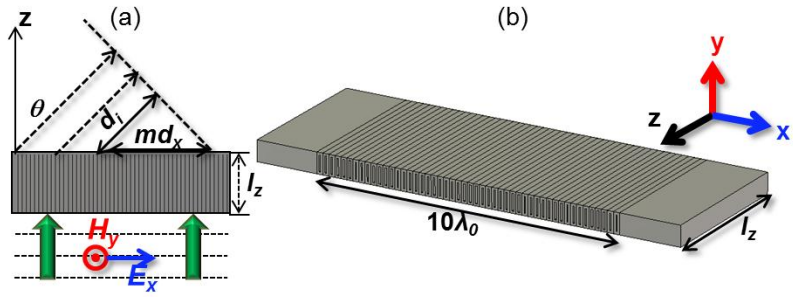

Figure 2.10. (a) Geometrical representation of the graded index beam steering structure. (b) Designed ENZ-GRIN structure for an output angle of 45º.

Simulation results showing the H_y-field distribution are presented in Fig. 2.11(b) and compared with analytical calculations using the Huygens-Fresnel approximation of isotropic point sources placed at each waveguide output position, with unit amplitude and phase, calculated as Eq. 2.15, that emit a cylindrical wave [Fig. 2.11(a)].

$$\phi^{(m)} = k_0 \sqrt{\varepsilon_{reff}^{(m)}}\, l_z \tag{2.15}$$

By applying this principle, the angular distribution of the power at a distance r for angles from 0º to +90º is calculated. The value of r has been selected to be 100 mm ($333.33\lambda_0$) in order to calculate the output angle far away from the steerer [see bottom panel of Fig. 2.11(a)]. These results demonstrate that both structures allow deflecting the incoming 0º plane wave to an output angle of 45º. Moreover, from Fig. 2.11(b), it can be seen that the wave front at the output has a better quality than the one observed with the prism in Fig. 2.9(b) because the edge diffraction has been minimized by placing more metal on both sides of the steerer, as shown in Fig. 2.10(b).

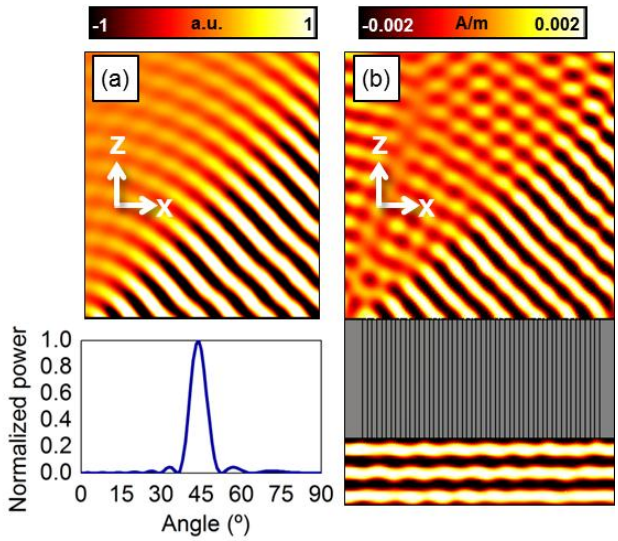

Figure 2.11. (e) Analytical results of the field distribution using the Huygens-Fresnel principle in *xz*-plane along with the normalized power distribution at a fixed distance of r = 100 mm from the steerer for angles from 0º to 90º in cartesian coordinates (bottom panel). (b) Simulation results for the ENZ-GRIN beam steerer designed with stacked rectangular waveguides using CST Microwave Studio®.

A standing wave at the input of the beam steerer reveals some impedance mismatch which is due to the design is done using the local periodicity approximation (as explained in section 2.1). Hence, the final design is not perfectly matched to free-space due to the different hollow dimensions of each stacked waveguide [TORR 12a]. The reflection coefficient ($|\Gamma|$) can be calculated as $(A_{max}/A_{min}) = (1+|\Gamma|)/(1-|\Gamma|)$ where A_{max} and A_{min} are the maximum and minimum values of the field magnitude. The approximate value obtained is $|\Gamma| = -7.2$ dB which represents a moderately good impedance matching. For the sake of comparison, a common millimeter-wave dielectric quasi-optical element made of silicon, with relative permittivity $\varepsilon_r = 11.9$, has $|\Gamma| \sim -5.5$ to -5.19 dB [FILI 93], [RAMA 98].

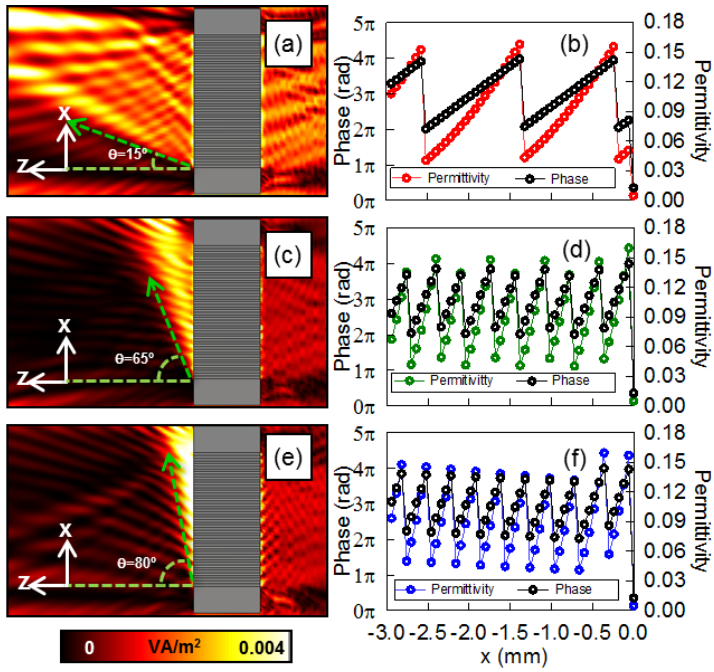

Figure 2.12. Numerical results of the power distribution on the *xz*- plane for several beam steerers designed for output angles of: (a) 15º, (c) 65º and (e) 80º. Phase delay difference introduced by each waveguide along with the corresponding values of the relative effective permittivity for the beam steerers designed for output angles of: (b) 15º, (d) 65º and (f) 80º.

Following the same procedure, several ENZ-GRIN beam steerers are designed for output angles of 15º, 65º and 80º. The numerical results are shown in Fig. 2.12. Also, the phase delay difference introduced for each waveguide along with the relative effective permittivity, calculated from Eq. 2.5b, are plotted at the right side of each structure. From these results, it is clear that the output angle for each case is in good agreement with the designed value. Moreover, ε_{reff} is close to 0 (maximum = 0.16) for each individual waveguide of all the structures. The reflection coefficient is –9.5 dB, –6 dB and –5.8 dB for the output angle of 15º, 65º and 80º, respectively. Note that the minimum $|\Gamma|$ is obtained for the 15º design which can be explained as follows: for small output angles the phase difference between waveguides and, therefore the difference in their dimensions [see Eqs. 2.9, 2.10 and 2.14] is less than for larger angles. Then, the design is better suited for small angles.

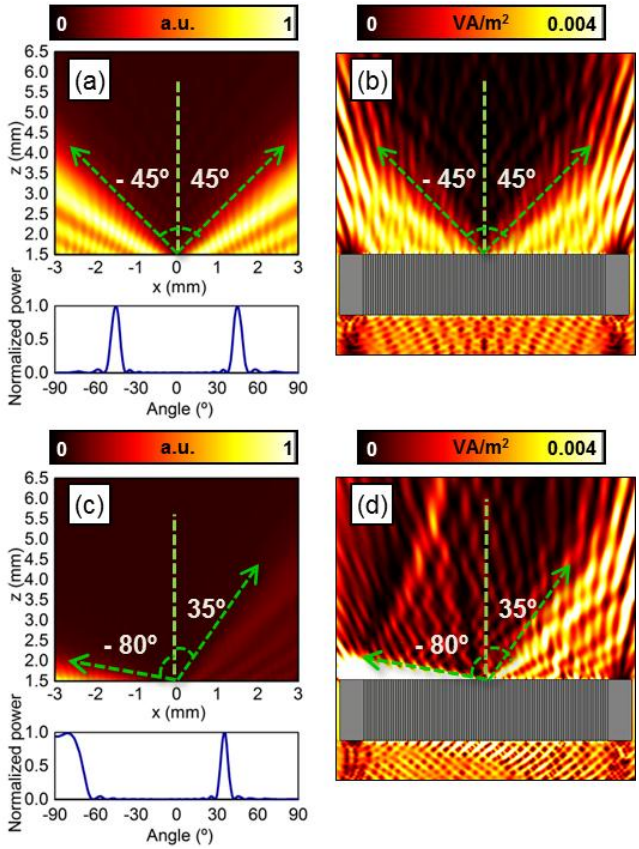

Figure 2.13. Analytical results of the power distribution on the *xz*-plane for: (a) a symmetric power splitter with output angle of ±45º and (c) an asymmetric power splitter with output angles -80º and +35º. The bottom panel of these two figures is the normalized power distribution at the fixed distance of r = 100 mm for angles from -90º to 90º calculated using the Huygens-Fresnel approximation. Simulation results of the power distribution on the *xz*- plane for: (b) a symmetric power splitter with output angle of ±45º and (d) an asymmetric power splitter for output angles -80º and +35º.

Finally, we can also apply this technique in order to deflect the incoming plane wave to two angles at the output of the ENZ device (i.e., to achieve power splitting). To evaluate the performance of such structures, several ENZ-GRIN power splitters are designed. The structures consist of 100 waveguides with a total width of $20\lambda_0$. To get the double angle operation, two waveguides with the dimensions shown in Fig. 2.8(a) are used as reference and placed at the extremes of the whole structure (one at the left and one at the right). Note that a straight way to design a power splitter with symmetrical output angles is by joining together side by side two of the blocks shown previously.

By using Eqs. 2.9, 2.10 and 2.14, two power splitters are designed: one with symmetric output angles (±45º) and one with different angles (–80º and +35º). The simulation results of the power distribution in *xz*-plane are presented in Fig. 2.13(b,d) for both designs, respectively. As it is shown, the output angles are in good agreement with the designed values with values of the reflection coefficient of –7.13 dB and –6.55 dB for each structure.

For the sake of completeness, we can also evaluate analytically the performance of these structures as it was done with the beam steerer. The analytical results of both power splitters using the Huygens-Fresnel principle are shown in Fig. 2.13(a,c) along with the normalized power distribution calculated for angles from –90º to 90º at r = 100 mm, as the beam steerer. The results are shown at the bottom of Fig. 2.13(a,c) for each design, respectively. As it can be observed, both analytical and numerical results are in good agreement, validating both designs.

2.3.2 Converging plano-concave lens

In this section, it is shown the first experimental demonstration of an ENZ-GRIN plano-concave lens working at THz frequencies [PACH 16a]. The lens is designed based on a similar procedure as discussed in the previous section using an array of narrow hollow rectangular waveguides emulating an ENZ MTM [TORR 12a]. The design frequency is 0.706 THz (λ=0.428mm) in order to transform an incoming plane wave into a narrow focus located at 6 mm (14λ) from the output of the lens.

As described in the previous section, each waveguide of the array must introduce a phase delay difference ($\Delta\Phi$) to produce the desired wavefront at the output of an ENZ-GRIN structure. For the case of the plano-concave lens here designed, assuming that the lens is discretized along both x and y axes, $\Delta\Phi$ can be expressed as follows:

$$\Delta\Phi^{(m,n)} = \beta^{(m,n)} l_z = \beta^{(0,0)} l_z - k_0 \sqrt{FL^2 + (md_x)^2 + (nd_y)^2} - FL + 2\pi\alpha \qquad (2.16)$$

where m and n are integers and are used to define the discretization (i.e., each waveguide) of the array along the x and y axes, $\beta^{(0,0)}$ is the propagation constant of the waveguide at the center of the array [i.e., the reference waveguide, whose dimensions are shown in Fig. 2.14(a)], FL is the focal length and α is an integer number (α = 1,2,3…).

Similar to the structures discussed before, the larger hollow dimension of the reference waveguide is designed to have its cut-off frequency of the TE_{01} mode at 0.7 THz ($h_y = \lambda_0/2$). However, it is expected to work near, but not exactly at the cut-off frequency.

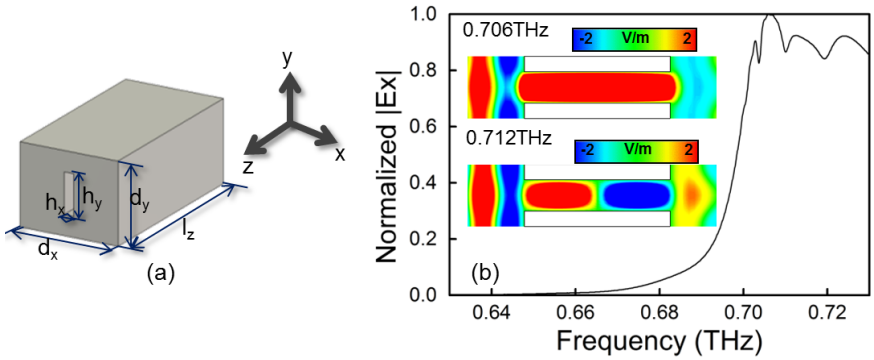

Figure 2.14. (a) Central waveguide used as the reference waveguide with dimensions: d_x = 537.5 and d_y = 428.6 μm, hollow dimensions of h_x = 53.57 μm, h_y = 214.28 μm and a thickness of l_z = 1000 μm. (b) Numerical results of the normalized E_x-field spectra at the output of the reference phase waveguide. The insets show the field distribution on the *yz*-plane at the ENZ and FP resonances.

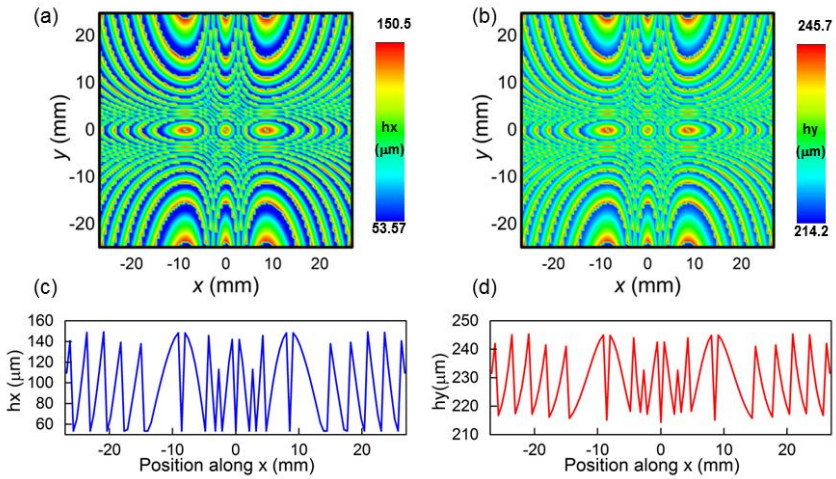

Figure 2.15. Contour plots showing the values of the hollow dimensions h_x (a) and h_y (b) for the designed ENZ-GRIN lens. Hollow dimensions along the *x* (c) and *y* (d) axis for the waveguides at the center of the lens; i.e., when *y* = 0.

The reference waveguide is simulated applying the local periodicity approximation with the same boundary conditions as discussed in Fig. 2.3 and Fig. 2.8 using the transient solver of the commercial software CST Microwave Studio®. The results of the E_x-field spectra are shown in Fig. 2.14(b). As it can be observed the ENZ and FP

operation frequencies occur at 0.706 THz and 0.712 THz, respectively. From here on, we will take the former frequency as the design frequency of the lens. Nevertheless, a slight deviation from this value can be anticipated due to the error introduced by the local periodicity approximation [TORR 12a]. Finally, the hollow dimensions of each waveguide of the lens can be calculated using Eq. 2.9, 2.10, 2.16 and are shown in Fig. 2.15.

The prototype consists of 11817 narrow hollow rectangular waveguides (101 × 117 waveguides along the *x* and *y* axes, respectively) with a total physical size of 54.1 mm × 50.14 mm × 1 mm ($x \times y \times z$). It is fabricated using a patented method based on a deep X-ray lithography (DXRL) technique [GENT 15], [KUZN].The necessity of using DXRL is explained by the relatively high aspect ratio and actual thickness of the designed structure whose production is unattainable with optical lithography. In the proposed fabrication method, the high-energy X-rays with a typical wavelength of 1 Å generated by a synchrotron radiation source are used for the lithographic patterning of a polymethyl methacrylate (PMMA) layer followed by its entire surface metallization. The PMMA layer has the thickness of the designed ENZ-GRIN lens (1 mm) and plays the role of carrying polymeric substrate, while the metallized (Ag/Al) layer deposited on the PMMA surface and having the typical thickness (~1 um) larger than the THz radiation skin depth allows the structure to act as fully metallic in terms of its EM response.

The three basic stages of the fabrication process are shown in Fig. 2.16. Firstly, the polished PMMA layer 1 ± 0.01 mm thick, which serves both as the X-ray-sensitive and the lens-core material, is exposed to X-rays through the X-mask [Fig. 2.16(a)]. The X-mask replicates the geometry of the designed ENZ-GRIN lens and is made as a patterned brass foil with the thickness 50 ± 1 um produced in advance via laser micromachining. At the second stage, due to radiation damage of molecular chains in PMMA upon its X-ray treatment, the irradiated parts of the PMMA layer are removed by chemical development [Fig. 2.16(b)]. Finally, the entire surface of the patterned polymeric structure including inner walls of the waveguide holes is metallized via chemical deposition of a silver layer 0.1 um thick, which is further "enhanced" through magnetron sputtering of additional silver and aluminum layers with the total thickness of 1 um to form the highly conductive corrosion-resistant metallic coating [Fig. 2.16(c)]. It is worth noting that the fabrication technique utilized here is much simpler and less expensive in comparison with a conventional LIGA technology [SAIL 09], which is normally used for producing high-aspect entirely metallic structures (with no dielectric core inside).

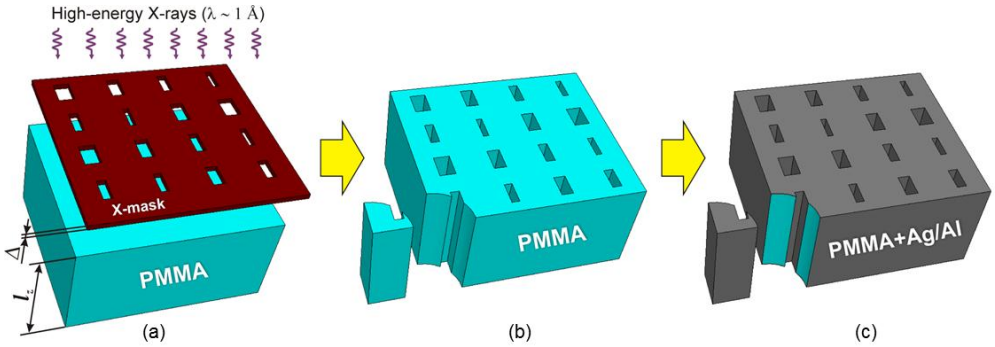

Figure 2.16. Fabrication stages for the ENZ-GRIN lens: (a) irradiation of the PMMA layer by "hard" X-rays through the X-ray mask. (b) chemical development of the patterned polymeric structure. (c) metallization of the entire dielectric surface via depositing thin Ag/Al layers. The structural slice is introduced in (b,c) to show that PMMA is patterned through, and all the waveguide holes have vertical walls.

The fabricated lens is placed on a circular holder with a clear radius of 25 mm [see Fig. 2.17(e)]. Microscope pictures showing several waveguides, the nine waveguides at the center of the structure and also the central waveguide used as reference in the design are shown in Fig. 2.17(f-h), respectively. From these images we can estimate that the fabrication is sufficiently accurate even taking into account the stringent aspect ratio of the waveguides: the narrow hollow dimension is of the order of just a few tens of microns whereas the length is 1 mm. This can be also observed by comparing these photographs with the designed lens [Fig. 2.17(b-d)], where a good comparison is shown between the fabricated and the designed prototype. Finally, by using Eq. 2.5b, we can retrieve the relative effective permittivity for each waveguide on the array. It is found that all waveguides work properly within the ENZ approximation, with $\varepsilon_{reff} < 0.25$ in all of them. The minimum permittivity value appears for the central waveguide ($\varepsilon_{reff} \sim 0.017$), as imposed by design [PACH 16a].

The lens is experimentally characterized with an ABmm™ VNA. A general sketch of the experimental setup is shown in Fig. 2.18. The ENZ-GRIN lens is placed in front of a standard diagonal horn antenna (WR-1.2) at 250 mm (~588λ at the design frequency of 0.706 THz). On the opposite side, a flange-ended rectangular waveguide (WR-1.2) is used as a receiver. It is placed on a translation stage in order to scan the power distribution near the focal plane. As a first step, the broadband response of the lens is evaluated by measuring the power distribution along the lens axis (z axis). The receiver is placed just at $x = y = 0$ and is moved along z from 4 mm to 8 mm with a very fine step of 0.05 mm (~0.117λ at the design frequency). With this configuration,

the power distribution at each position is measured from 0.630 THz to 0.730 THz with a high resolution step of 0.0002 THz (200 MHz).

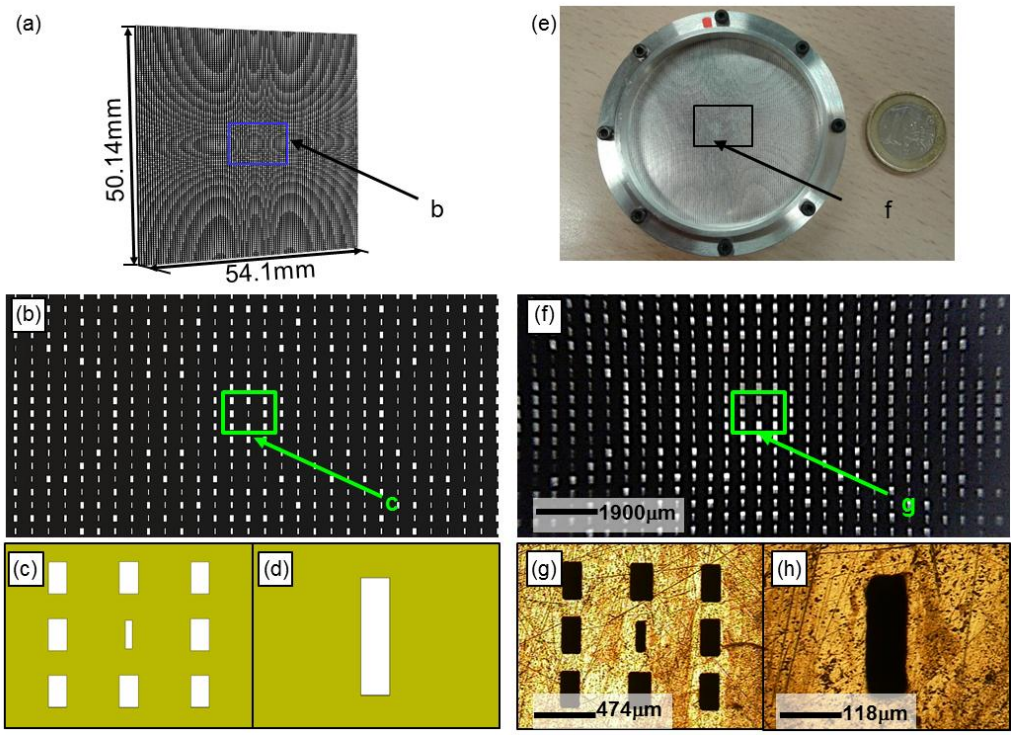

Figure 2.17. (a-d) Schematic representation of the lens showing: (a), the full lens, (b) a zoom-in of the lens showing more waveguides, (c) a zoom-in of the lens showing the nine central waveguides of the lens (green square from panel b) and (d) zoom-in of the lens showing the central waveguide of the lens; i.e., the waveguide used as reference in the design of the lens. (e-h), Photograph of the fabricated lens showing: (e) the full lens, (f) a zoom-in of the lens showing more waveguides, (g) a zoom-in of the lens showing the nine central waveguides of the lens (green square from panel f) and (h) zoom-in of the lens showing the central waveguide of the lens.

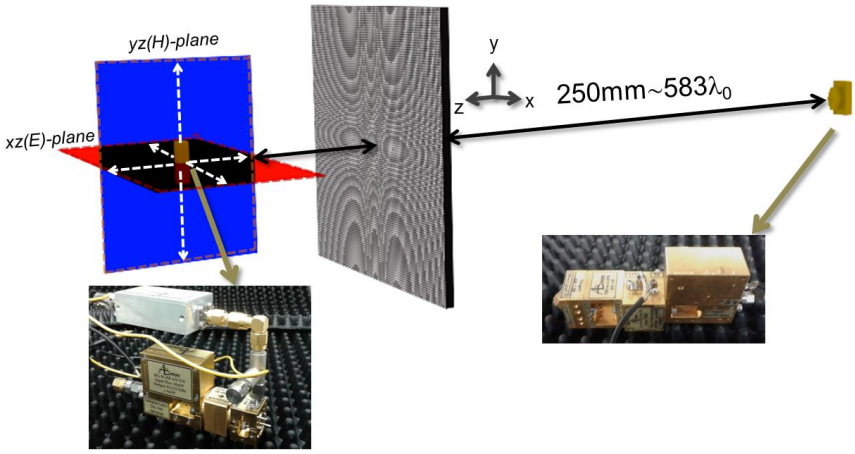

Figure 2.18. Schematic representation of the setup used to experimentally characterize the focal properties of the designed ENZ-GRIN lens

To validate the experimental data, the full ENZ-GRIN lens is numerically analyzed using the transient solver of the commercial software CST Microwave Studio®. A horizontally polarized planewave (E_x) is used to illuminate the lens from its back using Open+Add Space (i.e. perfectly matched layers) boundary conditions in all planes. Electric and magnetic symmetry planes are defined in the *yz* and *xz* planes, respectively, in order to reduce the simulation time. Aluminum is used as the material of the lens with a conductivity of $\sigma_{Al} = 3.56\times10^7$ S/m. A very fine meshing is used with a minimum and maximum mesh size of 0.0205 mm and 0.101 mm, respectively. With this configuration, the lens is simulated using a total number of ~82 million of cells. To characterize the broadband response of the lens, electric and magnetic probes are placed along the *z* axis (at $x = y = 0$) to record the field distributions at the same positions as in the experiment. Likewise, the frequency response is obtained in each position with the same spectral range and steps used in experiments. Finally, the broadband power distribution is calculated using the *x* and *y* components of the steady-state electric and magnetic field components, respectively, as $\frac{1}{2}(|E_x||H_y|)$.

The numerical and experimental results of the power distribution spectra along the propagation *z* axis are shown in Fig. 2.19(a,b), respectively. As it can be observed, a good agreement is generally found between the numerical and experimental results, and between both design constraints: in the experiment the focus appears at (*f*, *FL*) = (0.675 THz, 6 mm) whereas in the simulation it is at (*f*, *FL*) = (0.692 THz, 6.25 mm). Recall that in the design we imposed (*f*, *FL*) = (0.706 THz, 6 mm). Therefore, aside from a small frequency shift, it can be affirmed that the lens has an excellent performance. As mentioned earlier, the error comes probably from the local periodicity approximation which does not totally hold in our ENZ-GRIN prototype.

Moreover, there are different issues in the fabrication that might slightly alter the performance, such as waveguides not completely rectangular and slight deviations of the hollow dimensions from the nominal values. In any case, the frequency error is very small ~1.89% in the simulation and ~4.36% in the experiment, especially taking into account that the fabrication of this lens is highly challenging. For the sake of completeness, the experimental and numerical results of the power distribution along the *z* axis at the maximum frequency are shown in Fig. 2.19(c). From these curves we can obtain the depth of focus (*DF*, defined as the distance at which the power distribution has decayed half of its maximum along the propagation direction) which is another important parameter to assess a lens performance. The resulting values are $DF = 2.14\lambda_{exp}$ (0.95mm), and simulation results, $DF = 2.33\lambda_{sim}$ (1.01mm), demonstrating a nice agreement between both results.

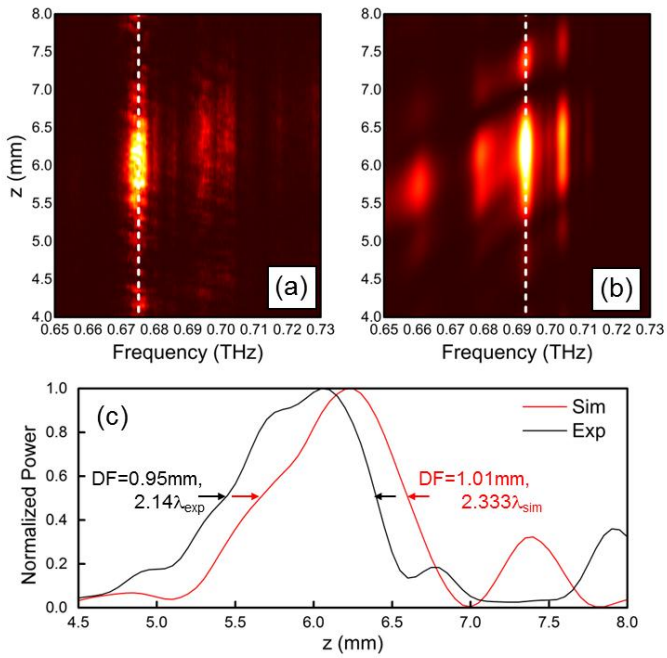

Figure 2.19. Experimental (a) and numerical results (b) of the power distribution spectra along the propagation *z* axis. (c) Experimental (black) and simulation (red) results of the power distribution along the z axis at frequency of maximum focus intensity [0.675 THz (experiment) and 0.692 THz (simulation)] extracted from the white dashed lines of panels (a) and (b), respectively.

Once we have characterized the broadband response of the ENZ-GRIN lens, the focal planes (*xz* and *yz*) are measured and numerically evaluated at the maximum

frequency. For the experiment, the same setup as shown in Fig. 2.18 is used but at a single frequency. The receiver is moved on the *xz* and *yz* planes in order to experimentally characterize the focusing properties of the lens on the *E* and *H* planes, respectively. A high resolution measurement is performed by moving the receiver from −1.5 mm to 1.5 mm with a step of 0.01 mm (0.024λ) along the *x*/*y* axes and from 4.5 mm to 7.5 mm along the *z* axis with a step 0.05 mm (0.117λ). The lens is also simulated with the same boundary conditions as described before in order to calculate the 3D power distribution in both principal planes at the maximum frequency obtained from Fig. 2.19(a).

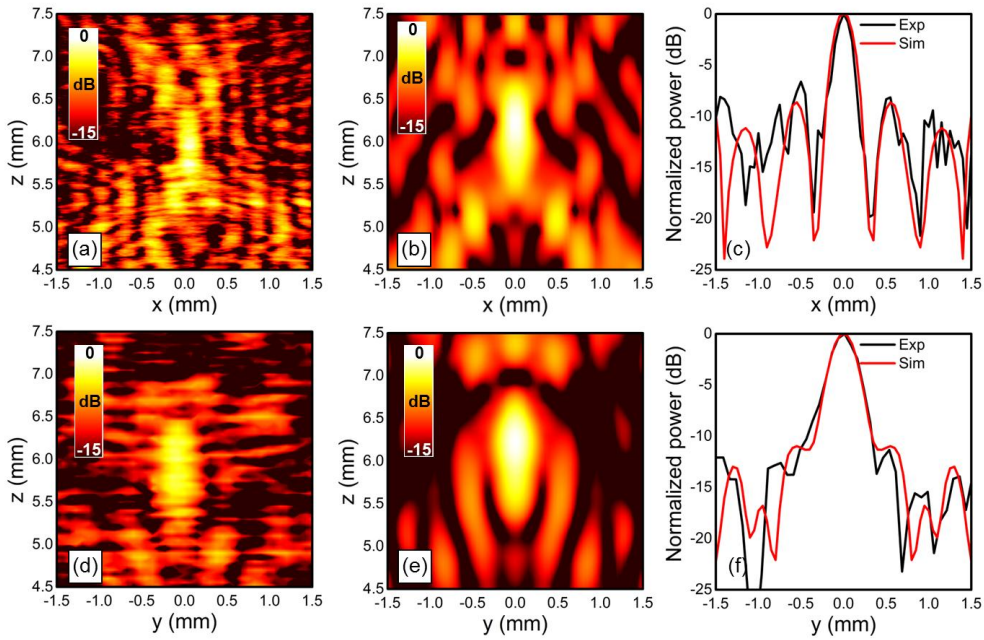

Figure 2.20. (a,d) Experimental results on the *xz* and *yz* planes, respectively at f = 0.675 THz. (b,e) numerical results on the *xz* and *yz* planes, respectively, at f = 0.692 THz. (c,f), experimental (black) and numerical (red) results of the power distribution at the focal position along the *x* and *y* axes, respectively.

The experimental and numerical results of the power distribution on the *E* and *H* planes are shown in Fig. 2.20(a,b) and Fig. 2.20(b,e), respectively. For the naked eye, it is evident that both results are in a good agreement demonstrating a very similar focus profile. It is clearly shown how the ENZ-GRIN lens can actually focus the incident wave into a focal spot. It produces a high power enhancement at the *FL* of ~42 times (16.23 dB) in the experiment and ~69 times (18.42 dB) in the simulation,

compared to the value without lens. The small difference between simulation and measurement can be attributed to errors in fabrication such as metal roughness, waveguide dimensions, etc.

To further compare these results, the power distribution at the focal plane along the x and y axis is shown in Fig. 2.20(c,f). We can obtain from these curves the Full-Width at Half-Maximum (*FWHM*, defined as the distance along the x or y axis at which the power has decayed half of its maximum). From the experimental results we get $FWHM_x = 0.217 \pm 0.01$ mm $= (0.488 \pm 0.025)\lambda_{exp}$ and $FWHM_y = 0.337 \pm 0.01$ mm $= (0.76 \pm 0.025)\lambda_{exp}$ (in the simulation these values are $FWHM_x = 0.238$ mm $= 0.55\lambda_{sim}$ and $FWHM_y = 0.337$mm $= 0.78\lambda_{sim}$), corroborating the good agreement between the numerical and the experimental results.

2.4 ENZ based sensor for subwavelength dielectrics

In this section, a systematic study of an ENZ based sensor is performed based on the transmission line theory. The structure is similar to the one shown in Fig. 2.1 which has been applied for sensing and to evaluate non-linear inclusions within the ENZ channel [ALÙ 08b], [POWE 09]. Here, we extend this study by considering a small dielectric placed within the ENZ narrow channel. The results are validated with numerical results using the commercial software CST Microwave Studio® [PACH 16b].

A schematic representation of the sensor under study is shown in Fig. 2.21(a). It consists of a narrow ENZ channel of length L filled with air (colored in blue) surrounded by two waveguides filled with a dielectric of relative permittivity ε_{wg} (colored in green). The width of all elements is b = $\lambda_0/2$, where λ_0 is the cut-off wavelength of the narrow channel filled with air. The height of the input and output waveguides is $a = b/2$ and that of the ENZ channel is $a_{ENZ} = a\Delta_a$, where Δ_a is a factor between 0 and 1. The vertical walls of the U-shaped channel along the z axis are equal to a_{ENZ}. Finally, a red particle representing the analyte, with dimensions $L_x \times L_z$ and permittivity ε_d is placed inside the ENZ channel at the point $(b/2+\Delta_x, L/2+\Delta_z)$, where $|\Delta_x|, |\Delta_z| \in [0, 1]$ so that $|\Delta_x|, |\Delta_z| = 0, 1$ means that the analyte is in the center or at the extremes, respectively. The cross sections on the xz- and xy- planes of the analyte are also shown as inset in the same figure.

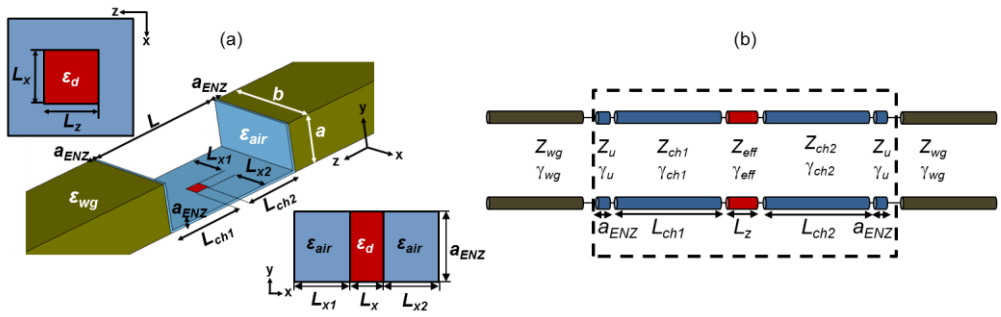

Figure 2.21. (a) Schematic representation of the ENZ sensor. (b) Equivalent transmission line model.

Finally, since a systematic study of the sensing performance for different widths and positions of the analyte will be done in the following sections, the dimensions of each section of the ENZ channel are defined as follows:

$$L_{x1,2} = \left(1/2\right)\left(b - L_x\right)\left(1 \mp \Delta_x\right) \tag{2.17}$$

$$L_{ch1,2} = \left(1/2\right)\left(L - L_z\right)\left(1 \mp \Delta_z\right) \tag{2.18}$$

Once we have defined all the geometrical parameters of the sensor, let us now apply the transmission line theory to analyze its response. The equivalent transmission line model is shown in Fig. 2.21(b). Each transmission line in the figure represents the different parts of the sensor: input and output waveguides (green), vertical walls filled with air and ENZ channel (blue), and analyte (red). As it is known, each element in the network (surrounded by the black dashed line) can be described with a transmission (ABCD) matrix, so that the overall response is [POZA 04]:

$$ABCD_{final} = \prod_m ABCD_m = \prod_m \begin{bmatrix} \cosh\left(\gamma_m L_m\right) & Z_i \sinh\left(\gamma_m L_m\right) \\ \left(1/Z_m\right)\sinh\left(\gamma_m L_m\right) & \cosh\left(\gamma_m L_m\right) \end{bmatrix} \tag{2.19}$$

with the subscript m representing each transmission line section with propagation constant γ_m, characteristic impedance Z_m and length L_m. As it was explained in the previous sections, the dispersive performance of a rectangular waveguide can be described with a relative effective permittivity as a Drude model [ALÙ 08a] which,

when the waveguide is homogeneously filled, can be calculated using Eq. 2.5b. Moreover, the propagation constant can be expressed as:

$$\gamma_i = jk_0\sqrt{\varepsilon_{reffm}} \tag{2.20}$$

On the other hand, if the waveguide is inhomogeneous (as happens when the analyte does not fill completely the cross-section), one should apply a homogenization procedure to calculate the propagation constant where it is assumed that the waveguide cross-section is completely filled with a block of effective permittivity $\varepsilon_{eff,m}$ [see inset in Fig. 2.21(a)]. The value of the propagation constant in that section is then obtained following the method discussed in [POZA 04] extended here to the three region case shown in Fig. 2.21(a). After applying the boundary conditions of vanishing tangent electric field at the metallic walls and the continuity of the tangential components of the electric and magnetic fields at the interfaces between the analyte and air, the next equations are obtained (see appendix C):

$$\frac{1}{k_d}\tan(k_d L_x)+\frac{1}{k_{air}}\left[\tan(k_{air}L_{x2})+\tan(k_{air}L_{x1})\right]-\frac{k_d}{k_{air}^2}\tan(k_{air}L_{x1})\tan(k_{air}L_{x2})\tan(k_d L_x)=0 \tag{2.21}$$

$$k_d = \sqrt{\varepsilon_d k_0^2 - \gamma_m^2} \tag{2.22}$$

$$k_{air} = \sqrt{k_0^2 - \gamma_m^2} \tag{2.23}$$

where k_d, k_{air} is the transverse wavenumber inside the dielectric and air regions shown in the inset of Fig. 2.21(a). From these expressions, the value of γ_m is retrieved and from it and applying Eq. 2.20 we obtain $\varepsilon_{eff,m}$. Note that the previous equations converge to the homogenously filled waveguide in the limit when $L_{x1,2} = 0$ and $L_x = b$.

Regarding the characteristic impedance, it can be calculated as follows:

$$Z_m = \frac{\eta_0}{\sqrt{\varepsilon_{eff,m}}}\frac{a}{b}\Delta_a \tag{2.24}$$

where $\eta_0 = 120\pi$ (Ω) is the free-space intrinsic impedance. In the previous equation $\Delta_a = 1$ for the input and output waveguides and the transition region of the channel and $\Delta_a << 1$ for the ENZ channel. Finally, the transmission coefficient of the sensor can be easily obtained and it is expressed as follows [POZA 04]:

$$T(f)=\frac{2}{A_{final}+B_{final}/Z_{wg}+C_{final}Z_{wg}+D_{final}} \tag{2.25}$$

It is important to note that in [ALÙ 08a], shunt capacitances reactance elements were used to model the evanescent modes excited at the abrupt interface between the transition region of the U-channel and ENZ channel. In the model shown in Fig. 2.21(b) these capacitances are not taken into account due to the fact that, under the ENZ approximation, the effective permittivity is close to zero so that in general $\sqrt{\varepsilon_{reff}} << \Delta_a$. This implies that the magnitude of the characteristic impedance is very high and hence, the elimination of the shunt capacitances does not strongly affect the performance in the ENZ peak (although it does affect the FP resonance peaks, as discussed below).

Let us now start with the study of the performance of the ENZ sensor under different configurations of the analyte sample and geometries of the narrow channel. The dimension b is selected as 101.6 mm. The input and output waveguides are filled with a homogeneous dielectric with relative permittivity $\varepsilon_{wg} = 2$. The ENZ channel is filled with air and has a length $L = 1.5b$. With these dimensions, the cut-off frequency is ~1.044 GHz for the input/output waveguides and ~1.476 GHz for the ENZ channel. In all the following studies, the results are normalized to the cut-off frequency of the ENZ channel.

We first study the case [ALÙ 08a] when the analyte is completely filling the transverse x axis [see inset of Fig. 2.22(c)]. For the calculations, the next parameters are defined: $L_x = b$, $L_z = 0.15b$ (= $0.1L$), $\varepsilon_d = 3$, $\Delta_a = (1/64)$.

In Fig. 2.22(a,b) it is shown the analytical and numerical results of the transmission coefficient as a function of the analyte position and the normalized frequency $\Delta_z \in [-1, 1]$ and $f \in [0.7, 1.3]$, showing a very good agreement. Two high transmission peaks are observed: one related to the ENZ operation at the normalized frequencies from 0.8-0.9 and the other due to the FP resonance which arises ~1.1-1.2. The field distributions of these peaks are shown in Fig. 2.22(d,e), which correspond to an empty channel. Note that the field has the same spatial distribution as the ENZ and FP resonances discussed in the previous sections. A good agreement between analytical and numerical results is observed at the ENZ frequency (first peak) with a larger deviation for the FP peak. The disagreement between the numerical and analytical results in the FP band is a consequence of having disregarded the shunt capacitive reactances at the interface between input/output waveguides and the ENZ channel. Nevertheless, our interest is in the ENZ band which has a negligible deviation. Hence, we will not take into account the capacitance in the following calculations for simplicity without incurring in a large error.

As observed in Fig. 2.22(a,b), the ENZ band experiences a slight frequency shift as Δ_z is varied, whereas the shift is more notable for the FP band. This distinct behavior is due to the different field distribution of each band. For the ENZ band the field is almost uniform along the channel, whereas at the FP resonance it presents a minimum exactly at the center with maxima at the extremes [see Fig. 2.22(d,e)]. Thus, in the latter case the peak position depends strongly on the analyte position. This is in contrast to what happens at the ENZ band which is very robust with respect to a change in Δ_z.

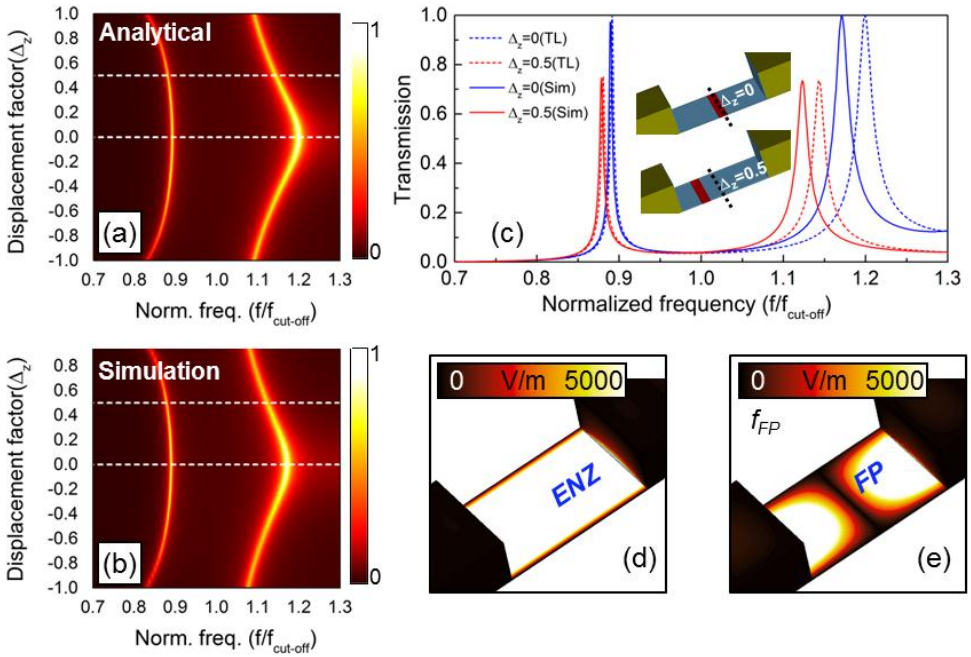

Figure 2.22. Analytical (a) and numerical (b) results of the transmission coefficient when an analyte slab with $\varepsilon_d = 3$ filling the x axis is shifted along z with a displacement factor from $\Delta_z = -1$ to $\Delta_z = 1$. (c) Analytical (dashed lines) and numerical (solid lines) results of the transmission coefficient for the cases highlighted with dashed lines in (a,b). Numerical results of the magnitude of the electric field at the ENZ (d) and FP (e) resonances (corresponding to an empty channel).

To better understand the features of each resonance, we select two different z positions of the analyte, $\Delta_z = 0$ and $\Delta_z = 0.5$ [white lines in Fig. 2.22(a,b)] and show the transmission coefficient in Fig. 2.22(c). From these results, it can be observed that the agreement is worse for the FP band and that the ENZ band experiences a small

downshift ~1.256% from 0.89 ($\Delta_z = 0$) to 0.88 ($\Delta_z = 0.5$), and the amplitude decreases moderately in the last case.

A remarkable result shown in Fig. 2.22 is that the ENZ peak takes place close but not exactly at the cut-off frequency of the input/output ENZ channels filled with air ($f_{c,ch1} = f_{c,ch2} = 1$, recall that the results are normalized to this frequency) and above the cut-off of the analyte section ($f_{c,a} = 0.57$). This indicates a tunneling of energy through the channels filled with air. Fortunately, this tunneling can be easily explained in impedance terms using the transmission line model as discussed next.

For simplicity let us consider the symmetric case when $\Delta_z = 0$ [see the equivalent transmission line problem in Fig. 2.23(a)]. From Eq. 2.5b we find that the effective permittivity of the air channel sections is negative, as they operate below cut-off. This implies that the propagation constant (Eq. 2.20) and the characteristic impedance (Eq. 2.24) are real and imaginary, respectively. Also, note that an aperture on a metallic plate operating below cut-off usually has an inductive character. This is so because the fundamental mode is normally TE that accumulates magnetic energy below cut-off [COLL 00].This means that the characteristic impedance is inductive. With these conditions and provided that the air channel is not too long, the imaginary component of input impedance looking from the analyte section towards the output waveguide [$Z_{in,1}$, black curve in Fig. 2.23(b)] has an inductive character. Note that the same impedance appears looking from the analyte towards the input waveguide, given that the structure is symmetric, $Z_{in,3} = Z_{in,1}$.

Now, we calculate the input impedance including the analyte section [$Z_{in,2}$, red curve in Fig. 2.23(b)] which can be expressed as:

$$Z_{in,2} = Z_a \frac{Z_{in,1} + Z_a \tanh(\gamma_a L_z)}{Z_a + Z_{in,1} \tanh(\gamma_a L_z)} \tag{2.26}$$

where Z_a, γ_a is the characteristic impedance and propagation constant at the analyte section. In this case we find that its imaginary part is also inductive for low frequencies but there is a resonance frequency where it diverges and changes its character from inductive to capacitive. This resonance frequency arises due to the denominator of $Z_{in,2}$, which depends of Z_a, γ_a and $Z_{in,1}$. Therefore, since γ_a also changes from real to imaginary when working below and above cutoff, the imaginary component of $Z_{in,2}$ can change its character from inductive to capacitive.

In Eq. 2.26 $Z_a = R_a$ (purely real), $Z_{in,1} \approx j\omega L$ (inductive with a negligible real part) and $\gamma_a = j\beta_a$ (the analyte section is above cut-off). Therefore, with the prescribed conditions, the denominator of Eq. 2.26 becomes $R_a - \omega L \tan(\beta_a L_z)$ and from here it is obvious that there is a frequency where Eq. 2.26 diverges and the impedance changes from inductive to capacitive.

Therefore, at the interface between the channel 1 and the analyte, the impedance looking towards the output ($Z_{in,2}$) is capacitive and looking towards the input ($Z_{in,3}$) is inductive. As it is shown in Fig. 2.23(b), the capacitive reactance of $Z_{in,2}$ is reduced for higher frequencies while the inductive reactance $Z_{in,3}$ increases. Thus, there is a frequency where both cancel (i.e. they are exactly complex conjugated) giving rise to the peak of transmission shown in Fig. 2.22(c). We have also plotted $Z_{in,2}$ - $Z_{in,3}^{*}$ in Fig. 2.23(c). As shown both real and imaginary components cross zero at the frequency of the ENZ peak (marked as vertical dashed line). Hence we have maximum transmission at this frequency. For the sake of completeness, we have depicted in the same figures the impedance difference at the input, $Z_{in,4} - Z_{wg}$ and we find that there is impedance matching exactly at the peak of transmission.

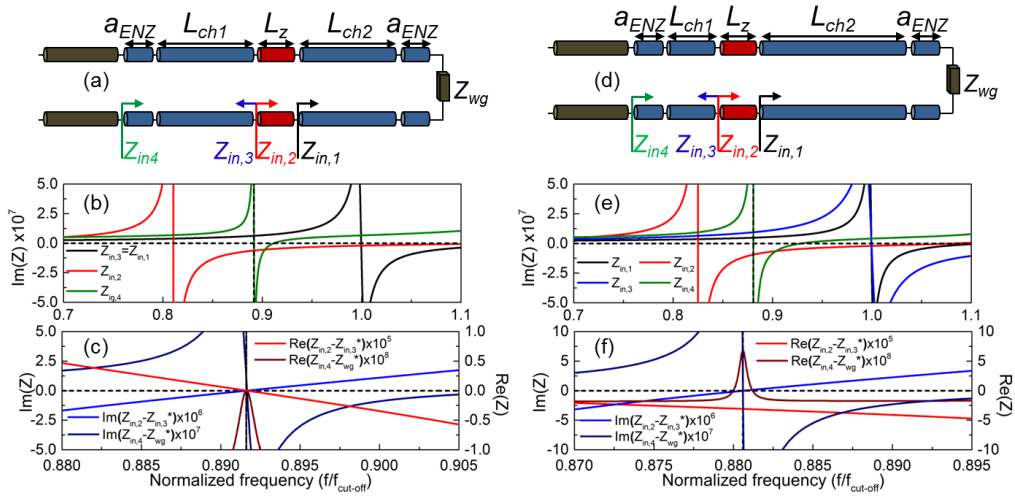

Figure 2.23. Schematic representation of the equivalent transmission line when the analyte of Fig. 2.20 is placed at $\Delta_z = 0$ (a) and $\Delta_z = 0.5$ (d). Analytical results of the imaginary part of the impedances $Z_{in,1}$ (black lines), $Z_{in,2}$ (red lines) $Z_{in,3}$ (blue lines) and $Z_{in,4}$ (green lines) when the analyte is placed at $\Delta_z = 0$ (b) and $\Delta_z = 0.5$ (e). Analytical results of the imaginary (blue lines) and real part (red lines) of the difference between the impedances $Z_{in,2}$ - $Z_{in,3}^{*}$ (light curves) and $Z_{in,4} - Z_{wg}^{*}$ (dark curves) for a displacement factor of $\Delta_z = 0$ (c) and $\Delta_z = 0.5$ (f)

For the case when the analyte is shifted to $\Delta_z = 0.5$ the impedances suffer a slight modification [see the equivalent transmission line in Fig. 2.23(d)] and the peak of transmission downshifts and its amplitude is reduced [see Fig. 2.22(c)]. This performance can be also explained by analyzing this case using the transmission line impedances. The results of the imaginary part of $Z_{in,1}$, $Z_{in,2}$, $Z_{in,3}$ and $Z_{in,4}$ for this

configuration are shown in Fig. 2.23(e). The performance is similar to the previous case. The peak of transmission (f = 0.8807) occurs when the Im{$Z_{in,2}$} = -Im{$Z_{in,3}$}. However, due to the asymmetry of the problem at this condition Re{$Z_{in,2}$} ≠ Re{$Z_{in,3}$} as shown in Fig. 2.32(f), so the impedances are not conjugate matched. Likewise, Re{$Z_{in,4}$} ≠ Re{Z_{wg}} and therefore the peak of transmission does not reach unity. From this analysis it is clear that the transmission line model is very powerful to explain even the most peculiar details of the spectrum.

Now that we have studied the case when the analyte completely fills the transversal x axis of the ENZ narrow channel, we will study the general case when it does not completely fills neither the transversal nor the longitudinal dimension. This study is performed for different sizes, permittivity values and positions of the analyte.

First we consider the case when the analyte has a square cross section on the xz-plane with transversal dimensions $L_x = L_z = 0.15b$ and permittivity (ε_d) varying from 1 to 3 placed at $\Delta_x = \Delta_z = 0$. Two different channel heights are evaluated Δ_a = (1/64) and Δ_a= (1/20). With these considerations, the analytical and numerical results of the transmission coefficient are shown in Fig. 2.24. By inspection of this figure it is observed that an increment of the analyte permittivity ε_d generates a noticeable redshift of the ENZ band. By looking at Eq. 2.21, increasing ε_d implies an increment of the propagation constant at the analyte section, $\gamma_{eff,a}$ and, by Eq. 2.5b also an increment of the effective permittivity, $\varepsilon_{reff,a}$. At the same time, the characteristic impedance, Z_a, decreases, see Eq. 2.24. All these conditions together make the denominator of Eq. 2.26 diverge at a smaller frequency as ε_d is augmented, producing a redshift of the ENZ peak. On the other hand, the FP band remains static. This is because the FP resonance has a minimum field intensity at $\Delta_z = 0$ so that the electric field barely interacts with the analyte and therefore it is insensitive to a change in permittivity.

By comparing the results with Δ_a = (1/64) and Δ_a = (1/20) it can be concluded that reducing the channel height produces an enhancement of the quality factor of the peaks, both for the ENZ and FP bands. This performance was explained in [ALÙ 08b] where it was argued that for extremely narrow channels the impedance matching bandwidth of the ENZ channel becomes more and more restrictive. It can be also explained following the same reasoning of the previous section. The characteristic impedance of the transmission lines is directly proportional to the factor Δ_a, see Eq. 2.24. Therefore, for small Δ_a the characteristic impedance is very small. From here it is clear that at any frequency (with the exception of resonance peaks) the magnitude of the impedances $Z_{in,1}$, $Z_{in,2}$ decrease for small Δ_a, as demonstrated in Fig. 2.24(c), which corresponds to the case ε_d = 3. Note that the ENZ frequency is slightly blue shifted from 0.9662 to 0.9675 when Δ_a = (1/64) and Δ_a = (1/20), respectively. This blue shifting can be also observed in Fig. 2.24(a,b) where the effective permittivity for each case is shown. This happens because the length of the walls used in the U-channel

changes when modifying Δ_a (see Fig. 2.21). However, since the height of the channel and the length of the walls are still ultra-narrow for both cases, the frequency shifting represents only ~0.14%. In the figure, it is clearly shown that the impedance matching bandwidth is less restrictive for Δ_a = (1/20). Thus, there are more frequencies around the ENZ frequency where the inductive and capacitive reactances of $Z_{in,1}$ and $Z_{in,2}$ are approximately complex conjugated. This produces a reduction of the Q factor and a widening of the transmission coefficient around the ENZ frequency.

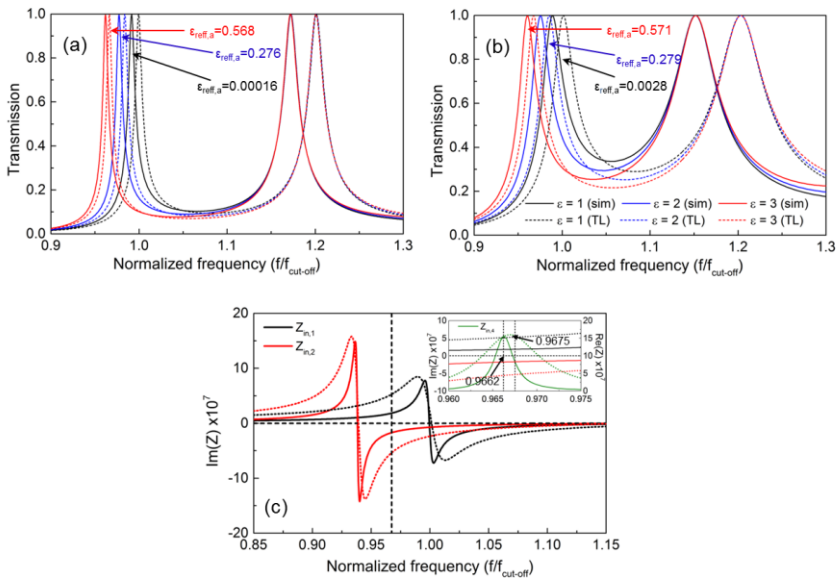

Figure 2.24. Analytical (dashed lines) and numerical (solid lines) results of the transmission coefficient when an analyte with transversal dimensions $L_x = L_z = 0.1L = 0.15b$ and relative permittivity $\varepsilon_d = 1$ (black), $\varepsilon_d = 2$ (blue) and $\varepsilon_d = 3$ (red) is placed in the middle of the channel with height $a_{ENZ} = (1/64)a$ (a) and $a_{ENZ} = (1/20)a$ (b). (c) Analytical results of the imaginary part of the impedances $Z_{in,1}$ (black), $Z_{in,2}$ (red) and real part of $Z_{in,4}$ (green) when the analyte with $\varepsilon_d = 3$ is placed within a narrow channel with height a_{ENZ} =(1/64)a (solid lines) and a_{ENZ} = (1/20)a (dotted lines).

It is interesting to note in Fig. 2.24(a,b) that it is still possible to detect a change of permittivity at the ENZ peak, even with extremely small analytes ($L_x = L_z = 0.075\lambda_0$, as in this case); which is a remarkable feature of this sensor.

Generally, the performance of a sensor is given by the sensitivity, *S*, and the figure of merit, *FoM*. The sensitivity is defined as the variation of the resonance wavelength divided by the variation of the index refraction, $S = \Delta\lambda_{res}/\Delta n$ [m/RIU], where RIU stands for refractive index unit [OHAR 12], [SING 14]. In our case, the sensitivity is given by the redshift of the ENZ peak when the refractive index of the analyte varies.

In sensing applications, besides a high *S*, a good selectivity (i.e. spectral resolution) is usually desired. Then, high Q-factor resonances, or equivalently, narrow FWHM values are preferred. The *FoM* relates both parameters: *FoM* = *S*/FWHM [dimensionless]. In Fig. 2.25, both analytical and simulation results of the *S* and *FoM* are shown, with a good agreement between them. A maximum *S* of 0.04 and 0.03 m/RIU is obtained in the simulation and analytical results, respectively. What is more, very competitive *FoM* values are obtained [NG 13] (up to 20), due mainly to the strongly sharp response of the ENZ peak.

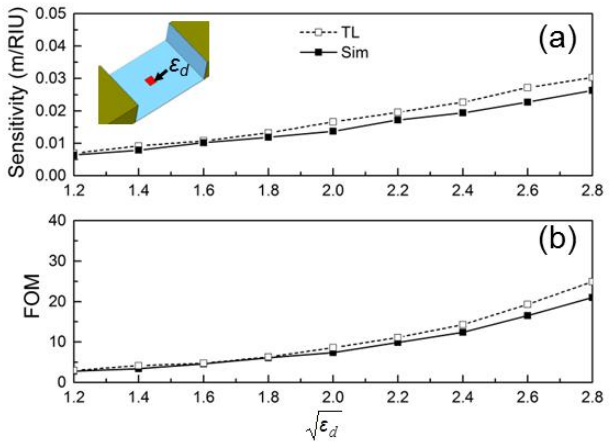

Figure 2.25. Sensitivity (a) and figure of merit *FoM* (b) results for an analyte of dimensions $L_x = L_z = 0.1L = 0.15b$ inside of an ENZ channel of height $a_{ENZ} = (1/64)a$.

Let us now evaluate the performance of the sensor when the position of the analyte is changed within the ENZ channel. The analytical and numerical results of the transmission coefficient as a function of the normalized frequency and Δ_x for a dielectric analyte with $\varepsilon_d = 3$ and dimensions $L_x = L_z = 0.1L = 0.15b$ placed at $\Delta_z = 0$, are shown in Fig. 2.26. A good agreement between numerical and analytical results is observed at the ENZ frequency with some deviation at the FP resonance, as expected.

As it is shown, when $\Delta_x = 0$ the ENZ peak takes place at $f = 0.963$ and shifts to $f = 0.997$ for $\Delta_x = \pm 1$. Expectedly, near the walls the electric field of the fundamental mode TE_{10} vanishes and therefore the interaction between the analyte and the electric field is very small, making that the ENZ frequency approaches the value of an empty channel. Conversely, the electric field magnitude at the center is maximum causing the largest frequency shift. For the sake of completeness the relative effective permittivity ($\varepsilon_{reff,a}$) within the frequency range of the ENZ frequency is shown in the inset of Fig. 2.26(a). Again, when the analyte is near the edges, $\varepsilon_{reff,a}$ approaches zero at lower

frequencies. In contrast, $\varepsilon_{reff,a}$ increases as the analyte is shifted towards the center, demonstrating an enhanced interaction between the electric field and the analyte. As for the FP peak, it is observed that it does not shift with Δ_x, since at Δ_z= 0 the electric field has a minimum for this resonance, as it has been explained in Fig. 2.22(d,e). The results of the transmission coefficient at the ENZ frequency [dashed vertical lines in Fig. 2.26(a,b)] are shown in Fig. 2.26(c), as a function of Δ_x, along with the values of $\varepsilon_{reff,a}$. In this figure, the influence of the analyte position on the performance of the ENZ sensor is evident. Moreover, the transmission coefficient for Δ_x = 0.2 and Δ_x = 0.8 [taken from the horizontal lines in Fig. 2.26(a,b)] are shown in Fig. 2.26(d) where it is clearly shown that the frequency shifting depends on the position of the analyte.

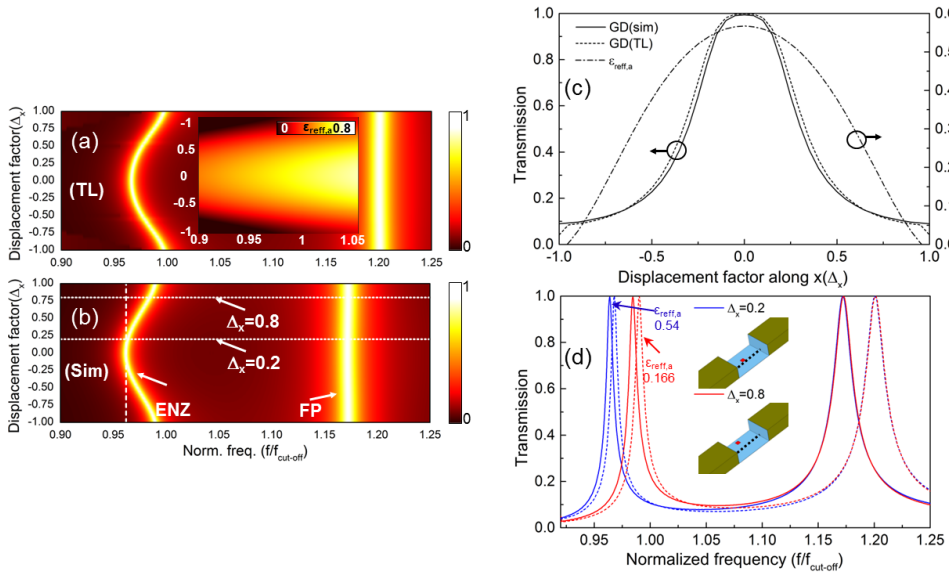

Figure 2.26. Analytical (a) and numerical (b) results of the transmission coefficient for an analyte with relative permittivity ε_d =3 placed at Δ_z = 0 with dimensions $L_x = L_z = 0.1L = 0.5b$ as a function of the displacement factor $-1<\Delta_x<1$ and the normalized frequency. (Inset) Idem for the analytical values of the relative effective permittivity ($\varepsilon_{reff,a}$). (c) Analytical (dashed) and numerical (solid) results of the transmission coefficient along with the analytical values of the effective permittivity $\varepsilon_{reff,a}$ (dash-dotted line) as a function of Δ_x at the ENZ frequency (taken from the vertical lines shown in panels a and b). (d) Numerical (solid) and analytical (dashed) results of the transmission coefficient for an analyte with $L_x = L_z = 0.1L = 0.5b$, and Δ_x = 0.2 (blue lines) Δ_x = 0.8(red lines) (results taken from the horizontal lines shown in panels a and b).

We can also evaluate the performance of the sensor considering the extreme case when the analyte fills completely the propagation *z* axis (i.e., $L_z = L$), keeping the same

permittivity $\varepsilon_d = 3$ and width $L_x = 0.1L = 0.5b$. The numerical and analytical results of the transmission coefficient at three different positions, $\Delta_x = 0$, $\Delta_x = 0.2$ and $\Delta_x = 0.8$, are shown in Fig. 2.27(a) (see the insets to better observe each position). From these results, three peaks of transmission are clearly observed: one due to the ENZ frequency and two related to with FP resonances. The field distribution of each peak is shown in Fig. 2.27(c-d), respectively. The increased peaks are due to the increment of the effective permittivity of the narrow ENZ channel which shifts the spectrum towards lower frequencies so that more resonances can be excited within the same length (L). The transmission peaks are moved to higher frequencies as Δ_x increases, with a similar performance as for the case of a dielectric particle. The main difference with the results shown in Fig. 2.24 is that now all the peaks are shifted. In the present configuration, the analyte covers completely the z axis enhancing the interaction with electric field, whereas in the previous case it was limited to the center, where the field has a minimum.

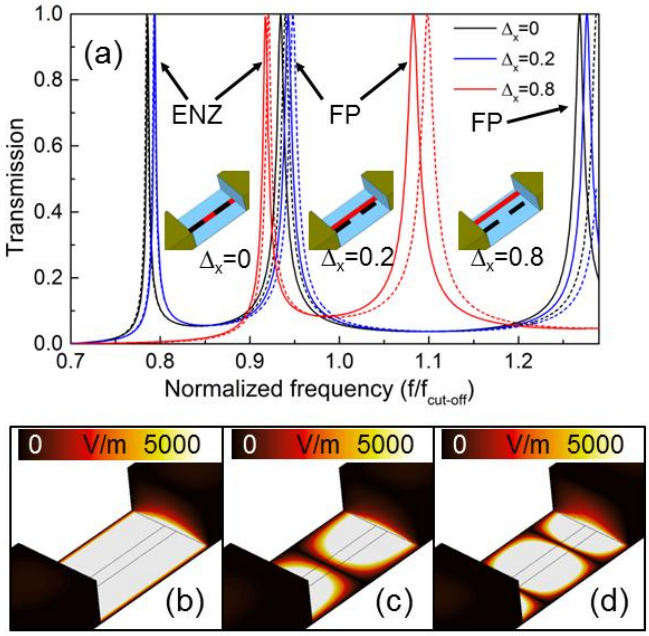

Figure 2.27. (a) Analytical (dashed lines) and numerical (solid lines) results of the transmission coefficient of an analyte with $\varepsilon_d = 3$, $L_x = 0.1L = 0.5b$ and $L_z = L$ moved along the transversal x axis with a displacement factor $\Delta_x = 0$ (black lines), $\Delta_x = 0.2$ (blue lines) and $\Delta_x = 0.8$(red lines). Field distribution at the ENZ (b) and the two FP resonances (c,d) for the case when the analyte is at the center of the narrow channel ($\Delta_x = 0$).

As a final study, we can also use the effective medium approach to evaluate the performance of the ENZ sensor considering that the cross section shown in Fig. 2.21 is

treated as an effective medium with permittivity $\varepsilon_{reff,a}$. Let us consider that a dielectric analyte with $\varepsilon_d = 3$, $L_x = 0.3b$ and $L_z = 0.15b$ is placed at $\Delta_z = 0$ and $\Delta_x = 0.5$, as shown in the inset of Fig. 2.28(a). From the transmission results of Fig. 2.28(a), and applying Eq. 2.5b and Eq. 2.21, we find that the effective permittivity of the analyte cross section is $\varepsilon_{reff,a} = 0.8883$ at the ENZ peak ($f = 0.95$). However, this is not the only possibility to obtain this effective permittivity. In fact, there are infinite combinations of size, position and permittivity of the analyte that lead exactly to the same $\varepsilon_{reff,a}$. In the upcoming, we will demonstrate that the transmission coefficient can be uniquely described by this effective permittivity value, giving exactly the same spectral performance, provided that we are always working at the same Δ_z (we saw in Fig. 2.22 that a change of Δ_z implies a modification of the sensor response) and keep the same value for L_z.

First, we keep the same dimensions but place the analyte at $\Delta_x = \Delta_z = 0$, as shown in the inset of Fig. 2.28(b). We can tune the permittivity to get the same effective permittivity ($\varepsilon_{reff,a} = 0.8883$) at the ENZ frequency (0.95). After the calculation, we get $\varepsilon_d = 2.697$. Note that this value is smaller than before, as expected, since the interaction of the analyte with the electric field increases when it is placed at the center, so a smaller permittivity is necessary to have the same response. The transmission coefficient for this configuration is depicted in Fig. 2.28(b), showing a good agreement with the previous case. We can also modify the width of the analyte, instead of its permittivity. Using the same procedure, we obtain $L_x = 0.2439b$, which is logically smaller than the initial case. The transmission coefficient for this case is shown in Fig. 2.28(c), where a good agreement is again observed. Finally, we can consider that the analyte fills completely the x axis and tune its permittivity. After applying the same procedure as before the calculated value is $\varepsilon_d = 2.0029$, which is smaller than the analyte in Fig. 2.28(a,b), as expected. The transmission coefficient for this case is shown in Fig. 2.28(d) with a nice agreement with the previous cases.

By comparing all the cases, it can be observed that the agreement is not only at the ENZ frequency but within the entire spectrum. This is due to the dispersive performance of the waveguide, even when the parameters of the analyte have been calculated at a single frequency. Hence, it is only necessary to calculate the permittivity at a single frequency and then we will obtain the same response for all the frequencies. Note that this performance is only valid provided the analyte is not dispersive (which is the most usual case, at least within a limited bandwidth) and it has $\varepsilon_d > 1$. These results demonstrate that the response of different configurations is identical if they can be reduced to the same effective permittivity.

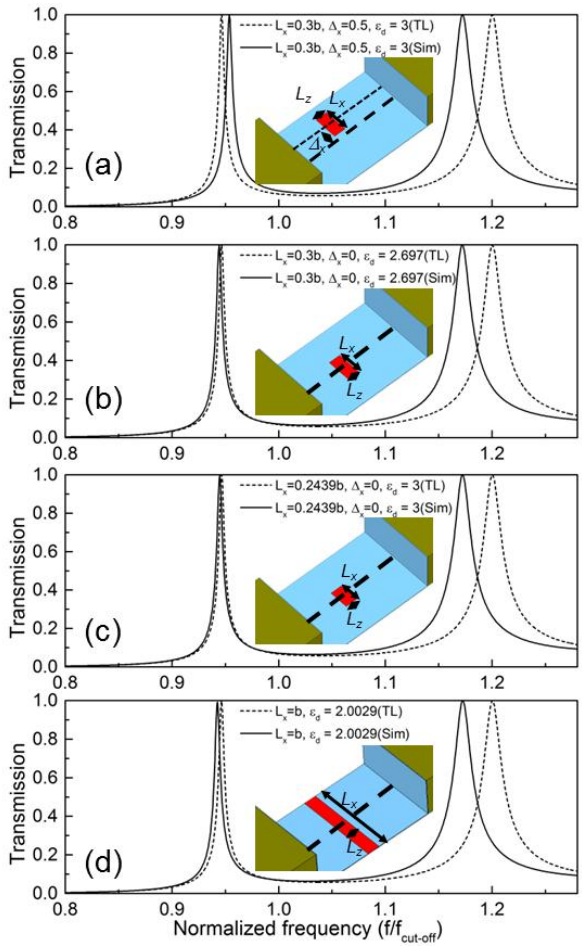

Figure 2.28. Analytical (dashed lines) and numerical (solid lines) results of the transmission coefficient for different configurations of the analyte inside of the ENZ channel synthetized using the effective permittivity approach: (a) a dielectric analyte shifted at $\Delta_x = 0.5$ with lateral dimensions $L_x = 0.3b$ and $\varepsilon_d = 3$, (b) a dielectric analyte at $\Delta_x = 0$ with the same dimensions but $\varepsilon_d = 2.697$, (c) a dielectric analyte at $\Delta_x = 0$ with lateral dimensions $L_x = 0.2439b$ and $\varepsilon_d = 3$ and (d) a dielectric analyte completely filling the transversal axis with and $\varepsilon_d = 2.0029$. $L_z = 0.15b$ in all cases.

2.5 ENZ metalenses operating at optical wavelengths

In the previous sections, we have designed and evaluated the performance of several ENZ MTM devices. They have been engineered using narrow hollow rectangular waveguides working from microwaves up to THz frequencies. Recently, it has been demonstrated that an ENZ MTM can also be scaled down to near infrared and visible wavelengths by using multilayered structures taking into account adequate metal models [SUBR 12], [MAAS 13], [GAO 13], [YANG 13]. Inspired by the flexibility and interesting features of ENZ media, in this section the dispersion of metal-insulator-metal plasmonic waveguides is exploited to artificially mimic an ENZ medium at optical wavelengths. First, we will discuss the operation principle of this structure in terms of its dispersive performance. Then, it is applied in the design of several converging metalenses: plano-concave smooth-profiled metalens and its step-wise approximation, an ENZ-GRIN plano-concave lens and an ENZ-GRIN biconcave lens.

2.5.1 Metal-Insulator-Metal (MIM) plasmonic waveguide

A schematic representation of the MIM plasmonic waveguide under study is shown in Fig. 2.29(a). It has an arbitrary length of l_z = 1000 nm and thickness d_x = 200 nm and it is infinite along y. It consists of a Silicon Dioxide (SiO_2) dielectric slab of thickness h_x sandwiched in between two metal plates of silver (Ag). The metal plates are modeled with a complex permittivity fitting the Palik's experimental data [PALI 85].

It is known that plasmonic parallel plate waveguides as the one used in this study can support two types of modes [KIM 06]: Surface plasmon modes (SPP) and parallel plates waveguide (PPW) modes. The former modes have their propagation constant larger than the wavenumber in free-space ($\beta > k_0$, as explained in Chapter 1). Therefore, they are also known as slow wave modes since they fall beyond the cone of light. On the other hand, the PPW modes have the complementary performance with $\beta < k_0$ and they are also named as fast wave modes. Here, we are interested in the second group of modes since it is not possible to use the SPP modes to artificially create an ENZ medium (SPP modes require a negative permittivity in order to exist). Thus, we look at the fundamental mode for the parallel plate plasmonic waveguide with the electric field parallel to the plates (E_y); i.e., the TE_1 mode.

It is important to highlight that, since the electric field is not perpendicular but parallel to the metal plates of the plasmonic waveguide, the TM mode is not excited. Hence, a background mode interfering with the desired mode is not present in this case, as it could happen if the orthogonal polarization (E_x) was used. For the latter polarization, the wise approach to emulate an ENZ medium is to work at the cut-off of the fundamental rectangular waveguide TE_{01} mode [ARGY 12], [FLEU 13].

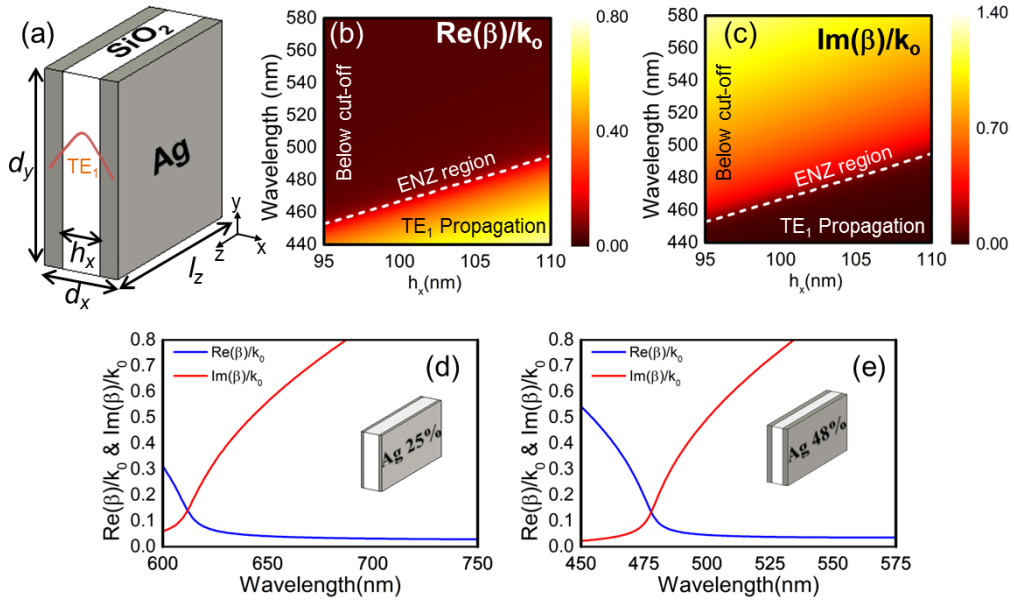

Figure 2.29. (a) Schematic representation of the MIM plasmonic waveguide with thickness d_x = 200 nm, length l_z = 1000 nm, height d_y = 500 nm and dielectric thickness h_x. Analytical results of the normalized real (b) and imaginary part (c) of β of the transverse electric TE_1 mode with respect to k_0 as a function of the operational wavelength and thickness of the dielectric. Analytical results of the real (blue lines) and imaginary (red lines) part of the normalized propagation constant for the case of the plasmonic parallel plate waveguides with a dielectric width of h_x = 150 nm (d) and h_x = 104 nm (e).

In the case under study, the TE_1 mode is a fast wave mode whose dispersion relation, assuming semi-infinite metals, can be expressed as follows [ALÙ 06]:

$$\tan\left(\frac{h_x}{2}\sqrt{\varepsilon_{SiO_2}k_0^2-\beta^2}\right)=\frac{\sqrt{\beta^2-\varepsilon_{Ag}k_0^2}}{\sqrt{\varepsilon_{SiO_2}k_0^2-\beta^2}} \qquad (2.27)$$

where ε_{SiO2} is the permittivity of the silicon dioxide in the middle of the waveguide, ε_{Ag} is the complex permittivity of the metal plates, k_0 is the wave number in free-space and β is the propagation constant of the TE mode.

From the latter expression, one can conclude that the dispersion of these plasmonic waveguides is directly related to the thickness of the dielectric slab sandwiched between the metallic plates. To better understand the features of this structure, we can calculate the real and imaginary parts of β using Eq 2.27 and normalize it with respect to the wave number in vacuum [Re(β)/k_0, Im(β)/k_0]. The results of these factors as a function of the free-space wavelength (λ_0) and transversal dimension (h_x) of the dielectric are shown in Fig. 2.29(b,c), respectively. Three regions of operation are observed: a) the cut-off region where the mode does not propagate in the structure, b) the propagation region where the mode exists and propagates in the waveguide and finally c) the ENZ region. Within the ENZ region, Re(β)/k_0<<1, i.e., it is possible to emulate an ENZ artificial medium working at these wavelengths. For the sake of completeness, the analytical results of these two factors for two waveguides with h_x =150 nm and h_x =104 nm are shown in Fig. 2.29(d,e), respectively, where the previous explanation can be easily observed with regions Re(β)/k_0<<1.

This analytical evaluation is a good starting point to ground the physics. However, it is only valid for the case of a single parallel plate plasmonic waveguide. Since this structure will be used in the design of metalenses by staking several of them, the potential coupling between neighbors should be considered. To take this effect into account, we use as unit cell the waveguide shown in Fig. 2.29(a) and employ the frequency domain solver of the commercial software CST Microwave Studio® to retrieve from the S-parameters the effective permittivity of the arrayed configuration [SMIT 05b]. We apply periodic boundary conditions on the left, right, top and bottom sides of the waveguide in order to realize an infinite array of waveguides along both *x* and *y* axes.

With this configuration, the effective permittivity was retrieved for three different metal filling fractions: 10%, 25% and 48% metal thickness which correspond to a thickness of the dielectric of h_x = 180 nm, h_x = 150 nm and h_x = 104 nm, respectively. The retrieved permittivity for each case is shown in Fig. 2.30(a-c), respectively. For the 10% case, the ENZ region emerges at 868.3 nm, where the real part of permittivity is 0.0034+ *i*0.0845 (here we use *i* as the convention for the imaginary component since it is the usually used in plasmonics). For the 25% case, the complex permittivity is 0.0059 +*i*0.0939 at 641 nm. And for the 48% case, the complex permittivity is 0.0951+ *i*0.1804 at 474.9 nm. This confirms the ability to tune the ENZ performance over a wide spectral range using the plasmonic parallel plate waveguide. For the sake of completeness, Fig. 2.30(d) shows the retrieved effective complex permittivity for the case of the plasmonic waveguide shown in Fig. 2.30(c) but with an increased length (l_z = 2600 nm). For such length, FP resonances appear in the spectrum of

interest, resulting into a distortion of the ideal Drude response. This effect is not observed for the case shown in Fig. 2.30(a-c) due to the reduced length of these plasmonic waveguides.

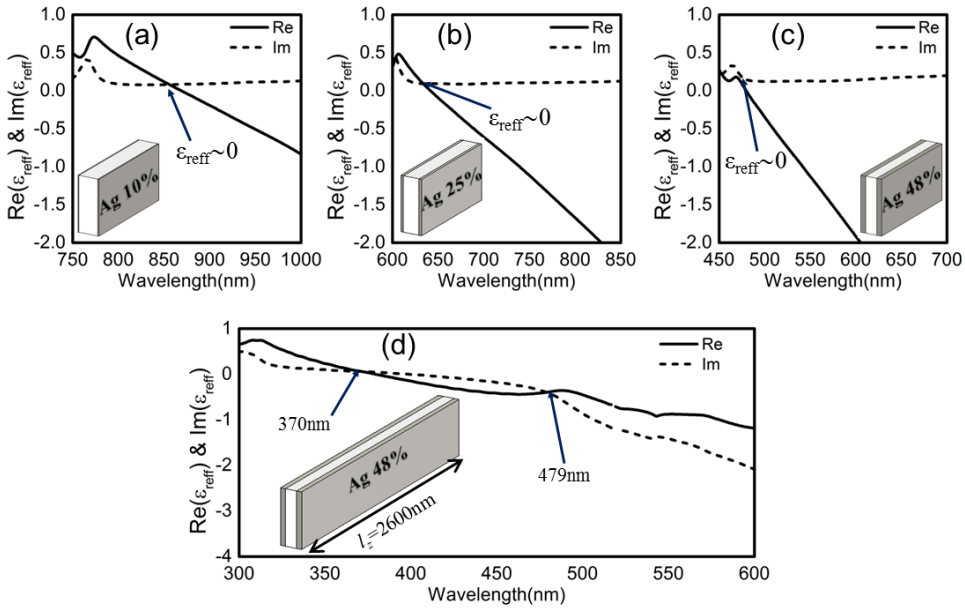

Figure 2.30. Retrieved values of the complex effective permittivity for the case of a plasmonic waveguide of length l_z = 1000 nm and metal thickness of 10% (a), 25% (b), 48%(c) and 48% with a length of l_z = 2600 nm (d).

To further validate the ENZ performance of the proposed structure, we can calculate the field distribution of one of the waveguides shown in Fig. 2.30. Here, we take the one with dielectric thickness h_x = 104 nm and length l_z = 1000 nm [see Fig. 2.30(c)]. The same solver was used as previously and the plasmonic waveguides were illuminated with a vertically polarized (E_y) plane-wave. An electric probe was placed at the output of the waveguide to record the transmitted electric field.

The numerical results of the normalized E_y-field as a function of wavelength are shown in Fig. 2.31(a) where two peaks of transmission emerge: one related to the ENZ regime and the second to the FP resonance (as it was discussed in the rectangular waveguide evaluated in the previous sections). To support the latter statement, the numerical results of the phase distribution of the E_y-field along the optical z axis together with the normalized field distribution on the yz-plane are shown in Fig. 2.31(b,c) for the first and second transmission peaks, respectively. The phase distribution inside the waveguide is almost constant at λ_0 = 474.9 nm [Fig. 2.31(b)]

while it is not the case for λ_0 = 445.2 nm [Fig. 2.31(c)]. This corroborates the assumption that each peak corresponds to the ENZ regime and the FP resonance, respectively. The normalized propagation constant extracted from the phase difference between the output and the input of the waveguide is 0.27 and 0.7 at λ_0 = 474.9 nm and λ_0 = 445.2 nm, respectively, which represent an effective permittivity of ε_{reff} = 0.09 and ε_{reff} = 0.38. Hence, by working at ε_{reff} = 474.9 nm, the plasmonic waveguide actually emulates an ENZ medium with almost zero values of phase variation and propagation constant.

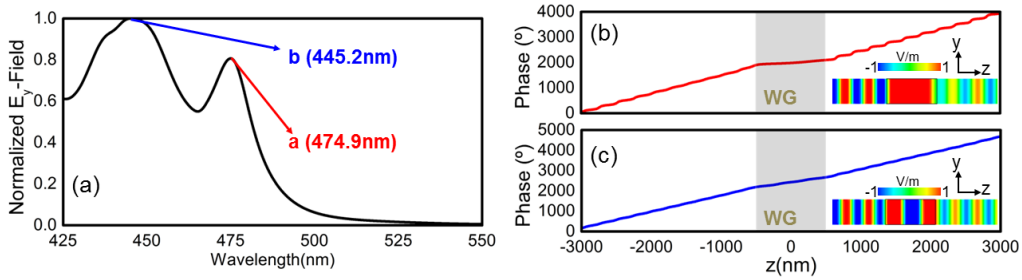

Figure 2.31. (a) Numerical results of the normalized E_y-field at the output of the parallel plate plasmonic waveguide with a dielectric thickness of h_x = 104nm corresponding to a 48% of metal. Numerical results of the phase distribution of the E_y-field along the optical axis z for the first two peaks of transmission panel (a): (b) at 474.9nm and (c) at 445.2 nm, along with the normalized field distribution on the yz-plane for each case (bottom-right inset).

2.5.2 ENZ metalenses: design and discussion

Now that we have shown how a plasmonic parallel plate waveguide can be used to emulate an ENZ medium, we can apply this structure in the design of ENZ metalenses. Here the waveguide with a dielectric thickness of h_x = 104 nm and length l_z = 1000 nm will be used as the reference waveguide. The metalenses are designed with a focal length of FL = 10.75λ_0 at λ_0 = 474.9 nm.

To begin with, let us first analyze the focusing properties of the simplest metalens with the input face flat. As discussed in Section 2.2, in order to produce optical focusing, the output face of a lens should be designed with a convex or concave profile depending on whether the refractive index of the lens is larger than 1 (such as in natural dielectrics) or smaller than 1 (our case) [KOCK 46]. Based on this, the designed full plano-concave metalens working at the previous described wavelength and *FL* is shown in Fig. 2.32(a). Note that this metalens has a smooth output surface in order to follow the corresponding circular profile. Also, a step-wise metalens is

designed following the same profile, as shown in Fig. 2.32(d). With the aim of evaluating the focusing performance of both metalenses under a vertically (E_y) polarized plane-wave illumination, the transient solver of the commercial software CST Microwave Studio® was used. Electric planes were defined at the top and bottom of the structures to make them infinite along the *y* axis, i.e., cylindrical metalenses, whereas open boundary conditions were applied to the rest of the boundaries to emulate an isolated metalens in free-space.

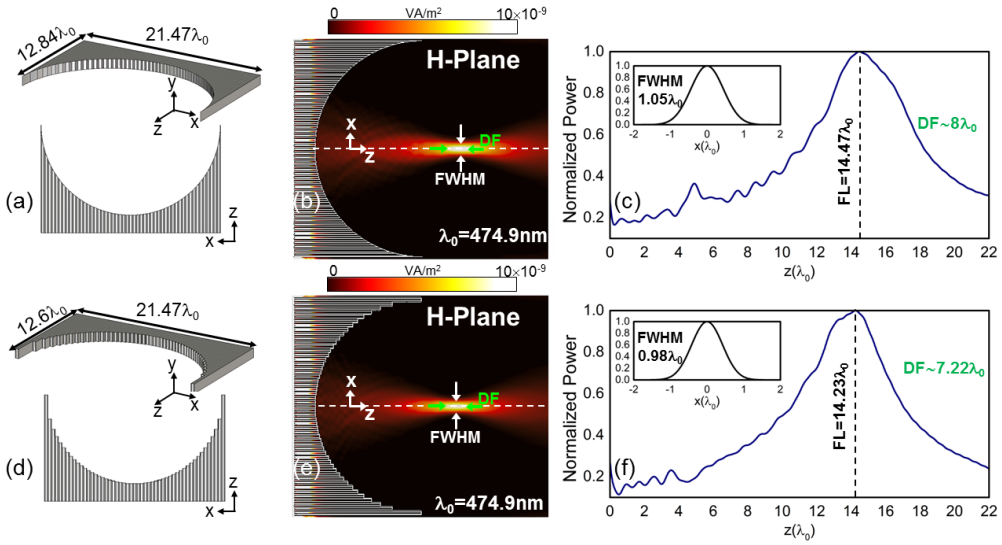

Figure 2.32. Schematic representation of the plano-concave smooth profiled (a) and step-wise metalens (d). Numerical results of the power distribution on the H-plane at the designed wavelength (λ_0 = 474.9 nm) for the smooth profiled (b) and step-wise metalens (e). Numerical results of the normalized power distribution along the optical z-axis for the smooth profiled (c) and step-wise metalens (f) together with the normalized power distribution along the transversal *x*-axis at each focal length (shown as inset).

The numerical results of the power distribution on the focal plane (*xz*-plane) for the plano-concave smooth and step-wise profiles are shown in Fig. 2.32(b,e), respectively, at the design wavelength. As it is shown, both structures are able to produce a focus at their output plane with a *FL* of $14.4\lambda_0$ and $14.23\lambda_0$, respectively. The *FL* is similar for both cases but they are strongly deviated $3.65\lambda_0$ and $3.48\lambda_0$, respectively, from the designed value ($10.75\lambda_0$). This is mainly due to the influence of the waveguides far away from the central ones. Each waveguide in the array shows a slightly different dispersion due to their notable length difference, as it has been shown in Fig. 2.30(d) for the case of an increased length of a plasmonic waveguide. The FP resonances that appear in longer waveguides deteriorate the ideal Drude response of the plasmonic waveguides, destroying the homogeneity of the lens in terms of effective permittivity.

As a consequence, the different parts of the metalenses do not work together coherently to produce the desirable focusing. As we will see later, this problem can be solved by applying the GRIN technique, whereby the lengths of the plasmonic waveguides are kept constant.

To evaluate the focusing performance quantitatively, the normalized power distribution along the optical *z*-axis at (x = 0, y = 0) nm for the smooth and step-wise metalenses is shown in Fig. 2.32(c,f), respectively. Furthermore, the power distribution along the transversal *x*-axis at each focal length is shown as inset in the same figures. From the power distribution along the *z*-axis, the *DF* is $8\lambda_0$ and $7.22\lambda_0$, for the smooth and step-wise metalenses, respectively. These large values of *DF* are expected due to the detrimental influence of the lateral waveguides, as explained before. Finally, the transversal *FWHM* is $1.04\lambda_0$ and $0.98\lambda_0$ for each design, respectively, demonstrating that similar results can be obtained with both structures.

As it has been discussed, these metalenses can be improved by applying the GRIN technique. Following the procedure described in section 2.3.2, and taking into account that here the discretization of the lens is only along the *x* direction; the phase delay difference that each waveguide should introduce for optical focusing can be calculated as:

$$\Delta\Phi^{(m)} = \beta^{(m)} l_z = \beta_0 l_z - k_0 \sqrt{FL^2 + (md_x)^2} - FL + 2\pi\alpha \tag{2.28}$$

where *m* is the integer used to define the discretization (i.e., each waveguide) of the array along the *x* axis, β_0 is the propagation constant of the waveguide at the center of the array [i.e., the reference waveguide, whose dimensions are shown in Fig. 2.29(e)]. The propagation constant for each waveguide is extracted from Eq. 2.28 and introduced in Eq. 2.27 in order to calculate each dielectric thickness (h_x) to produce the required phase distribution. The resulting GRIN-ENZ plasmonic plano-concave lens is then designed and it is schematically shown in Fig. 2.33(a). This metalens is numerically evaluated using the same numerical setup as the previous metalenses.

The power distribution on the *xz*-plane at the design wavelength is shown in Fig. 2.33(b). For this metalens, the *FL* is obtained at $10.23\lambda_0$, which is even closer to the designed *FL* compared with the previous metalenses with a small deviation of $0.52\lambda_0$. Also, the normalized power distribution along the optical *z* axis and along the transversal *x* axis at the *FL* is shown in Fig. 2.33(c). Regarding the resolution of the metalens, the *DF* and *FWHM* are $2.84\lambda_0$ and $0.58\lambda_0$, respectively, with an improved resolution for this design. Finally, a reduction of volume of 52.3% is obtained with this lens (compared with the volume of the full concave metalens) improving at the same time the spatial resolution.

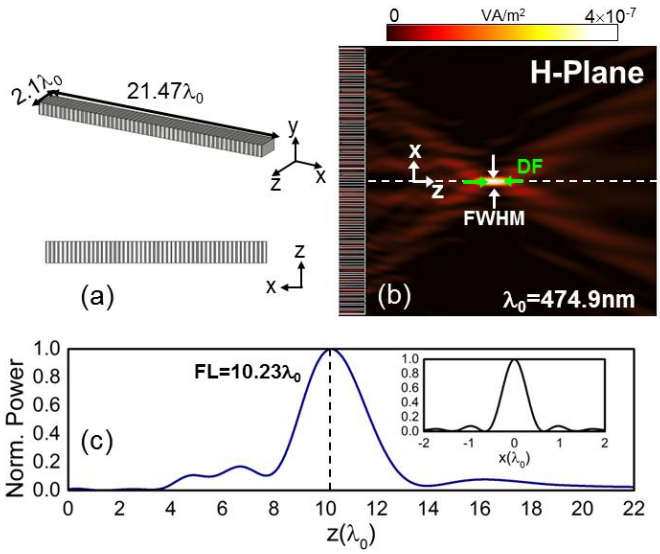

Figure 2.33. (a) Schematic representation of the designed GRIN metalens. (b) Numerical results of the power distribution on the H plane at the designed wavelength. (c) Numerical results of the normalized power distribution along the optical *z* axis for the GRIN metalens along with the normalized power distribution along the transversal *x* axis at the focal length (shown as inset).

To sum up the results obtained with these plano-concave metalenses, the values of *FL*, *DF*, *FWHM* and volume for each design are shown in Table 2.3. As it is shown, the best performance is obtained with the ENZ-GRIN metalens with a reduction of volume of 52.3% which is an advantage in order to use these designs in integrated systems.

Lens profile	FL[a] (λ_0)	DF[b] (λ_0)	FWHM[c] (λ_0)	Volume(%)[d]
Smooth concave	14.4	8	1.04	100
Step-wise concave	14.23	7.22	0.98	103
GRIN	10.23	2.84	0.58	47.74

Table 2.3. Focusing performance of the designed ENZ metalenses

[a] *FL* is the Focal length.
[b] *DF* is the Depth of focus.
[c] *FWHM* is the full-width at half-maximum along the transversal x-axis at the *FL*.
[d] Volume normalized to the volume of the smooth concave metalens.

As a final study, we can also design a bi-concave ENZ lens using the GRIN technique. For this case, the phase delay difference that should be introduced for each waveguide of the array is defined as follows [PACH 13a], [PACH 16c]:

$$\Delta\Phi^{(m)} = \beta^{(m)} l_z = \beta_0 l_z - 2k_0 \sqrt{FL^2 + (md_x)^2} - FL + 2\pi\alpha \tag{2.29}$$

Following the same procedure as the ENZ-GRIN plano-concave lens, we calculated the required h_x dimension by using Eq. 2.27 and Eq. 2.29. The numerical results of the power distribution on the *xz*-plane along with the electric field magnitude along the optical *z* axis are shown in Fig. 2.34(a,b), respectively. Here, it is clearly observed the focusing performance of the proposed structure. The *FL* is slightly deviated from the designed value and it is at $\sim 11\lambda_0$ which may be due to the discretization of the structure along the *x* axis. Also, the *DF* and *FWHM* are $\sim 3\lambda_0$ and $0.65\lambda_0$, respectively. These results demonstrate that the structure is capable to focus the incoming field distribution at its output.

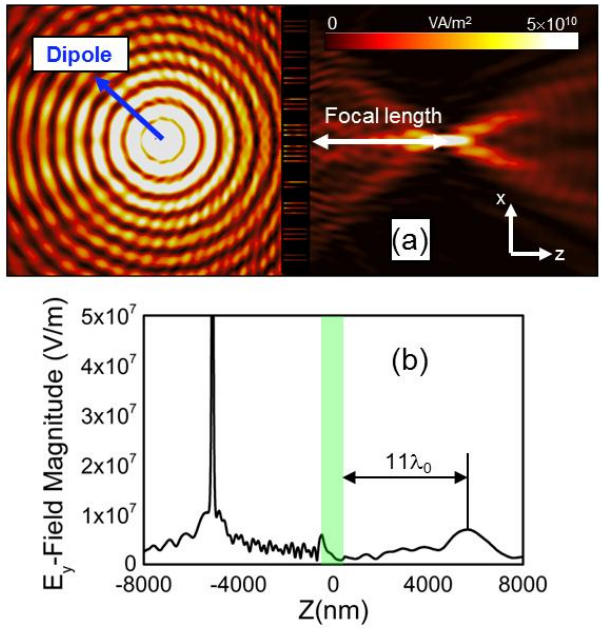

Figure 2.34. Numerical results of the power distribution on the H-plane (a) along with the electric field magnitude along the optical *z* axis (b) for a GRIN biconcave lens designed with a focal length of $10\lambda_0$.

Chapter 3

Extraordinary Transmission metalenses

The field of lenses has greatly benefited from MTMs research. The perfect lens [PEND 00], superlens [FANG 05] hyperbolic lenses [LIU 07], [MONT 12], [ENGH 06], advanced designs on the basis of transformation optics [DEME 11], [KWON 09] or extreme refractive index values [NAVA 11b], [NAVA 12], [TORR 12a] show the merits of applying MTMs concepts throughout the whole EM spectrum. Different implementations have been proposed for lenses to fulfill the particular requirements of each spectral window. For instance, the classical arrangement of SRR and wires has been widely used at microwaves frequencies [PARA 04], [GREE 05]. However, for higher frequencies, these structures are limited due to their increasing losses. Among the large number of MTM structures reported in the last years, the fishnet MTM has proven to provide the best performance for high frequency and quasi-optical applications [SOUK 11], [ZHAN 05], [DOLL 06]. It has been demonstrated that by designing a free-standing fishnet MTM with two in-plane periods, a very low-loss structure can be fabricated in the millimeter-wave range [BERU 07a], [NAVA 08] (see Chapter 1). In addition, through manipulation of permittivity and permeability a good (ideally perfect) matching to free-space can be obtained, as reported previously using a plano-concave lens [BERU 08], [NAVA 10a], [NAVA 10b], [NAVA 11b].

A major drawback of the above mentioned lenses is the large volume occupied by the lens material which leads to a considerable weight of the structure. To mitigate this problem, one can apply the zoning technique whereby parts of the lens are removed when their phase variation with respect to free-space propagation is an integer multiple of 2π [KOCK 46], [GOLD 92]. In this chapter, we exploit this technique to propose several compact low-weight fishnet metalenses. We start the chapter with a description of the zoning technique. Then, a zoned fishnet metalens is designed and compared with its full profiled counterpart. Also, the reference phase and phase reversal techniques are described and applied together with the zoning technique in order to improve the performance of the lenses in terms of *SLL* reduction, position of the *FL* and operation bandwidth.

3.1 Zoning technique applied to fishnet metalenses

In this section, the operation principle of the zoning technique is described and applied in the design of a plano-concave zoned metalens using the fishnet MTM. The focusing performance and the radiation pattern of this structure is evaluated both numerically and experimentally and compared with its full profiled counterpart. The metalenses are designed to operate at f = 56.7 GHz (λ_0 = 5.29 mm), where the fishnet MTM behaves as a NRI medium with n_{lens} = -0.25, with a FL of 47.62 mm = 9λ_0. The design and numerical analyses are made using the commercial software CST Microwave Studio®.

3.1.1 Operation principle of the zoning technique

As discussed in Chapter 1, the profile of a lens depends directly on the refractive index of the material used. Hence, a lens made upon commercial dielectrics (with n > 1) has an elliptical convex profile. However, since MTMs allow the control of the EM response of a medium, it is possible to design lenses with different profiles such as concave parabolic or circular when the refractive index of the artificial media is n = -1 or n = 0 respectively [NAVA 11b]. In our case, the required profile for a full profiled (non-zoned) metalens is a concave ellipse. This profile is however modified by the zoning technique into a multi-level stepwise structure.

The zoned procedure relies on sequentially removing material from the metalens profile when phase variation with respect to free-space propagation is equal to integer multiples of 2π. This phase variation of the waves traveling through the metalens is achieved by reducing the profile each time a maximum thickness (t) is reached. It can be mathematically calculated as follows:

$$t = \frac{\lambda_0}{1 - n_{lens}} \tag{3.1}$$

where λ_0 is the free-space wavelength and n_{lens} is the refractive index of the medium used for the lens. According to the above equation, the zoned metalens is inevitably frequency-dependent in its behavior. However, this is not a drawback for MTM-based lenses since they are already narrow band. By combining the fishnet MTM and the zoning techniques, it is possible to design compact focusing metadevices with a flat face and a zoned-stepped face at its input and output, respectively.

The zoned profile at the output of the structure is obtained by using the well-known general equation of an ellipse together with the condition of maximum thickness defined by Eq. 3.1. The design equation is as follows:

$$z = \mathrm{mod}\left[\frac{FL\left(1-n_{lens}\right)-\sqrt{FL^2\left(1-n_{lens}\right)^2-x^2\left(1-n_{lens}^2\right)}}{\left(1-n_{lens}^2\right)}, t\right] \tag{3.2}$$

where *mod* is the modulus operation. With the above equations, the metalens profile using the fishnet MTM is designed considering n_{lens} = –0.25 (the synthesis of this refractive index will be shown in the next section), $FL = 9\lambda_0$ and f = 56.7 GHz (λ_0 = 5.29 mm) and its profile is shown in Fig. 3.1 as a green solid line. The red line corresponds to the profile of the lens when no zoning is applied and the gray solid lines are the successive profiles (which define the steps of the zoned profile once its thickness is reduced because of the value of t). From Eq. 3.1, at the design wavelength the maximum thickness is $t = 0.8\lambda_0 \approx 4.23$ mm, which is plotted as a black horizontal dashed line. Note that each time the thickness limit is reached, the profile is reduced. Moreover, note that the thickness of the zoned profile is slightly above the limit t. This is due to the periodicity of the fishnet MTM along the z axis (as it will be presented in the following section) which produces a discretization of the profile.

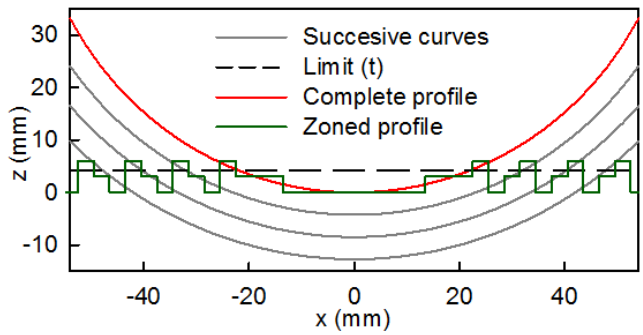

Figure 3.1. Calculated profile of the metalens: full profile (red curve), successive steps (grey lines), thickness limit (black dashed line) and the zoned profile (green curve).

In the following sections, the performance of the fishnet metalens with zoned profile shown in the above figure will be discussed and compared with the full profiled case.

3.1.2 Focusing performance

The unit cell used for the fishnet MTM is shown in the top inset of Fig. 3.2. Its dimensions are: d_x = 3 mm, d_y = 5 mm, d_z = 1.5 mm (air gap of 1 mm and metal thickness w = 0.5 mm) and hole diameter a = 2.5 mm. First, the effective index of refraction of an infinite fishnet MTM with this unit cell is computed using the eigenmode solver of the commercial software CST Microwave Studio®. For this simulation perfect electric conductor (PEC) is used as the material of the structure because it is a good approximation at millimeter-waves. The resulting refractive index for the fundamental band is presented in Fig. 3.2. As it is shown, the MTM has a strongly dispersive effective NRI. At the design frequency f = 56.7 GHz (λ_0 = 5.29 mm), the effective refractive index is n = –0.25. We have selected this frequency due to the fact that the dispersion is stronger for frequencies between 53-56 GHz but it is smoother close to the design frequency minimizing possible experimental errors of the *FL* and frequency, i.e., chromatic aberration.

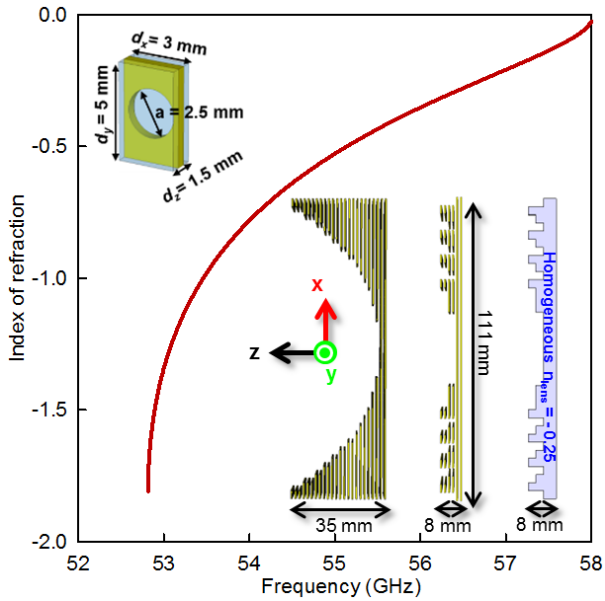

Figure 3.2. (a) Index of refraction for a MTM made of an infinite number of SSHA. (Top inset) Schematic representation of the unit cell with parameters: d_x = 3 mm, d_y = 5 mm, d_z = 1.5 mm, a = 2.5 mm and metal thickness w = 0.5 mm. (Bottom inset) From left to right: full concave profile and zoned metalens using the fishnet MTM and zoned lens using an isotropic homogeneous medium with n_{lens} = -0.25.

Using this unit cell, the zoned fishnet metalens is designed with the profile shown in Fig. 3.1. It is schematically shown in Fig. 3.2 as inset (center figure). The whole structure comprises a total number of 37 × 27 holes along *x* and *y* directions, respectively, and between 2 and 6 stacked plates along *z* axis. Thus, the metal structure of the lens can be enclosed by a box with dimensions $21\lambda_0 \times 25.5\lambda_0 \times 1.5\lambda_0$. It is designed to obtain a cylindrical focus to ease the assembly. Notice that the total thickness of $1.5\lambda_0$ is not in contradiction with Eq. 3.1, since that equation only accounts for the thickness limit corresponding to the profiled interface, i.e., the zoned face. The total value, however, is composed of such thickness ($t = 0.8\lambda_0$) and the additional structure at the back of the lens (2 holey plates). This metalens will be compared with two more idealized structures to evaluate its performance: a full profiled metalens (with a profile extracted from the red curve of Fig 3.1) and an isotropic homogeneous zoned lens with $n_{lens} = -0.25$. Their profiles are shown in Fig. 3.2 as insets.

To begin with, the homogenous structure is simulated using the frequency-domain solver of CST Microwave Studio®. We are interested in evaluating its performance for a single frequency (f = 56.7 GHz). Therefore, by using this solver, it is simulated without the need of a dielectric dispersion model such as Drude material to mimic the NRI behavior. This way, simulation time is reduced. Moreover, periodic boundary conditions are imposed along *y* so that the lens is effectively infinite in that direction, whereas open boundary conditions (i.e., perfectly matched layers) are used along *x* and *z*. The other designs (full profiled and zoned fishnet metalenses) are simulated using the transient solver in order to evaluate their spectral response within the millimeter-wave V-band. The metal used for these two structures is aluminum with a conductivity $\sigma_{Al} = 3.56 \times 10^7$ S/m. The excitation is done with a vertically polarized (E_y) plane-wave impinging on the flat face. Given the twofold symmetry, magnetic and electric symmetries are used at the *yz*- and *xz*-planes, respectively, in order to reduce computation effort, and perfectly matched layers are used for the rest of the simulation box boundaries. A hexahedral mesh with a resolution up to 0.25 mm × 0.5 mm × 0.27 mm is chosen to map accurately the geometry of the lenses.

Simulation results of the spatial power distribution in *xz*-plane for the three structures at the working frequency f = 56.7 GHz (λ_0 = 5.29 mm) are shown in Fig. 3.3. It is evident that they all work as focusing devices and that they have similar *FL*: the full profiled metalens has *FL* = 47.4 mm ($= 8.96\lambda_0$) which is very close to the homogenized zoned structure *FL* = 47.63 mm ($= 9.01\lambda_0$), whereas the zoned metalens presents a slightly different value, *FL* = 49.5 mm ($= 9.35\lambda_0$). The small difference ($0.34\lambda_0$ = 3.7%) between the ideal *FL* obtained with the isotropic homogeneous structure and the zoned fishnet metalens validates the design here presented.

The power distribution at the focal plane along the transversal axis for each design is presented on top of each two-dimensional color map. The *FWHM* along *x* at the

focal plane is very similar in all considered cases, namely $0.47\lambda_0$, $0.57\lambda_0$, and $0.56\lambda_0$ for the full profiled, zoned fishnet and homogenized structures, respectively. Moreover, it can be observed that the lateral lobes are more prominent for both zoned devices. This is explained by the smaller output numerical aperture of the zoned designs compared with the full profiled case. However, these results demonstrate that the zoned fishnet metalens does not exhibit major deterioration on the overall performance.

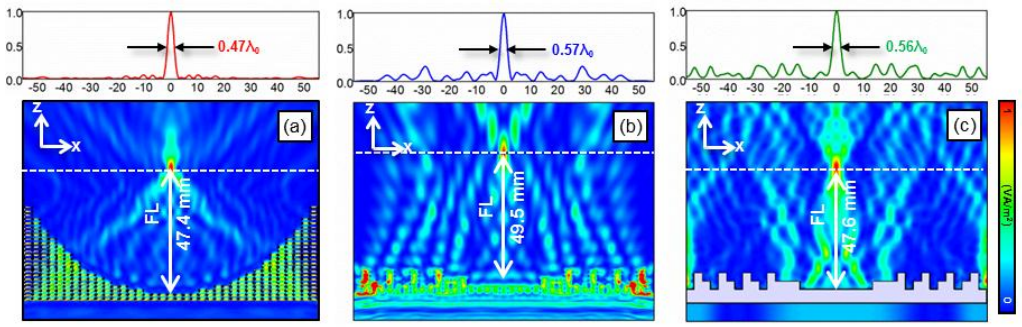

Figure 3.3. Normalized power distribution on the *xz*-plane: (a) Full profiled and (b) zoned fishnet metalens, (c) zoned lens using an isotropic homogeneous medium with n_{lens} = -0.25. The top panel of each figure is the power at the *FL* along the white dashed line (*x*-axis in mm) depicted in each two-dimensional color map.

As observed in Fig. 3.3, there is a disagreement in the *FL* obtained with the zoned lens compared to the homogenized design. In order to explain this phenomenom, it is important to know how it behaves when the number of plates is changed. This is due to the fact that the lens profile has been calculated considering the refractive index of an ideal infinite number of stacked metal plates (Fig. 3.2). For this purpose, the frequency domain solver is used to retrieve the refractive index [SMIT 05b] using 2, 4 and 6 plates (which are the same number of plates used for the steps in the zoned design). Simulation results of the retrieved real part of the refractive index for these numbers of plates are shown in Fig. 3.4(a). Note that the fishnet MTM is strongly dependent on the number of plates. However, at the design frequency (f = 56.7 GHz) the retrieved values are n_1 = -0.00822, n_2 = -0.1664 and n_3 = -0.2083 using 2, 4 and 6 plates, respectively; i.e., the fishnet MTM is still working in the NNZ regime. To evaluate the effect of these variations, we obtained the power distribution on the *H*-plane for the 2D-zoned lens shown in Fig. 3.4(b) which is composed of homogeneous blocks with refractive index n_1 (red), n_2 (green), and n_3 (blue). Note that a good agreement is obtained comparing these results with those shown in Fig. 3.3(b,c) and

the *FL* is close to the designed value in all the cases. Moreover, note that it is almost at the same position as the zoned lens, which again validates the design here presented.

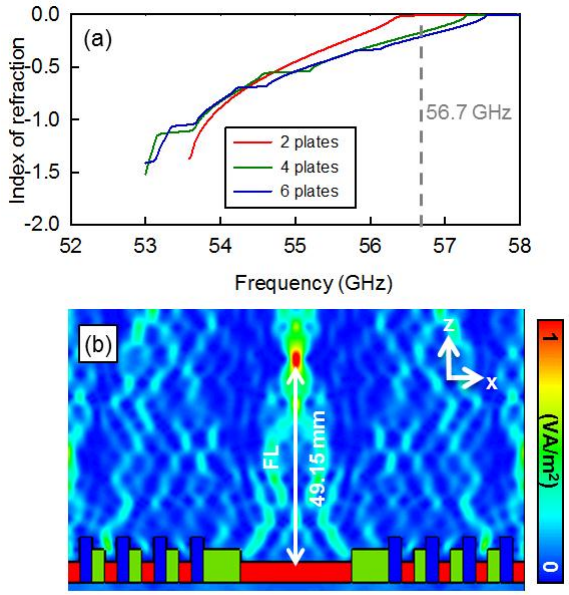

Figure 3.4. (a) Retrieved refractive index using 2 (red), 4 (green) and 6 (blue) plates with holes along *z* axis. (b) Simulation results of the power distribution on the *xz*-plane using homogeneous blocks with the retrieved refractive index at the design frequency which are equivalent to use 2 (red blocks), 4 (green blocks) and 6 (blue blocks) plates of the fishnet MTM.

To experimentally study the focusing properties of the zoned metalens, a prototype is fabricated [see photograph in Fig. 3.5(a)]. First, its spectral response is evaluated following a procedure similar to that described in section 2.3.2. The measurements are done using an AB Millimetre™ quasi-optical VNA. A sketch of the experimental setup is presented in Fig. 3.5(b). A V-band corrugated horn antenna connected to the VNA is used as a transmitter located 3300 mm away from the flat face of the metalens for quasi-plane-wave illumination. At this position the diameter of the beam waist of the Gaussian beam radiated by the corrugated horn antenna is ~ 400 mm ($75.6\lambda_0$) for the working wavelength (λ_0 = 5.29 mm), around 4 times larger than the metalens side. Hence, the whole fishnet device is uniformly illuminated. On the other side, a flange ended rectangular waveguide (WR-15) connected to the VNA is used as receiver. This waveguide is placed on an *xz* translation stage to scan the electric field along the *z* axis from 20 to 70 mm away from the center of the metalens in steps of 0.5 mm. In order to reduce diffraction and interferences by undesirable reflections, absorbers are used to

cover the whole setup. For the numerical simulations, a set of probes placed every 0.5 mm along the optical axis (from 20 mm to 70 mm from the center of the metalens) is used (following a similar procedure as described in section 2.3.2).

With this setup, simulation and experimental results of the spectral power distribution along the *z* axis are shown in Figs. 3.5(c) and (d), respectively. In general terms, the overall experimental map agrees well with the simulation results. In both color maps the peak of power (i.e. focus) occurs at 56.7 GHz, which corresponds to the design frequency. However, the spatial position of the focus is slightly different. For the simulation, it is located at z = 49.5 mm = 9.35λ_0 whereas it is at z = 46.5 mm = 8.79λ_0 for the experiment. To facilitate the comparison, the normalized power distribution along the *z* axis for both, simulation and experimental, cases at the design frequency 56.7 GHz is plotted together in Fig. 3.5(e). Moreover, note that both, simulation and experimental *FL* are located at a distance close to the designed value (9λ_0.). The *DF* obtained from simulation and experiment is 11.16 mm = 2.1λ_0 and 17.8 mm = 3.24λ_0, respectively. The small discrepancy of these results can be attributed to experimental tolerances such as the spatial averaging introduced by the non-ideal point detection done with the flange ended waveguide and also some imperfections on the fabrication and assembly process. Meanwhile, the larger *DF* compared to the isotropic homogeneous case [with a value of DF = 1.39λ_0, taken from Fig. 3.3(c)] arises due to the fishnet MTM effective refractive index displays dispersion with the number of SSHAs, as shown in Fig. 3.4 [NAVA 10b]. Increasing the number of SSHAs on the back of the lens would make it behave closer to the ideal condition, but at the expense of increasing losses. Also, note that for the experimental case, ripples are present even though the setup is covered with absorbing material. It can be due to standing waves generated between receiver and the metalens and appear for the whole range of frequency [see Fig. 3.5(e)].

A second peak can be also observed in both, numerical and experimental results, located at z ~ 38 mm and f ~ 53 GHz, with intensity approximately 5 dB lower than the main peak at 56.7 GHz. This peak is related to the effective refractive index $n_{lens} \approx -1.8$, which happens to require a similar, but obviously not identical, zoned profile. Moreover, note that there are also two other peaks at z = 25 mm and z = 65 mm around the design frequency. These peaks are those observed before and after the focus at 56.7 GHz in Fig. 3.5(e) which are produced by the waves emerging from the farthest parts of the lens that do not reach the *FL* at the same position. It is important to note that in both cases, simulation and experiment, there is an absolute minimum at 60 GHz. This is related to the Wood's anomaly, which appears at $f = c/d_y$ = 60 GHz [WOOD 35], as described in Chapter 1. According to the dispersion diagram (Fig. 3.2), transmission through the fishnet MTM is prohibited below 52.3 GHz. This is demonstrated as well in both color maps where the detected power vanishes below 52 GHz for any *z*.

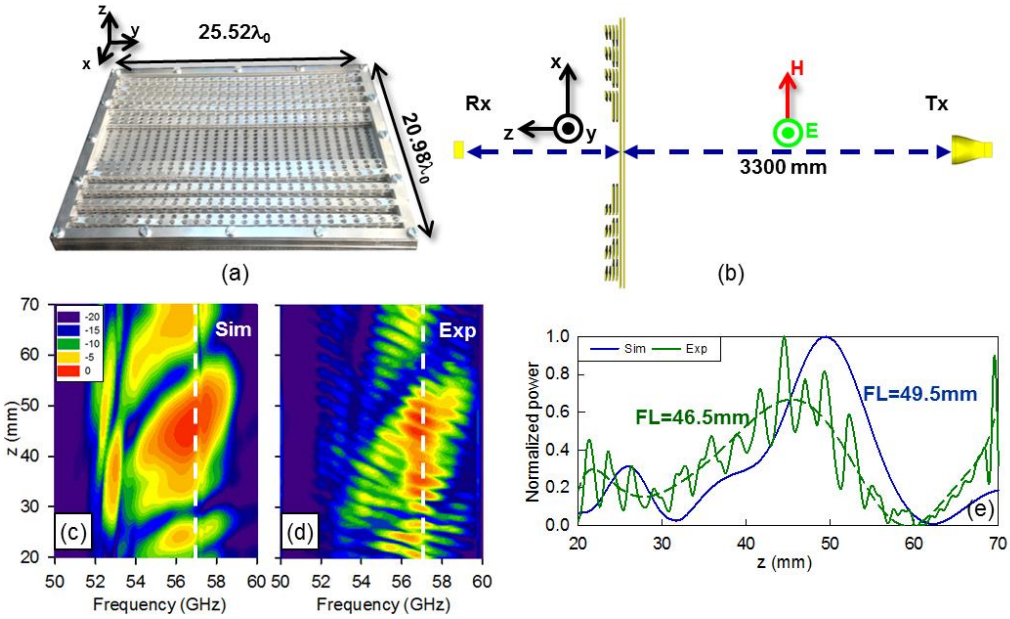

Figure 3.5. (a) Picture of the fabricated prototype. (b) Schematic representation of the setup used to experimentally evaluate the focusing performance of the metalens: it is placed in between a horn antenna (transmitter, Tx) and a flange ended rectangular waveguide (receiver, Rx). Numerical (c) and experimental (d) results of the power distribution spectra along the propagation *z* axis. (e) Simulation and experimental results of the normalized power distribution along z axis for the frequency f = 56.7 GHz (extracted from the white dashed lines of panel (c,d).

Once the spectral response of the metalens has been evaluated, we can move on into the experimental characterization of its focal plane at the design frequency (f = 56.7 GHz). For this case, the *xz*-plane is scanned experimentally with the flange ended waveguide. The scanning area comprises a square zone of the image plane going from 20 mm to 70 mm in the *z* axis and from –20 mm up to 20 mm along the *x* axis in steps of 0.5 mm. Simulation and experimental results of the normalized power distribution for the *xz*-plane are presented in Fig. 3.6(a,b), respectively. For the naked eye, it is evident the good agreement between simulation and experimental measurements with the same number of lateral lobes in both cases. Furthermore, the maxima are clearly observed and the small difference of the *FL* location is almost imperceptible for both, simulation and experimental results. Here, we can estimate the remaining focal property, the *FWHM*. For clarity, the power distribution along *x* at the *FL* is plotted in Fig. 3.6(c). The *FWHM* values from simulation ($0.57\lambda_0$) and experimental

measurements ($0.67\lambda_0$) are in good agreement with a small difference of only $0.1\lambda_0 \approx$ 15%.

Regarding the power enhancement at the *FL*, the zoned metalens has a value of 11 dB and 11.1 dB from simulation and experimental results, respectively, which is in agreement with previous designed plano-concave and biconcave lenses with parabolic profiles using the fishnet MTM [BERU 08], [NAVA 09b], [NAVA 11c].

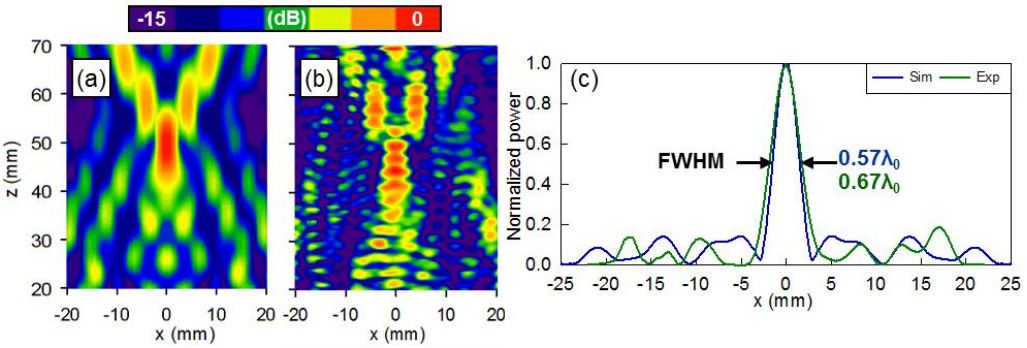

Figure 3.6. Numerical (a) and experimental (b) results of the power distribution in the *xz*-plane at f = 56.7 GHz. (c) Simulation and experimental results of the normalized power distribution along *x*-axis at each *FL*.

Lens Design	FL	FWHM	DF	Vol. (mm3)
Zoned lens homogeneous	$9.01\lambda_0$	$0.56\lambda_0$	$1.39\lambda_0$	78.9
Full concave lens	$8.96\lambda_0$	$0.47\lambda_0$	$1.27\lambda_0$	196.8
Zoned lens fishnet MTM (sim)	$9.35\lambda_0$	$0.57\lambda_0$	$2.1\lambda_0$	78.9
Zoned lens fishnet MTM (Exp)	$8.79\ \lambda_0$	$0.67\lambda_0$	$3.24\lambda_0$	78.9

Table 3.1. Simulation and experimental results for different lens designs along with the experimental results.

To summarize all the results here presented and ease the comparison among the different focusing devices here shown, the numerical results of the *FL*, *FWHM*, *DF* and the total volume for all the structures are presented in Table 3.1 along with the experimental results. As it can be observed, the overall response of the zoned metalens is similar to the case of the full concave profile. Moreover, note that the reduction of volume by applying the zoning technique is approximately 60%. These results

demonstrate that the zoned fishnet metalens is attractively compact and its performance is competitive with the full concave and ideal homogeneous cases.

3.1.3 Radiation pattern: steering millimeter waves

To evaluate the radiation pattern of the zoned metalens, we will first consider the case when a short dipole, used as the transmitter, is placed at the *FL* obtained from the previous section. The zoned structure is numerically compared with its full concave counterpart. Both metalenses are evaluated using the transient solver of the commercial software CST Microwave Studio®. As it was done before, the full three-dimensional structures are simulated with the same dimensions as the previous section. Far-field monitors are used to record the radiation pattern of the two structures within the frequency range 50-60 GHz with a step of 0.5 GHz. Note that this is an approximated study because of the chosen feeder. This is done in order to evaluate the performance of the fishnet metalenses when an idealized excitation (omnidirectional) is used.

The numerical results for the power distribution of the co- and cross-polar components on the *H*(*xz*)-plane are shown in Fig. 3.7(a,b) and Fig. 3.7(c,d) for the full concave and zoned cases, respectively. As it is shown, the co-polar enhancement for the full concave (12.9 dB) is slightly better than that of the zoned case (11.2 dB). Hence, the directivity (defined as the ratio between the radiated power density in the direction of maximum emission, 0º in this case, and the power density radiated by an ideal isotropic source emitting the same total power) obtained with the full concave and zoned metalens is 15.2 dBi and 14.5 dBi, respectively.

Note that cross-polar lobes appear at ∼43º and ∼37.2º for each metalens, respectively at the design frequency. They are more prominent for the zoned case with a cross-polar level of −144.9 dB and −142.2 dB for the full concave and zoned lenses, respectively [see Fig. 3.7(b,d)]. These side lobes, and also those observed for the co-polar at ∼15º-20º can be arguably assigned to grating lobes [ORAZ 15b], [NAVA 10c] as the white dashed lines in Fig. 3.7(a-d) demonstrate.

The better performance of the full concave design can be explained on the basis of the spillover efficiency, η_{so} (i.e., the ratio between the power reemitted from the metalens and the total power radiated by the transmitter) which gives an idea of the total power radiated from the source that is intercepted by the metalens. According to the simulations, η_{so} is 0.25 and 0.19 for the full concave and zoned cases, respectively. These results again corroborate that the zoned fishnet design has a small deterioration on its properties compared to its full concave counterpart.

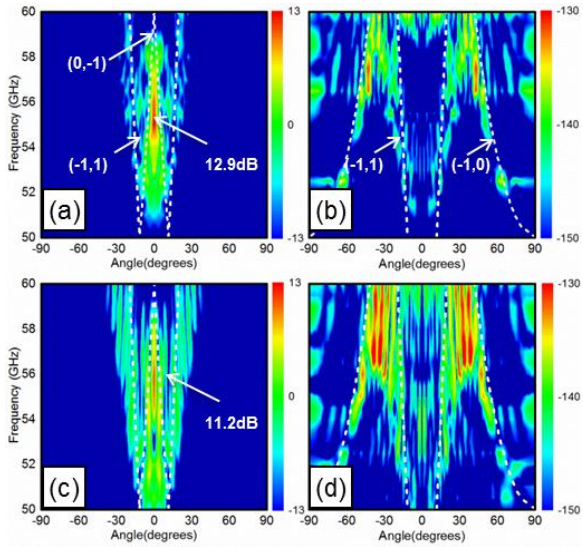

Figure 3.7. Numerical results of the radiation pattern spectra (in dB) when a point source is placed at the focal point: co- (left column) and cross-polarization (right column) of the full concave (first row) and zoned (second row) fishnet MTM lens. The white dashed lines represent the analytical positions of the grating lobes of order (0,–1), (–1,0) and (–1,1).

As explained, using an omnidirectional transmitter, as the point source, corresponds to an ideal illumination of the lens because Eq. 3.2 is defined considering that a point focus will be produced when illuminating the metalens from its planar face using a plane wave (i.e., a point source illumination from its zoned face by reciprocity). However, it is more interesting to evaluate its response using a realistic transmitter. For this purpose, a rectangular flange ended waveguide will be used to illuminate the structure and its performance will be evaluated both numerically and experimentally.

For the experimental case, the same equipment as the one used to evaluate the focusing performance is used. The procedure followed to experimentally evaluate the radiation pattern is as follows: the flange ended rectangular waveguide (WR-15) is placed at the experimental FL = 46.5 mm = 8.79λ_0 (obtained in the previous section) to excite the metalens. Both elements, flange ended waveguide and metalens, stand on a rotating platform in order to make angular measurements from –90º to +90º, with a step of 1º. A high gain standard horn antenna is placed at 4000 mm from the flat face of the lens to detect the radiated power [see Fig. 3.8(a) for the schematic representation of the setup]. First, a calibration of the system is made by recording the transmitted power in absence of the focusing device. Next, the zoned metalens is placed between the receiver and transmitter.

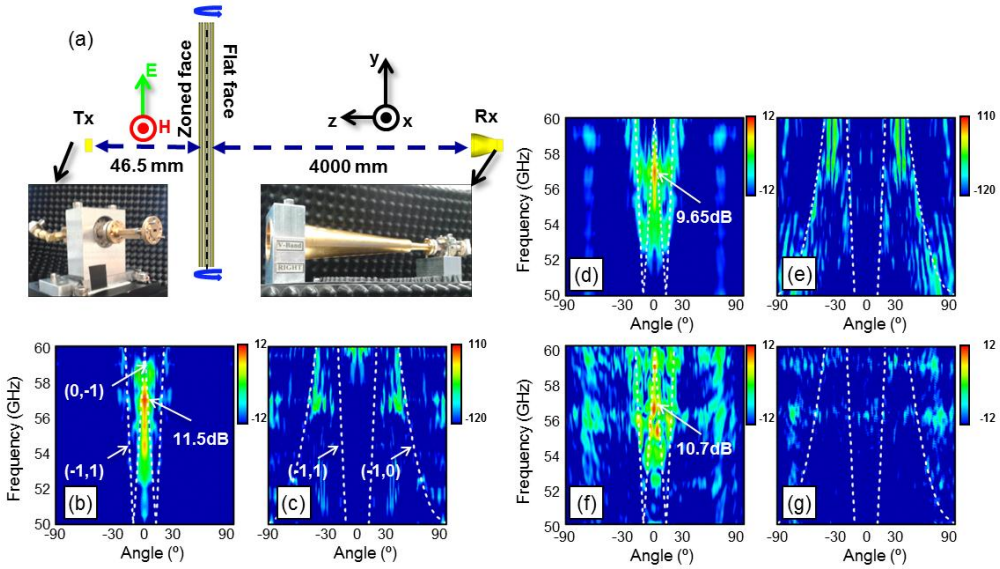

Figure 3.8. (a) Schematically representation of the experimental setup used to characterize the radiation pattern of the zoned metalens. Numerical (b-e) and experimental (f-g) results of the radiation pattern: co- (b,d,f) and cross-polarization (c,e,g) for the case of the full concave (b,c) and zoned fishnet metalens (d-g)

To better compare the performance of the fabricated prototype, simulations are also launched for the three-dimensional full concave and zoned fishnet structures by using a realistic flange ended rectangular waveguide (WR-15) as transmitter at the numerically-estimated focal point. As it was done for the point source illumination, far-field monitors are used to record the radiation pattern of the two structures within the frequency range 50-60 GHz with a step of 0.5 GHz.

The simulation results for the power distribution of the co- and cross-polar components on the *H(xz)*-plane are shown in Fig. 3.8(b,c) and Figs. 3.8(d,e) for the full concave and zoned designs, respectively. The experimental results for the co- and cross-polarizations of the zoned metalens are presented in Figs. 3.8(f,g). By inspection of the measurement and the simulation results from Fig. 3.8 along with the simulations shown in Fig. 3.7, it clear that using a realistic waveguide models significantly better the experiment. From these results, the spillover efficiency is 0.9 and 0.86 for the full concave and zoned cases, respectively, and arguably can explain the closer performance between them.

A high enhancement of the radiation pattern is obtained for the zoned design in the experiment (10.7 dB), which is slightly better than the simulation value (9.65 dB). A

very narrow *H*-plane beamwidth is found (θ_{3dB} = 3.5º), demonstrating its good performance. From the numerical results of the full concave metalens, an enhancement of 11.5 dB is obtained which is slightly better than that of the zoned case, in good agreement with the numerical results discussed under point source illumination. In the zoned metalens, the co-polar component presents side lobes near ±70º, which are observed in both simulation and experimental results within the whole frequency range, with a magnitude between −12 to −10 dB (i.e., −22.7 to −20.7 dB relative to the main lobe) in the experiment, see Fig. 3.8(f). In the simulation they have slightly smaller values, see Fig. 3.8(d). These side lobes are due to the spillover. Hence, they are frequency independent. This performance is more evident by looking at the radiation pattern of both designs at the operation frequency of f = 56.7 GHz [see Fig. 3.9(a)]. Note that prominent side lobes due to spillover are observed at ±70º and ±90º for the zoned and full concave lens, respectively. A simple approach to reduce spillover side lobes in the zoned metalens would be to decrease the focal length-to-diameter ratio, as will be performed in the next section. For completeness the analytical positions of the first order grating lobes (0,−1), (−1,0) and (−1,1) are also plotted as white dashed lines in Fig. 3.8(b-g), revealing clearly the origin of all the side lobes observed in the diagram. Finally, the numerical and experimental results of the normalized radiation pattern of the zoned metalens are shown in Fig. 3.9(b), where a good a greement can be observed.

With the aim to fully characterize the radiation performance of this structure, the numerical and experimental gain (defined as the ratio of the radiated power density in the direction of maximum emission, 0º in this case, and the power density radiated by an ideal lossless isotropic radiator that emits all the power fed by the source) for the zoned fishnet MTM lens is presented in Fig. 3.9(c). The experimental gain has been calculated using the gain comparison method [IEEE 79]. A high gain of 12.26 dB is found, close to the numerical value (14.9 dB), which is directly calculated by using the far-field monitors. Again, the gain is slightly better for the full concave case (16.5 dB; black curve). The small difference obtained between simulation and experimental results can be due to the imperfections in the fabrication and assembly of the lens. Anyway, in general, simulation and experimental results are in good agreement.

As demonstrated in Section 2.2.1, it is interesting to evaluate the mechanical beam steering capabilities of a lens working in a lens-antenna configuration. To evaluate this for the case of the zoned design, we employ the experimental setup shown in Fig. 3.8(a). The procedure to evaluate the beam steering performance is similar to the one used in Section 2.2.1 for the ENZ plano-concave lens: first, we find the experimental (*x*,*z*) coordinates on the *xz*-plane where the transmitter should be placed to steer the output angle from 0º to 20º in 5º steps; next, we characterize the radiation diagram of the radiated beam.

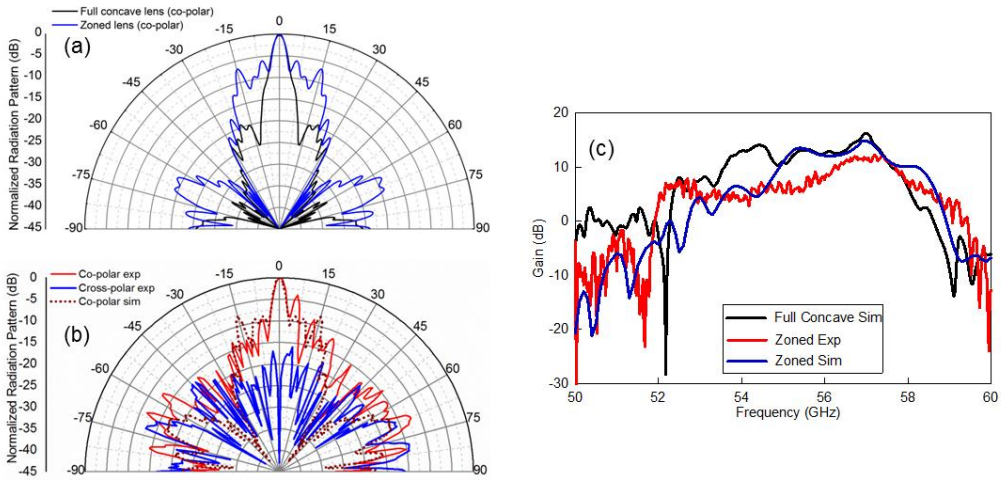

Figure 3.9. (a) Simulation results of the radiation pattern (dB) at the design frequency (f = 56.7 GHz) and co-polar component for the full concave (black) and zoned case (blue). (b) Simulation (dotted) and experimental results (solid) of the normalized radiation pattern at the design frequency (f = 56.7 GHz): co-(red) and cross-polarization (blue). (c) Numerical (blue) and experimental (red) gain of the zoned fishnet metalens (dB) along with the results of the full concave case (black) in the frequency range 50-60 GHz.

To find experimentally the position on the *xz*-plane of the flange ended waveguide (transmitter) we fix whole system at each measured output angle (0º, 5º, 10º, 15º and 20º). Then, we move the transmitter on the *xz*-plane until we find maximum power (the scanning region is 0-15 mm and 20-70 mm along *x* and *z*, respectively, with a step of 0.5 mm). This way, the focal point coordinates on the *xz*–plane are obtained accurately. To illustrate this, the numerical result of the power distribution on the *xz*-plane under oblique incidence (10º) for the zoned metalens is shown in Fig. 3.10(b). As it is shown, the focus is deflected at the output of the metalens, as expected. With this configuration, we obtain the experimental (*x*,*z*) coordinates for each output angle, shown in Fig. 3.10(a) as filled circles (compared to the simulation values represented as filled triangles). The numerical values are calculated by simply illuminating the lens under oblique incidence and extracting the position of the focus (see section 2.2.1 for a full description of this process). Note that the experimental positions shown in Fig. 3.10(a) are slightly different from the simulation coordinates, yet the trend is maintained. This small discrepancy can be assigned to experimental tolerances such as the accuracy of the transmitter position.

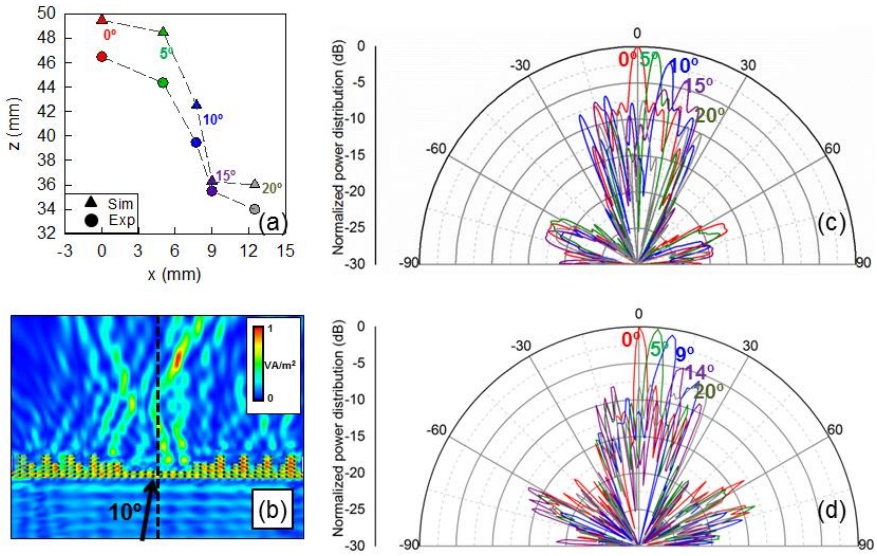

Figure 3.10. (a) Simulation (triangles) and experimental (circles) results of the (*x*,*z*) coordinates of the *FL* on the *xz*-plane for each output angle. (b) Numerical result of the power distribution on the *xz*-plane when a plane wave illuminates the flat face of the metalens at oblique incidence (10º). Numerical (c) and simulation (d) results of the radiation pattern for each output angle

Once the position of the focus is obtained for each output angle, the transmitter is placed at each *FL* illuminating the structure. The numerical and experimental results of the radiation pattern at the design frequency for the output angles from 0º to 20º with a step of 5º are shown in Fig. 3.10(c,d), respectively. Simulations are now performed by placing the flange ended rectangular waveguide (WR-15) at the numerically-estimated positions. By comparing Fig. 3.10(c,d), it is shown that the experimental output angles are indeed very close to the values obtained by simulations.

To better compare these results, a summary of the beam steering performance of the zoned metalens is shown in Table 3.2 in terms of the output angles, *H*-plane *HPBW* and *SLL*. As it can be observed the experimental results are in an excellent agreement with the numerical values for almost all the output angles. For the case of 20º, a clear deterioration of the radiation pattern is obtained in terms of the beamwidth along with an increased *SLL*. Moreover, it is shown that the lowest *SLL* is obtained for the output angle 0º and 5º for simulation and experiment, respectively. From these results and taking into account the standard scan loss of −3 dB for a suitable beam steering, the structure here designed has a beam steering capability up to ±10º. Note that this value is below the one obtained in section 2.2.1 for the ENZ lens. This is an

expected result given that the illuminated surface of a full concave lens is higher than the case of a zoned lens (as discussed before).

Output angles (º)		HPBW (º)		SLL (dB)	
Sim	Exp	Sim	Exp	Sim	Exp
0	0	3.8	3.5	7.5	7.93
5	5	3.6	4	6.1	8
10	9	4	4	5.7	5.76
15	14	4.3	4	5.6	4.71
20	20	3.3	8	5.4	1.56

Table 3.2. Results of the beam steering performance

3.2 The reference phase technique applied to the zoned fishnet metalens

In the previous section, it has been shown how the zoning technique can be applied in the design of ultra-compact metalenses based on the fishnet MTM without a strong deterioration on its performance, compared with the full concave case. In this section, another technique is included in the design of metalenses together with the zoning: the *reference phase*. This section starts with a description of this approach and how it is possible to combine it with the zoning for the design of metalenses. Then, several fishnet metalenses are designed and experimentally evaluated demonstrating that their performance, in terms of *SLL* reduction, can be optimized by adding a reference phase to the central zone of the metalenses.

3.2.1 Reference phase and zoning technique

In addition to the refractive lenses (as those shown in the previous section and also discussed in Chapter 1), diffractive elements like Fresnel zone plates antennas (FZPA) have been extensively studied since they were proposed in 1866 by Augustin Fresnel in his seminal paper [FRES 66]. Such radiating arrangements consist of a transmitter (antenna) placed at the focal position of a diffractive lens which, in its simplest topology, combines alternated transparent and opaque rings with the purpose of improving the radiation characteristics of the transmitter. The original idea of FZPA was proposed at optical frequencies but nowadays it has been applied at different frequency bands of the EM spectrum such as microwave and millimeter waves [HRIS 00], [MINI 04] and also using all-dielectric lenses [VAN 94], [HRIS 95], [GUO 02], [HRIS 11] demonstrating that the concept is universal.

Reducing the first *SLL* of lens antennas in millimeter-wave and terahertz frequencies without perturbing the rest of radiation parameters is usually challenging. Commonly used materials such as high-resistivity (HR) silicon have a large dielectric permittivity [GRIS 90], which leads to large impedance free-space mismatch that results into a resonance response rather than an ideal lens response [LLOM 12], [SEED 13]. This resonance behavior can lead typically to an increment of side lobe and cross-polarization levels [LLOM 12]. One possible solution to reduce this impedance free-space mismatch is using materials with lower dielectric permittivity. However, with such materials a thicker lens profile is required. Alternatively, graded index lenses could be used [DEME 11]. Nevertheless, this solution remains elusive with dielectrics at millimeter-wave and terahertz frequencies because of fabrication challenges and has only been achieved so far with metalenses [SAVI 12], [NEU 13], [NGUY 09].

As a matter of fact, the problem of first *SLL* reduction has been already addressed in planar FZPA in a simple way. It has been demonstrated that a free-parameter dubbed *reference phase* can be tuned to lower the first *SLL* without deteriorating the rest of radiation characteristics [MINI 90], [MINI 05], [STOU 06], [MINI 11]. Commonly, no reference phase is used (i.e., zero reference phase) in the design of circular planar Fresnel zone plate antennas (CFZPA) and the radii of each zone is obtained from the general equation of Fresnel zones. However, this parameter can be modified and applied to CFZPA. These antennas are designed with transparent and opaque rings alternated each time a phase difference of π is reached. When the reference phase is used, an extra phase advance between 0 to π can be introduced to each radius of the lens antenna (since values from π to 2π are the complementary ones and transparent and opaque's rings interchange their positions). By changing this parameter, the dimension of the first radius (zone) may be increased (decreased) if a positive (negative) value of reference phase is introduced. Note that, since the first radius (zone) is modified with this technique, the radii of the successive zones will be increased or reduced; i.e., the introduction of this parameter makes it possible to correct the dimension of the first radius and also the successive ones [MINI 11]. Therefore, if a fixed diameter for the lens antenna is selected, the total number of zones will be changed. An equivalent approach can be arguably applied to the design of zoned metalenses.

As described in the previous section, the zoning technique is based on the reduction of the profile of the lens each time a phase advance of 2π is reached inside the material (with respect to free-space propagation, see section 3.1). This phase advance is directly related to the thickness of the lens. Hence, its profile is reduced each time a thickness limit (t) is reached, as shown in Eq. 3.1.

Therefore, unlike planar FZPA, the extra phase advance introduced with the reference phase for zoned lenses may be modulated from 0 to 2π, so that the total

phase advance is between 0 and 4π. This implies an increase of the thickness of each zone, that can be calculated mathematically as follows:

$$\Delta t = qt = q\frac{\lambda_0}{1-n_{lens}} \tag{3.3}$$

where Δt denotes the extra thickness introduced due to the reference phase and q is a factor between 0 and 1 that corresponds to an additional phase advance from 0 to 2π. Therefore, when the reference phase is used along with the zoning technique, the lens profile is stepped when a thickness $t_{total} = t + \Delta t$ is reached and Eq. 3.2 becomes:

$$z = \mathrm{mod}\left[\frac{FL\left(1-n_{lens}\right)-\sqrt{FL^2\left(1-n_{lens}\right)^2-x^2\left(1-n_{lens}^2\right)}}{\left(1-n_{lens}^2\right)}, t_{total} = t\left(\pm q+1\right)\right] \tag{3.4}$$

From the above equation, when $q = 0$, it converges to a classical zoned lens (Eq. 3.2) [KOCK 46]. Moreover, note that similarly to the reference phase applied to a CFZPA, since a positive/negative reference phase can be introduced, the length (thickness) of the first and successive zones is increased/reduced depending on the value of q. It is important to highlight that the technique here proposed may be used as a general approach to design zoned lenses with different materials (such as dielectrics). However, we opt to design all-metallic zoned fishnet metalenses in order to improve the performance of the prototype discussed in the previous section.

3.2.2 Design and numerical evaluation

Let us now apply the reference phase together with the zoning technique in the design of several fishnet metalenses. Here, we will center the attention on the case when a positive reference phase is applied (Eq. 3.4 with $0 < q < 1$). Cylindrical metalenses (with translation symmetry along y) are considered, as we did previously.

To begin with, the unit cell of the fishnet MTM is the same as the one used in the last section, shown in Fig. 3.2. The design frequency is also $f = 56.7$ GHz (at which we have $n_{lens} = -0.25$). All the cylindrical fishnet metalenses are designed with a $FL = 4.5\lambda_0$ and a value of focal length to lateral size ratio (F/D) of $F/D_{xz} = 0.214$ and $F/D_{yz} = 0.207$ in the xz- and yz- planes, respectively, where D_{xz} and D_{yz} is the lateral size of the lens in the xz- and yz plane, respectively. Note that this factor is reduced compared

with the metalenses discussed in section 3.1 (F/D_{xz} = 0.428 and F/D_{yz} = 0.353) to follow now the standard criterion of having an edge taper value of −12dB for an efficient illumination of the metalens [BALA 05]. This is illustrated in Fig. 3.11 where simulation and experimental results of the normalized radiation pattern of the standard flange ended WR-15 waveguide in the *xz(H)*-plane are presented (which will be used as a source when evaluating the lens antenna configuration). Note that, since the metalenses here designed are cylindrical (with the focus in the *xz(H)*-plane) we consider only the *xz(H)*-plane. The simulated −12 dB beamwidth is 128.4º in the *xz(H)*-plane. From the experiment, it is 133.6º while the angular aperture of the metalenses calculated from the designed F/D_{xz} is 133º.

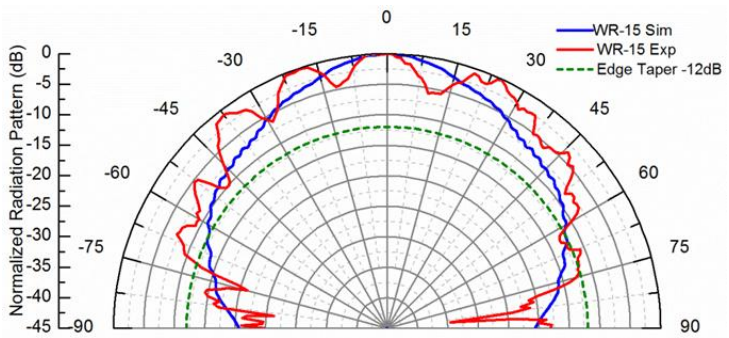

Figure 3.11. Simulation (blue line) and experimental (red line) results of the normalized radiation pattern of the standard flange ended WR-15 waveguide in the *xz(H)*-plane along with the -12 dB edge taper standard for an efficient illumination (green dashed line).

Four different cases of the factor +q are evaluated: q = 0, q = 0.35, q = 0.7 and q = 1 which correspond to a reference phase of 0, 0.7π, 1.4π and 2π, respectively; i.e., an extra thickness (Δt) of 0, 0.28λ_0, 0.56λ_0 and 0.8λ_0, respectively. The resulting zoned profile for each structure is calculated using Eqs. 3.3-3.4, see Fig. 3.12. All the metalenses are designed with perforated metallic layers with 37×23 holes along x and y axes, respectively, and total lateral dimensions of 21λ_0 × 21.73λ_0 (111mm × 115mm). In Fig. 3.12 it is evident that the thickness (dimension along z-axis) increases with increasing reference phase as expected from the theory [MINI 11].

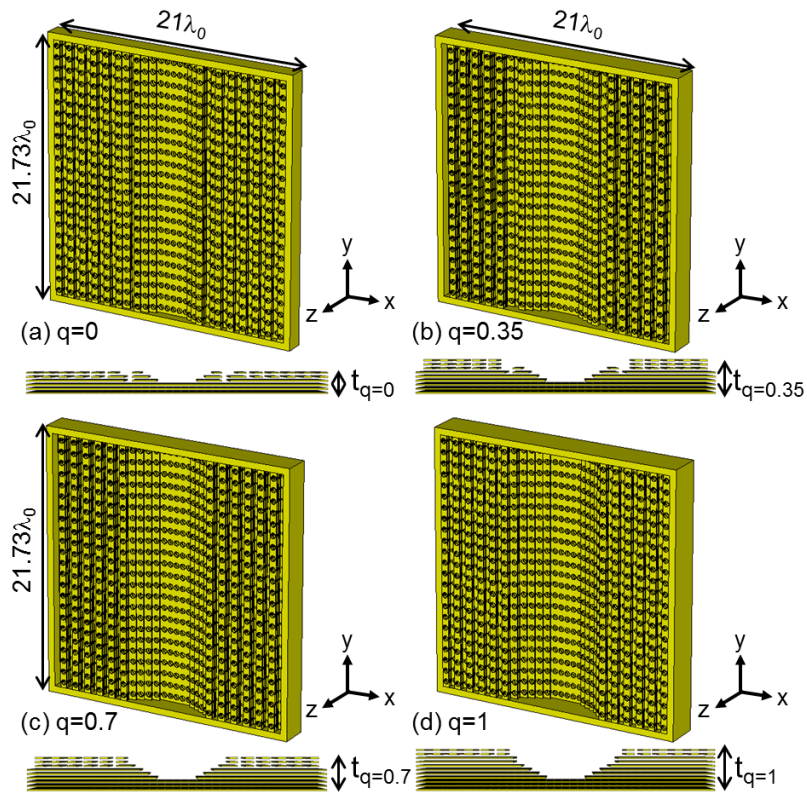

Figure 3.12. Schematic representation, perspective (top) and top view (bottom), of the profiles of the zoned fishnet metalenses under study using different values of reference phase with factors: (a) q = 0, (b) q = 0.35, (c) q = 0.7 and (d) q = 1 with a total thickness of $t_{q=0}$ = 1.51λ_0, $t_{q=0.35}$ = 2.36λ_0, $t_{q=0.7}$ = 2.36λ_0 and $t_{q=1}$ = 2.93λ_0 for each design, respectively.

The focusing performance of the designs is then studied numerically using the transient solver of the commercial software CST Microwave Studio®. The metal used is aluminum with a finite conductivity of $\sigma_{Al} = 3.56 \times 10^7$ S/m. The same boundary conditions and symmetries as in Section 3.1 are used. Also, the full 3D metalenses are modeled. A hexahedral mesh is used with a resolution up to $0.056\lambda_0 \times 0.056\lambda_0 \times 0.028\lambda_0$ along x, y and z axis, respectively. The numerical results of the enhancement of the power distribution along the metalenses optical axis as a function of frequency for the designs under study are shown in Fig. 3.13. From these results, the maximum power is obtained for all cases slightly shifted compared to the designed value. Specifically, it emerges slightly above (~0.25 GHz) the designed operational

frequency (f = 56.7 GHz). This could be due to the discretization of the profiles along all directions due to the unit cell used or to unavoidable numerical errors.

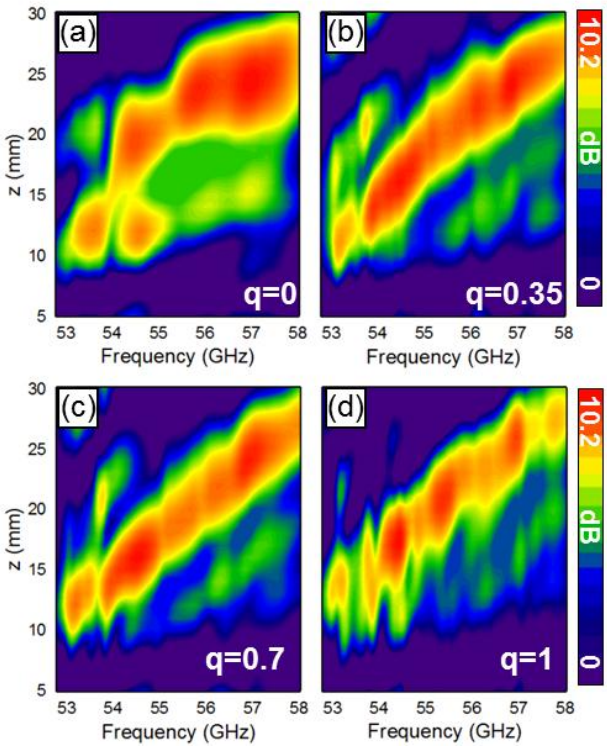

Figure 3.13. Numerical results of the enhancement of the power distribution along z-axis at x = 0 mm from the center of the metalenses as a function of frequency for the designs with factor of reference phase: (a) q =0, (b) q =0.35, (c) q =0.7 and (d) q =1.

From these results, the values of the FL at the design frequency are $FL_{q=0} = 4.57\lambda_0$, $FL_{q=0.35} = 4.52\lambda_0$, $FL_{q=0.7} = 4.42\lambda_0$ and $FL_{q=1} = 4.8\lambda_0$, for each metalens, demonstrating a good agreement with the theoretical value ($FL = 4.5\lambda_0$). Note that the error between the calculated and the designed FL is smaller for the lenses with q = 0 (error = 1.56%) and q = 0.35 (0.44%) and it is slightly higher for the designs q = 0.7 (1.78%) and q = 1 (6.67%), and may be due to the discretization of the metalenses. However, regarding the enhancement of the power distribution at each FL, the maximum power enhancement, 10.2 dB, is obtained for the design with q = 0.35, while it is ~0.3 dB, ~0.07 dB and ~0.72 dB lower for the designs q = 0, q = 0.7 and q = 1 respectively.

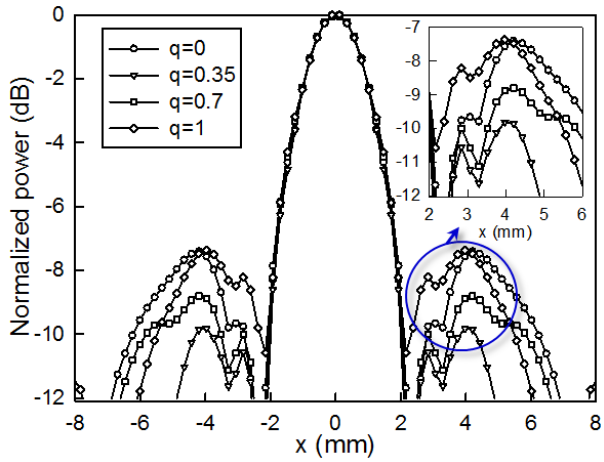

Figure 3.14. Simulation results of the normalized power distribution along the transversal *x* axis at each *FL* for the four zoned fishnet metalenses under study by applying a reference phase with a factor of $q = 0$ (circle), $q = 0.35$ (triangles), $q = 0.7$ (squares) and $q = 1$ (diamonds).

Next, we extract from the simulations the normalized power distribution along the transversal *x* axis at each *FL* for $f = 56.7$ GHz, see Fig. 3.14 (results normalized with respect to the maximum from all cases). It can be observed that the *FWHM* is preserved for all the designs with a value of $\sim 0.43\lambda_0$. Furthermore, the *SLL* is minimum for $q = 0.35$ and $q = 0.7$ with a value of 9.7 dB and 8.6 dB below the main lobe, while for $q = 0$ and $q = 1$ it is 7.5 dB below the main lobe. Also, the minimum level of first null is achieved for $q = 0.35$, with a magnitude of 17 dB below the main lobe. These results (displayed for all q values in Table 3.3) demonstrate that the reference phase modulates the *SLL* as well as the first null, and that for our particular fishnet design, $q = 0.35$ is the optimum reference phase value.

Metalens design	FL (λ_0)	FL Error (%)	NP[a] at each FL (dB)	SLL (dB)	First null (dB)
$q = 0$	4.57	1.56	-0.3	7.5	16.2
$q = 0.35$	4.52	0.44	0	9.7	17
$q = 0.7$	4.42	1.78	-0.07	8.6	14.3
$q = 1$	4.8	6.67	-0.72	7.5	10.6

Table 3.3. Numerical results of the focusing performance for the zoned fishnet metalenses with reference phase

[a]NP is the normalized power.

3.2.3 Experimental evaluation

Based on the results discussed above, two metalenses are fabricated q = 0 and q = 0.35. The former case is used as reference and the other design is meant to show the advantages of tuning the reference phase. The prototypes are made of aluminum using the laser-cutting technique and the metal plates are stacked and separated by a 5 mm wide frame with screws. The final fabricated metalenses are shown in Fig. 3.15(a,b) for the designs with q = 0 and q = 0.35, respectively. The same experimental setup, as shown in Section 3.1 is used to experimentally evaluate the focusing and radiation pattern performances of the metalenses.

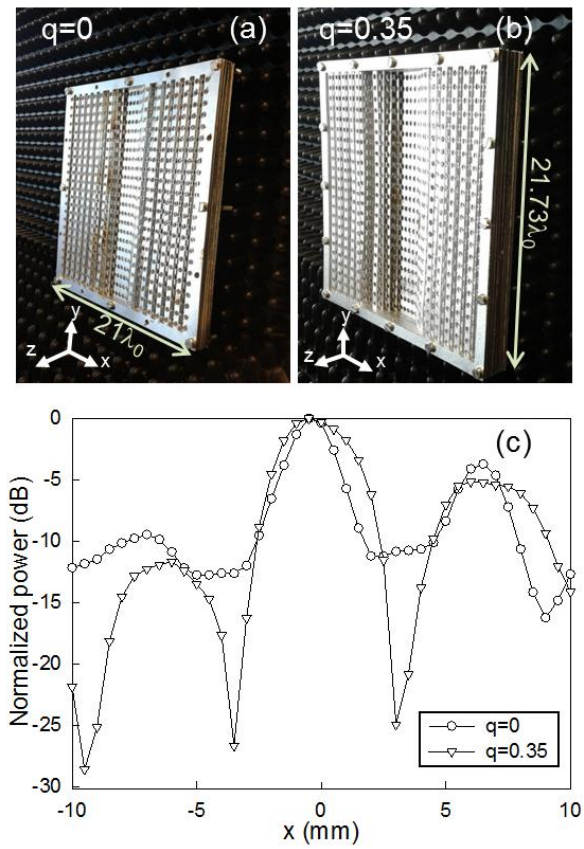

Figure 3.15. Photographs of the fabricated prototypes applying the reference phase with factor: (a) q = 0 and (b) q =0.35. (c) Experimental results of the normalized power distribution along the transversal x axis at each *FL* for the zoned fishnet metalenses designed with a reference phase with a factor of q = 0 (circles) and q = 0.35 (triangles).

First, the power distribution along the optical *z*-axis is obtained by moving the receiver from 5 to 30 mm with a step of 0.25 mm at the operational frequency (f = 56.7 GHz) to find the experimental *FL*. The results are: $FL_{exp\_q=0} = 4.06\lambda_0$ and $FL_{exp\_q=0.35} = 4.16\lambda_0$. Note that a disagreement of 9.7% and 7.56% from the theoretical *FL* ($4.5\lambda_0$) appears for the designs with $q = 0$ and $q = 0.35$, respectively, which may be due to fabrication tolerances. Similarly to the numerical results shown Fig. 3.13, the experimental *FL* obtained for the case $q = 0.35$ is closer to the theoretical value.

Afterwards, the transversal power distribution is measured by moving the receiver along the *x* axis from −10 mm to 10 mm with a step of 0.5 mm, see results in Fig. 3.15(c). A good agreement between simulation and experimental results is evident by comparing Fig. 3.14 and 3.15, with a reduction of *SLL* and a deep first null for q = 0.35 compared to $q = 0$. Note that the focii in the experimental cases are not completely symmetric, probably due to fabrication tolerances or misalignments in the experimental setup. The experimental *FWHM* are $FWHM_{exp\_q=0} = 0.42\lambda_0$ and $FWHM_{exp\_q=0.35} = 0.61\lambda_0$. Note that the experimental *FWHM* for $q = 0.35$ is deviated from the simulations values where a $FWHM = 0.43\lambda_0$ was obtained for both designs. A reduction of 2.5 dB in the *SLL* is obtained when the reference phase of 0.7π is applied to the zoned fishnet metalens, in good agreement with the theoretical predictions: as observed in the figure, the experimental *SLL* is −10 dB and −12.5 dB for $q = 0$ and $q = 0.35$.

As it has been shown, the focusing performance of a zoned fishnet metalens is improved when the reference phase concept is applied along with the zoning technique. It is then reasonable to assume that a zoned fishnet metalens antenna configuration will also benefit from the reference phase tuning (as it was demonstrated in [STOU 06], [MINI 11] with CFZPAs). In the following, we confirm this assumption numerically and experimentally.

The numerical simulation is done using the transient solver of the commercial software CST Microwave Studio® with the parameters described in section 3.1. The realistic flange-ended WR-15 waveguide is used as a transmitter. It is fully modeled and placed at the *FL* obtained in the simulation results for each design in order to illuminate the metalenses from their profiled face. Moreover, farfield monitors are used in the frequency range 50-60 GHz with a step of 0.1 GHz. Open-add space boundary conditions are used in the simulation box to model a situation where the lens antenna system is alone in free-space.

For the experimental characterization, the prototypes are placed between a standard flange ended WR-15 waveguide used as a transmitter and located at each experimental *FL* ($FL_{exp\_q=0} = 4.06\lambda_0$ and $FL_{exp\_q=0.35} = 4.16\lambda_0$) and a high gain horn antenna placed at 4000 mm from the flat face, which is used as a receiver. Both, transmitter and metalens are fixed on a rotatory platform in order to perform the angular scan from

–90º to +90º with a step of 0.5º. Measurements are carried out using the VNA mentioned in section 3.1.

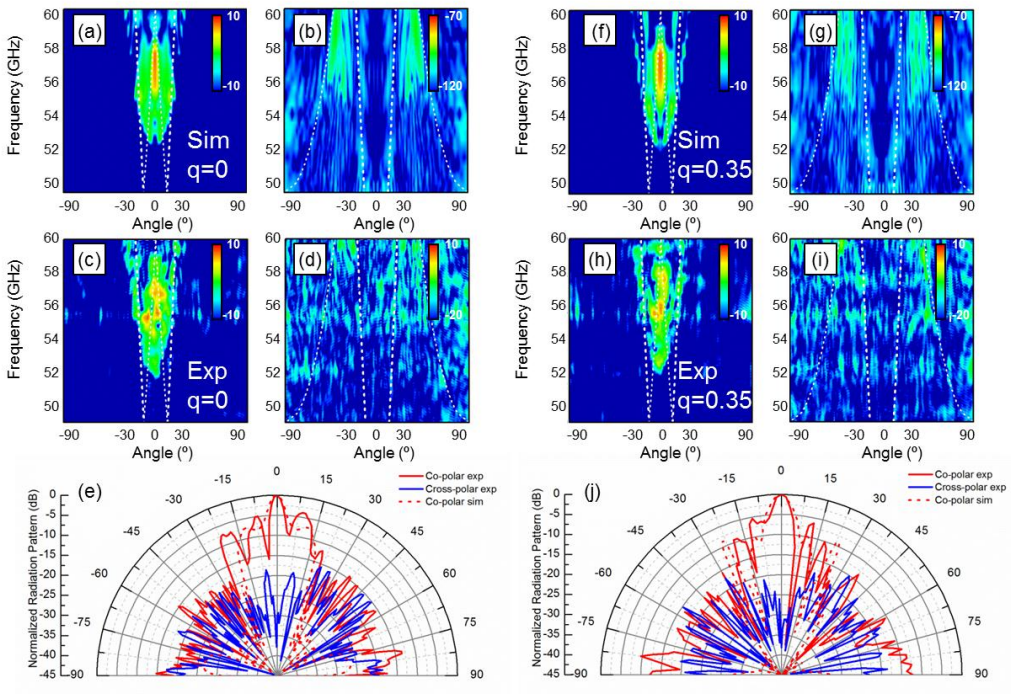

Figure 3.16. Numerical (first row) and experimental (second row) results of the radiation pattern as a function of frequency (from 50-60 GHz) and angle (from -90º to+90º) of the co-polarization (first and third columns) and cross-polarization (second and fourth columns) for the zoned fishnet metalenses designed with factor: q = 0 (a-d) and q = 0.35 (f-i), respectively. The white dashed curves plotted in panels (a-d) and (f-i) are the analytic angular positions of the first order grating lobes (0, –1), (–1.0) and (–1,1). Results of the normalized radiation pattern at the operational frequency of f = 56.7 GHz for the simulation (red dashed line) and experimental (red solid line) results of the co-polarization along with the measured cross-polarization (blue solid line) of the designed zoned fishnet metalenses using reference phase with factor (e) q = 0 and (j) q = 0.35, respectively.

Simulation and experimental results of the radiation pattern of the co- and cross-polar components on the *xz(H)*-planes as a function of frequency and angle are shown in Fig. 3.16(a-d) for q = 0 and in Fig. 3.16(f-i) for q = 0.35. Again, a good agreement between simulation and experimental results is obtained. Due to the periodicity of the fishnet, grating lobes related to the (0,–1), (–1,0) and (–1,1) diffraction orders appear in the plots, as discussed in Fig. 3.8, and are marked as dashed white lines. It is

important to remark that, given the −12 dB edge taper criterion followed in this work, spillover side lobes do not appear here, at difference with the previous case, Fig.3.8.

From the numerical results, a gain of 13.2 dB and 13.7 dB is obtained at the operational frequency (f = 56.7 GHz) for the designs q = 0 and q = 0.35, respectively. The experimental gain is obtained by applying the gain comparison method [IEEE 79]. The resulting value is slightly lower than the simulation results and, giving values of 9.53 dB and 11.30 dB at the working frequency. However, note that in both, simulation and experimental results, the gain obtained for q = 0.35 is always higher than for q = 0. To better compare the results obtained from simulation and measurements, the co- and cross-polar components of the normalized radiation pattern at the operational frequency for both designs, q = 0 and q = 0.35, are shown in Fig. 3.16(e) and Fig. 3.16(j), respectively. Also, a summary of the radiation pattern characteristics is shown in Table 3.4.

The simulated main lobe *HPBW* is $HPBW_{q=0}$ = 4.8º and $HPBW_{q=0.35}$ = 6º. Similar results are obtained in the experiments with values of $HPBW_{exp\_q=0}$ = 4.5º and $HPBW_{exp\_q=0.35}$ = 5º for each design, respectively. Regarding the *SLL*, the results obtained in the simulations are $SLL_{q=0}$ = −7.35 dB and $SLL_{q=0.35}$ = −11 dB, and in the experiment we get $SLL_{exp\_q=0}$ = −3.91 dB and $SLL_{exp\_q=0.35}$ = −6.31 dB. Note that the experimental side lobes for both metalenses are higher than the values obtained from numerical simulations. However, a reduction of ~2.4 dB of the first side lobe is achieved when a reference phase with factor q = 0.35 is used (compared with the *SLL* with q = 0). These results demonstrate that the reference phase concept applied along with the zoning technique improves also the level of the first *SLL* in a lens-antenna configuration.

Metalens design	HPBW Sim (º)	HPBW Exp (º)	SLL Sim (dB)	SLL Exp (dB)	Gain Sim (dB)	Gain Exp (dB)
q = 0	4.8	4.5	-7.35	-3.91	13.23	9.53
q = 0.35	6	5	-11	-6.31	13.71	11.3

Table 3.4. Numerical and experimental results of the radiation pattern for the zoned fishnet metalenses with reference phase

3.3 Zoned metalenses with a small focal length

In the previous section, we have studied the performance of the zoned fishnet metalens using positive reference phase when the *FL* is designed with a value of $4.5\lambda_0$. In this section, an evaluation of the focusing properties of several zoned metalenses is carried out by introducing positive or negative values of the reference phase. Also, the *FL* is designed closer to the metalenses ($1.5\lambda_0$) at the design frequency of 55 GHz (λ_0 = 5.45mm), where the fishnet MTM has a refractive index of $n_{lens} \sim 0.68$, in order to study the possibility of these metalenses for being used in compact systems.

3.3.1 Positive and negative reference phase evaluation

To begin with, the unit cell used in this study is shown in the inset of Fig. 3.17(a) with dimensions: w = 0.35 mm, d_x = 3 mm, d_y = 5 mm, d_z = 1.35 mm and a = 2.4 mm. Moreover, copper ($\sigma_{Cu} = 5.8\times10^7$ S/m) is used as metal. Notice that the unit cell has been changed from the one used in the previous sections due to fabrication purposes. With these parameters, the eigenmode solver of the commercial software CST Microwave Studio® is used to retrieve the refractive index of the infinitely replicated unit cell (as it was done in Fig. 3.2). The results are shown in Fig. 3.17(a).

As in the previous studies, the NNZ condition has been selected in the design of the metalenses in order to work within the region were the refractive index of the fishnet MTM has smooth variation. However, by inspecting Eq. 3.4 one can find that the smaller the value of $|n_{lens}|$, the thicker the first zone will be due to the thickness limit, t_{total}, condition. Since a small *FL* is used in the design, the first zone would be closer (just a few millimeters) to the center of the metalens ($x = y = 0$) which may difficult the experimental characterization of the focal properties. Additionally, we also want to avoid the frequencies where the values of n_{lens} are close to −1 due to the fact that n_{lens} changes abruptly within this region and could result in a strong spectral deviation of the focus from the designed value. Therefore, as a trade-off between these two conditions, the design frequency was chosen to be 55 GHz (λ_0 = 5.45mm) at which the effective of the fishnet MTM refractive index is $n_{lens} \sim 0.68$.

With these factors considered, three metalenses are designed: i) with negative (q = -0.35), ii) positive (q = 0.35) and iii) without reference phase (q = 0) in order to compare their performance. For the design, the well-known equation of a conical section is used considering the thickness limit condition when reference phase is applied (see Eq.3.4). The resulting final profiles are shown in Fig. 3.17(b-d).

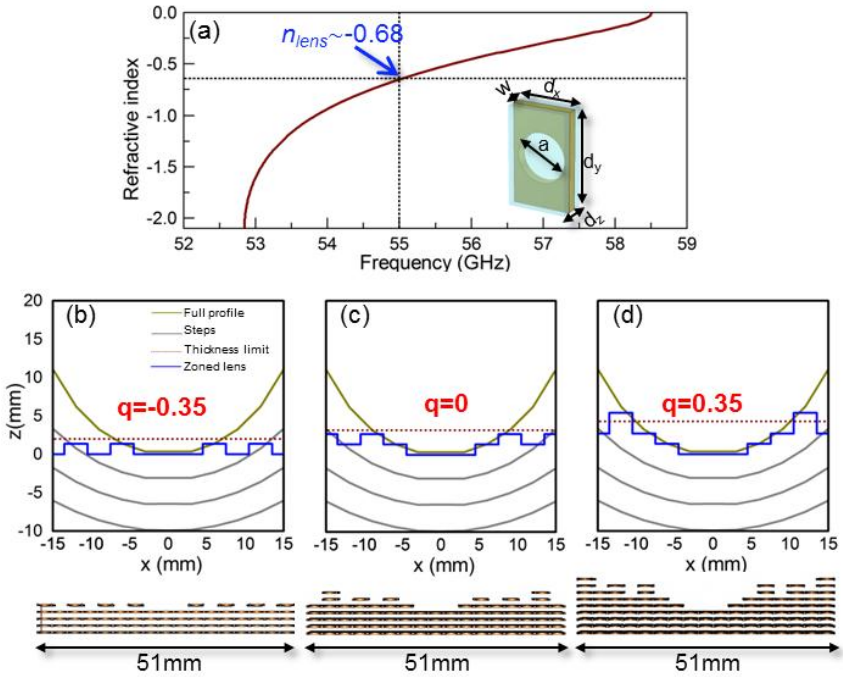

Figure 3.17. (a) Refractive index for a MTM made of an infinite number of SSHA. (inset) Schematic representation of the unit cell with parameters: d_x = 3 mm, d_y = 5 mm, d_z = 1.35 mm, a = 2.4 mm and metal thickness w = 0.35 mm. Calculated profile of the metalenses with: (b) q = –0.35, (c) q = 0 and (d) q = 0.35. Each curve represents: the full concave profile (green curve), successive steps (grey lines), thickness limit (red dotted line) and the zoned profile (blue curve). A top view of each profile using the fishnet MTM is shown at the bottom of panels (b-c).

The focusing performance of the metalenses is evaluated both numerically and experimentally. The numerical simulations are carried out using the transient solver of the commercial software CST Microwave Studio® following the same procedure as in the previous sections. First, an evaluation of the structures is performed in terms of frequency and *FL*. For this purpose, the complete cylindrical metalenses are simulated with a total number of 17×13 holes along the x and y axis, respectively, with total dimensions of $9.35\lambda_0 \times 11.91\lambda_0$. The central part of the metalenses has four perforated plates, two more than in the lenses discussed in the previous section. This is because we are working within the limit where n_{lens} has abrupt or smooth variations (as discussed before). Therefore, more metal plates are required to obtain a similar performance to the ideal infinite fishnet MTM. Finally, electric a magnetic probes are also defined along the propagation z axis at $x = y = 0$ (i.e., the center of the

metalenses) from z = 3 mm to z = 20 mm with a step of 0.2 mm to record the field distribution as a function of frequency.

For the experiment, the ABmm™ VNA is used working in the V-band of millimeter waves. A schematic representation of the experimental setup is shown in Fig. 3.18(a). The metalenses are placed in between of a high gain horn antenna located far (3500 mm) from their flat face (in order to illuminate them with a planewave) and an open ended probe which is used as a receiver. The probe is placed on a translation stage to record the electric field distribution on the focal plane. Similarly to the numerical study, we first evaluate the spectral response of the metalenses to find the position of the focus. The pictures of the fabricated prototypes and their final dimensions are shown in Fig. 3.18(b-d) for the designs with q = –0.35, q = 0 and q = 0.35, respectively.

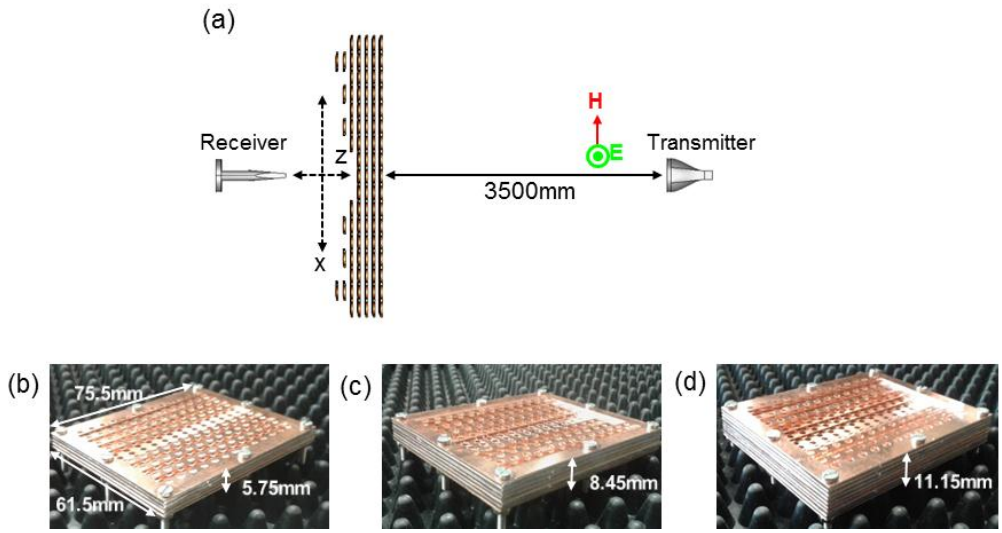

Figure 3.18. (a) Schematic representation of the experimental setup used to characterize the focusing performance of the metalenses. Photographs of the fabricated prototypes with: (b) q = –0.35, (c) q = 0 and (d) q = 0.35.

The numerical and experimental results of the normalized power distribution spectra along the propagation z axis are shown in Fig. 3.19(a,c,e) and Fig. 3.19(b,d,f), respectively, for each metalens. In general terms, the experimental results are in good agreement with the numerical simulations. For the latter case, the peak of power occurs at 55 GHz for all the designs, which corresponds to the design frequency. From the experimental values, the maximum happens at the frequency of 55.5 GHz (λ_0 = 5.4 mm), which corresponds to a very small error of 0.9% from the designed value. This small error may be due to experimental misalignments and fabrication tolerances.

From here on, these frequencies are used for the numerical and experimental study, respectively.

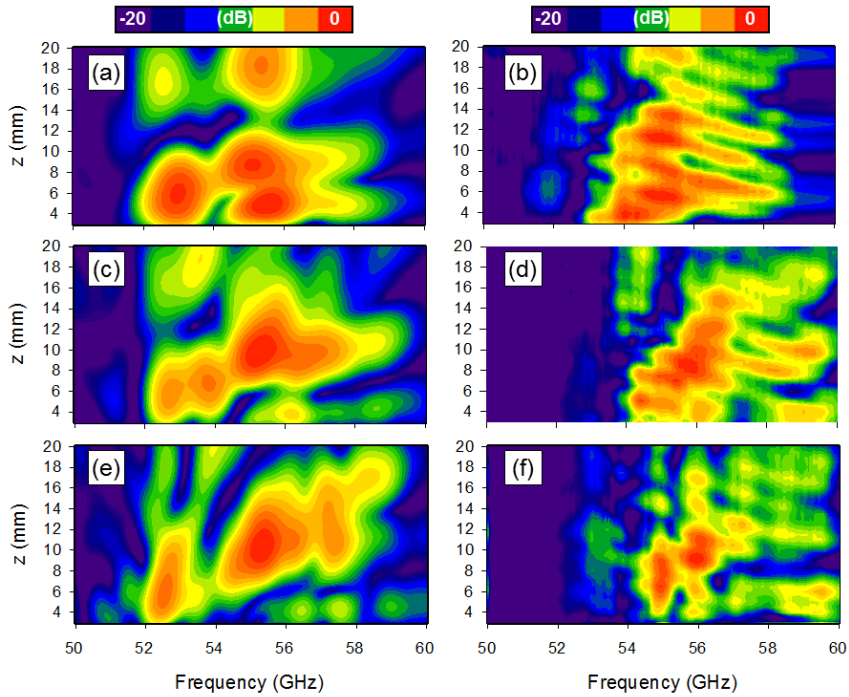

Figure 3.19. Numerical (left column) and experimental (right column) results of the normalized power distribution spectra along *z*-axis at x = 0 mm from the center of the metalenses for the designs with a factor of reference phase: q = –0.35 (first row), q = 0 (second row) and q = 0.35 (third row).

From the simulations, the *FL* of each metalens is $FL_{sim\_q=-0.35}$ = 8.2 mm (1.5λ_0), $FL_{sim\_q=0}$ = 8.71 mm (1.59λ_0), $FL_{sim\_q=0.35}$ = 8.6 mm (1.57λ_0) and from the experiment, they are $FL_{exp\_q=-0.35}$ = 8.4 mm (1.55λ_0), $FL_{exp\_q=0}$ = 8.5 mm (1.57λ_0), $FL_{exp\_q=0.35}$ = 8.5 mm (1.57λ_0). As it can be observed, the *FL* is close to the designed value of 8.18 mm (1.5λ_0) for all the designs, demonstrating the good agreement between the numerical, experimental and designed values. For the sake of completeness, the numerical and experimental results of the power distribution at each *FL* as a function of frequency are shown in Fig. 3.20(a,b), respectively, where again it is clear the agreement between both results.

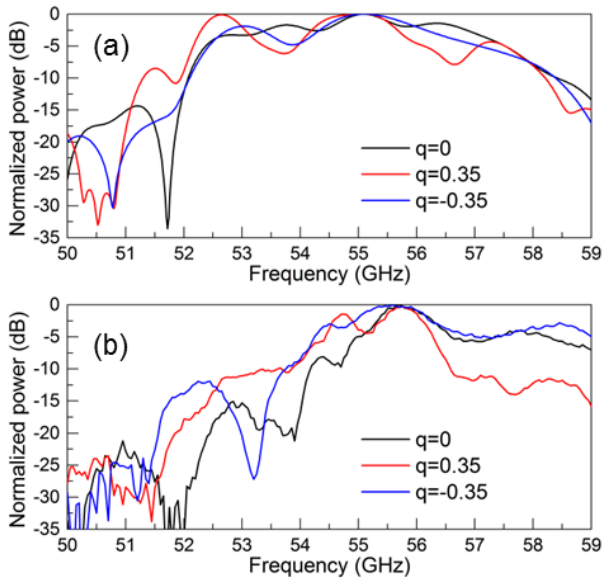

Figure 3.20. Numerical (a) and experimental (b) results of the normalized power distribution spectra at each *FL* for the designs with q = –0.35 (blue), q = 0 (black) and q = 0.35 (red).

After the spectral response has been studied, the focusing performance of the metalenses is evaluated at the frequency of 55 GHz and 55.5 GHz for the numerical and experimental case, respectively. The results of the power distribution on the focal plane (*xz*) are shown in the first and second row of Fig. 3.21, respectively, for the cases of the designs with q = 0 (first column), q = 0.35 (second column) and q = –0.35 (third column). As it can be observed, there is a good agreement between the numerical and the experimental results. Moreover, a clear focus is obtained for the designs with q = 0 and q = 0.35 while the focus is strongly deteriorated when a negative reference phase is used (q = –0.35). This is due to the fact that, with the latter design, the metalens only has one zoned plate [see Fig. 3.17(b) and Fig. 3.18(b)]. Hence, the profile of the lens is almost a single grating which produces a focus with strong side lobes.

To better compare these results, we have plotted the numerical and experimental results of the power distribution along the *x* axis at each *FL* for the three designs in Fig. 3.21(g,h), respectively. A good agreement is observed between these results. Note that the side lobes are reduced when using a positive reference phase in both numerical and experimental results which is in a good agreement with the designs discussed in the previous section. When a negative value is introduced, the side lobes are increased due to the influence of only one zone, as explained before. A summary

of the focusing properties are shown in Table 3.5 in terms of the *FL*, *FWHM*, *DF* and power enhancement.

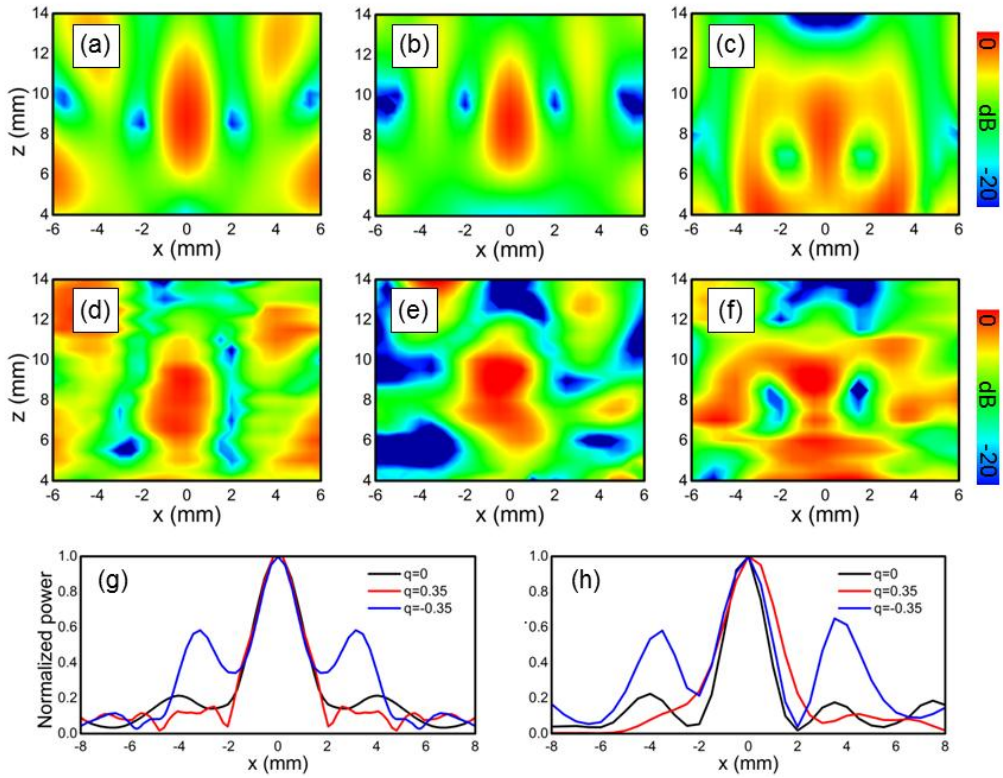

Figure 3.21. Numerical (first row) and experimental (second row) results of the normalized power distribution in the *xz*-plane for the metalens with q = 0 (first column), q = 0.35 (second column) and q = –0.35 (third column) at the numerical and experimental frequency of 55 GHz and 55.5 GHz, respectively. Numerical (g) and experimental (h) results of the power distribution along the transversal *x* axis at each *FL*for the designs with q = 0 (black), q = 0.35 (red) and q = –0.35 (blue).

As it can be observed, the best performance is achieved when q = 0.35 in terms of the *FL*, *DF* and power enhancement, in good agreement with the metalenses studied in the previous section with a *FL* of $4.5\lambda_0$. Also, note that the power enhancement for these metalenses is below the values obtained in section 3.1 and 3.2 and other advanced metalenses [ORAZ 15a], [ORAZ 15d], due to the fact that more plates are used at their center, increasing the loss in the structures. However, these results demonstrate that the reference phase can be also applied in the design of metalenses

with small *FL* obtaining the best performance for positive values of *q*, reducing the *SLL* at the focal position

	$q = 0$		$q = 0.35$		$q = -0.35$	
	Sim	Exp	Sim	Exp	Sim	Exp
FL	$1.59\lambda_0$	$1.57\lambda_0$	$1.57\lambda_0$	$1.57\lambda_0$	$1.5\lambda_0$	$1.55\lambda_0$
$FWHM_x$	$0.38\lambda_0$	$0.33\lambda_0$	$0.37\lambda_0$	$0.39\lambda_0$	$0.41\lambda_0$	$0.35\lambda_0$
DF	$1.01\lambda_0$	$0.83\lambda_0$	$0.96\lambda_0$	$0.65\lambda_0$	$1.19\lambda_0$	$0.92\lambda_0$
Enh.	6.3 dB	6 dB	6.4 dB	6.2dB	2.6 dB	2.5dB

Table 3.5. Numerical and experimental results of the focusing performance of the metalenses with positive, negative and without reference phase. The numerical and experimental values are given at the frequency of 55 GHz and 55.5 GHz, respectively.

3.3.2 Reversing the profile of the zoned metalenses: convex focusing elements

In this section, the profile of the zoned fishnet metalenses discussed in the previous section is changed to convex in order to evaluate their performance when the phase distribution inside of them is reversed. Before, it has been shown that the best performance is achieved when a positive reference phase is used. Therefore, here the same profiles with a *FL* of $1.5\lambda_0$ using $q = 0$ and $q = 0.35$ at the design frequency of 55 GHz are used. The unit cell is the same as in the previous section [see Fig. 3.17(a)].

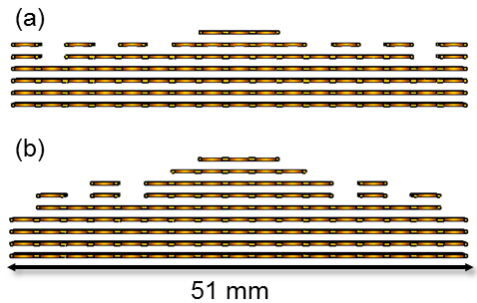

Figure 3.22. Top view of the schematical representation of the zoned fishnet metalenses obtained by reversing the profiles of Fig. 3.17 for the case with $q = 0$ (a) and $q = 0.35$ (b).

The profiles of the metalenses here studied are shown in Fig. 3.22(a,b). Each of them correspond to the case without and with reference phase (q = 0 and q = 0.35) but the regions with air and the fishnet MTM are exchanged. Hence, convex instead of concave metalenses are obtained. Notice that, when q = 0 we are dealing with a metalens with only phase reversal, while when q = 0.35 we have both techniques applied: reference phase and phase reversal.

For the numerical and experimental characterization of the focusing performance, the same setup described in Section 3.3.1 is used. Cooper is also used as metal for the structures, with $\sigma_{Cu} = 5.8\times10^7$ S/m. The fabricated prototypes are shown in Fig. 3.23. Note that they have the same thickness as the concave structures, as expected because we have only exchanged the air-metal regions which results in a fixed volume of the metalenses.

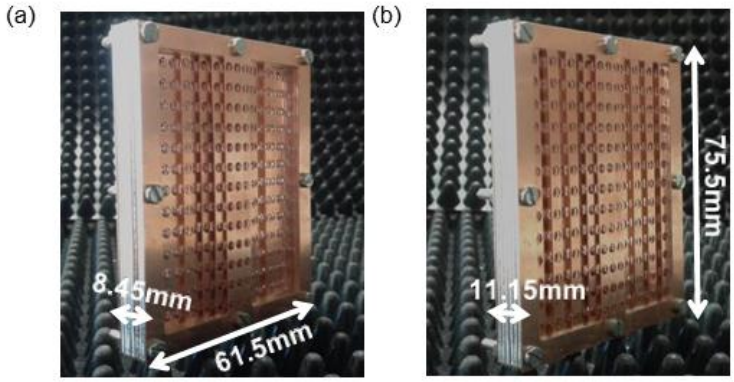

Figure 3.23. Pictures of the fabricated prototypes with: (a) q = 0 and phase reversal and (b) q = 0.35 and phase reversal.

First, the spectral response of the designed metalenses is evaluated. The numerical and experimental results of the normalized power distribution spectra along the propagation z axis for each design are shown in Fig. 3.24(a,c) and Fig. 3.24(b,d), respectively. In general, it can be observed a good agreement between both results. Note that with these designs the chromatic dispersion is reduced (i.e., the shifting of the focus when changing the operational frequency), compared with the concave profiles. Therefore, it is shown that a focus is expected almost at the same position even when the frequency is changed from 54-56 GHz which is a high bandwidth of 2 GHz considering the intrinsic narrow band response of the fishnet MTM [BERU 08], [BERU 09], [TORR 12b]. Moreover, the peak of maximum power (focus) obtained from simulations is observed at the frequency of 55 GHz (λ_0 = 5.45 mm) at z = 10.25 mm (1.87λ_0) and z = 9.8 mm (1.79λ_0) for q = 0 and q = 0.35, respectively. In the experiment, the focus appears at 55.5 GHz (λ_0 = 5.45 mm), in good agreement with

the concave metalenses discussed in the previous section, with a *FL* at z = 10.5 mm ($1.94\lambda_0$) and z = 9.5 mm ($1.75\lambda_0$), for each design, respectively. The slight deviation of $\sim 0.3\lambda_0$ from the designed value ($1.5\lambda_0$) for all the metalenses could be due to the fact that the waves emerging from the farthest zones (along the x axis) of a convex profile reach the focal plane at different positions along the z axis; i.e., spherical aberrations of the lens. However, we can consider that this deviation is small taking into account that the *FL* for each metalens is close to the design value. For the sake of completeness, the numerical and experimental results of the power distribution spectra at each *FL* are shown in Fig. 3.24(e,f), respectively, demonstrating that the operational bandwidth is increased with these designs compared with the concave profiles.

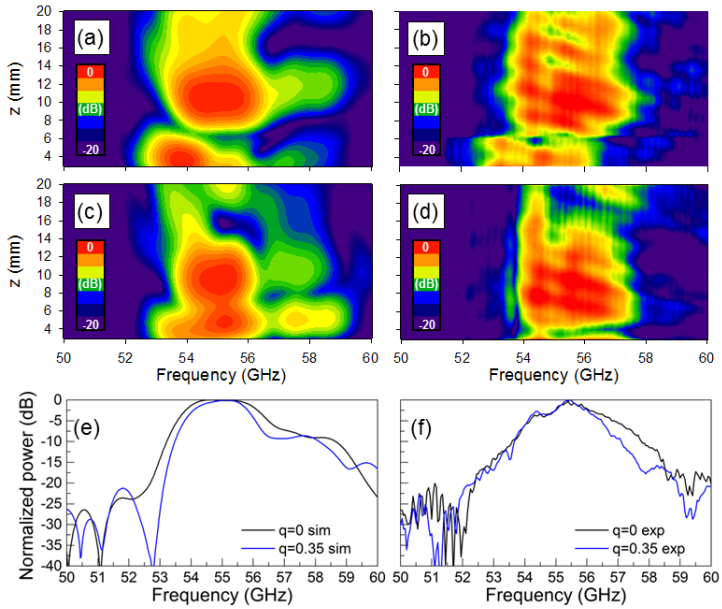

Figure 3.24. Numerical (first column) and experimental results (second column) of the power distribution spectra along the propagation z axis for the phase reversal designs with q = 0 (first row) and q = 0.35 (second row). The numerical and experimental results of the power distribution spectra at each *FL* are shown in panels (e) and (f), respectively.

Finally, the numerical and experimental results of the power distribution in the xz plane for each metalens design are shown in Fig. 3.25. For the naked eye, it is evident the good agreement between both results with a clear focus produced by each structure. To better compare the focal properties, the numerical and experimental values of the power distribution along the x axis at each *FL* are shown in Fig. 3.25(e,f), respectively, where again a nice agreement is observed. Moreover, it is

shown that the lateral lobes in the focal plane are reduced for the case when q = 0.35 and the phase reversal technique is used, in agreement with the concave prototype discussed before. A summary of the focal properties of these metalenses is shown in Table 3.6 in terms of the *FL*, *FWHM*, *DF*, and power enhancement at the *FL*.

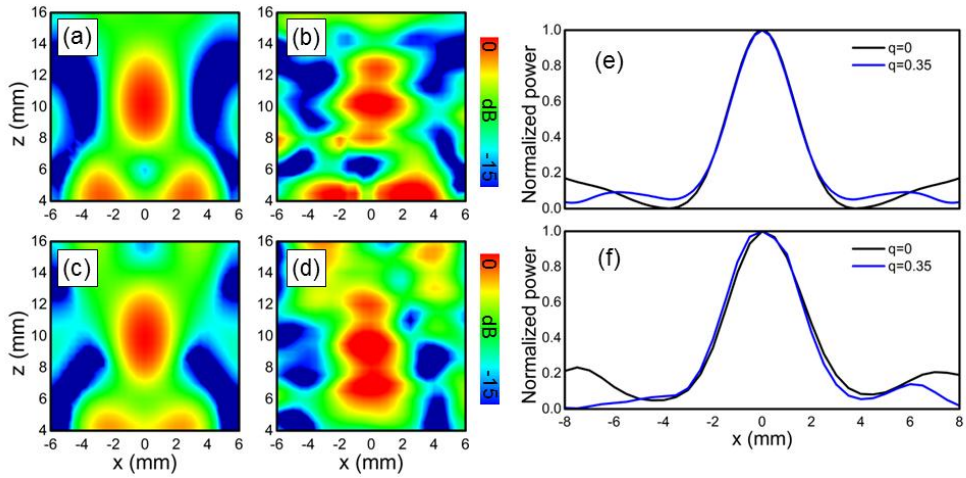

Figure 3.25. Numerical (first column) and experimental results (second column) of the power distribution in the *xz*-plane for the designs with phase reversal and q = 0 (a,b) and q = 0.35 (c,d). Numerical (e) and experimental (f) results of the power distribution along the transversal x axis at each *FL* for the designs with phase reversal and q = 0 (black curves) and q = 0.35 (blue curves)

	q = 0		q = 0.35	
	Sim	Exp	Sim	Exp
FL	1.87 λ_0	1.94 λ_0	1.79 λ_0	1.75 λ_0
$FWHM_x$	0.55 λ_0	0.555 λ_0	0.54 λ_0	0.55 λ_0
DF	0.93 λ_0	0.925 λ_0	0.94 λ_0	0.97 λ_0
Enh	5.7 dB	4.5 dB	8.2 dB	6.5 dB

Table 3.6. Numerical and experimental results of the focusing performance of the metalenses with reference phase and phase reversal. The numerical and experimental values are given at the frequency of 55 GHz and 55.5 GHz, respectively.

As it is shown, the best performance is obtained for the design with q = 0.35 and phase reversal with a higher power enhancement, reduced *FWHM* and *DF* and a *FL* closer to the designed value. By comparing these results with those shown in Table 3.5, the metalenses with phase reversal suffer from spherical aberrations because the

DF is increased compared with the concave structures, as explained before. However, these results demonstrate that convex metalenses with small *FL* can be also designed using the fishnet MTM. Moreover, they can be used in applications where a wideband response is needed due to the fact that these designs have a reduced chromatic aberration of the *FL*.

Chapter 4

Mesoscale focusing elements: photonic nanojets

As it is known, the resolution of an imaging system is intrinsically limited by the diffraction of the EM waves [BORN 99]. Therefore, in order to distinguish the subwavelength features of an object, this fundamental limitation should be overcome. In the past, different solutions have been reported to solve this problem involving MTMs [PEND 00], [SHEL 01], [PODD 13], [FANG 05], [LIU 07], microspherical particles [LU 00], [WANG 11], [MASL 16] plasmonics [LEE 09a], [ROGE 12], solid immersion lenses [HAO 11] and diffractive optics [MINI 06] [MINI 14], to name a few.

Several years ago, Photonic Nanojets (PNJs) were proposed as an alternative to overcome the diffraction limit using microscaled cylindrical (2D) and spherical (3D) dielectrics at optical frequencies [CHEN 04], [LI 05], [HEIF 06], [HEIF 09]. PNJs are high intensity and narrow beams located at the output surface of a dielectric particle under plane wave illumination, demonstrating the ability to obtain a resolution below the diffraction limit. It has been shown, that the ratio between the refractive index of the dielectric and the surrounding medium should be less than 2:1 in order to produce the PNJ just at the output surface of the structure [HEIF 09]. Different geometries of the dielectric have been proposed: spherical/cylindrical [CHEN 04], [LI 05] non-spherical [LIU 14], [MINI 15a], core-shell microcylinders [CHEN 15], and even graded index dielectric ellipsoids [GEIN 11], [LIU 13]. Some of the envisioned applications encompass backscattering enhancement of metal/dielectric particles [HEIF 06], optical waveguiding [CHEN 06b], [COLE 06], [ALLE 14], optical switching [BORN 15], [BORN 16] and also have been applied in optical fibers [ZELG 16].

In this chapter, it is discussed a new mechanism to produce jets using 3D dielectric cuboids working at sub-THz and THz frequencies (Terajets) under plane wave illumination. First, a systematic study of its performance is carried out in terms of the ratio between the refractive index of the dielectric and the surrounding medium and also the dimensions of the cuboid at the design frequency. Its performance is also evaluated at different frequency harmonics in order to study its broadband response. Practical applications such as backscattering enhancement of metals spheres and all dielectric waveguides are also analyzed. Moreover, the terajets formation is evaluated

by using the 3D cuboids in reflection mode; i.e., the terajets are produced in the region of the incident plane wave. The proposed mechanism is also translated to higher frequencies using SPPs to excite the cuboids placed on top of a metal. They are evaluated in terms of the effective refractive index of the regions with and without the cuboids, as in [SMOL 10], [ZENT 11], [JU 13]. It is shown that PNJs can be excited at the output surface of the cuboids and its position along the propagation axis can be controlled by simply changing the cuboid height and/or the lateral dimensions, as happened under plane wave illumination. Finally, this structure is proposed to be used at telecommunications (telecom) wavelengths to double the propagation of SPPs by simply arranging several cuboids in a chain.

4.1 Three dimensional dielectric cuboids at THz frequencies (Terajets)

4.1.1 Parametric evaluation of the Terajet performance

The proposed 3D dielectric cuboid is schematically shown in Fig. 4.1. It has lateral dimensions $L \times L \times H$, along the x,y and z axis, respectively.

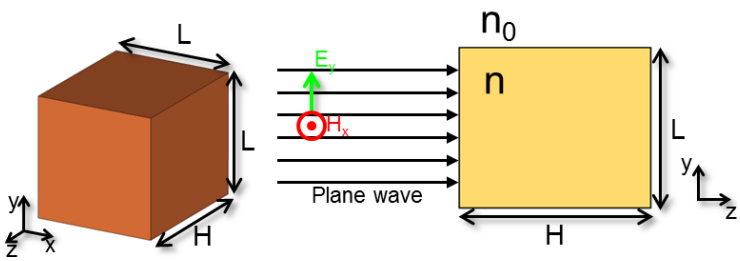

Figure 4.1. (a) Schematic representation of the 3D dielectric cuboid: perspective view (left) and lateral view (right).

To evaluate the focusing performance of the structure, the transient solver of the commercial software CST Microwave Studio® is used along with an extra fine hexahedral mesh with a minimum mesh size of $\lambda_0/45$. In the simulation the 3D cuboid is illuminated with a vertically (E_y) polarized plane wave at the frequency of 0.1 THz (λ_0 = 3 mm). Vacuum (n_0 = 1) is used as the background medium and expanded open

boundary conditions are used in order to insert the 3D cuboid within an infinite medium.

First, the performance of the terajets is evaluated considering a mesoscale cuboid (of the order of the operational wavelength) with fixed lateral dimensions $L = \lambda_0$ and $H = 1.2\lambda_0$ while the refractive index n is changed within the range from 1 to 2. Numerical results of the power distribution on the *yz*-plane and *xz*-plane are shown in the left and right column of Fig. 4.2, respectively, for values of n = 2, 1.75, 1.41 and 1.2. It can be observed that the terajet is located inside the dielectric structure for high values of refractive index, as happened with the PNJs produced by cylindrical and spherical dielectrics [HEIF 09]. When n is reduced, the terajet is moved away from the output surface of the 3D cuboid along the optical axis (z) with less power at its focal position. As the refractive index of the cuboid approaches that of the surrounding medium the focusing properties of the 3D cuboid diminish accordingly, as expected based on the spherical/cylindrical dielectric case.

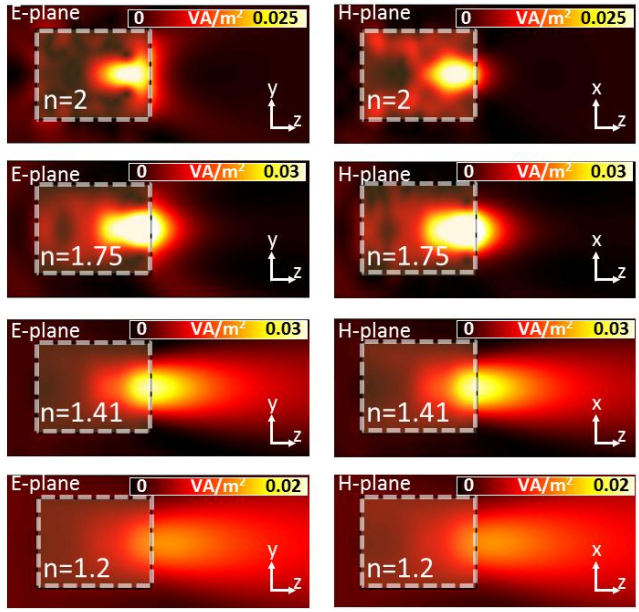

Figure 4.2. Simulation results of the terajet performance for different values of the refractive index: n = 2 (first row), n = 1.75 (second row), n = 1.41 (third row) and n = 1.2 (fourth row) on the *yz*-plane (left column) and *xz*-plane (right column).

Regarding the resolution of the terajets, the *FWHM* along both, *x* and *y* transversal directions for several positions from 0 up to $1\lambda_0$ along the *z* axis (with a step of $0.2\lambda_0$) are shown in Fig. 4.3(a,b) for the values of n under study. Moreover, the power

enhancement along z (calculated as the power distribution with and without the dielectric cuboids) is shown in Fig. 4.4(c). From these results, the best resolution is obtained for n = 1.75 with $FWHM_{x,y} < 0.4\lambda_0$ and a power enhancement of ~15 times just at the output surface of the 3D cuboid (z = 0). However, for n = 1.41 a quasi-symmetric terajet is obtained with similar values of $FWHM_{x,y}$ and a power enhancement factor of ~10 times. For instance, just at the surface of the 3D cuboid, the terajet has a $FWHM_{x,y}$ equal to $0.47\lambda_0$ and $0.45\lambda_0$, respectively. Note that for n = 2, *FWHM* values are not represented for all the distances along the optical axis. This is because the terajet is located inside the 3D cuboid and focusing is only observed on the *xz*-plane for distances up to 0.6 λ_0. From Fig. 4.3(c), it can be observed that, even though the power enhancement for n = 1.41 near the cuboid is lower than for n = 1.75, it decays more smoothly, which could be an advantage for applications such as backscattering enhancement [HEIF 06] to detect metal particles away from the surface of the 3D cuboid (as it will be discussed in section 4.1.2).

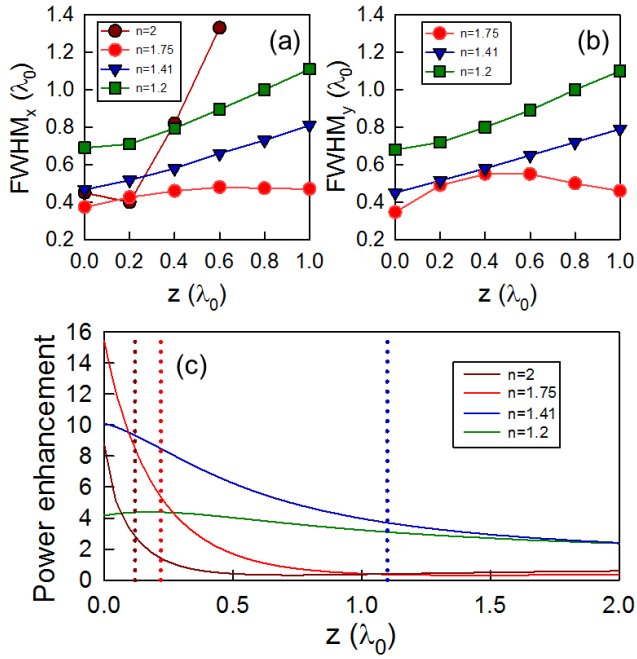

Figure 4.3. Numerical results of the *FWHM* along the x (a) and y (b) axis for a 3D dielectric cuboid with lateral dimensions $L = \lambda_0$ and $H = 1.2\lambda_0$ immersed in vacuum (n_0 = 1) and several values of refractive index n. (c) Power enhancement along the propagation z axis for a 3D dielectric cuboid with the same lateral dimensions as (a,b) and several values of n. The vertical lines correspond to the value of Δ_z obtained for each case of n.

To further study the performance shown in Fig. 4.3(c), we can define the parameter "terajet decay length", denoted as Δ_z, as the distance from the surface at which the power has decayed $1/e$ of its maximum (note that it is implicitly assumed that the maximum appears at the surface, since this is the preferred scenario for microscopy applications). From Fig. 4.3(c) (dotted lines) it is obvious that the exploration range for $n = 1.41$ is $\Delta_z = 1.1\ \lambda_0$ notably larger than for $n = 1.75$, $\Delta_z = 0.22\lambda_0$. Thus, the case $n = 1.41$ can be considered as a good trade-off between the power enhancement and length of the Δ_z. The lower power enhancement at the focal position is obtained for the case when $n = 1.2$ (~4) with value of Δ_z of about $7\lambda_0$ (not shown in the vertical lines of panel c) because the focus is away from the surface of the dielectric cuboid. Thus, in order to generate terajets at the surface of the dielectric cuboid a refractive index contrast relative to the background medium less than 2:1 is required when using a 3D cuboid with lateral dimensions on the order of one wavelength, in agreement with the results of PNJs at optical frequencies using circular/spherical (2D/3D) dielectrics [CHEN 04], [LI 05], [HEIF 06], [HEIF 09].

Now, we evaluate the performance of the terajets when the dimensions of the cuboid are changed. For this case, a value of $n = 1.41$ is chosen following the best performance observed in the previous study. Fig. 4.4(a) shows the simulation results of the power distribution along the z axis at the operational frequency ($f = 0.1$ THz, $\lambda_0 = 3$ mm) when the dimensions of the cuboid are scaled by a factor α from 1 to 4 with a step of 0.5 (where $\alpha = 1$ represents the initial dimensions of the cuboid $L \times L \times H$). The curves are normalized to the maximum power among all the cases, obtained for $\alpha = 2$, i.e. when the dimensions are doubled. From these results, it is clearly observed that the terajet characteristics depend on the dimensions of the cuboid: the terajet is produced just at the output boundary ($z = 0$) of the 3D dielectric cuboid for $\alpha \leq 2.5$. Moreover, very similar peak magnitudes are obtained for $\alpha = 1.5$ and 2, which are more than 1.5 times the magnitude for $\alpha = 1$. Also, two peaks appear for $\alpha = 3$: one at the output of the 3D cuboid and another at $z \sim 2\lambda_0$. For values of $\alpha > 3$, the maximum peak is shifted away from the output face of the structure and the terajet vanishes. From these results, it can be concluded that the dimensions of the 3D dielectric cuboid can be increased up to ~2.5 - 3 times the initial values without penalizing severely the terajet performance.

Finally, the terajet produced by the proposed structure is experimentally evaluated at sub-THz frequencies. Here, the terajet is evaluated at the frequency of f_{exp}=35GHz (λ_{exp} = 8.57mm). The dimensions of the 3D cuboid are the same as before considering $\lambda_0 = \lambda_{exp}$. The measurements of the power distribution are carried out using the method of movable probe [MINI 14b]. The experimental and simulation results of the normalized power distribution along the transversal x axis at $z = 0.1\lambda_0$, i.e., close to the output face of the 3D cuboid of Teflon ($n = 1.46$) are shown in Fig. 4.4(b). From these results, it is obvious that both simulation and experimental results are in good

agreement, with a maximum error between them of 7% and a focusing enhancement of ~10 times. Note that this value is also in good agreement with Fig. 4.3(c) where an enhancement of ~9.5 times was obtained at the same distance using a cuboid with n = 1.41.

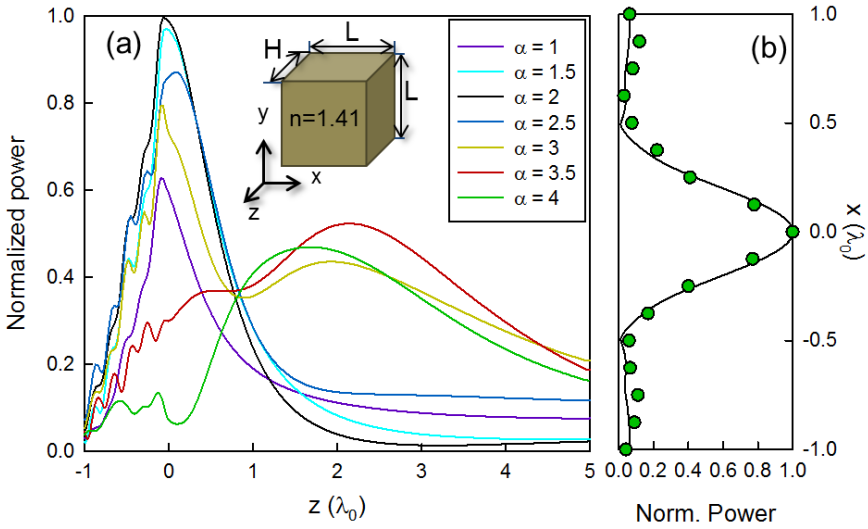

Figure 4.4. (a) Simulation results of the normalized power distribution along the optical z axis for several dielectric cuboids with refractive index n = 1.41 immersed in vacuum (n_0 = 1) when the dimensions are scaled by a factor α. (Inset) scheme of the dielectric cuboid. (b) Simulation (solid line) and experimental (green circles) results of the normalized power distribution along the transversal x axis at $z = 0.1\lambda_{0exp}$ from the output face of the dielectric cuboid at 35 GHz.

4.1.2 Backscattering enhancement using 3D dielectric cuboids

An interesting application of PNJs is the backscattering enhancement produced when metal particles are inserted within the jet region [CHEN 04], [HEIF 06]. This property has been proposed recently and has been experimentally demonstrated at optical frequencies using dielectrics with a cylindrical/spherical shape. Here, we discuss the possibility of using 3D dielectric cuboids to achieve this performance at THz frequencies.

To begin with, the backscattering enhancement is numerically studied using the same simulation properties described previously considering a 3D cuboid with n = 1.41 and lateral dimensions $L = \lambda_0$ and $H = 1.2\lambda_0$. First a gold sphere (with

conductivity $\sigma_{Au} = 4.5\times10^7$ S/m) is placed in the vicinity of the output surface of the 3D cuboid and moved along the z axis from $z = 0.2\lambda_0$ up to $z = 2\lambda_0$ with a step of $0.0833\lambda_0$ [see Fig. 4.5(a)]. Note that a finite conductivity model is used for the gold sphere, which is a good approximation for frequencies below 10 THz (as discussed in Chapter 1). For higher frequencies, a Drude model could fit better the dispersive behavior of metals. With this configuration, the Radar Cross Section (RCS) at the backward direction is obtained with and without the gold sphere. The backscattering enhancement is calculated as $S = S_{3D+mp}/S_{3D}$, where W_{3D+mp} is the calculated RCS in the backward direction for the whole system 3D cuboid + metal sphere and W_{3D} is the RCS in the backward direction calculated with the 3D cuboid alone.

The numerical results are shown in Fig. 4.5(b) for a diameter (d) of the gold sphere ranging from $0.1\lambda_0$ to λ_0. It can be observed that the backscattering enhancement changes periodically and the maximum and minimum peaks are located at the same position ($0.5\lambda_0$) along z for all the considered cases with a periodic oscillation of $0.6\lambda_0$. Moreover, note that the bigger the diameter of the spheres the higher the enhancement of the backscattering radiation. This is an expected result because the interaction between the high field concentration produced by the terajet and the surface of the sphere is increased for higher values of d. To better observe this performance, the results for three spheres with diameters $d_1 = 0.15\lambda_0$, $d_2 = 0.22\lambda_0$ and $d_3 = 0.27\lambda_0$ are shown in Fig. 4.5(c), where an enhancement of the backscattering of 3.29 dB, 7.61 dB and 10.21 dB is obtained, respectively. Note that these values are found within the terajet decay length (which extends up to 1.1 λ_0 along z axis) as expected due to the high power confinement inside this region. For distances far from the terajet, the backscattering is reduced monotonically. To further evaluate the backscattering enhancement achieved with the proposed configuration, the simulation results along the transversal x axis are shown in Fig. 4.5(d) when the gold spheres are placed at $z = 0.5\lambda_0$ (the position of the first maximum) and moved from $-0.6\lambda_0$ to $0.6\lambda_0$. Also, the results for the three mentioned diameters are shown in Fig. 4.5(e). These results demonstrate the ability of the cuboid to enhance the backscattering from small metal spheres along the optical and transversal axes.

For the sake of completeness, the backscattering enhancement of 2D and 3D dielectric cuboids are compared. For the 2D case, the dimension of the cuboid along y is changed to $6L$ ($6\lambda_0$) in order to evaluate its performance as a quasi-infinite structure. By using this configuration, the focusing performance along the yz-plane is changed and a cylindrical terajet ("teraknife") is obtained [see Fig. 4.6(a-b)]. For both, 2D and 3D, cases several gold spheres with different diameters (d_i) are placed at $z_i = d_i/2$, where $i = 1, 2, 3\ldots$ represents the sphere number, in order to evaluate the backscattering produced by the system when the spheres are touching the output face of the 2D/3D cuboids. The numerical results of the backscattering enhancement are shown in Fig. 4.6(c) as a function of d_i. As it is shown, higher values are obtained for

the 3D case, in good agreement with previous results [CHEN 04], [LI 05]. This better performance is due to the ability of 3D cuboids to generate terajets on both planes. However, it is shown how the 2D cuboids producing teraknifes still can be used to detect particles recording its backscattering radiation when they are moved along the propagation axis of the cuboid.

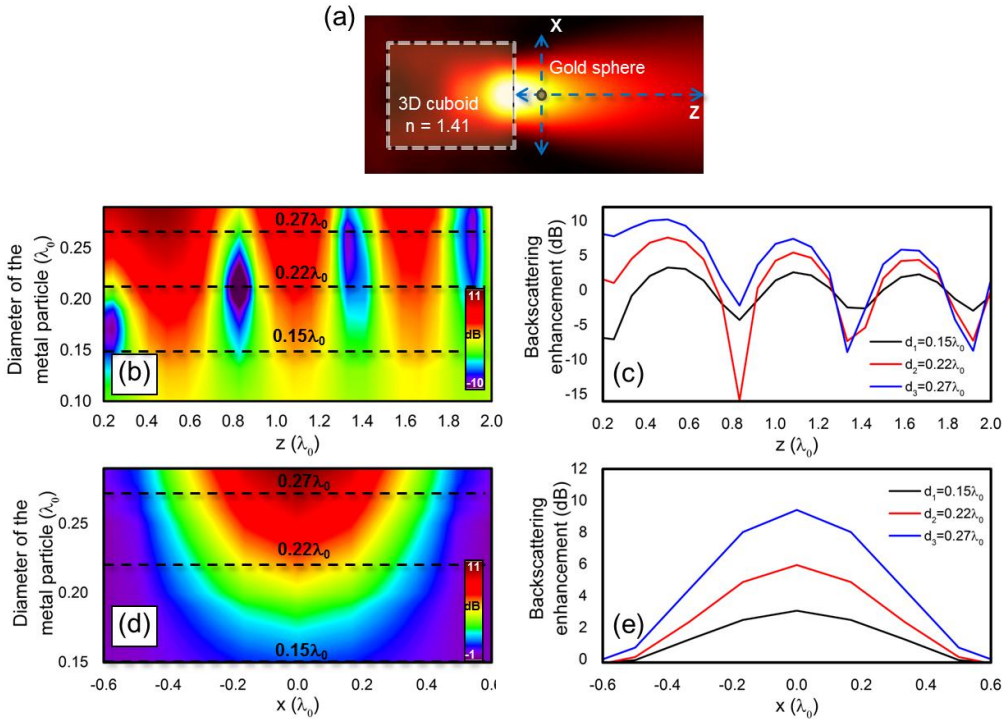

Figure 4.5. (a) Schematic representation of the setup used to evaluate the backscattering enhancement. Numerical results of the backscattering enhancement when a gold sphere with different diameters is moved along the optical axis at $x = y = 0$ (b) and along the transversal x axis at $z = 0.5\lambda_0$ (d). Panels (c) and (e) are extracted from the black dashed lines in (b) and (d), respectively, for metal spheres with diameter $d_1 = 0.15\lambda_0$ (black lines), $d_2 = 0.22\lambda_0$ (red lines) and $d_3 = 0.17\lambda_0$ (blue lines).

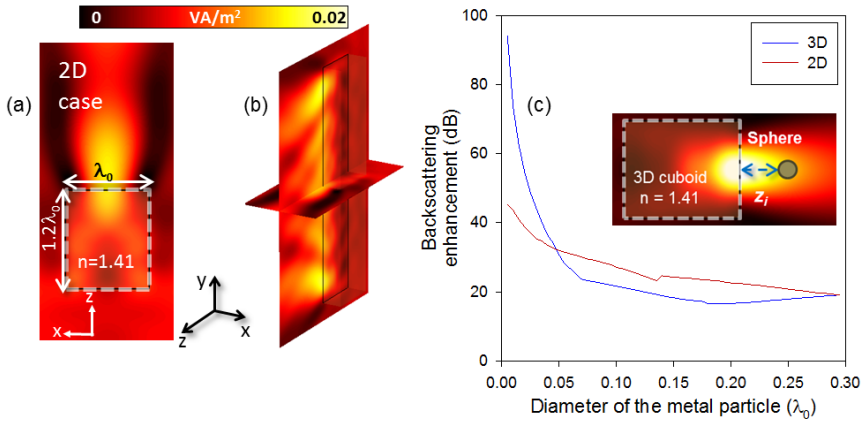

Figure 4.6. Numerical results of the teraknife generated for a 2D dielectric cuboid with refractive index n = 1.41 and lateral dimensions $L = \lambda_0$, $6L = 6\lambda_0$ and H = 1.2 λ_0 along the x, y and z axis, respectively: power distribution on the xz-plane (a) and yz-plane (b). (c) Backscattering enhancement of the system 2D/3D cuboid + metal particle relative to the metal particle alone for different diameters of gold spheres placed at the distance $z_i = d_i/2$ from the output face of the cuboids. (Inset) Setup used to evaluate the Backscattering of metal spheres for both, 2D and 3D, cuboids.

4.1.3 Multifrequency and angular response

In the previous sections, the performance of the terajets has been evaluated at a single frequency. However, it is also important to study its response when the operational frequency is changed from the designed value while fixing the geometry of the cuboids. Here, a study of the multifrequency response is carried out using the same parameters of the cuboids as the best case found from Fig. 4.2 (thickness H = 1.2L and refractive index n = 1.41 embedded in vacuum, n_0 = 1). For the simulations, the same mesh and boundary conditions are also used and the cuboids are excited using a vertically polarized plane wave (E_y). Moreover, frequency and wavelength are normalized as $f' = fL/c$ and $\lambda' = \lambda/L$, where primed magnitudes are normalized values, unprimed ones are physical values and c is the velocity of light in vacuum.

With this setup, the numerical results of the power distribution in the yz plane and xz plane at the normalized fundamental frequency (f'_0 = 1, λ'_0 = 1) and also at the first (f'_1 = 2, λ'_1 = 1/2) and second (f'_2 = 3, λ'_2 = 1/3) frequency harmonics are shown in Fig. 4.7(a-c). Note that the terajet is produced in all cases but is slightly deteriorated at the second harmonic (λ'_2 = 1/3), with higher side lobes than the other cases. By comparing both planes at each frequency, an interesting feature can be observed: a

quasi-symmetric focus is maintained in all cases, demonstrating that it is possible to use the same structure at different harmonics while maintaining its resolution.

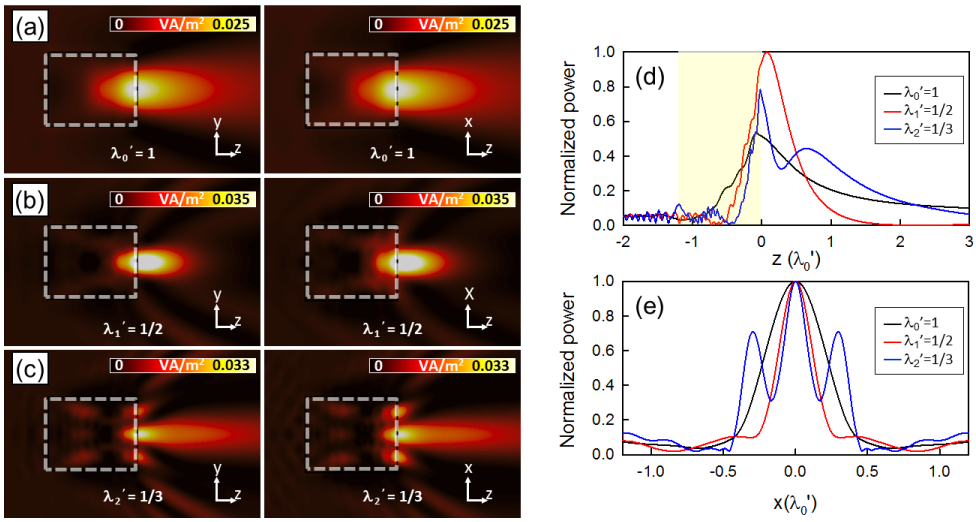

Figure 4.7. Numerical results of the power distribution in the *yz*-plane (left column) and *xz*-plane (right column) when the 3D dielectric cuboid (with dimensions $L \times L \times H$) is illuminated with a plane wave under normal incidence at: (a) the fundamental $\lambda'_0 = 1$ and the (b) first $\lambda'_1 = 1/2$ and (c) second $\lambda'_2 = 1/3$ frequency harmonics. (d) Normalized power distribution (with respect to the maximum value obtained among all the frequencies, first harmonic in this case) along the *z* axis when the 3D dielectric cuboid (yellow) is evaluated at each frequency under study. (e) Normalized power distribution (with respect to the maximum for each case) along the transversal *x* axis just at the output surface of the cuboid working at different normalized frequencies.

To better compare this performance, the numerical results of the normalized power distribution along the propagation *z* axis are shown in Fig. 4.7(d). From these results, the *FL* is $-0.077\lambda'_0$, $0.16\lambda'_1$ (= $0.08\lambda'_0$) and $-0.067\lambda'_2$ (= $0.022\lambda'_0$) for the fundamental, first and second harmonics, respectively. As it can be observed, the highest power distribution is obtained for the first harmonic. Regarding the decay length, the values obtained are $\Delta_z = 1.1\lambda'_0$, $1.2\lambda'_1$ (= $0.6\lambda'_0$) and $0.84\lambda'_2$ (= $0.28\lambda'_0$), respectively. As mentioned above, the terajet generated at the second harmonic is slightly deteriorated and an evident secondary peak is observed away from the output surface of the cuboid at $z \sim 2.1\lambda'_2$ (=$0.7\lambda'_0$), whereas the focusing properties of the terajet are not changed for the first harmonic. The *FWHM* along the transversal *x* axis can be also evaluated. For this purpose, the numerical results of the power distribution

along this axis just at the output surface of the cuboid are shown in Fig. 4.7(e). The values of *FWHM* are $0.47\lambda'_0$, $0.52\lambda'_1$ (= $0.26\lambda'_0$) and $0.62\lambda'_2$ (= $0.21\lambda'_0$), respectively. Also, a power enhancement factor of ~10, ~18 and ~14 is obtained for each case demonstrating that the terajets can be also obtained at the three frequencies but with high lateral lobes when working at the third harmonic.

It is also important to evaluate the multifrequency response of the terajet when the dimensions of the cuboid are changed, similar to the results shown in Fig. 4.4. Here, the lateral dimensions along the transversal x and y axes are fixed to $L = \lambda'_0$ following the same values as used in the previous sections. Whereas the thickness along z (H) is scaled by a factor α ($\alpha = 1 = \lambda'_0$) in order to study the influence of this parameter in the performance of the terajet. The numerical results of the normalized power distribution spectra along the propagation z axis for values of α of 0.2, 0.6, 1, 1.2 and 1.6 are shown in Fig. 4.8 (the schematic representation of the cuboid for each case is shown as inset in each panel). As it can be observed, when H is increased the terajet is closer to the output surface of the cuboid. Moreover, note that when $\alpha = 0.2$, the terajet is far away from the cuboid for all the spectral range under study, in good agreement with the results shown in Fig. 4.4 when all the dimensions of the cuboid are scaled. Moreover, it can be observed that the thicker the cuboid the smaller the multifrequency response. For instance, when $\alpha = 1.6$, a single terajet is generated just at the output surface without a secondary focus along the z axis for frequencies from $1 < f' < 2.2$. Moreover, when $\alpha < 1.2$, the terajets are produced for almost the entire spectral range without secondary focus.

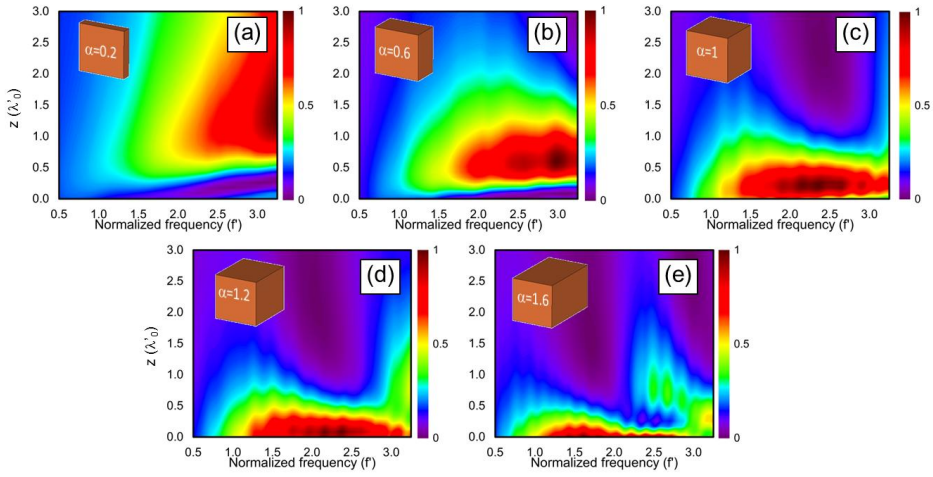

Figure 4.8. Normalized power distribution as a function of the normalized frequency and distance along the z axis at $x = y = 0$ (i.e., the center of the structure) of a 3D dielectric cuboid with $n = 1.41$ immersed in vacuum and lateral dimensions: $L = \lambda_0$ along the x and y axis, and a thickness H scaled by a factor α equal to (a) 0.2, (b) 0.6, (c) 1, (d) 1.2 and (e) 1.6.

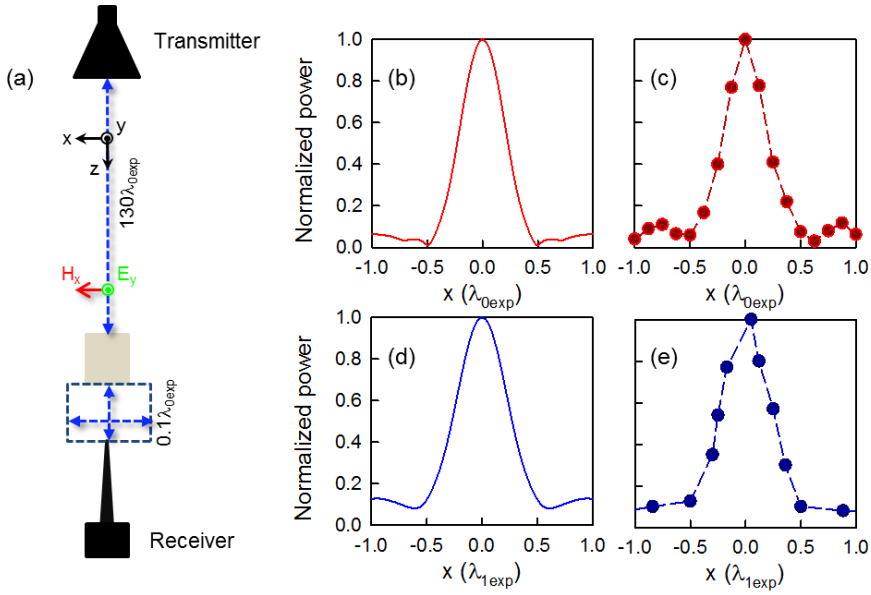

Figure 4.9. (a) Schematic representation of the experimental setup used to characterize the multifrequency response of terajets. Simulation (b,d) and experimental (c,e) results of the normalized power distribution along the transversal x axis for the fundamental frequency f_{0exp} = 35 GHZ, λ_{0exp} = 8.57 mm (red plots) and first harmonic f_{1exp} = 70 GHz, λ_{1exp} = 4.28 mm (blue plots) at $z = 0.1\lambda_{0exp}$

The multifrequency response is also evaluated experimentally at sub-THz frequencies following the same method as before. The experimental frequencies are f_{0exp} = 35 GHz (λ_{0exp} = 8.57 mm) and f_{1exp} = 70 GHz (λ_{1exp} = 4.28 mm) for the fundamental frequency and first harmonic, respectively. The schematic representation of the setup is shown in Fig. 4.9(a): a high gain horn antenna is placed far from the cuboid to illuminate it with a plane wave. Also, a flange ended probe is located on the other side of the cuboid to record the power received at $z = 0.1\lambda_{0exp}$. Again, Teflon is used as the material of the cuboid (n = 1.46) with dimensions $L = \lambda_{0exp}$ and $H = 1.2\lambda_{0exp}$. The numerical and experimental results of the normalized power distribution along the transversal x axis under normal incidence are shown in Fig. 4.9(b,d) and Fig. 4.9(c,e), respectively, demonstrating a good agreement between them. The experimental (numerical) values of $FWHM_x$ are $0.46\lambda_{0exp}$ ($0.47\lambda_{0exp}$) and $0.52\lambda_{1exp}$ ($0.53\lambda_{1exp}$) for the fundamental and first frequency harmonic, respectively. These results demonstrate the capability of dielectric cuboids to generate jets working with frequency harmonics.

Finally, the focusing properties of the terajet are evaluated under oblique incidence in order to characterize its robustness at different angles. The numerical results of the

normalized power distribution in the *xz*-plane for input angles of the plane wave from 0° to 80° are shown in Fig. 4.10. Here, the results are particularized to the fundamental frequency, $f' = 1$. As it can be observed, the terajet is deflected when the input angle is changed.

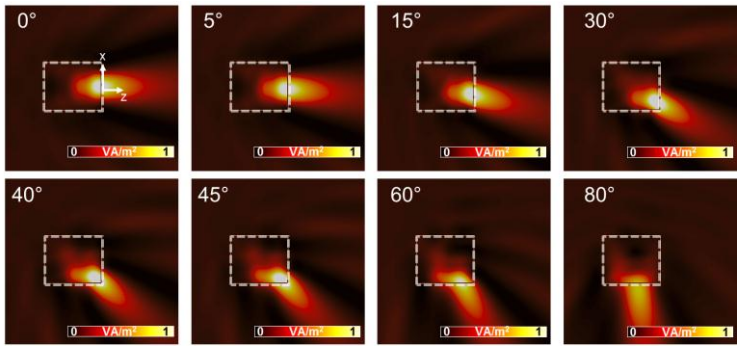

Figure 4.10. Numerical results of the normalized power distribution in the *xz*-plane when the 3D dielectric cuboid is illuminated with an oblique incident plane wave. The input angles are shown in each panel.

For this study, the experimental measurements are carried out at 100 GHz ($\lambda_{0exp} = 3$ mm) and the dimensions of the cuboid are normalized to this wavelength ($L = \lambda_{0exp}$, $H = 1.2\lambda_{0exp}$). The experimental setup along with the pictures of the probe used as receiver, the cuboid and the horn antenna used as transmitter are shown in Fig. 4.11(a-d). The cuboid is placed in a screen surrounded with absorbers in order to avoid undesirable reflections. The transmitter is placed at the back face of the cuboid and is rotated at the needed input angle. The receiver is first fixed at the same angle and then a 2D scanning on the *x'z'*-plane is performed with the aim to obtain the exact position of the maximum power and from here retrieve the output angle. For a better comparison with the experimental results, numerical simulations are carried out and the results of the output angles as a function of the input angles are shown in Fig. 4.11(e) as a solid line along with the experimental data (symbols). As it is observed, a good agreement between both results is obtained. Due to experimental limitations the maximum angle in the experiment is 40º. From this figure, the beam deviation factor (output angle/input angle) has an almost constant slope with a value of 1 for input angles from 0° to 45º. Also, the power distribution of the terajet at the output face of the cuboid is not reduced for these angles, contrarily to the behavior at 60° and 80° (as it can be observed in Fig. 4.10). For the case of the first and second frequency harmonics (not shown) the same dependences are obtained, demonstrating that the terajet produced by the cuboid has a robust performance even under oblique incidence with relatively high incidence angles.

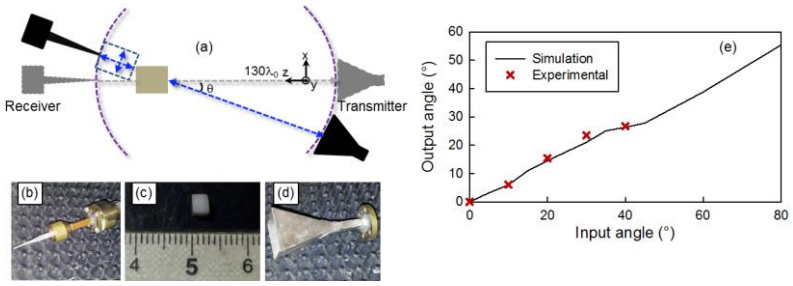

Figure 4.11. (a) Schematic representation of the experimental setup used to characterize the terajet performance under oblique incidence. Pictures of: (b) probe used as receiver, (c) 3D dielectric cuboid made of Teflon with n = 1.46 and (d) horn antenna used as transmitter. (e) Numerical (solid line) and experimental (symbol) results of the output angle of the terajet with respect to the input angle of the incident plane wave under oblique incidence. The input angles go from 0º to 80º and from 0º to 40º for simulation and experiment, respectively.

4.1.4 All dielectric chain with arrays of 3D dielectric cuboids

In this section, it is discussed the capability to produce periodically induced terajets along a chain of mesoscale 3D dielectric cuboids separated with an air-gap of different lengths. The schematic representation of the proposed dielectric chain is shown in Fig. 4.12. All the cuboids are immersed in vacuum and have the same lateral dimensions ($L = \lambda_0$, at difference with the studies shown in the previous sections, here regular hexahedrons are used) with a refractive index n = 1.46.

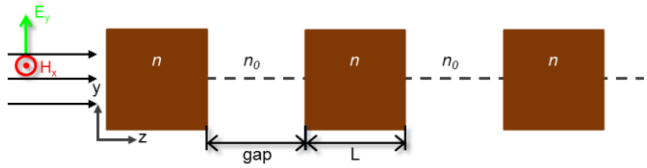

Figure 4.12. Schematic representation of a chain made of 3D dielectric cubes immersed in vacuum with an air-gap between them. The cubes have the same lateral dimensions $L \times L \times L$ with $L = \lambda_0$ and a value of n = 1.46.

The whole structure is illuminated with a vertically polarized plane wave (E_y) propagating from left to right and the numerical results are carried out using the

transient solver of the commercial software CST Microwave Studio® with the same boundary conditions as the previous studies. Note that the gap between the cuboids is different from the chains reported using 2D/3D cylinders/spheres [ASTR 04], [CHEN 06b], [COLE 06], [ALLE 11], [ALLE 14], where the dielectrics are very close to each other.

First, the focusing performance and wave guiding properties of the dielectric chain are evaluated using three cubes and changing the air-gap between them. The numerical results of the normalized power distribution on the *xz*-plane for values of the air-gaps between cubes varying from $0.25\lambda_0$ to $2.5\lambda_0$ are shown in Fig. 4.13. As it can be observed, when the air-gap is smaller than λ_0 the terajet is produced inside the cubes [Fig. 4.13(a-c)] and the highest power distribution is obtained in the central cube (close to its output surface). In these cases, the terajets are somewhat blurred for the first and third cubes. On the other hand, when this distance is increased, the terajets are clearly formed just at the output surface of each cube. Note that the best performance is achieved when the air-gap is $2.5\lambda_0$, where the power distribution of the terajets is increased for all the cubes [see Fig. 4.13(f)].

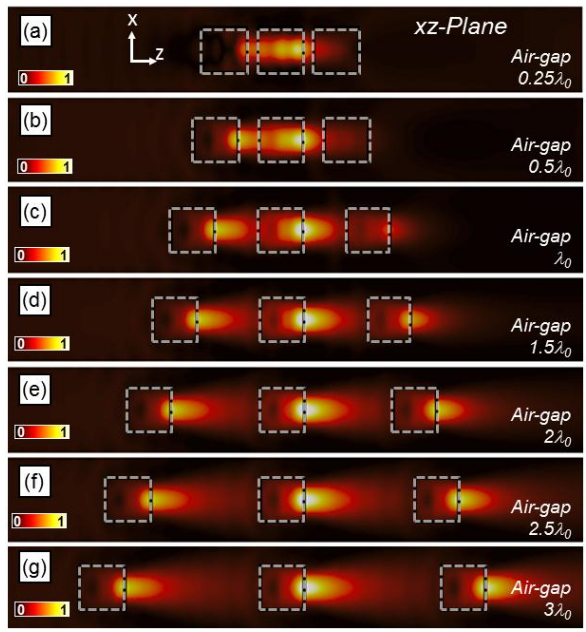

Figure 4.13. Numerical simulations of the power distribution on the *xz*-plane for several chains of 3D dielectric cuboids with dimensions $L = \lambda_0$ along all directions when the air-gap between each cuboid is: (a) $0.25\lambda_0$, (b) $0.5\lambda_0$, (c) λ_0, (d) $1.5\lambda_0$, (e) $2\lambda_0$, (f) $2.5\lambda_0$, and (g) $3\lambda_0$ Results normalized with respect to the maximum power distribution achieved from all the structures (air-gap of $2.5\lambda_0$ in this case)

For the sake of completeness, the numerical results of the *FWHM* along both transversal *x* and *y* axes at each terajet position for the case with an air gap of $2.5\lambda_0$ are shown in Table. 4.1. Here the cube number 1, 2 and 3 corresponds to the left, central, and right cube of the chain. It can be observed that a similar resolution is achieved for all the terajets along both directions with values below $0.5\lambda_0$ for all cases. The ellipticity (defined as the ratio between both transversal resolutions $FWHM_x/FWHM_y$) of all terajets is close to 1. Therefore, a quasi-spherical spot is obtained for the chain configuration in good agreement with the previous results discussed in Fig. 4.3.

Regarding the decay length, the maximum value is obtained for the first cube while it is reduced for the rest. For this chain, the maximum enhancement is ~11.6 in good agreement with the results of a single cuboid (see Fig. 4.3). Thus, it is observed that a mesoscale dielectric cube-air-chain waveguide is mainly characterized by the periodicity of jets corresponding to the optimal air-gap distance between cubes when a fixed geometry and material is chosen. This fact contrasts with the results found in optical chains of dielectric microspheres where the periodical focusing of light in straight chains of touching microspheres is characterized with the periodicity of PNJs corresponding to the size of two spheres [CHEN 06b], [COLE 06], [ALLE 11], [ALLE 14].

Cube number	$FWHM_x$ (λ_0)	$FWHM_y$ (λ_0)	Δ_z (λ_0)	Ellipticity	Enhancement
1	0.47	0.44	1.53	1.068	8.5
2	0.49	0.43	1.12	1.1395	11.6
3	0.48	0.44	0.99	1.0909	10.8

Table 4.1. Numerical results of the terajet resolution for a dielectric chain made of three cubes and an air-gap of $2.5\lambda_0$ between them.

To further study the performance of the chain, it is important to evaluate the effect dielectric losses which might be important THz frequencies. Numerical results of the normalized power distribution on the *xz*- and *yz*-plane when the periodicity is $2.5\lambda_0$ and the cubes have a loss tangent of $\delta = 0.05$ and $\delta = 0.1$ at the working wavelength λ_0 are shown in Fig. 4.14(a,b) and Fig. 4.14(c,d), respectively. Note that we overestimated losses since, for example, a typical δ for Teflon (with a similar refractive index as the one here used) is ~0.008 at 1 THz [JIN 06]. To better compare these results, the power distribution along the propagation axis at $x = y = 0$ is shown in Fig. 4.14(e,f) for each value of δ, respectively. It can be observed that the terajets are slightly shifted away from the output surface of each cube and its length is increased when losses are introduced. Moreover, the power distribution at each output is reduced up to ~1/3 when $\delta = 0.1$ (compared with the lossless case). These results are not surprising since a change in δ modifies the refractive index of the cubes and therefore a shift of the focus should occur, as discussed previously and depicted in Fig. 4.2.

To better compare these results the focusing properties of the terajets produced at the output surface of each cube for the same values of δ are summarized in Table 4.2. In general, the resolution of each terajet is deteriorated when losses are increased. However, the results obtained are very close to the lossless cases even with highly overestimated dielectric losses.

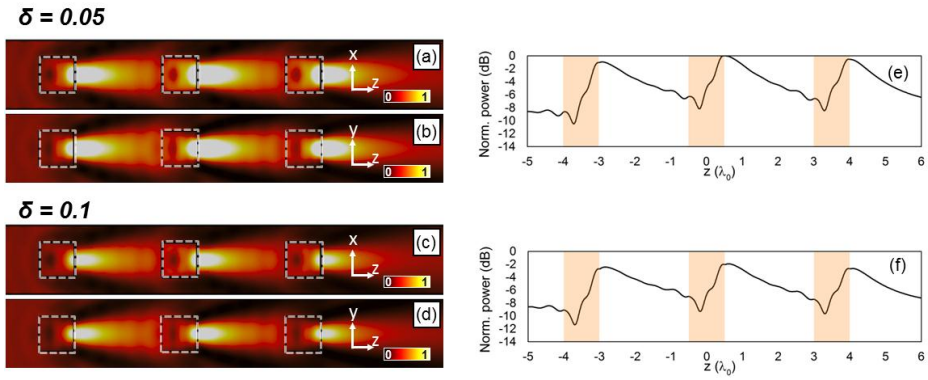

Figure 4.14. Numerical simulations of the power distribution on the *xz*- (a,c) and *yz*- (b,d) planes for a chain of 3D dielectric cubes with dimensions $L = \lambda_0$ along all directions and an air-gap between each cuboid with a value of $2.5\lambda_0$ when dielectric losses are introduced to the cuboids with a value of: (a,b) $\delta = 0.05$ and (c,d) $\delta = 0.1$. Results of the power distribution along the propagation axis (normalized to the maximum from all cases, second cuboid of the chain with $\delta = 0.05$ in this case) for a chain with $\delta = 0.05$ (e) and $\delta = 0.1$ (f).

Cube number	$FWHM_x$ (λ_0)		$FWHM_y$ (λ_0)		Δz (λ_0)	
	δ=0.05	δ=0.1	δ=0.05	δ=0.1	δ=0.05	δ=0.1
1	0.49	0.5	0.45	0.47	1.72	2.14
2	0.5	0.51	0.43	0.45	1.47	1.97
3	0.49	0.5	0.43	0.44	1.3	1.86

Table 4.2. Terajet performance produced in a cube-air-chain with an air gap of $2.5\lambda_0$ for different values of loss tangent δ.

For the sake of completeness, the normalized power distribution along the *z* axis for two chains of 11 cuboids with the previous values of δ is shown in Fig. 4.15. It can be observed that the power decays exponentially at half its maximum at the fifth cuboid. Also, from there on, the relative power at each terajet still decays but with small losses (~0.26 dB/cuboid and ~0.4 dB/cuboid for the cases with $\delta = 0.1$ and $\delta = 0.05$, respectively), compared with the first five terajets. It is important to note that these values are calculated using Fig. 4.15 where the values are normalized to the

maximum from each case. Therefore, even when the decay of power at each terajet position is lower for the case with δ = 0.1, the total power at the terajet maxima are below those obtained with δ = 0.05, as it has been explained before and can be corroborated in Fig. 4.14(e,f). Finally, regarding the *FWHM* along the transversal *x* axis for the first, fifth and last cuboid of Fig. 4.15, the resulting values are $0.49\lambda_0$, $0.48\lambda_0$ and $0.49\lambda_0$, respectively, for the case with δ = 0.05 while they are $0.5\lambda_0$, $0.49\lambda_0$ and $0.5\lambda_0$, when δ = 0.1. This demonstrates that the spatial resolution of the terajets is maintained along both chains. Based on these results, the robustness of the wave guiding configuration here proposed even in the presence of high losses is demonstrated.

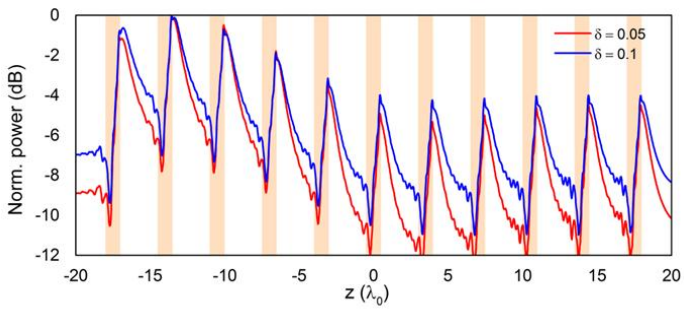

Figure 4.15. Normalized power distribution along the propagation *z* axis for a chain of 11 dielectric cuboids with the same dimensions as Fig. 4.14 and two values of δ = 0.05 (red line) and δ = 0.1 (blue line). The results are normalized to the maximum of each case.

4.1.5 Terajets in reflection mode

All the studies presented in the previous sections have been carried out using 3D dielectric cuboids working in the transmission regime. Here, it is discussed the capability to produce terajets when the cuboids work in reflection mode. In this case, the whole structure is illuminated with a plane wave from its front side and a terajet is produced close to the surface of the dielectric cuboid but in the opposite direction of the incident EM field, as it should be expected. The numerical results are performed using the transient solver of the commercial software CST Microwave Studio® with the same boundary conditions and mesh as in the previous sections. Since the 3D dielectric cuboids can be scaled at different frequency ranges, here both wavelength and frequency are normalized as $\lambda_m' = \lambda_m / \lambda_0$ and $f_m' = f_m' / f_0$; where the unprimed and primed variables represent the physical and normalized values, respectively, m = 0, 1, 2 and refers to the fundamental (m = 0) and higher order harmonics (m = 1, 2) and L is the dimension of the cuboid along both transversal *x* and *y* axes.

A schematic representation of the 3D dielectric cuboid working in the reflection regime is shown in Fig. 4.16. The cuboid, with a refractive index of n = 1.46, has lateral dimensions $L = \lambda_0$ and thickness H and is placed at the front side of an aluminum plate (with conductivity $\sigma_{Al} = 3.56 \times 10^7$ S/m) of dimensions $2L \times 2L \times 0.33L$. All the dimensions are normalized to the fundamental wavelength λ_0. A vertically polarized (E_y) plane wave is used as a source illuminating the cuboid from its front side; i.e., with propagation along the negative z axis (see Fig. 4.16). To evaluate the terajets performance, it is considered that the whole structure is immersed in vacuum ($n_0 = 1$).

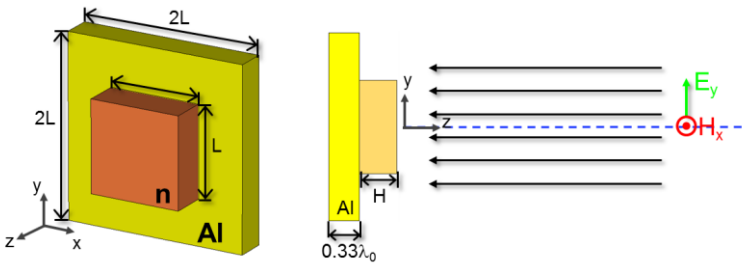

Figure 4.16. Schematic representation of the 3D dielectric cuboid working in reflection mode: perspective (left) and lateral (right) view.

First, the focusing performance of the terajets is evaluated at the normalized fundamental frequency ($f_0' = 1$, $\lambda_0' = 1$) using several 3D dielectric cuboids with the same transversal dimensions (along x and y axis) and changing the dimension along the propagation axis (H). The numerical results of the power distribution on the xz-plane for different values of the cuboid thickness ranging from $0.2\lambda_0$ to $0.8\lambda_0$ with a step of $0.2\lambda_0$ are shown in Fig. 4.17. It can be observed that the terajet is produced for all the geometries. However, for values of $H = 0.6\lambda_0$ and $0.8\lambda_0$ the focus is inside the cuboid. By decreasing the axial dimension below $0.4\lambda_0$, the terajet is moved toward the cuboid and it is close to the output surface when $H = 0.4\lambda_0$ and completely outside the cuboid for $H = 0.2\lambda_0$. To better compare these results, the normalized power distribution along the propagation z axis is shown at the bottom of each panel in Fig. 4.17, for each value of H (the output surface of the cuboid is plotted as an orange dotted line in all cases as a reference and the power distribution without the presence of the cuboid is plotted as a gray line).

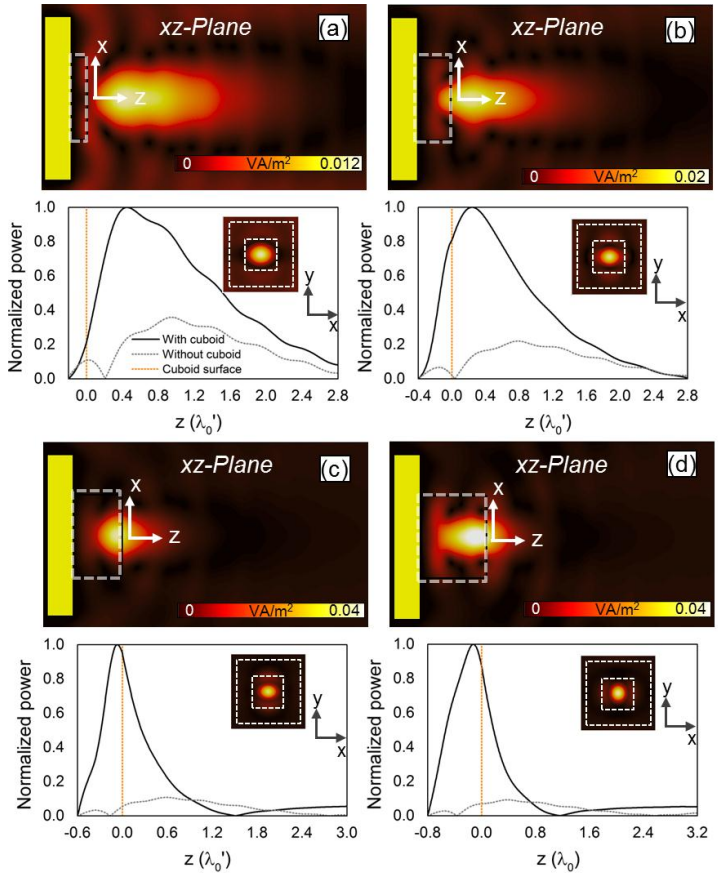

Figure 4.17. Numerical simulations of the power distribution on the *xz*-plane (a-d) along with the normalized power distribution along the propagation *z* axis (bottom panels) for different cuboids when the transversal dimensions are fixed with a value of $L = \lambda_0'$ along both *x* and *y* axis, while the dimension along *z* axis is changed with values of: (a) $H = 0.2\lambda_0'$, (b) $H = 0.4\lambda_0'$, (c) $H = 0.6\lambda_0'$ and (d) $H = 0.8\lambda_0'$. In the plots at the bottom of each panel, the output surface of the cuboid is plotted as orange dotted line, the power distribution without the cuboid is plotted as gray dotted line and the power distribution on the *xy*-plane at each *FL* is shown as inset (the cuboid and the metal square are plotted as white dashed lines).

From these results, the optimum value of *H* should be $H < 0.4\lambda_0$, in order to produce the terajet just at the surface of the cuboid for the fundamental frequency. Note that this dimension is optimal for the refractive index here used ($n = 1.46$) and this should be changed for other values of *n*. For instance, we found that if $H = 0.8\lambda_0$ a value of $n = 1.2$ should be used for the cuboid in order to obtain the terajet just at the surface of the dielectric (not shown here).

Next, to study the broadband behavior of the terajets, several structures are evaluated for values of H ranging from $0.2\lambda_0$ to $0.4\lambda_0$ with a step of $\sim 0.07\lambda_0$ at the fundamental frequency ($f_0' = 1$, $\lambda_0' = 1$) and the first frequency harmonic ($f_1' = 2$, $\lambda_0' = 1/2$). The focusing properties are summarized in Table 4.3 in terms of the *FL* and power enhancement. Note that in this case the maximum value is selected to be at the *FL* and not at the surface of the cuboid, because the focus may be outside the cuboid and not just at the surface for different values of H, as explained previously. From these results, the best performance at the fundamental frequency is obtained for a value of $H = 0.33\lambda_0$, where the terajet is closer to the output surface of the cuboid and a maximum enhancement of ~7.3 is achieved. For the first frequency harmonic, the best performance is achieved when $H = 0.4\lambda_0$ with an enhancement of ~17. Note that, in general, the enhancement achieved with the first frequency harmonic is higher for all the values of H here evaluated, in good agreement with the results obtained in transmission, Section 4.1.3. Therefore, this structure may be used for both frequency harmonics.

Frequency	H	FL	Enhancement
$f_0' = 1$	$0.4\lambda_0$	$0.245\lambda_0'$	~7.25
$f_1' = 2$		$0.874\lambda_1'$	~17
$f_1' = 1$	$0.33\lambda_0$	$0.188\lambda_0'$	~7.3
$f_1' = 2$		$0.749\lambda_1'$	10.3
$f_0' = 1$	$0.27\lambda_0$	$0.269\lambda_0'$	~6.6
$f_1' = 2$		$1.33\lambda_1'$	~13.6
$f_0' = 1$	$0.2\lambda_0$	$0.45\lambda_0'$	~4.5
$f_1' = 2$		$2.12\lambda_1'$	~7.8

Table 4.3. Terajet performance working in reflection mode at the fundamental frequency ($f_0' = 1$, $\lambda_0' = 1$) and first frequency harmonic ($f_1' = 2$, $\lambda_1' = 1/2$) using 3D dielectric cuboids with the same transversal dimensions (x and y) and different values along the propagation axis (z).

For completeness, the numerical results of the $FWHM_x$ and $FWHM_y$ at the fundamental and first frequency harmonic are plotted in Fig. 4.18(a-b) for the same range of H. Moreover, the ellipticity for both frequencies is plotted in Fig. 4.18(c). At the fundamental frequency, it is shown that again the best performance is achieved when $H = 0.33\lambda_0$ with a resolution of $FWHM_x = 0.44\lambda_0$' and $FWHM_y = 0.41\lambda_0$'. This design also produces a nearly symmetric jet, with an ellipticity of 1.073, i.e., a quasi-spherical spot is achieved. The best design for the first frequency harmonic is when $H = 0.4\lambda_0$ with values of $FWHM_x = 0.55\lambda_1$'and $FWHM_y = 0.57\lambda_1$' with an ellipticity of 0.96 which is also an almost spherical focus.

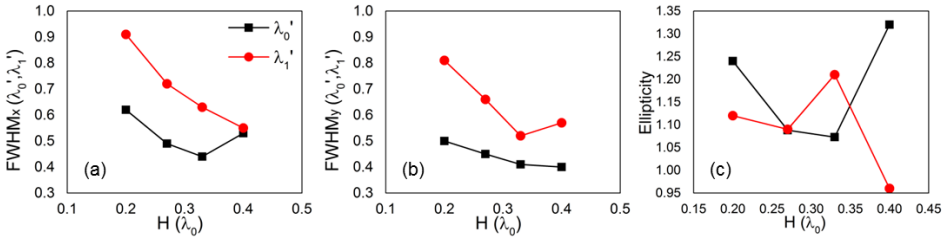

Figure 4.18. Results at the fundamental (black) and first frequency harmonic (red) of: (a) $FWHM_x$, (b) $FWHM_y$ and (c) ellipticity ($FWHM_x/FWHM_y$).

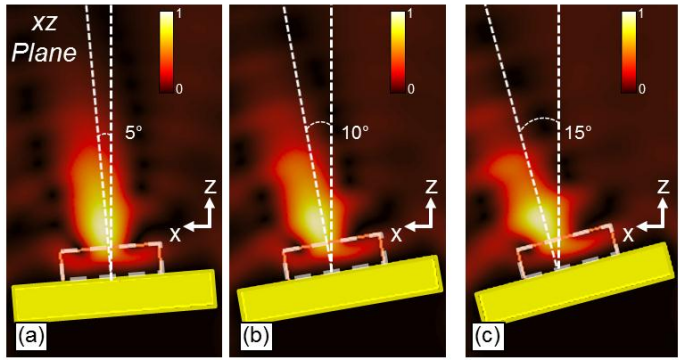

Figure 4.19. Numerical results of the normalized power distribution on the *xz*-plane for a 3D dielectric cuboid under oblique incidence working in reflection mode at the fundamental frequency ($\lambda_0' = 1$) when the whole structure is rotated at (a) 5º, (b) 10º and (c) 15º.

Finally, it is also interesting to evaluate the focusing performance of a cuboid in reflection regime under oblique incidence. Numerical results of the normalized power distribution on the *xz*-plane are shown in Fig. 4.19 at the fundamental frequency ($f_0' = 1$, $\lambda_0' = 1$) when the whole structure is rotated from 5º to 15º with a step of 5º. We use the cuboid with the best focusing performance, as discussed above (dimensions $\lambda_0 \times \lambda_0 \times 0.33\lambda_0$). As it can be observed, a spillover of energy around the edges of the cuboids is observed in the direction of rotation. As a result of the destructive interference, the shape of the photonic jet is distorted. Regarding the focusing enhancement the values are ~7.14, ~7.39 and ~7.4 for the rotation angles 5º, 10º and 15º, respectively, demonstrating that the terajet is preserved and the performance is not fully deteriorated. Also, it can be observed that its direction is clearly dependent on the rotation angle and therefore it may be rotated in the space.

4.2 Photonic nanojets excited by Surface Plasmons

In this section, it is shown how the PNJs can be scaled up to higher frequencies using SPPs for the excitation of dielectric cuboids placed on top of a metal surface. The study is carried out based on the effective refractive index of the SPPs traveling in the regions with and without the cuboids, as it has been reported in [SMOL 10], [ZENT 11], [JU 13], [SMOL 16]. This structure is then applied in the design of dielectric chains at telecom wavelengths with the aim to increase the SPP propagation distance.

4.2.1 Analytical approach based on the effective refractive index

A schematic representation of the proposed structure is shown in Fig. 4.20(a). It consists of a gold film with thickness t = 100 nm on top of a dielectric substrate with a refractive index n = 1.5. The dispersive refractive index of gold is modeled following the Johnson & Christy experimental data [JOHN 72]. A 3D dielectric cuboid of Silicon Nitride (Si_3N_4) with dimensions $L_x \times L_y \times L_z$ is placed on top of the metal film and the whole structure is immersed in air (n_1 = 1). The refractive index of Si_3N_4 is also dispersive in the considered bandwidth (750 - 2000 nm) with values ranging from ~1.97 to ~1.99. Given that this variation is of the order of 10^{-2} within this wide spectral band, a constant refractive index n_2 = 1.97 is considered here for simplicity. Numerical simulations are done using the transient solver of the commercial software CST Microwave Studio®. The structure is excited by an extremely narrow waveguide placed at the back of the plasmonic structure, see Fig. 4.20(d). With this configuration, surface plasmons propagating along z are excited at the abrupt interface between the waveguide aperture and air on top of the gold film, as it is shown in Fig. 4.20(b), with the electric field along the y and z axes and magnetic field along the x axis (i.e., a TM wave). With this setup, first, the SPP propagation on this structure is analyzed. In Fig. 4.20(c), a perspective view of the structure is shown. The SPPs propagate from left to right along z. As it can be inferred, there are two different regions depending of the materials present in the structure [JU 13]: the first region (denoted as “I”) corresponds to the air-metal interface and the second one (marked as “II”) to the air-cube-metal.

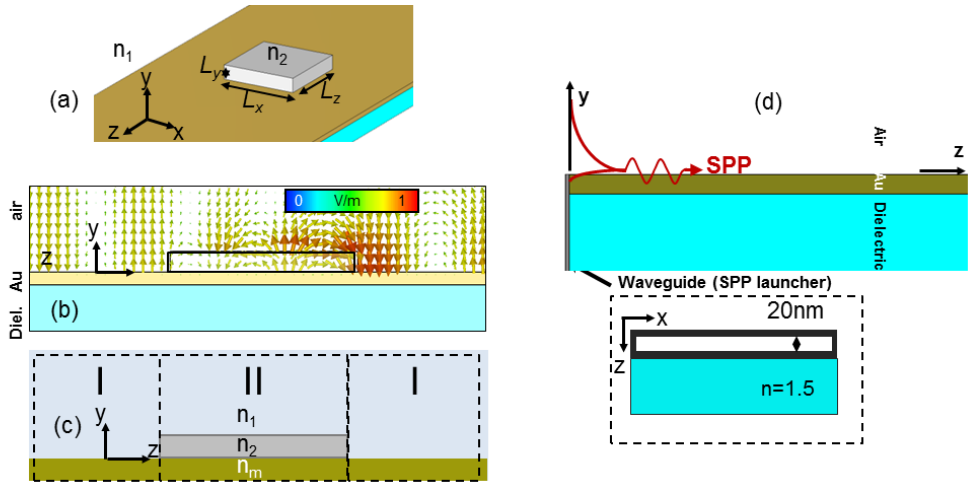

Figure 4.20. Schematic representation of the structure proposed to produce PNJs using a 3D dielectric cuboid of Si_3N_4 with a refractive index of 1.97 and lateral dimensions $L_x = L_z = \lambda_0 = 1550$ nm and a variable height L_y on top of a gold film of thickness $t = 100$ nm lying on top of a dielectric substrate (see inset). (b) Electric field distribution at the operation wavelength (λ_0) on the *yz*-plane. (c) Lateral view of the proposed device showing regions I and II which include the interfaces air-metal (I) and air-cuboid-metal (II), respectively. (d) Lateral view of the structure without the cuboid. The ultra-narrow waveguide launcher is on the left side of the figure and the SPPs propagate along the *z*-axis.

As it is known, a metal film can be considered semi-infinite when its thickness is larger than the skin depth [BRUK 86], [KRAS 10] which is about 30 nm for gold. Hence, in a real scenario a metal thickness of 100 nm is a good approximation for a semi-infinite slab. This approximation has been extensively used at different wavelengths, such as telecom wavelengths, giving rise to applications such as waveguiding and focusing of SPPs, to name a few [STEE 06], [FENG 08], [KRAS 10], [JU 13], [KHAL 14]. For completeness a thorough study to validate this approximation both analytically and numerically is carried out and shown in Appendix A. With the assumption of semi-infinite metal, the analytical complexity of the structure shown in Fig. 4.20 can be largely reduced. The analysis below is done in terms of the propagation constant in each region and from it we extract the effective refractive index seen by the SPPs (n_{spp}) in each case.

To calculate the effective propagation constant in region I, the well-known expression of SPPs excited at a dielectric-metal interface can be used (Eq. 1.13) [BRUK 86]. The complete deduction of this expression can be found in Appendix A. Particularizing Eq. 1.13 to the case under study, the following equation is obtained:

$$\beta_{(I)} = k_0 \sqrt{\frac{n_1^2 n_m^2}{n_1^2 + n_m^2}} \tag{4.1}$$

where k_0 is the wavenumber in free space and n_1 and n_m are the refractive indexes of air and gold, respectively.

On the other hand, for the case of the region II, three different materials must be considered: air, Si_3N_4 and gold [see Fig. 4.20(c)]. After evaluating the problem as a multilayered system, the propagation constant for this region can be obtained by solving the following transcendental equation (a complete derivation of this expression can be found in Appendix A):

$$\tanh(k_2 L_y) = -\left(\frac{\varepsilon_m \varepsilon_2 k_2 k_1 + \varepsilon_1 \varepsilon_2 k_m k_2}{\varepsilon_m \varepsilon_1 k_2^2 + \varepsilon_2^2 k_m k_1} \right) \tag{4.2}$$

where 1, 2 and *m* represent the different materials of the region: air, Si_3N_4 and Au, respectively, and $k_i = \{[\beta_{(II)}]^2 - \varepsilon_i [k_0]^2\}^{1/2}$ is the wave number of each medium with i = 1, 2, *m*. Note that the above expression has an explicit dependence on the height (L_y) of the 3D dielectric cuboid. Hence, $\beta_{(II)}$ can be tuned with this parameter. From here, it is straightforward to calculate the complex effective refractive index, as follows:

$$n_{spp}^{(I),(II)} = \frac{\beta_{(I),(II)}}{k_0} \tag{4.3}$$

In Fig 4.21(a) it is shown the variation of $n_{spp}^{(I)}$ between 750 nm and 2000 nm calculated with Eq. 4.1 and Eq. 4.3. As observed, within all the considered spectral range $n_{spp}^{(I)} > 1$ and it approaches asymptotically unity in the long wavelength limit. This means that SPPs are strongly coupled to the surface of the Au film only for relatively small wavelengths. In particular, at the telecommunication wavelength of 1550 nm, SPPs are weakly coupled. Nevertheless, as it will be shown later, the proposed structure can be engineered to focus the incoming SPPs on a narrow spot of high intensity even at this wavelength. Also, the analytical results of the complex $n_{spp}^{(II)}$ for $0 < L_y < 500$ nm for the same spectral range are shown in Fig. 4.21(b,c). At a given wavelength, increasing the height L_y of the cuboid generates an increment of both $\mathrm{Re}\{n_{spp}^{(II)}\}$ and $\mathrm{Im}\{n_{spp}^{(II)}\}$. Importantly, $\mathrm{Im}\{n_{spp}^{(II)}\} << \mathrm{Re}\{n_{spp}^{(II)}\}$ in all considered cases, demonstrating that the structure has low losses.

In Fig. 4.22 is ploted the real part of effective index contrast, denoted as *c*, between regions II and I. Here, three zones are marked depending on the contrast: (i) $c < 1.3$, (ii) $1.3 < c < 1.75$ and (iii) $c > 1.75$. From the results discussed in the previous sections, we can foresee that the PNJ will be generated outside, close to the output interface and inside the cuboid when working in region (i), (ii) and (iii), respectively.

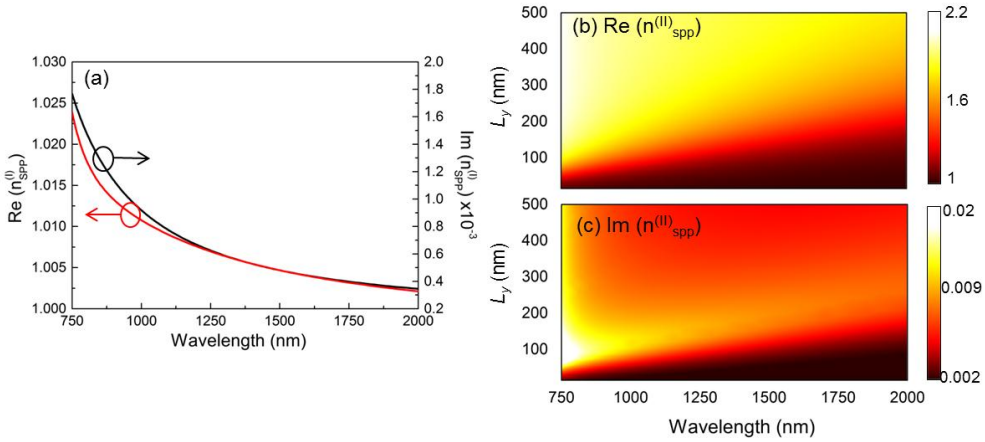

Figure 4.21. (a) Real (red) and imaginary (black) parts of the effective refractive index for the region I corresponding to the air-Au interface. Real (b) and imaginary (c) part of the effective refractive index in region II as a function of L_y and wavelength.

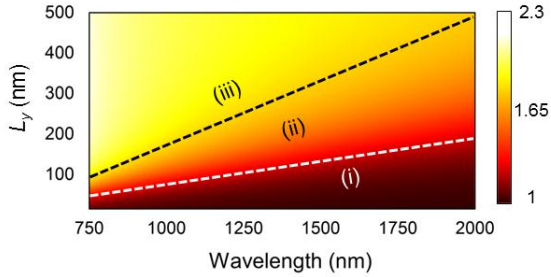

Figure 4.22. Real part of the refractive index contrast spectra between region II and I as a function of L_y. The regions where the contrast is $c < 1.3$, $1.3 < c < 1.75$ and $c > 1.75$ are marked as zones (i), (ii) and (iii), respectively.

4.2.2 Parametric evaluation of the PNJs

Now that the effective refractive index contrast has been calculated, the performance of the PNJ produced by the proposed structure can be evaluated. Based on the results shown in section 4.1, the dimensions of the cuboid should be of the order of the operational wavelength to produce the PNJ at the output surface of the dielectric. Hence, here the dimensions of the cuboid are $L_x = L_z = \lambda_0 = 1550$ nm with a variable height, L_y. The rest of dimensions of the structure are as shown in Fig. 4.20(a).

With this configuration, the contrast c at 1550 nm is extracted from Fig. 4.22 as a function of L_y, see Fig. 4.23(a). It evolves from values close to unity for small L_y to values near 1.9 for large L_y. In the figure, the three regions [(i)-(iii)] mentioned above are marked and three representative points are selected: L_y = 100 nm, L_y = 160 nm (this value is chosen because it is found to be the optimal, although is near the limit of the region) and L_y = 350 nm. The numerical results of the power distribution on the *xz*-plane (i.e., just at the surface of the Au film) are shown in Fig. 4.23(b-d). It is demonstrated that for L_y = 100 nm, where the contrast is ~1.11, the PNJ is moved away from the cuboid and the peak is located at a *FL* of 275 nm ($0.18\lambda_0$), along the *z* axis. For L_y = 160 nm where the contrast is 1.35 the PNJ is just at the output surface of the cuboid. Finally, when L_y = 350 nm, where the contrast is 1.85, most of the power is inside the dielectric cuboid, compared with the case when l_y = 160 nm.

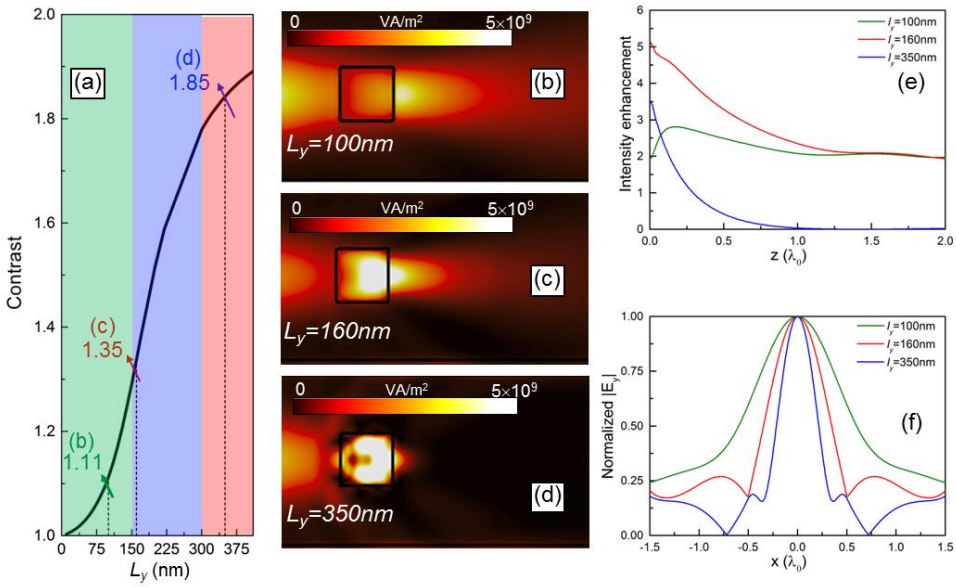

Figure 4.23. (a) Analytical refractive index contrast between region II and region I at λ_0 = 1550nm as a function of L_y. The regions where the contrast is c < 1.3, 1.3 < c < 1.75 and c >1.75 are filled in green, blue and red, respectively. Numerical results of the power distribution on the *xz*-plane just at the surface of the Au film (b-d) for different values of L_y. Numerical results of the intensity enhancement along the *z* axis (e) and normalized magnitude of the electric field along the *x* axis at each *FL* for a cuboid with lateral dimensions L_x = L_z = 1550 nm and L_y = 100 nm (green lines), L_y = 160 nm (red lines) and L_y = 350 nm (blue lines).

For a better comparison of these results, the intensity enhancement along the *z* axis for the three heights under study is plotted in the same figure. Here it is clearly observed that the maximum is outside the cuboid when L_y = 100 nm while it is at the output interface when L_y = 160 nm. The enhancement at each *FL* is ~2.8, ~5.05 and ~3.4 for each height under study. These values are below those obtained under plane wave illumination at THz frequencies (see Section 4.1). This is due to the fact that the SPPs are not strongly coupled to the surface of the metal film at 1550 nm, as explained before. A larger enhancement could be obtained by designing the structure at smaller wavelengths where the coupling of SPPs to the metal film increases [JU 13]. However, the aim here is to show that at 1550 nm it is possible to have a relatively large enhancement thanks to the excitation of a PNJ with SPPs since this is the standard telecommunications wavelength [LAUR 11], [THAC 15]. With the results shown, it is successfully demonstrated that the PNJs produced with this configuration are able to enhance more than two times the SPP intensity at the *FL*.

For completeness, the numerical results of the normalized magnitude of the electric field for each height under study are shown in Fig. 4.23(f). Here, the results are normalized to the maximum of each case. By looking at this plot, the $FWHM_x$ at each *FL* is $1.197\lambda_0$, $0.68\lambda_0$ and $0.43\lambda_0$ for L_y = 100, 160, and L_y = 350 nm, respectively. Note that the best resolution is achieved for the case L_y = 350 nm. However, the power of the PNJ decays faster along the propagation direction, as it is shown in Fig. 4.23(e). The best trade-off between the resolution, enhancement and distance of propagation of the SPPs is achieved when L_y = 160 nm.

We can also evaluate the multi-wavelength response of the PNJs produced with this structure. For this purpose, the dimensions of the cuboid are fixed to $L_x = L_z = \lambda_0$ = 1550 nm and L_y = 160 nm, which correspond to the best performance, as discussed above. The results of the refractive index contrast particularized to the case L_y = 160 nm is shown in Fig. 4.24(a). Here the three working zones depending on the value of *c* are clearly observed: (i) λ > 1600 nm, $c <$ 1.3 so the PNJ is detached from the cuboid; (ii) 1050 < λ < 1600 nm where 1.3 < c < 1.75 and the PNJ is produced at the surface of the cuboid, as demonstrated in Fig. 4.23; (iii) λ < 1050 nm where c > 1.75 and therefore the PNJ is inside the cuboid. The case of region (ii) has been already evaluated in Fig. 4.23, thus the efforts are centered here in the evaluation of the PNJ performance in zones (i) and (iii).

The Simulation results of the power distribution on the *xz*-plane at λ_1 = 800 nm and λ_2 = 1900 nm are shown in Fig. 4.24(b,c). Also, the normalized magnitude of the electric field along the propagation axis for each wavelength is shown in panels (d) and (e), respectively. It can be observed that the PNJ is produced inside the cuboid at λ_1 = 800 nm and therefore a blurred focus is generated at the output of the structure, as expected [HEIF 09]. The opposite behavior is observed at λ_2 = 1900 nm where the PNJ is moved far away from the output surface of the cuboid ($FL = 0.2\lambda_2$). For this

case a transversal resolution $FWHM_x = 0.97\lambda_2$ is obtained with an enhancement of ~1.82.

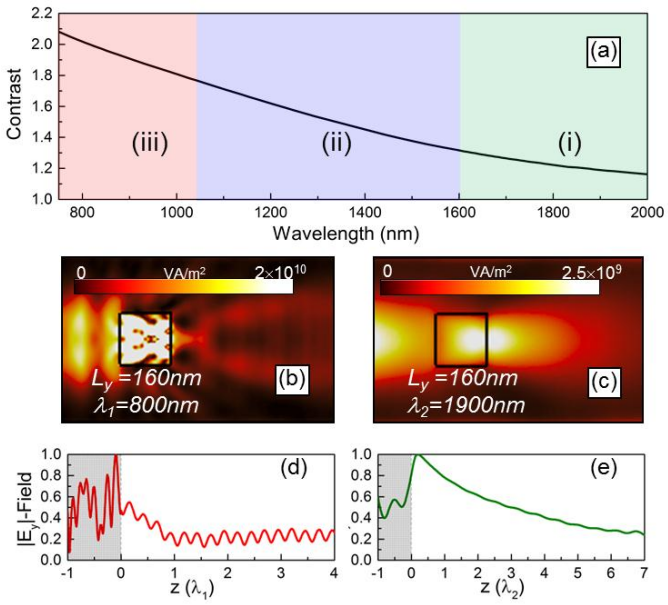

Figure 4.24. (a) Analytical refractive index contrast between region II and I for a 3D dielectric cuboid with $L_x = L_z = 1550$ nm and $L_y = 160$ nm. The regions where the contrast is $c < 1.3$, $1.3 < c < 1.75$ and $c > 1.75$ are marked as zones (i), (ii) and (iii), respectively. Numerical results of the power distribution on the *xz*-plane (b,c) along with the normalized magnitude (relative to the maximum of each case) of the electric field E_y along the *z*-axis (d,e) at the working wavelength of $\lambda_1 = 800$ nm (b,d) and $\lambda_2 = 1900$ nm (c,e).

Finally, we evaluate the performance of the PNJ when the lateral dimensions of the cuboids are changed. The height of the cuboid is fixed as $L_y = 160$ nm and the study is done at the same operation wavelength (1550 nm). The numerical results of the magnitude of the electric field along the propagation axis are shown in the first row of Fig. 4.25 for the cases when the lateral dimensions of the cuboid (L_x and L_z) are scaled by a factor $\alpha = 1.25$, $\alpha = 1.5$ and $\alpha = 2$ ($\alpha = 1$ corresponds to $L_x = L_z = 1550$ nm). The PNJ is moved far from the surface of the cuboid as the lateral dimensions are increased. In each of the considered cases the *FL* is $1.35\times10^{-3}\lambda_0$, $5.41\times10^{-3}\lambda_0$ and $0.168\lambda_0$, respectively, in good agreement with the previous findings using a plane wave excitation (see Fig. 4.4). The magnitude of the electric field along the transversal axis at each *FL* is also shown in the second row of Fig. 4.25. It is clearly observed that

the transversal resolution is strongly affected by an increment of the size of the cuboid, resulting in a wider focus for higher values of α.

The results of the *FL*, $FWHM_x$ and enhancement at the *FL* for the structures here studied along with the case with $\alpha = 1$ are gathered in Table 4.4. The $FWHM_x$ evolves from $0.68\lambda_0$ to $1.638\lambda_0$ when the cuboid is scaled from $\alpha = 1$ to $\alpha = 2$. The enhancement at the *FL* is also reduced as the dimensions of the cuboid are increased and has a minimum value of 2.37 for $\alpha = 2$. Note that this is still a relatively large enhancement considering that the SPPs are not strongly coupled to the surface of the metal film at the working wavelength. However, in order to work with the best quality of the PNJ in terms of the *FL*, $FWHM_x$ and enhancement, the lateral dimensions of the cuboid should be of the order of the operational wavelength, as it can be corroborated in the same table.

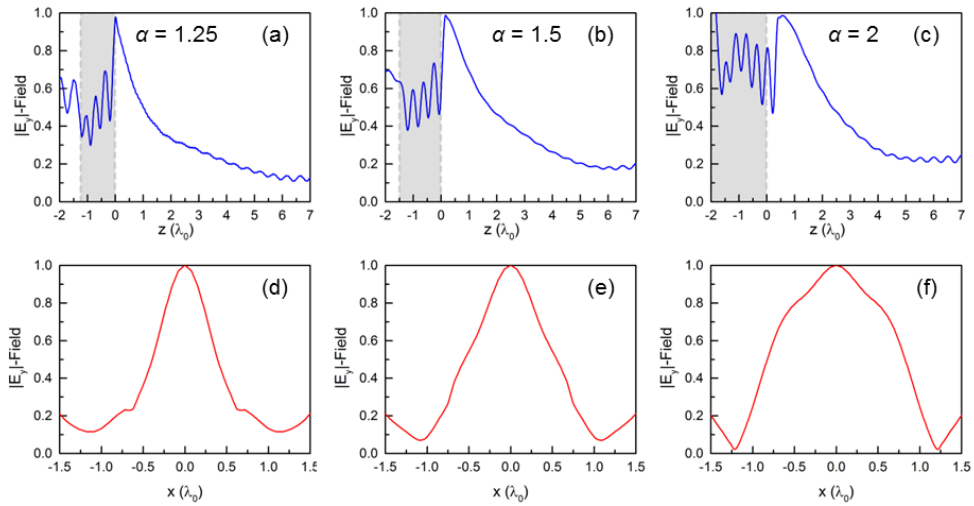

Figure 4.25. Numerical results of the magnitude of the electric field along the *z* (a-c) and *x* (d-f) axis (at each *FL*) when the dimensions of the 3D dielectric cuboid are scaled by a factor α equal to: 1.25 (a,d), 1.5 (b,e) and 2 (c,f).

Scale Factor (α)	FL	$FWHM_x$ (λ_0)	Enhancement
1	0	0.68	5.05
1.25	1.35×10^{-3}	0.78	4.50
1.5	5.41×10^{-3}	1.096	3.95
2	0.168	1.638	2.37

Table 4.4. Numerical results of the PNJ performance at the wavelength of 1550 nm for a dielectric cuboid with height L_y = 160 nm and lateral dimensions scaled by a factor α.

4.2.3 Backscattering enhancement

The sensing capability of PNJs has been demonstrated in section 4.1.2 using 3D cuboids under planewave illumination via the backscattering enhancement. The aim here is to shown that the photonic structure here proposed might be also used to detect small metal particles.

A schematic representation of the system is shown in Fig. 4.26(a). The dimensions of the dielectric cuboid are $L_x = L_z = \lambda_0 = 1550$ nm and $L_y = 160$ nm. An electric probe is used at the back of the dielectric cuboid to register the field. A metallic silver (Ag) sphere of radius $0.1\lambda_0$ with a dispersive dielectric permittivity following the Johnson & Christy experimental data [JOHN 72] is introduced within the PNJ region and moved along the optical *z* axis.

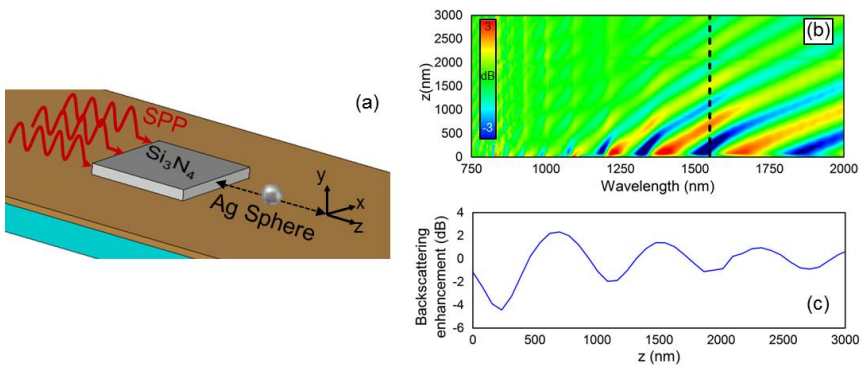

Figure 4.26. (a) Schematic representation of the configuration used to evaluate the backscattering enhancement of a silver sphere. (b) Numerical results of the backscattering enhancement spectra as a function of the position of the sphere along the propagation axis. (c) Backscattering enhancement extracted from the black dashed line of panel b corresponding to the operational telecom wavelength of 1550 nm.

With this configuration, the numerical results of the backscattering enhancement (calculated as the ratio between the received electric field with and without sphere) as a function of wavelength (750 - 2000 nm) and sphere position along the *z* axis [0 - 3000 nm with a step of 77.5 nm ($0.05\lambda_0$)] are shown in Fig. 4.26(b). There are oscillations of the backscattering magnitude that depend on the operational wavelength, in good agreement with previous results under plane wave illumination. Moreover, it is clearly shown that for wavelengths below 1300 nm, an enhancement of

backscattering is no longer possible since the PNJ falls inside the dielectric cuboid and the intensity of SPPs that reach the sphere is reduced, as demonstrated in Fig. 4.24.

To better assess the performance, the backscattering enhancement at 1550 nm [shown as a dashed line in Fig. 4.26(b)] as a function of the position of the sphere is shown in Fig. 4.26(c). The same oscillatory pattern with period of $\sim 0.6\lambda_0$ as for the plane wave case is obtained and the first maximum happens at $z = 0.45\lambda_0$. At this position, an enhancement of 2.44 dB is obtained, demonstrating the possibility to use this structure for sensing applications. Moreover, it is important to note that an interesting advantage of this structure compared with the structure under plane wave illumination is that the metal film provides a platform to place the particle within the PNJ region. Hence the experimental alignment of the particle with the 3D dielectric cuboid is comparatively easier.

4.2.4 Increasing SPP propagation using a chain of dielectric cuboids

As discussed before, the SPPs are not strongly coupled to the metal surface at the telecom wavelength of 1550 nm given that the effective index of the SPPs (1.0043) is very close to the value in vacuum. The aim of this section is to show that an array of periodically spaced cuboids can be used to extend the propagation distance of SPPs even at this wavelength.

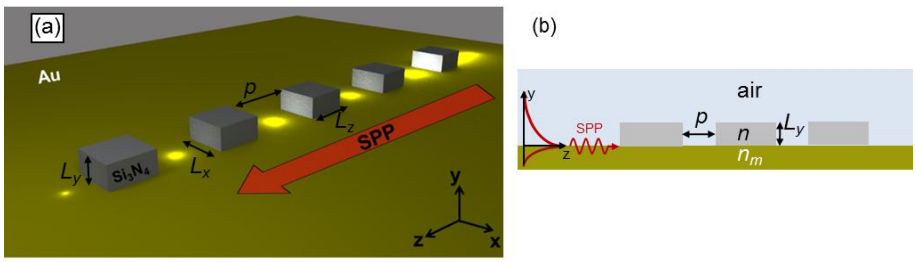

Figure 4.27. Schematic representation of the cuboid chain: (a) perspective and (b) lateral view. The dielectric cuboids have dimensions $L_x \times L_y \times L_x$ and are periodically placed along the z axis with an air gap p between them.

The chain of 3D dielectric cuboids considered here is schematically shown in Fig. 4.27. It consists of an array of 6 cuboids with dimensions $L_x \times L_y \times L_z$ separated by a gap p placed on top of a metal layer of gold. The same materials as before are used for the metal and cuboids. Also, the dimensions of the metal film are selected as 100 nm in order to consider it as a semi-infinite metal and simplify the study of the structure.

Finally, the whole structure is immersed in air. With this configuration, the SPPs are excited from the back of the chain (using the same narrow waveguide as shown in Fig. 4.20) and propagate along the *z* axis. The numerical simulations are also done using the transient solver of the commercial software CST Microwave Studio®. As it can be observed in Fig. 4.27(b), the same two regions of SPP propagation can be distinguished, namely: with and without cuboids. Therefore, the same procedure is followed in order to increase the propagation distance of SPPs by changing the height of the cuboids and also the air-gap between them.

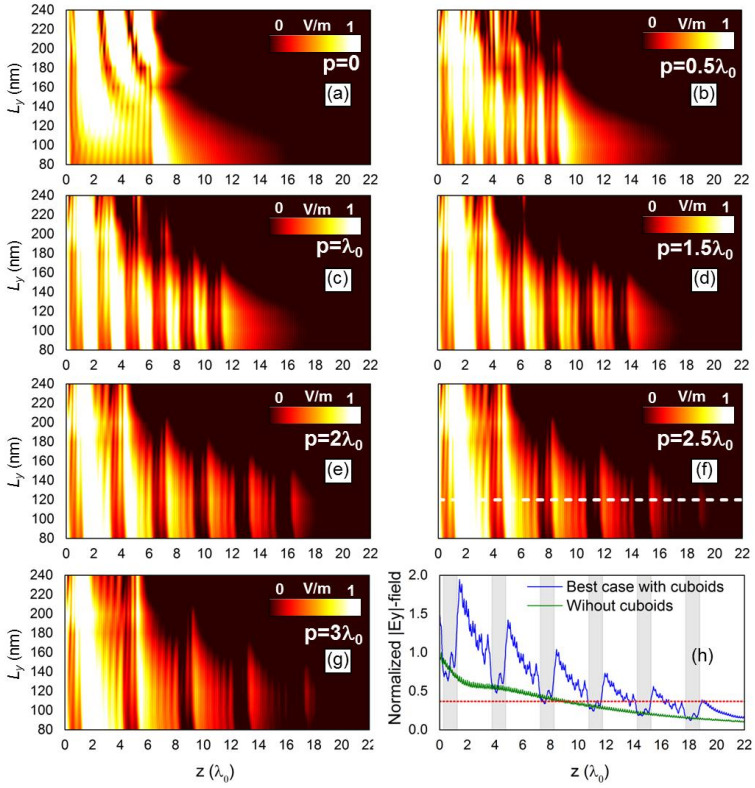

Figure 4.28. Normalized magnitude of the E_y-field as a function of the propagation *z*-axis and height l_y of the cuboids when the distance between them is: (a) $p = 0$, (b) $p = 0.5\lambda_0$, (c) $p = \lambda_0$, (d) $p = 1.5\lambda_0$, (e) $p = 2\lambda_0$, (f) $p = 2.5\lambda_0$ and (g) $p = 3\lambda_0$. (h) Results of the normalized magnitude of the electric field along the propagation axis at the surface of the metal for the optimal case, $p = 2.5\lambda_0$ and $L_y = 120$ nm [extracted from the dashed line shown in panel (f)] (blue curve) and a flat metal film (green curve). The red curve corresponds to a decay of 1/e with respect to the amplitude of the incident SPP at the input. The 3D cuboids are also shown as grey blocks.

By using the lateral dimensions $L_x = L_z = 1550$ nm the performance of the chain is evaluated for different values of p ranging from 0 to $3\lambda_0$ with a step of $0.5\lambda_0$ and a height of cuboids L_y varying from 80 nm to 240 nm with a step of 20 nm. As it has been demonstrated before, this dimension is critical in the performance of the PNJ, as it directly allows tuning the effective refractive index of the region where the cuboid is present. Contour plots showing the magnitude of the E_y-field at the design wavelength as a function of the propagation z axis and l_y are shown in Fig. 4.28(a-g) for each value of p under study. All the results have been normalized to the incident electric field amplitude at the back of the structure. This figure gives us all the information to evaluate the performance of the chain. Let us first study the influence of the gap between the cuboids. The worst case is observed when $p = 0$ where the decay of the SPPs is stronger compared with the other values. This is an expected result, as this corresponds to touching cuboids hence only one PNJ is excited at the end of the structure ($z \sim 7\lambda_0$). As the cuboids are taken far apart, several peaks of high electric field concentration appear between cuboids. These peaks are the PNJs excited by each cuboid. The propagation length increases as p is increased because the PNJ excited by each cuboid produces an enhancement of the electric field at the *FL*. Note that this propagation length increases until it reaches a maximum at $p = 2.5\lambda_0$, and from there on it decreases again. The best case is when $p = 2.5\lambda_0$ and $L_y = 120$ nm [highlighted with a dashed white line in Fig. 4.28(f)]. The magnitude of the E_y-field is plotted in Fig. 4.28(h) along the propagation axis for this optimum case compared to a flat metal film. The SPP propagation length is $\sim 19\lambda_0$, i.e. it is enhanced by a factor greater than two compared to the case without the cuboids (which reached only $\sim 9\lambda_0$).

When the height of the cuboids is changed, it can be observed that in all cases the longest SPPs propagation lengths are obtained for values of L_y between approximately 100 nm and 140 nm. This performance can be easily explained in terms of the effective index, n_{SPP}. For this analysis we concentrate on $p = 2.5\lambda_0$, which can be considered representative of all the studied cases. The calculated power distributions on the surface of the metal film for different values of L_y are shown in Fig. 4.29(a-e). Then, the propagation length for all the values of L_y considered are extracted and the results are plotted in Fig. 4.29(f) along with the analytical values of the effective index contrast between the regions with and without cuboids. For small height values (L_y = 80 nm; 100 nm) the contrast is close to 1 and hence, the PNJs are produced far away from the output surface of the cuboids, giving as a result a poor illumination of the neighboring cuboid in the chain. On the other hand, for large height values ($L_y > 120$ nm) the index contrast increases as L_y is increased. This implies that the PNJs are produced inside of the cuboids, as observed in Fig. 4.29(d,e). Therefore, the excitation of consecutive cuboids is not efficient and the propagation length is reduced.

The longest propagation length is obtained when $L_y = 120$nm, in which c is ~1.2. Note that with this value the PNJs are produced very near but slightly away from

output surface of the cuboids (approximately at $0.16\lambda_0$) as can be observed in Fig. 4.29(b). Since the PNJs are not just at the output surface of the cuboids, it allows obtaining the optimal illumination of the next cuboids of the chain. Note that this value of L_y is different from the optimal case we found in previous sections (160 nm). Recall that there the aim was to produce the PNJ just at the output surface of a single cuboid and not to extend the SPP propagation. Anyway, it is interesting to highlight that the SPP propagation distance is enhanced for a wide range of values of L_y. This is an important feature in terms of the allowed tolerances for fabrication purposes. If 120 nm is taken as a reference, the height of the cuboids may be fabricated with a tolerance of ~40 nm without strongly altering the SPP propagation distance.

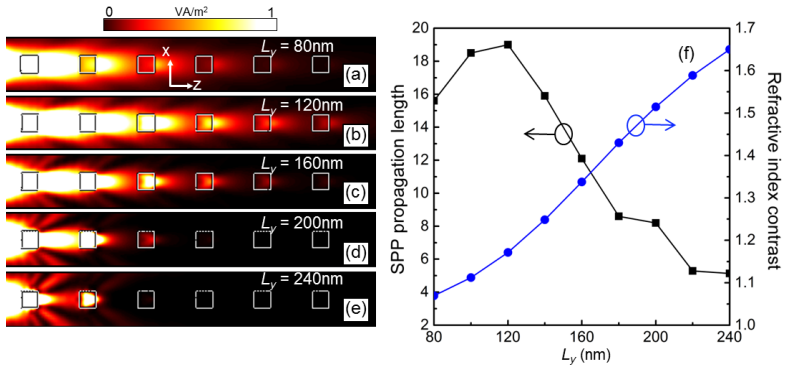

Figure 4.29. Power distribution on the *xz*-plane just at the surface of the metal for the case of 3D dielectric cuboids placed periodically with an air gap of $p = 2.5\lambda_0$ and height: (a) L_y = 80 nm, (b) L_y = 120 nm,(c) L_y = 160 nm,(d) L_y = 200 nm and (e) l_y = 240 nm. (f) Numerical results of SPP propagation length (black curve) and index contrast (blue curve) as a function of the cuboid height.

Chapter 5

Plasmonic nanoantennas excited by localized emitters: A study based on the conformal transformation technique

The recent advances in nanofabrication and plasmonics research have made possible the design of metallic structures with nanometer features that are able to strongly interact with light [MAIE 04]. This has led to the realization of nanophotonics systems allowing the coupling between LSP modes and quantum emitters [LIU 09a], [CHEN 12], [LERE 12], [STRA 16], [LIN 15], [COLE 16]. An interesting feature is that this interaction is produced in a similar fashion as transmission lines and antennas do with microwaves [EGGL 15]. Thus, one could think that microwave engineering techniques may be applicable also in photonic devices like nanoantennas. Breaking the diffraction limit of classical optics, these nanometric devices enable near-to-far-field coupling (and vice versa) of optical signals with unprecedented efficiency [GIAN 11]. This nanoscale control over the propagation and confinement of visible light has found applications in different areas such as spectroscopy [HATA 10], biosensing [NIE 97], [ANKE 08], photovoltaics [ATWA 10], photodetection [KNIG 11] and nonlinear optics [AOUA 14].

Similar to radio and microwave antennas, the EM response of nanoantennas is governed by the material properties and their geometries. However, since metals have a more complex description at visible frequencies, the modeling and optimization of these nano-structures are more challenging from a theoretical point of view. Therefore, an analytical treatment can only be found for some simple geometries such as cylinders, spheres and cuboids [BOHR 07], [MASS 13]. Just a few years ago, a quasi-analytical method of more complex nano-devices has been developed using transformation optics [LUO 10], [PEND 12], [FERN 12], [PEND 13], [AUBR 13] which is similar to conformal mapping [DUHA 57], [CARR 58], [RAMO 94], [HEIB 75] but working exactly at the level of Maxwell Equations [XU 14].

In this chapter, it is shown a full analytical description based on transformation optics of a localized emitter (modelled as a point dipole) in an arbitrary position close to bowtie and tripod nanoantennas. It is shown how these nano-structures can be mapped into a multiple parallel-plate transmission line problem with analytical solution, allowing explaining the performance of the original problem (validated using full-wave simulations) and gaining at the same time physical insight of the underlying mechanism. The results here discussed pave the way for a full analytical description of realistic scenarios where quantum dots or dye molecules are placed near a metallic bowtie/tripod nanoantenna, filling the gap of design methodologies for nano-devices.

5.1 Bowtie nanoantenna

Bowtie nanoantennas are composed by two triangular-shaped metal nanoparticles facing against each other, connected at their apexes or separated by a nanometric gap. This is one of the most thoroughly investigated structures in the literature. Experimental and numerical reports have shown the suitability of this antenna and its variations for the implementation of optical receivers and transmitters [YU 07], [KINK 09], [HATA 10], [KO 11], [NAVA 12a], [AOUA 12], [SIVI 13], [ROXW 14], [HENT 16]. Compared to the other geometries examined under transformation optics such as crescents and cylindrical dimers [AUBR 13], bowtie nanoantennas provide stronger degree of field localization and enhancement. This benefits and it is indeed essential for a myriad of plasmonic applications: for instance, the stronger the local field, the brighter the fluorescence/harmonic-signal is. In this section, these nano-structures are analytically treated using transformation optics. They are studied in terms of the non-radiative decay spectra (power absorbed under dipole illumination, P_{abs}) and the LSP modes supported depending on the geometrical parameters of the nanoantenna.

5.1.1 Applying the conformal transformation to the bowtie nanoantenna

The schematic representation of the problem under study is shown in Fig. 5.1(a). It consists in the coupling of a line dipole (nanoemitter) with an arbitrary orientation close to a bowtie nanoantenna made of silver. As observed in the inset of the same figure, the tip of the bowtie nanoantenna is considered concave in order to ease the conformal mapping. The dipole is located on the x' axis 1 nm away from the center of the bowtie. This is indeed a more realistic situation than placing the dipole inside the gap, since nanometer-size gaps are in general inaccessible for nano- and micrometer-size emitters. The nanoantenna is defined by the arm length, $L_1'+L_2'$, the arm angle,

θ', and the gap between arms. The total length of the bowtie (l') is defined by the arm length along with the gap. Here, the study is restricted considering bowtie geometries much smaller than the illumination wavelength in order to work in the quasi-static approximation (see Chapter 1). In this scenario, magnetic and electric fields are decoupled, and the latter can be fully described by an electrostatic potential satisfying Laplace's equation. For simplicity, the bowtie geometries are embedded in vacuum, and the dielectric function of Ag is taken from Palik's experimental data [PALI 85].

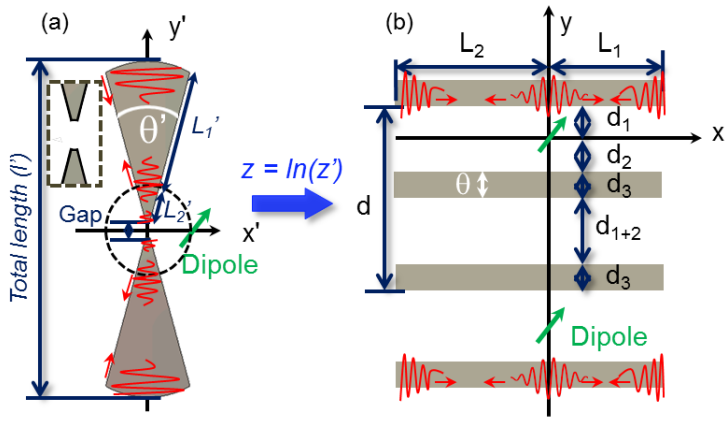

Figure 5.1. Schematic representation of a metallic bowtie nanoantenna with a gap on its center (a) along with the transformed geometry (b). The nanoantenna is illuminated with a dipole placed at (x', y') = (1 nm, 0) (green arrow)

This system operation can be qualitatively explained with a simple heuristic analysis. The radiation from the localized oscillating dipole (an atom or a quantum dot in an excited state, for instance) is coupled to the different LSP modes supported by the bowtie nanoantennas. This pumped electromagnetic energy is eventually dissipated due to metal absorption, i.e., non-radiative damping. Given the subwavelength size of the bowtie, radiation loss, i.e., radiative damping, is negligible. The strength of the coupling, and thus, the non-radiative damping, depends on the position of the dipole within the field distribution of the LSP modes.

In general, the problem of finding the optimum set of parameters for a specific experiment is addressed by performing only numerical computations [LIN 15]. An alternative to reduce the computational requirements is devising analytical solutions. Here, the problem is transformed into a geometry that can be easily solved analytically, simplifying the calculation and analysis of the original problem.

The bowtie can be transformed into the multiple parallel-plate transmission line geometry shown in Fig. 5.1(b) by applying the following conformal transformation:

$$z = \ln(z') \tag{5.1}$$

where $z = x+iy$ and $z' = x'+iy'$ are the spatial coordinates in the transformed and original frame, respectively. Through this conformal transformation, circular (radial) lines in the original geometry are mapped into vertical (horizontal) lines in the transformed frame [LUO 10], [NAVA 12a].This results in a multi-slab geometry with the dimensions of all metal slabs as L_1+L_2 and θ (= d_3) along the x and y axis, respectively. The original dipole is meanwhile converted into an array of dipoles with the same strength placed along the y axis with a periodicity 2π, i.e., at ($x = 0$, $y = 2\pi m$), where m is an integer.

By looking at the transformed geometry, a qualitative and quantitative (described in the following sections) understanding of the LSP modes supported by the bowtie nanoantenna can be achieved. As it is shown in Fig. 5.1(b), the dipole array emission triggers SPPs propagating along both positive and negative directions of x in the multi-slab geometry; which are mapped into the plasmonic modes excited by the single emitter along both arms of the bowtie nanoantenna. Because of the finite length of the slab/bowtie-arms, these SPPs are reflected back and forth between the two ends of the structure, forming a standing wave pattern that gives rise to the LSP modes. Hence, the continuous SPP spectrum of an infinite slab/bowtie is converted into a finite set of discrete LSPs characterized by the mode order n, as it will be demonstrated next [LUO 12], [LUO 12a].

The 2D conformal transformation ensures that the material properties remain unchanged, unlike the 3D counterpart [FERN 12], [PEND 12], [PEND 13], [AUBR 13]. Also, it preserves the potential in each coordinate system [LUO 12]:

$$\phi(x,y) = \phi'(x',y') \tag{5.2}$$

where ϕ and ϕ' are the electrostatic potentials in the transformed and original frames, respectively. Therefore, the x' and y' components of the electric field distribution ($E'_{x'}$ and $E'_{y'}$, respectively) in the original geometry can be directly deduced from the above equation as [AUBR 11], [LUO 12a]:

$$E'_{x'} = -\frac{\partial\phi'}{\partial z'}\frac{\partial z}{\partial x'} - \frac{\partial\phi'}{\partial z'^*}\frac{\partial z'^*}{\partial x'} = -\frac{\partial\phi'}{\partial z'} - \frac{\partial\phi'}{\partial z'^*} \tag{5.3}$$

$$E'_{y'} = -\frac{\partial\phi'}{\partial z'}\frac{\partial z}{\partial y'} - \frac{\partial\phi'}{\partial z'^*}\frac{\partial z'^*}{\partial y'} = -i\frac{\partial\phi'}{\partial z'} + i\frac{\partial\phi'}{\partial z'^*} \tag{5.4}$$

Thus, by solving the problem in the multi-slab frame, the bowtie scenario is solved straightforwardly. Notice that, in the multi-slab geometry, the field distribution along the y direction (E_y) actually represents the azimuthal component of the electric field ($E'_{\varphi'}$) in the bowtie scenario, which can be calculated from the x' and y' components

(Eqs. 5.3-5.4) as $E'_{\varphi'} = -E'_{x'}\sin(\varphi') + E'_{y'}\cos(\varphi')$, with $\varphi' = \tan^{-1}(y'/x')$. On the other hand, the field distribution along the x direction (E_x) is directly transformed into the radial component of the electric field in the original geometry ($E'_{\rho'}$), which can be obtained as $E'_{\rho'} = E'_{x'}\cos(\varphi') + E'_{y'}\sin(\varphi')$. From here on, the azimuthal and radial components will be used to represent the electric field distribution in the bowtie nanoantennas here studied.

5.1.2 Quasi-static solution

Now that the general features of the conformal mapping have been introduced, let us apply it to the bowtie nanoantenna of Fig. 5.1. As mentioned before, taking into account that the dimensions of the nanoantenna are sufficiently smaller than the operational wavelength ($l' << \lambda_0$), the near-field approximation can be used and thus, the electric field can be fully described by an electrostatic potential satisfying Laplace's equation. As it is known, in the multi-slab geometry shown in Fig. 5.1(b), it is possible to excite surface plasmon modes in both transversal and longitudinal directions, with their propagation along the x and y axis, respectively. However, the interest here is focused in the derivation of the surface plasmon modes excited in the multi-slab geometry when $L_1 + L_2 >> \theta$. Thereby, the contribution of the longitudinal LSP modes (i.e., those with phase variation along y) can be neglected and assume that the excited LSP modes are mainly due to the transversal modes (i.e., those with phase variation along x). Based on this, the electrostatic potentials outside and inside the metal strips in Fig. 5.1(b) can be calculated as a sum of all discrete transverse modes, as follows:

$$\sum_k \left[\frac{1}{1-e^{2ik(L_1+L_2)+2i\Delta\varphi}} \left(e^{ikx} + e^{-ikx+2ikL_1+i\Delta\varphi}\right)\left(A_+ e^{-ky} + B_+ e^{-ky} + B_- e^{ky}\right)\right], 0 < y < d_1 \tag{5.5}$$

$$\sum_k \left[\frac{1}{1-e^{2ik(L_1+L_2)+2i\Delta\varphi}} \left(e^{ikx} + e^{-ikx+2ikL_1+i\Delta\varphi}\right)\left(A_- e^{ky} + B_+ e^{-ky} + B_- e^{ky}\right)\right], -d_2 < y < 0 \tag{5.6}$$

$$\sum_k \left[\frac{1}{1-e^{2ik(L_1+L_2)+2i\Delta\varphi}} \left(e^{ikx} + e^{-ikx+2ikL_1+i\Delta\varphi}\right)\left(E_+ e^{-ky} + E_- e^{ky}\right)\right], -(d_1+2d_2+d_3) < y < -(d_2+d_3) \tag{5.7}$$

$$\sum_k \left[\frac{1}{1-e^{2ik(L_1+L_2)+2i\Delta\varphi}} \left(e^{ikx} + e^{-ikx+2ikL_1+i\Delta\varphi}\right)\left(C_+ e^{-ky} + C_- e^{ky}\right)\right], -(d_1+2d_2+2d_3) < y < -(d_1+2d_2+d_3) \tag{5.8}$$

$$\sum_k \left[\frac{1}{1-e^{2ik(L_1+L_2)+2i\Delta\varphi}} \left(e^{ikx} + e^{-ikx+2ikL_1+i\Delta\varphi}\right)\left(D_+ e^{-ky} + D_- e^{ky}\right)\right], -(d_2+d_3) < y < -d_2 \tag{5.9}$$

where $\Delta\varphi$ is the correction of phase applied to the bowtie nanoantenna to take into account the complex reflection experienced by the surface plasmon waves at the extremes of the nanoparticle, A_+ and A_- are the expansion coefficients of the incident potential, B_+ and B_- are the coefficients related to the scattering potential in the region where the dipole is placed ($d_2 < y < d_1$), E_+ and E_- are the coefficients associated to the scattering potential in the region where a dipole is absent ($d_2 + d_1$), C_+, C_-, D_+ and D_- are those corresponding to the potential inside the metal strips (d_3), and k is the wave vector of the transverse LSP modes calculated as:

$$k = \frac{n\pi - \Delta\varphi}{L_1 + L_2} \tag{5.10}$$

with n = 1, 2, 3,… representing the discrete transverse LSP mode. The coefficients associated with the incident potential can be obtained by expanding the dipole potential along the x direction using a FT:

$$A\pm = \frac{\pm p_y - ip_x \,\mathrm{sgn}(k)}{2\varepsilon_0} \tag{5.11}$$

where p_y and p_x are the components of the dipole moment along the x and y directions, respectively, and ε_0 is the permittivity in vacuum. The other eight unknown coefficients B_+, B_-, C_+, C_-, D_+, D_-, E_+ and E_- can be solved by applying boundary conditions at each interface of Fig. 5.1(b). First, the condition of conservation of the parallel component of the electric field at the boundaries d_2, d_2+d_3, d_1 and d_1+2d_2+2d_3 is applied, as follows:

$$A_- e^{-kd_2} + B_+ e^{kd_2} + B_- e^{-kd_2} = D_- e^{-kd_2} + D_+ e^{kd_2} \tag{5.12}$$

$$E_+ e^{k(d_2+d_3)} + E_- e^{-k(d_2+d_3)} = D_- e^{-k(d_2+d_3)} + D_+ e^{k(d_2+d_3)} \tag{5.13}$$

$$A_+ e^{-kd_1} + B_+ e^{-kd_1} + B_- e^{kd_1} = C_- e^{-k(d_1+2d_2+2d_3)} + C_+ e^{k(d_1+2d_2+2d_3)} \tag{5.14}$$

$$E_+ e^{k(d_1+2d_2+d_3)} + E_- e^{-k(d_1+2d_2+d_3)} = C_- e^{-k(d_1+2d_2+d_3)} + C_+ e^{k(d_1+2d_2+d_3)} \tag{5.15}$$

Also, the condition of conservation of the normal component of the displacement field at the same boundaries as the above equations is applied:

$$A_- e^{-kd_2} - B_+ e^{kd_2} + B_- e^{-kd_2} = \varepsilon D_- e^{-kd_2} - \varepsilon D_+ e^{kd_2} \tag{5.16}$$

$$E_+ e^{k(d_2+d_3)} - E_- e^{-k(d_2+d_3)} = -\varepsilon D_- e^{-k(d_2+d_3)} + \varepsilon D_+ e^{k(d_2+d_3)} \tag{5.17}$$

$$A_+e^{-kd_1} + B_+e^{-kd_1} - B\_e^{kd_1} = -\varepsilon C\_e^{-k(d_1+2d_2+2d_3)} + \varepsilon C_+e^{k(d_1+2d_2+2d_3)} \tag{5.18}$$

$$-E_+e^{k(d_1+2d_2+d_3)} + E\_e^{-k(d_1+2d_2+d_3)} = \varepsilon C\_e^{-k(d_1+2d_2+d_3)} - \varepsilon C_+e^{k(d_1+2d_2+d_3)} \tag{5.19}$$

where ε is the permittivity of the metal used in the structure (silver in this case). The solutions of the potentials in the real space for the region where there is ($d_2 < y < d_1$) and there is not a dipole ($d_2 + d_1$), ϕ_1^s and ϕ_2^s, respectively, can be then obtained by applying an inverse FT to the induced potentials:

$$\phi_1^s = \frac{1}{2\varepsilon_0(L_1+L_2)} \sum_n \left\langle \Theta \begin{Bmatrix} p_x\left[\sin(kx) - \sin(kx - 2kL_1 - \Delta\varphi)\right] + \\ p_y\left[\cos(kx) + \cos(kx - 2kL_1 - \Delta\varphi)\right] \end{Bmatrix} \left(B_+e^{-ky} + B\_e^{ky}\right) \right\rangle \tag{5.20}$$

$$\phi_2^s = \frac{1}{2\varepsilon_0(L_1+L_2)} \sum_n \left\langle \Theta \begin{Bmatrix} p_x\left[\sin(kx) - \sin(kx - 2kL_1 - \Delta\varphi)\right] + \\ p_y\left[\cos(kx) + \cos(kx - 2kL_1 - \Delta\varphi)\right] \end{Bmatrix} \left(E_+e^{-ky} + E\_e^{ky}\right) \right\rangle \tag{5.21}$$

Similarly, the potentials inside both metallic slabs (ϕ_1^m and ϕ_1^m) are:

$$\phi_1^m = \frac{1}{2\varepsilon_0(L_1+L_2)} \sum_n \left\langle \Theta \begin{Bmatrix} p_x\left[\sin(kx) - \sin(kx - 2kL_1 - \Delta\varphi)\right] + \\ p_y\left[\cos(kx) + \cos(kx - 2kL_1 - \Delta\varphi)\right] \end{Bmatrix} \left(C_+e^{-ky} + C\_e^{ky}\right) \right\rangle \tag{5.22}$$

$$\phi_2^m = \frac{1}{2\varepsilon_0(L_1+L_2)} \sum_n \left\langle \Theta \begin{Bmatrix} p_x\left[\sin(kx) - \sin(kx - 2kL_1 - \Delta\varphi)\right] + \\ p_y\left[\cos(kx) + \cos(kx - 2kL_1 - \Delta\varphi)\right] \end{Bmatrix} \left(D_+e^{-ky} + D\_e^{ky}\right) \right\rangle \tag{5.23}$$

where Θ is defined as:

$$\Theta = \frac{1}{\left\{1 - \cos\left[2k\left(L_1+L_2\right) + 2\Delta\varphi\right] - \sin\left[2k\left(L_1+L_2\right) + 2\Delta\varphi\right]\right\}} \tag{5.24}$$

Finally, the x and y components of the electric field can be calculated by simply differentiating the potentials:

$$E_{1x}^s = \sum_n - \frac{k}{2\varepsilon_0(L_1+L_2)} \left\langle \begin{Bmatrix} p_x\left[\cos(kx) - \cos(kx - 2kL_1 - \Delta\varphi)\right] \\ -p_y\left[\sin(kx) + \sin(kx - 2kL_1 - \Delta\varphi)\right] \end{Bmatrix} \left(B_+e^{-ky} + B\_e^{ky}\right) \right\rangle \tag{5.25}$$

$$E_{2x}^{s}=\sum_{n}-\frac{k}{2\varepsilon_0(L_1+L_2)}\left\langle\begin{Bmatrix}p_x\left[\cos(kx)-\cos(kx-2kL_1-\Delta\varphi)\right]\\-p_y\left[\sin(kx)+\sin(kx-2kL_1-\Delta\varphi)\right]\end{Bmatrix}\left(E_{+}e^{-ky}+E_{-}e^{ky}\right)\right\rangle \tag{5.26}$$

$$E_{1x}^{m}=\sum_{n}-\frac{k}{2\varepsilon_0(L_1+L_2)}\left\langle\begin{Bmatrix}p_x\left[\cos(kx)-\cos(kx-2kL_1-\Delta\varphi)\right]\\-p_y\left[\sin(kx)+\sin(kx-2kL_1-\Delta\varphi)\right]\end{Bmatrix}\left(C_{+}e^{-ky}+C_{-}e^{ky}\right)\right\rangle \tag{5.27}$$

$$E_{2x}^{m}=\sum_{n}-\frac{k}{2\varepsilon_0(L_1+L_2)}\left\langle\begin{Bmatrix}p_x\left[\cos(kx)-\cos(kx-2kL_1-\Delta\varphi)\right]\\-p_y\left[\sin(kx)+\sin(kx-2kL_1-\Delta\varphi)\right]\end{Bmatrix}\left(D_{+}e^{-ky}+D_{-}e^{ky}\right)\right\rangle \tag{5.28}$$

$$E_{1y}^{s}=\sum_{n}-\frac{k}{2\varepsilon_0(L_1+L_2)}\left\langle\begin{Bmatrix}p_x\left[\sin(kx)-\sin(kx-2kL_1-\Delta\varphi)\right]+\\p_y\left[\cos(kx)+\cos(kx-2kL_1-\Delta\varphi)\right]\end{Bmatrix}\left(-B_{+}e^{-ky}+B_{-}e^{ky}\right)\right\rangle \tag{5.29}$$

$$E_{2y}^{s}=\sum_{n}-\frac{k}{2\varepsilon_0(L_1+L_2)}\left\langle\begin{Bmatrix}p_x\left[\sin(kx)-\sin(kx-2kL_1-\Delta\varphi)\right]+\\p_y\left[\cos(kx)+\cos(kx-2kL_1-\Delta\varphi)\right]\end{Bmatrix}\left(-E_{+}e^{-ky}+E_{-}e^{ky}\right)\right\rangle \tag{5.30}$$

$$E_{1y}^{m}=\sum_{n}-\frac{k}{2\varepsilon_0(L_1+L_2)}\left\langle\begin{Bmatrix}p_x\left[\sin(kx)-\sin(kx-2kL_1-\Delta\varphi)\right]+\\p_y\left[\cos(kx)+\cos(kx-2kL_1-\Delta\varphi)\right]\end{Bmatrix}\left(-C_{+}e^{-ky}+C_{-}e^{ky}\right)\right\rangle \tag{5.31}$$

$$E_{2y}^{m}=\sum_{n}-\frac{k}{2\varepsilon_0(L_1+L_2)}\left\langle\begin{Bmatrix}p_x\left[\sin(kx)-\sin(kx-2kL_1-\Delta\varphi)\right]+\\p_y\left[\cos(kx)+\cos(kx-2kL_1-\Delta\varphi)\right]\end{Bmatrix}\left(-D_{+}e^{-ky}+D_{-}e^{ky}\right)\right\rangle \tag{5.32}$$

Here, the complete solution of each constant is not shown because of their complexity. Hence, the coefficients are used in order to reduce the equations of potentials and electric field. However, these solutions can be directly obtained either manually or using a mathematic software.

Since the energy is conserved in the transformation, the power dissipation is the same in both frames. Hence, the non-radiative decay of the nanoemitter can be deduced by calculating the power dissipated in the multi-slab geometry. This can be obtained by evaluating the electric field at the dipole position in the original frame, as follows:

$$P_{nr}=P_{abs}=-\frac{1}{2}\omega\,\mathrm{Im}\left\{p_x E_{1x}^{s}(x,y=0)+p_y E_{1y}^{s}(x,y=0)\right\} \tag{5.33}$$

where P_{nr} is the non-radiative power emission, $\omega = 2\pi c/\lambda_0$ is the angular frequency at the working wavelength λ_0 and c is the velocity of light in vacuum. Importantly, in these calculations, an intrinsic quantum yield equal to 1 is assumed for the nanoemitter, which allows identifying the non-radiative decay experienced by the

emitter and the power absorbed by the bowtie nanoantenna [GIAN 10]. Moreover, note that as the above expression is derived in the quasi-static approximation, the expression for the extincted power by a point dipole can be used to describe the nanoemitter non-radiative decay.

Let $\Gamma_0(\omega)$ and $\Gamma_{nr}(\omega)$ be the isolated dipole radiative rate and the non-radiative decay rate for the full system. From here, we can define the non-radiative Purcell enhancement rate spectra $[\Gamma_{nr}(\omega)/\ \Gamma_0(\omega)]$ as the ratio of the power absorbed by the nanoparticle, P_{nr}, and the total power radiated by the localized emitter P_0, i.e., $\Gamma_{nr}(\omega)/\ \Gamma_0(\omega) = P_{nr}/P_0$. [NOVO 12], [AUBR 13], [LIU 09a]. Therefore, by considering Eq. 5.33 and the power radiated by the dipole $P_0 = (1/16)(\omega^3\mu_0)(|p|^2)$, with μ_0 the permeability of vacuum and $|p|$ the magnitude of the dipole moment, respectively, the $\Gamma_{nr}(\omega)/\ \Gamma_0(\omega)$ can be analytically calculated as follows:

$$\frac{\Gamma_{nr}(w)}{\Gamma_0(w)} = \frac{-\mathrm{Im}\left(p_x E_{1x}^s + p_y E_{1y}^s\right)}{32\omega^2\mu_0|p|^2};(x, y=0) \tag{5.34}$$

5.1.3 Plasmonic response evaluation

Let us now evaluate the performance of a bowtie nanoantenna made of silver with a total length of l' = 20 nm. First, a fixed normalized gap between both arms is considered with a value of $0.05l'$. The analytical results of $\Gamma_{nr}(\omega)/\ \Gamma_0(\omega)$ as a function of the angle of the arms θ' calculated using Eq. 5.34 are shown in Fig. 5.2(a,e) when the nanoantenna is illuminated with a vertical and a horizontal dipole, respectively.

The analytical results are compared with numerical calculations done with the commercial software Comsol Multiphysics®. For this case, the bowtie nanoantennas are immersed in a vacuum modeled as a two-dimensional square of 600 nm × 600 nm. In order to reduce undesirable reflections from the system, scattering boundary conditions (i.e., perfectly matched layers) have been applied to the boundaries of the square of vacuum. The 2D point dipole used to illuminate the nanoantenna is modeled using two anti-parallel in-plane magnetic currents with a separation of 5 pm. Also, an extremely refined mesh is used with a maximum and minimum mesh size of 2 nm and 3 pm, respectively for the box of vacuum. For the bowtie nanoantennas, a refined mesh twice smaller than the mesh used for the box of vacuum is applied to ensure accurate results.

The analytical results for the vertically oriented dipole case [Fig. 5.2(a)] show that the maximum of $\Gamma_{nr}(\omega)/\ \Gamma_0(\omega)$ shifts from ~698 nm to ~394 nm when the angle θ' is changed from 5º to 45º. This peak is originated from the first (n = 1) LSP mode supported by the bowtie nanoantenna (as it will be shown below through the field distribution inspection). Similarly, for a horizontal dipole, the first non-radiative peak

due to the first LSP mode is blue-shifted from ~650 nm to ~337 nm, see Fig. 5.2(e). Although similar trends are observed in the full-wave simulations, there is an evident blue-shift between simulation results [Fig. 5.2(c,g)] and analytical calculations for both dipole orientations. The blue-shift arises from the assumption that the LSP modes acquire a phase shift of π upon reflection at each end of the metal slabs, i.e., at the open boundaries (at L_1 and $-L_2$). To account for a different reflection phase shift, a correction is introduced in the form of an extra phase $\Delta\varphi$ (as shown in Eq. 5.5-5.9). The calculation of $\Delta\varphi$ is done by fitting the analytically-computed wavelength of the fundamental mode (n = 1 LSP mode) to the simulations. Since higher order LSP modes may experience different reflection conditions than the fundamental one, this correction may not apply for higher order modes. Hence, a slight spectral deviation is expected for these modes. The values of $\Delta\varphi$ for a vertical and horizontal dipole as a function of the angle θ' are shown in Fig. 5.2(d,h), respectively. A linear slope is obtained for angles from 5º to 15º while this tendency is not hold for larger angles. The corrected $\Gamma_{nr}(\omega)/\ \Gamma_0(\omega)$ is shown in Fig. 5.2(b,f) for a vertical and horizontal dipole, respectively. Now, a good agreement between analytical and numerical results is obtained. From now on, $F_{nr} = \Gamma_{nr}(\omega)/\ \Gamma_0(\omega)$ will refer to the corrected results.

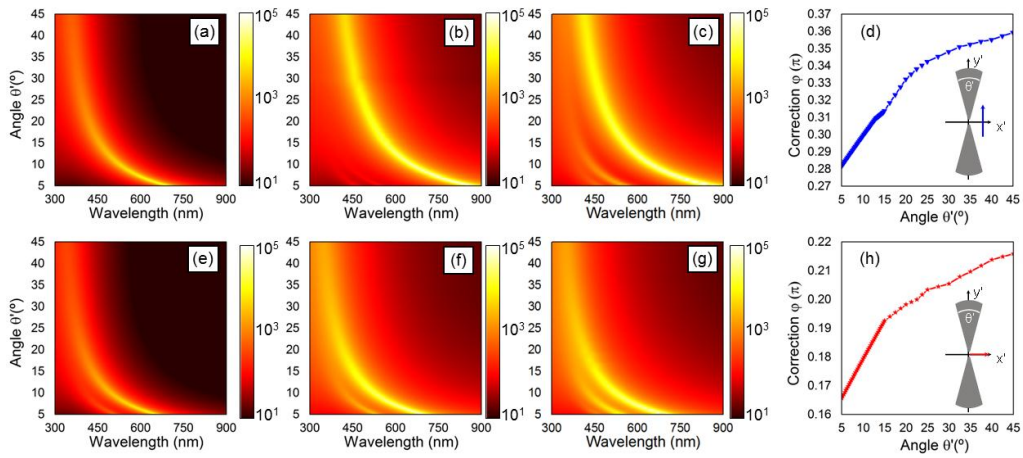

Figure 5.2. Non-radiative Purcell enhancement rate spectra for different angles of a bowtie nanoantenna illuminated with a vertical (first row) and a horizontal (second row) dipole: analytical results without $\Delta\varphi$ (first column) along with the numerical (second column) and analytical results with $\Delta\varphi$. (d,e) Values of the correction $\Delta\varphi$ used for each polarization.

As explained before, due to the finite size of the bowtie nanoantennas (and the equivalent transformed problem) the LSPs are distributed as a set of discrete modes in the spectra following a resonant condition defined as:

$$\frac{\left\{(\varepsilon-1)^2\left[e^{k(3d_1+6d_2+2d_3)}-e^{k(d_1+4d_2+4d_3)}\right]-(\varepsilon+1)^2\left[e^{k(d_1+4d_2+2d_3)}-e^{k(3d_1+6d_2+4d_3)}\right]\right\}^2}{\left\{2(\varepsilon^2-1)\left[e^{k(3d_1+6d_2+3d_3)}-e^{k(d_1+4d_2+3d_3)}\right]\right\}^2}-1=0 \quad (5.35)$$

This resonant condition is derived from the formulation shown in Eqs. 5.5-5.19 taking into account the condition of divergence of the coefficients of the scattered potential (B±).

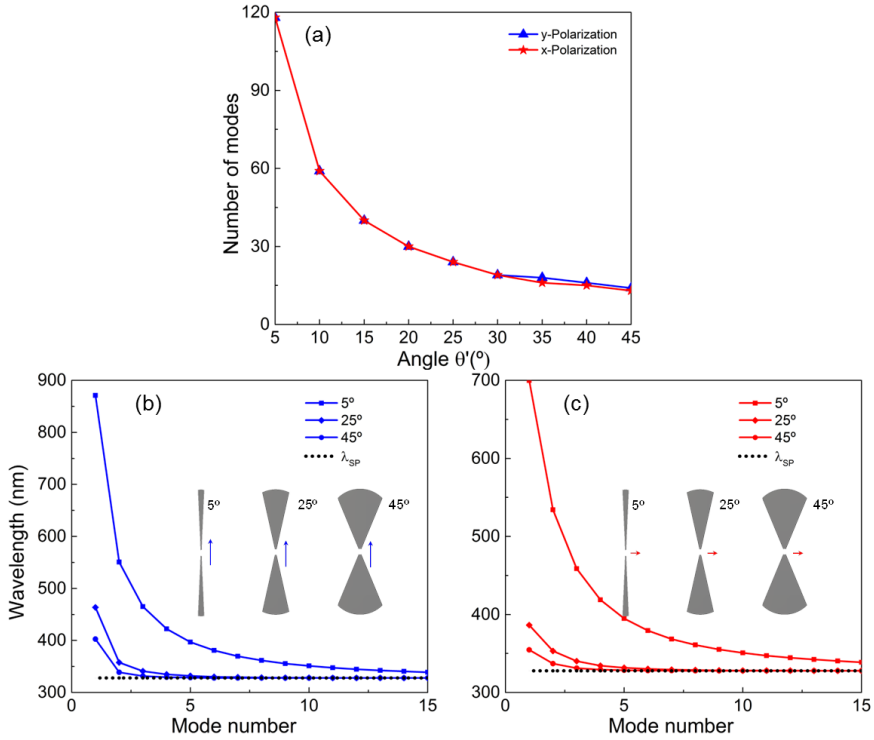

Figure 5.3. (a) Number of modes as a function of θ' for a dipole illuminating the bowtie with vertical (blue) and horizontal (red) polarization. Analytical cut-off wavelength for each mode number for bowtie angle 5° (squares), 25° (diamonds) and 45° (circles) when the illuminating dipole is vertically (b) and horizontally polarized (c) as shown in the insets. The discrete points in (b,c) have been connected with a solid line to guide the eye.

By using the above equation, the number of LSP modes supported by the bowtie nanoantenna under study as a function of θ' is shown in Fig. 5.3(a) when a vertical and horizontal dipole is used. As it can be observed, the larger the θ' is, the lower the number of LSP modes exist. This is because the LSP modes are directly related to θ (i.e., d_3) when the dimensions L_1 and L_2 are fixed (see Eq. 5.35). The distribution of

the first 15 LSP modes in the spectrum for three specific bowtie nanoantennas with angles 5º, 25º and 45º is shown Fig. 5.3(b,c) for a vertically and horizontally polarized dipole, respectively. It is shown that each resonance of the LSP modes is red-shifted when the angle of the antenna is decreased for both polarizations, which is in good agreement with Fig. 5.2. Moreover, it can be observed that the higher-order LSP modes are compressed when their resonances approach the surface plasmon wavelength (λ_{sp}, plotted as a black dotted line).

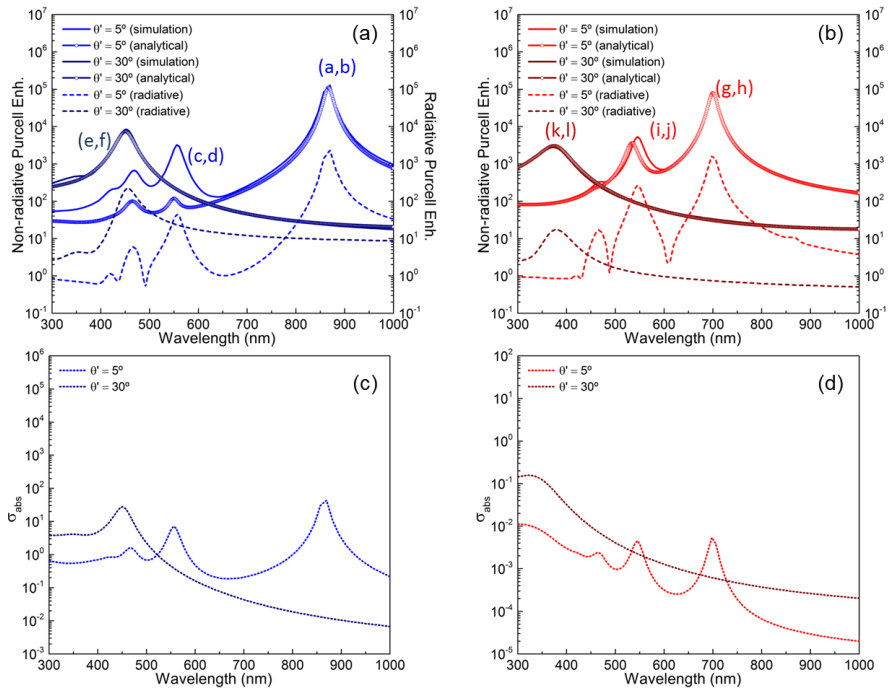

Figure 5.4. Analytical (dots) and simulation (solid lines) results of the non-radiative Purcell enhancement spectra along with the simulation results of the radiative Purcell enhancement spectra (dashed lines) for two bowties with angle θ' = 5° (light lines) and θ' = 30° (dark lines) when a vertical (a) and horizontal (b) dipole is used as a radiative source. The letters next to the peaks refer to the different panels in Fig. 5.5. Numerical results of the absorption cross section for the two bowtie nanoantennas under study when a vertically (c) and a horizontally (d) polarized plane wave is used a source.

Next, the analytical and simulation results of the non-radiative Purcell enhancement spectra are analyzed in detail for the case of two bowtie nanoantennas with θ' = 5º and 30º excited by a vertical [Fig. 5.4(a)] and horizontal dipole [Fig. 5.4(b)]. Letting $\Gamma_r(\omega)$ be the radiative decay rate for the full system, the simulation results of the radiative Purcell enhancement $F_r = \Gamma_r(\omega)/\Gamma_0(\omega)$ (calculated as the ratio of

the power radiated by the system enclosed by the nanoparticle-dipole P_r and P_0; $\Gamma_r(\omega)/\Gamma_0(\omega) = P_r/P_0$) [NOVO 12], [AUBR 13], [LIU 09a] are also shown in the same figure. Notice that Γ_r is consistently at least two orders of magnitude smaller than Γ_{nr}, and thus negligible, as it was assumed initially. A good quantitative agreement between analytical and numerical results is shown in Fig. 5.4(a,b) for the first non-radiative peak while the other peaks are slightly blue-shifted, as expected from the above discussion on $\Delta\varphi$. An average blue-shift of 0.9% and 2% is observed between the simulation and analytical results for the peak associated to the $n = 2$ LSP mode for the bowtie nanoantenna with $\theta' = 5^{\circ}$ using a vertical and horizontal dipole, respectively. For completeness, the absorption cross section under plane wave illumination are also shown in Fig. 5.4(c,d) for a vertical and horizontal polarization, respectively, where it can be observed that the values are also smaller than Γ_{nr} using the nanoemitter close to the bowtie nanoantennas.

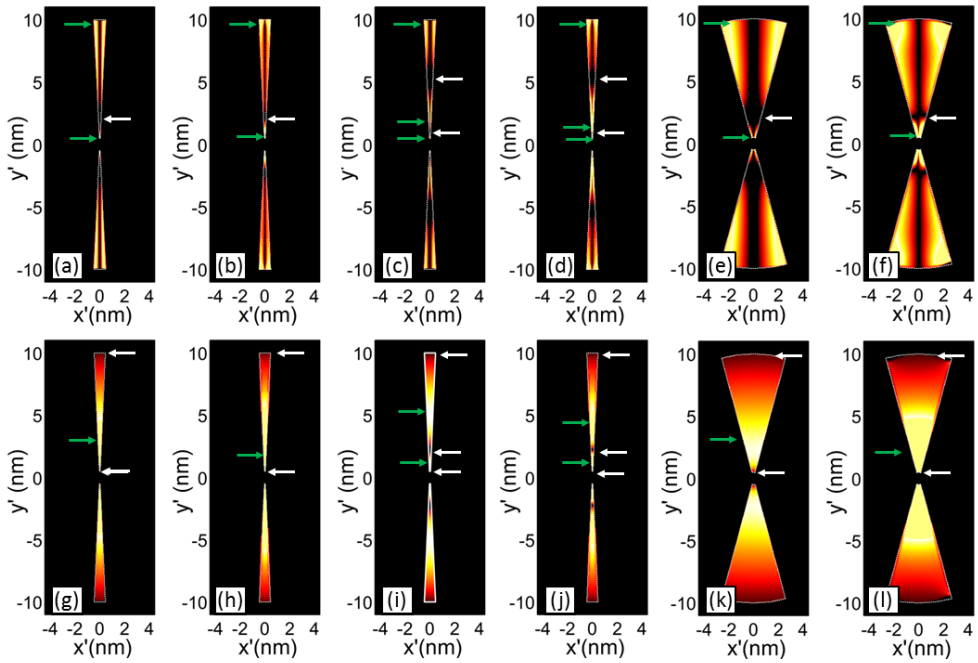

Figure 5.5. Analytical (a,c,e,g,i,k) and simulation-computed (b,d,f,h,j,l) absorption for the bowtie with angle $\theta' = 5°$ (a-d,g-j) and $\theta' = 30°$ (e-f,k-l) when the illuminating dipole is vertical (first row) and horizontal (second row): fundamental (a-b,e-h,k-l) and second non-radiative decay rate peak (c-d,i-j) within the spectral window of interest. The scale color bar is saturated to facilitate the intelligibility. Horizontal green and white arrows indicate respectively the location of the maxima and minima on the top arm of each bowtie.

In Fig. 5.5 it is shown the spatial absorption profiles across the bowtie nanoantenna with $\theta' = 5°$ and $\theta' = 30$ and different dipole orientation calculated at the wavelengths highlighted in Fig. 5.4. A good agreement between analytical and simulation results is noticed. As expected, when several absorption maxima exist, the absolute one is obtained closer to the apexes for all cases. This is a consequence of the larger field concentration close to the gap which happens due to the spatial compression of the surface plasmon modes [NAVA 12a]. The spatial absorption distribution for the fundamental mode under a vertical dipole illumination [Fig. 5.5(a,b) and Fig. 5.5(e,f)] has an absorption minimum pointed out by white horizontal arrows at $y' = 2.2$ nm ($y' = 2.36$ nm) in the analytical (numerical) calculation. This absorption minimum represents the node of the $n = 1$ LSP mode. For the peaks associated to the $n = 2$ LSP mode, Fig. 5.5(c,d), it can be however noticed a local maximum at $y' = 2.06$ nm ($y' = 1.8$ nm) in the analytical (numerical) results located at each arm of the bowtie nanoantenna, pointed out by horizontal green arrows. This is because this position corresponds to the anti-node of the $n = 2$ LSP mode. Under horizontal dipole illumination, the positions of the maxima and minima change according to the anti-nodes of the corresponding LSP modes, as it is demonstrated next through electric field distribution patterns. Therefore, the bowtie nanoantennas investigated here have a multi-band absorption response that arises from the efficient coupling of the localized emitter to the multiple LSP modes supported within the range from 300 nm to 900 nm.

A snapshot of the field distribution for a bowtie nanoantenna with $\theta' = 5^{o}$ is shown in Fig. 5.6 for the first and second peak of F_{nr} of each dipole orientation. For convenience, here $E'_{\varphi'}$ and $E'_{\rho'}$ are plotted for the vertical and horizontal dipole excitation, respectively. From these color plots the mode order of the various LSPs can be clearly identified. Under a vertical dipole illumination, the azimuthal field distribution at the first peak has a null between the field maxima at the edges of each bowtie arm [Fig. 5.6(a)]. For the second peak [Fig. 5.6(b)], three anti-nodes and two nulls along the radial direction in each arm are observed, which corresponds to the $n = 2$ LSP mode. On the other hand, for the case of an horizontally oriented emitter, two minima are obtained at both ends of each arm with an anti-node between them at the lowest F_{nr} peak [Fig. 5.6(c)], which is related to the $n = 1$ LSP mode. At the second peak [Fig. 5.6(d)] the field distribution can be linked to the $n = 2$ LSP mode as it has three nulls (one at the center and two at the extremes of each arms) and 2 maxima in between consecutive nulls. Notice that the electric field is stronger at the anti-nodes nearby the apex of the bowties, as expected from the spatial absorption profiles.

Alternatively, the field distribution can be easily associated to standing wave patterns in the transformed frame, as follows: in the multi-slab geometry, for a vertically polarized dipole, the field distribution for the $n = 1$ LSP mode has a field distribution with anti-nodes at both extremes of the slab (L_1 and $-L_2$) and a node in the

center. Similarly, the n = 2 LSP mode has two electric field nodes and three anti-nodes, located at the extremes of the slab and in the center in-between the nodes. On the other hand, for a horizontal emitter, the n = 1 LSP mode has a field distribution with nodes at both extremes of the slab and an anti-node in the center; while for the n = 2 LSP mode, the field distribution has three nodes (in the center and at both extremes of the slab) and two anti-nodes. The field distribution in the multi-slab geometry for different LSP will be shown in the next study.

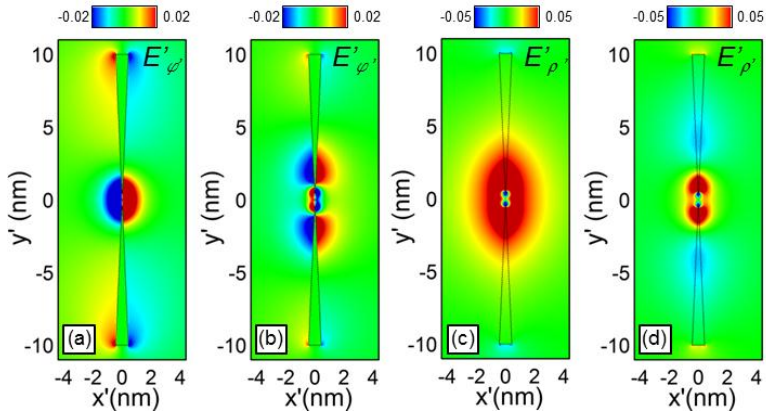

Figure 5.6. Snapshot of E'_{φ}-field (a,b) and E'_{ρ}-field (c,d) for a bowtie nanoantenna with angle θ' = 5° and illuminated with a vertical (a,b) and an horizontal (c,d) dipole at the peaks in Fig. 5.4: (a) 869 nm, (b) 556 nm, (c) 698 nm and (e) 545 nm. Note that the scale bar has been saturated from –0.02 to 0.02 and from –0.05 to 0.05 to better appreciate the field distribution across the whole space.

The results discussed until now have been obtained considering bowtie nanoantennas with varying θ'. Next, the influence of the gap size in the non-radiative spectra of two bowtie nanoantennas with θ' = 5º and θ' = 30º is discussed, for a fixed antenna length (l' = 20 nm). The analytical results for F_{nr} as a function of the gap distance between both arms are shown in the first row of Fig. 5.7 when a vertical [Fig. 5.7(a,c)] and an horizontal [Fig. 5.7(b,d)] dipole is placed at (x'= 1 nm, y'= 0 nm). It can be observed that all peaks (related to a specific LSP mode) for both polarizations and angles are blue-shifted when the gap is increased. This blue-shift can be easily explained in terms of the transformed multi-slab geometry: an increment of the gap between both arms of the bowtie nanoantenna is equivalent to reducing the total length of the slabs in the transformed frame (i.e., $L = L_1 + L_2$ is reduced). Hence, the resonance condition (of the standing wave pattern) is achieved at shorter wavelengths.

With the aim to ease the description and comparison, the corresponding numerical spectra are shown in the second row of Fig. 5.7. These panels demonstrate a very good

agreement with the analytical results. For $\theta' = 5^{o}$ and a vertical dipole [Fig. 5.7(a,e)] the F_{nr} peak related to the $n = 1$ LSP mode is blue-shifted from ~1132 nm (not shown) to ~845 nm when the normalized gap goes from $0.01l'$ to $0.06l'$. Interestingly, this peak is not always the F_{nr} absolute maximum, in contrast to what is observed for the absorption cross section for a bowtie under plane wave illumination (shown in the bottom row of Fig 5.7). For instance, F_{nr} is larger for the $n = 2$ LSP mode for a normalized gap of $0.01l'$. Hence, there are preferred positions to increase the transfer of energy from the radiative dipole source to the different LSP modes. In particular, for the case $0.01l'$, the vertical dipole is located at a field distribution null of the $n = 1$ LSP eigen-mode (not shown here). Hence the peak associated to this mode vanishes. For the case of a horizontal dipole [Fig. 5.7(b,f)] the peak due to the $n =1$ LSP mode is blue-shifted from ~769 nm to ~697 nm when the normalized gap is increased from $0.01l'$ to $0.06l'$. The two other non-radiative peaks (related to the $n = 2$ and $n = 3$ LSP modes, respectively) are also blue-shifted as the gap is increased. Here, the analytical F_{nr} peaks due to second and third higher order mode are also blue-shifted from simulation results by an averaged percentage of 1.1% and 1.37%, respectively, for a vertical dipole, and 1.67% and 1.2% for a horizontal dipole. The blue-shift is smaller for a horizontal dipole because of the comparatively shorter phase correction applied to this configuration.

Finally, for the case with $\theta' = 30^{o}$, the F_{nr} peak due to the $n = 1$ LSP mode [Fig. 5.7] has a higher non-radiative Purcell enhancement within the entire range of normalized gaps. The second F_{nr} peak is observed as a shoulder for a vertical dipole (see third column of Fig. 5.7) while it is beyond the spectral window here evaluated under horizontal illumination (see fourth column of Fig. 5.7). For this nanoantenna, the F_{nr} peak due to the $n = 1$ LSP mode is also blue-shifted from ~555 nm to ~444 nm (vertical) and from ~382 nm to ~370 nm (horizontal), when the gap is changed between $0.01l'$ and $0.06l'$. Note that, again, for a vertical dipole [Fig. 5.7(c,g)] the F_{nr} linked to the first LSP mode vanishes for certain gap sizes, such as $0.01l'$, while such behavior is not observed in the absorption cross section. This underlines the key role played by the position and orientation of the localized emitter. For this bowtie nanoantenna, the analytical F_{nr} peak due to the $n = 2$ LSP mode is slightly blue-shifted with an average value of 2.9% when the bowtie nanoantenna is illuminated with a vertical dipole while, as it has been described, this higher order LSP mode is not observed under a horizontal illumination. For the sake of completeness, the numerical results of F_{r} are shown in the third row of Fig. 5.7. Not surprisingly, higher radiative decay rate is observed for the dipolar $n = 1$ LSP mode for both dipole polarizations, but still is negligible compared to F_{nr}.

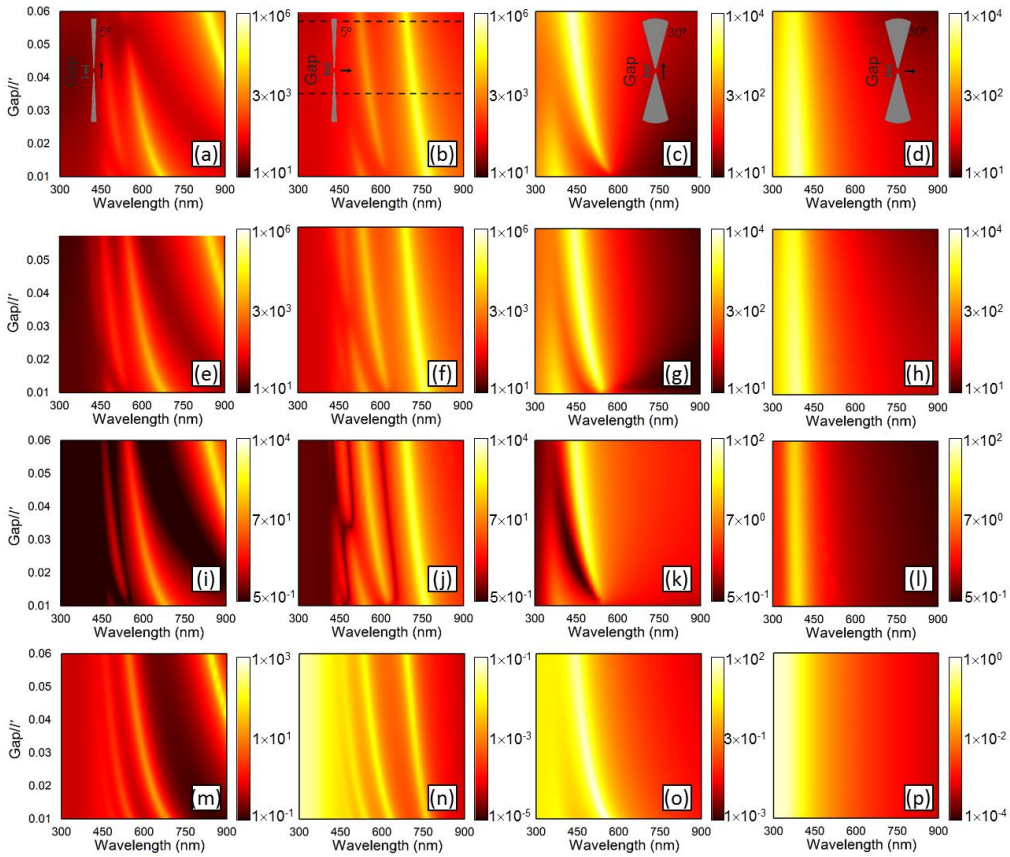

Figure 5.7. Analytical (first row) and simulation-computed (second row) non-radiative Purcell enhancement spectra along with the simulation results of the radiative Purcell enhancement spectra (third row) and absorption cross section (fourth row) as a function of the gap between the arms for the bowtie with θ' = 5° (first and second columns) and θ' = 30° (third and fourth columns) when a vertically (first and third columns) and a horizontally (second and fourth columns) polarized dipole (top three rows) or plane wave is used as a source (bottom row).

As described before, depending of the angle θ', gap, and orientation of the dipole, the localized emitter cannot transfer energy efficiently to the LSP modes (displayed as minima in the non-radiative Purcell enhancement). This phenomenon can be easily explained by looking at the multi-slab geometry. Let us then analyze the case of the bowtie with θ' = 5º illuminated with a horizontal dipole [Fig. 5.7(b,f), analytical and simulation results, respectively). As it is shown, there is a range of gaps between $\sim 0.028l'$ to $\sim 0.038l'$ where the peak linked to the n = 3 LSP mode vanishes. To better

investigate this feature, the F_{nr} for this bowtie nanoantenna using a horizontal dipole is shown in Fig. 5.8(a,e) for a normalized gap of 0.057*l'* and 0.035*l'*, respectively [extracted from the black dashed lines of Fig. 5.7(b)]. For the case of a gap of 0.057*l'* [Fig. 5.8(a)], three peaks are observed at ~691 nm, ~522 nm and ~454 nm which are those related to the LSP modes with n = 1, 2 and 3, respectively. On the other hand, when the gap is 0.035*l'* [Fig. 5.8(e)] all peaks are red-shifted, as expected, to ~721 nm, ~556 nm and ~433 nm. Nevertheless, the LSP mode with n = 3 at ~433 nm is strongly reduced and almost disappears.

This phenomenon can be explained by analyzing the fields in the transformed geometry, as follows: first, the analytical results of the normalized magnitude of the electric field distribution in the multi-slab geometry for the case of a gap of 0.057*l'* at the first, second and third peaks is shown in Fig. 5.8(b-d), respectively. The field distribution at these peaks are related to the field distribution of the LSP modes with n = 1, 2 and 3, respectively, as explained before. For the case of the first LSP mode (n = 1) the horizontal dipole (shown as a horizontal green arrow) is placed close but not just at the node at $-L_2$ (i.e., the node in the standing wave pattern) of the field distribution; therefore, the dipole can be coupled to this LSP mode. However, for n = 2 [Fig. 5.8(c)] the dipole is closer to the first node, where a weakly transfer of energy between the dipole to the LSP is expected. Hence, a reduction of F_{nr} is obtained for this mode compared to the first one. Similar performance can be observed for n = 3. In this case, the dipole is even closer to the node compared with the first and second modes; therefore, the amplitude of the peak is reduced although it still appears in the spectrum.

Now, let us analyze the case when the gap is 0.035*l'*. For this geometry, the normalized magnitude of the electric field at 721, 556 and 433 nm is shown in Fig. 5.8(f-h), respectively. As it is shown in Fig. 5.8(h), the field distribution is related to the LSP mode with n = 3, as explained before. Moreover, it is observed that the horizontal dipole is exactly at the position where the distribution of the electric field has a node. Therefore, the electromagnetic energy released by the dipole is not efficiently coupled to this LSP mode giving rise to a null in F_{nr}. On the contrary, for the case of the first and second peaks [see Fig. 5.8(f,g), respectively] the horizontal dipole is located at a more favorable position for energy transfer to the LSP modes than for the case of n = 3 and the n = 1 and 2 LSP modes for 0.057*l'* gap. Hence, the non-radiative decay rate is higher for them.

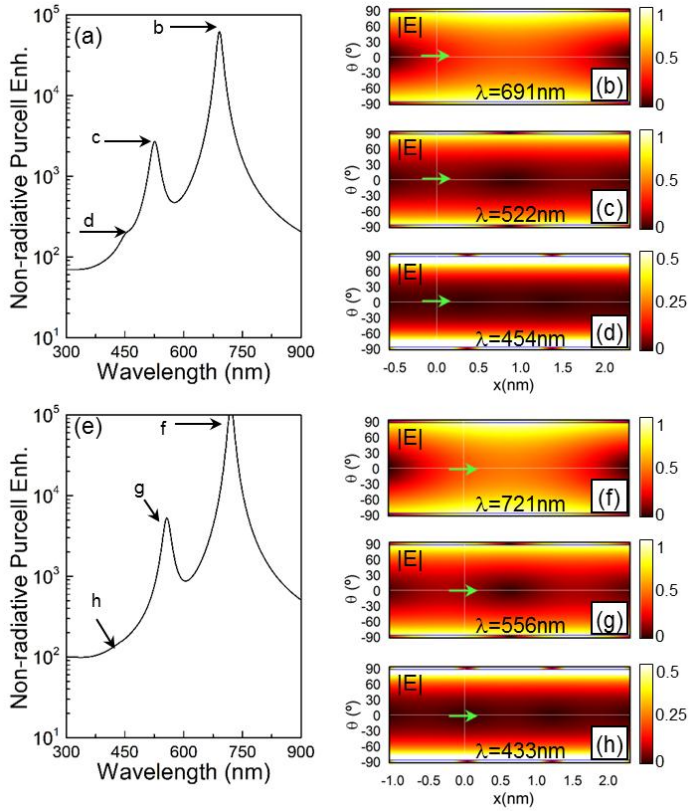

Figure 5.8. Analytical non-radiative Purcell enhancement spectra for a bowtie with θ'= 5° and gap = 0.057l' (a) and 0.035l' (e). Analytical normalized magnitude of the electric field for the parallel-plate geometry at the relevant spectral position shown in (a) and (e). The position of the illuminating horizontal dipole is shown as a green arrow for aid. Note that the scale maximum in (d) and (h) has been saturated to 0.5 to better observe the field distribution

5.2 Tripod nanoantenna

Here, the plasmonic response of tripod nanoantennas is evaluated using conformal transformation optics. Similar to the bowtie nanoantennas, the tripod nano-structures are composed by three triangular-shaped metal nanoparticles facing against each other with arms connected or separated by a nanometric gap [CHEN 03], [GIAN 10a], [WATS 15], [ALCA 15], [FORE 16]. Here, the attention is centered in the latter case in order to reduce the complexity of the study. The connected case is now under study and it is expected to show its response in the near future.

5.2.1 Quasi-static solution

The schematic representation of the tripod nanoantenna is shown in Fig. 5.9(a). Aluminum (Al) with a complex permittivity following Palik's experimental data [PALI 85] is used as a metal for these nanoantennas since it has been demonstrated to be a good candidate for applications in the ultra-violet spectral range [MOSC 12], [MART 13], [KNIG 14], [LIU 15], [HAO 15], [CHOU 16]. A total length l' = 18 nm and a gap of 0.055l' is used and the nano-structures are embedded in vacuum. The nanoemitter (dipole) has an arbitrary polarization and it is placed at (x'= 1 nm, y' = 0). By applying the conformal transformation shown in Eq. 5.1, the tripod nanoantennas are transformed into the multiple parallel-plate transmission line geometry shown in Fig. 5.9(b). As for the case of the bowties, the metal slabs have dimensions L_1+L_2 and θ (= d_3, d_5 and d_7) along the x and y axis, respectively. Here, $d_3 = d_5 = d_7$ is considered to reduce the complexity of the structure. However, the quasi-static solution for the electric field of each region of the tripod will be obtained without considering this equality, in order to deduce the complete solution of the problem. Moreover, the case when the slabs have different thicknesses (angles of each arm of the tripod) is now under study and the results will be presented in the near future).

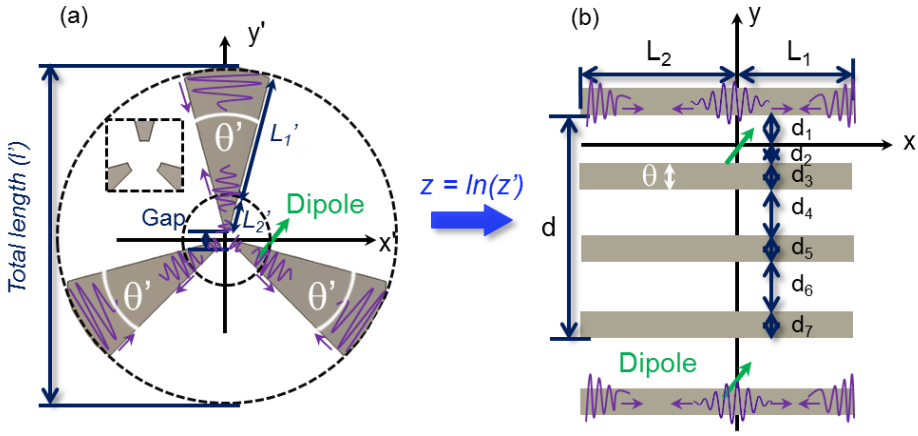

Figure 5.9. Schematic representation of a metallic tripod nanoantenna with a gap in its center (a) along with the transformed geometry (b). The nanoantenna is illuminated with a dipole placed at (x', y') = (1 nm, 0) (green arrow)

Again, the original dipole is converted into an array of dipoles with the same strength placed along the y axis with a periodicity 2π, i.e., at (x = 0, y = 2πm), where m is an integer. By comparing Fig. 5.9(b) with the transformed geometry of the bowtie nanoantenna [Fig. 5.1(b)] it can be clearly observed that an air region without the

dipole and an extra metal slab is added in order to take into account the other arm of the tripod.

Now, a similar procedure as for the bowtie nanoantenna (see section 5.1.2) is followed in order to characterize the plasmonic response of the tripod nano-structures in the quasi-static region. Here, the contribution of the longitudinal LSP modes (i.e., those with phase variation along *y*) are also neglected assuming that LSP modes are mainly due to the transversal modes. Based on this, the electrostatic potentials outside and inside the metal strips in Fig. 5.9(b) can be calculated as a sum of all discrete transverse modes, as follows:

$$\sum_k \left[\frac{1}{1-e^{2ik(L_1+L_2)+2i\Delta\varphi}} \left(e^{ikx} + e^{-ikx+2ikL_1+i\Delta\varphi}\right)\left(A_+ e^{-ky} + B_+ e^{-ky} + B\_e^{ky}\right)\right], 0 < y < d_1 \tag{5.36}$$

$$\sum_k \left[\frac{1}{1-e^{2ik(L_1+L_2)+2i\Delta\varphi}} \left(e^{ikx} + e^{-ikx+2ikL_1+i\Delta\varphi}\right)\left(A\_e^{ky} + B_+ e^{-ky} + B\_e^{ky}\right)\right], -d_2 < y < 0 \tag{5.37}$$

$$\sum_k \left[\frac{1}{1-e^{2ik(L_1+L_2)+2i\Delta\varphi}} \left(e^{ikx} + e^{-ikx+2ikL_1+i\Delta\varphi}\right)\left(F_+ e^{-ky} + F\_e^{ky}\right)\right], -(d_2+d_3+d_4) < y < -(d_2+d_3) \tag{5.38}$$

$$\sum_k \left[\frac{1}{1-e^{2ik(L_1+L_2)+2i\Delta\varphi}} \left(e^{ikx} + e^{-ikx+2ikL_1+i\Delta\varphi}\right)\left(G_+ e^{-ky} + G\_e^{ky}\right)\right], \; y \begin{cases} > -(d_2+d_3+d_4+d_5+d_6) \\ < -(d_1+2d_2+d_3) \end{cases} \tag{5.39}$$

$$\sum_k \left[\frac{1}{1-e^{2ik(L_1+L_2)+2i\Delta\varphi}} \left(e^{ikx} + e^{-ikx+2ikL_1+i\Delta\varphi}\right)\left(D_+ e^{-ky} + D\_e^{ky}\right)\right], -(d_2+d_3) < y < -d_2 \tag{5.40}$$

$$\sum_k \left[\frac{1}{1-e^{2ik(L_1+L_2)+2i\Delta\varphi}} \left(e^{ikx} + e^{-ikx+2ikL_1+i\Delta\varphi}\right)\left(E_+ e^{-ky} + E\_e^{ky}\right)\right], \; y \begin{cases} > -(d_2+d_3+d_4+d_5) \\ < -(d_2+d_3+d_4) \end{cases} \tag{5.41}$$

$$\sum_k \left[\frac{1}{1-e^{2ik(L_1+L_2)+2i\Delta\varphi}} \left(e^{ikx} + e^{-ikx+2ikL_1+i\Delta\varphi}\right)\left(C_+ e^{-ky} + C\_e^{ky}\right)\right], \; y \begin{cases} > -(d_2+d_3+d_4+d_5+d_6+d_7) \\ < -(d_2+d_3+d_4+d_5+d_6) \end{cases} \tag{5.42}$$

where A_+ and A_- are the expansion coefficients of the incident potential, B_+ and B_- are the coefficients related to the scattering potential in the region where the dipole is placed ($d_2 < y < d_1$), F_+, F_-, G_+ and G_- are the coefficients of associated to the scattering potential in the region where a dipole is absent (d_4 and d_6) and C_+, C_-, D_+, D_-, E_+ and E_- are those corresponding to the potential inside the metal strips (d_7, d_3 and d_5, respectively). The wave vector k and the coefficients A_+ and A_- are defined as shown in Eq. 5.10 and Eq. 5.11, respectively.

The other twelve unknown coefficients B_+, B_-, C_+, C_-, D_+, D_-, E_+, E_-, F_+, F_-, G_+ and G_- can be solved by applying the boundary conditions at each interface of Fig. 5.9(b). First, the condition of conservation of the parallel component of the electric field at the

boundaries d_2, d_2+d_3, $d_2+d_3+d_4$, $d_2+d_3+d_4+d_5$, d_1 and $d_2+d_3+d_4+d_5+d_6$ is applied, as follows:

$$A\_e^{-kd_2} + B_+e^{kd_2} + B\_e^{-kd_2} = D\_e^{-kd_2} + D_+e^{kd_2} \tag{5.43}$$

$$F_+e^{k(d_2+d_3)} + F\_e^{-k(d_2+d_3)} = D\_e^{-k(d_2+d_3)} + D_+e^{k(d_2+d_3)} \tag{5.44}$$

$$F_+e^{k(d_2+d_3+d_4)} + F\_e^{-k(d_2+d_3+d_4)} = E\_e^{-k(d_2+d_3+d_4)} + E_+e^{k(d_2+d_3+d_4)} \tag{5.45}$$

$$G_+e^{k(d_2+d_3+d_4+d_5)} + G\_e^{-k(d_2+d_3+d_4+d_5)} = E\_e^{-k(d_2+d_3+d_4+d_5)} + E_+e^{k(d_2+d_3+d_4+d_5)} \tag{5.46}$$

$$A_+e^{-kd_1} + B_+e^{-kd_1} + B\_e^{kd_1} = C\_e^{-k(d_2+d_3+d_4+d_5+d_6+d_7)} + C_+e^{k(d_2+d_3+d_4+d_5+d_6+d_7)} \tag{5.47}$$

$$G_+e^{k(d_2+d_3+d_4+d_5+d_6)} + G\_e^{-k(d_2+d_3+d_4+d_5+d_6)} = C\_e^{-k(d_2+d_3+d_4+d_5+d_6)} + C_+e^{k(d_2+d_3+d_4+d_5+d_6)} \tag{5.48}$$

Also, the condition of conservation of the normal component of the displacement field at the same boundaries as the above equations is applied:

$$A\_e^{-kd_2} - B_+e^{kd_2} + B\_e^{-kd_2} = \varepsilon D\_e^{-kd_2} - \varepsilon D_+e^{kd_2} \tag{5.49}$$

$$F_+e^{k(d_2+d_3)} - F\_e^{-k(d_2+d_3)} = -\varepsilon D\_e^{-k(d_2+d_3)} + \varepsilon D_+e^{k(d_2+d_3)} \tag{5.50}$$

$$-F_+e^{k(d_2+d_3+d_4)} + F\_e^{-k(d_2+d_3+d_4)} = \varepsilon E\_e^{-k(d_2+d_3+d_4)} - \varepsilon E_+e^{k(d_2+d_3+d_4)} \tag{5.51}$$

$$G_+e^{k(d_2+d_3+d_4+d_5)} - G\_e^{-k(d_2+d_3+d_4+d_5)} = -\varepsilon E\_e^{-k(d_2+d_3+d_4+d_5)} + \varepsilon E_+e^{k(d_2+d_3+d_4+d_5)} \tag{5.52}$$

$$A_+e^{-kd_1} + B_+e^{-kd_1} - B\_e^{kd_1} = -\varepsilon C\_e^{-k(d_2+d_3+d_4+d_5+d_6+d_7)} + \varepsilon C_+e^{k(d_2+d_3+d_4+d_5+d_6+d_7)} \tag{5.53}$$

$$-G_+e^{k(d_2+d_3+d_4+d_5+d_6)} + G\_e^{-k(d_2+d_3+d_4+d_5+d_6)} = \varepsilon C\_e^{-k(d_2+d_3+d_4+d_5+d_6)} - \varepsilon C_+e^{k(d_2+d_3+d_4+d_5+d_6)} \tag{5.54}$$

The solutions of the potentials in the real space for the region where there is ($d_2 < y < d_1$) and there is not a dipole (d_4, d_6), ϕ_1^s, ϕ_2^s and ϕ_3^s, respectively, can be then obtained by applying an inverse FT to the induced potentials:

$$\phi_1^s = \frac{1}{2\varepsilon_0(L_1+L_2)} \sum_n \left\langle \Theta \begin{Bmatrix} p_x\left[\sin(kx) - \sin(kx - 2kL_1 - \Delta\varphi)\right] + \\ p_y\left[\cos(kx) + \cos(kx - 2kL_1 - \Delta\varphi)\right] \end{Bmatrix} \left(B_+e^{-ky} + B\_e^{ky}\right) \right\rangle \tag{5.55}$$

$$\phi_2^s = \frac{1}{2\varepsilon_0(L_1+L_2)}\sum_n \left\langle \Theta\begin{Bmatrix} p_x\left[\sin(kx)-\sin(kx-2kL_1-\Delta\varphi)\right]+ \\ p_y\left[\cos(kx)+\cos(kx-2kL_1-\Delta\varphi)\right] \end{Bmatrix}\left(F_+e^{-ky}+F_-e^{ky}\right)\right\rangle \tag{5.56}$$

$$\phi_3^s = \frac{1}{2\varepsilon_0(L_1+L_2)}\sum_n \left\langle \Theta\begin{Bmatrix} p_x\left[\sin(kx)-\sin(kx-2kL_1-\Delta\varphi)\right]+ \\ p_y\left[\cos(kx)+\cos(kx-2kL_1-\Delta\varphi)\right] \end{Bmatrix}\left(G_+e^{-ky}+G_-e^{ky}\right)\right\rangle \tag{5.57}$$

The potentials inside the three metallic slabs (ϕ_1^m, ϕ_2^m and ϕ_3^m) are:

$$\phi_1^m = \frac{1}{2\varepsilon_0(L_1+L_2)}\sum_n \left\langle \Theta\begin{Bmatrix} p_x\left[\sin(kx)-\sin(kx-2kL_1-\Delta\varphi)\right]+ \\ p_y\left[\cos(kx)+\cos(kx-2kL_1-\Delta\varphi)\right] \end{Bmatrix}\left(C_+e^{-ky}+C_-e^{ky}\right)\right\rangle \tag{5.58}$$

$$\phi_2^m = \frac{1}{2\varepsilon_0(L_1+L_2)}\sum_n \left\langle \Theta\begin{Bmatrix} p_x\left[\sin(kx)-\sin(kx-2kL_1-\Delta\varphi)\right]+ \\ p_y\left[\cos(kx)+\cos(kx-2kL_1-\Delta\varphi)\right] \end{Bmatrix}\left(D_+e^{-ky}+D_-e^{ky}\right)\right\rangle \tag{5.59}$$

$$\phi_3^m = \frac{1}{2\varepsilon_0(L_1+L_2)}\sum_n \left\langle \Theta\begin{Bmatrix} p_x\left[\sin(kx)-\sin(kx-2kL_1-\Delta\varphi)\right]+ \\ p_y\left[\cos(kx)+\cos(kx-2kL_1-\Delta\varphi)\right] \end{Bmatrix}\left(E_+e^{-ky}+E_-e^{ky}\right)\right\rangle \tag{5.60}$$

Finally, by differentiating the potentials of each region, the *x* and *y* components of the electric field can be calculated, as follows:

$$E_{1x}^s = \sum_n -\frac{k}{2\varepsilon_0(L_1+L_2)}\left\langle \begin{Bmatrix} p_x\left[\cos(kx)-\cos(kx-2kL_1-\Delta\varphi)\right] \\ -p_y\left[\sin(kx)+\sin(kx-2kL_1-\Delta\varphi)\right] \end{Bmatrix}\left(B_+e^{-ky}+B_-e^{ky}\right)\right\rangle \tag{5.61}$$

$$E_{2x}^s = \sum_n -\frac{k}{2\varepsilon_0(L_1+L_2)}\left\langle \begin{Bmatrix} p_x\left[\cos(kx)-\cos(kx-2kL_1-\Delta\varphi)\right] \\ -p_y\left[\sin(kx)+\sin(kx-2kL_1-\Delta\varphi)\right] \end{Bmatrix}\left(F_+e^{-ky}+F_-e^{ky}\right)\right\rangle \tag{5.62}$$

$$E_{3x}^s = \sum_n -\frac{k}{2\varepsilon_0(L_1+L_2)}\left\langle \begin{Bmatrix} p_x\left[\cos(kx)-\cos(kx-2kL_1-\Delta\varphi)\right] \\ -p_y\left[\sin(kx)+\sin(kx-2kL_1-\Delta\varphi)\right] \end{Bmatrix}\left(G_+e^{-ky}+G_-e^{ky}\right)\right\rangle \tag{5.63}$$

$$E_{1x}^m = \sum_n -\frac{k}{2\varepsilon_0(L_1+L_2)}\left\langle \begin{Bmatrix} p_x\left[\cos(kx)-\cos(kx-2kL_1-\Delta\varphi)\right] \\ -p_y\left[\sin(kx)+\sin(kx-2kL_1-\Delta\varphi)\right] \end{Bmatrix}\left(C_+e^{-ky}+C_-e^{ky}\right)\right\rangle \tag{5.64}$$

$$E_{2x}^m = \sum_n -\frac{k}{2\varepsilon_0(L_1+L_2)}\left\langle \begin{Bmatrix} p_x\left[\cos(kx)-\cos(kx-2kL_1-\Delta\varphi)\right] \\ -p_y\left[\sin(kx)+\sin(kx-2kL_1-\Delta\varphi)\right] \end{Bmatrix}\left(D_+e^{-ky}+D_-e^{ky}\right)\right\rangle \tag{5.65}$$

$$E_{3x}^{m} = \sum_{n} -\frac{k}{2\varepsilon_0 (L_1 + L_2)} \left\langle \begin{Bmatrix} p_x [\cos(kx) - \cos(kx - 2kL_1 - \Delta\varphi)] \\ -p_y [\sin(kx) + \sin(kx - 2kL_1 - \Delta\varphi)] \end{Bmatrix} \left(E_+ e^{-ky} + E_- e^{ky} \right) \right\rangle \quad (5.66)$$

$$E_{1y}^{s} = \sum_{n} -\frac{k}{2\varepsilon_0 (L_1 + L_2)} \left\langle \begin{Bmatrix} p_x [\sin(kx) - \sin(kx - 2kL_1 - \Delta\varphi)] + \\ p_y [\cos(kx) + \cos(kx - 2kL_1 - \Delta\varphi)] \end{Bmatrix} \left(-B_+ e^{-ky} + B_- e^{ky} \right) \right\rangle \quad (5.67)$$

$$E_{2y}^{s} = \sum_{n} -\frac{k}{2\varepsilon_0 (L_1 + L_2)} \left\langle \begin{Bmatrix} p_x [\sin(kx) - \sin(kx - 2kL_1 - \Delta\varphi)] + \\ p_y [\cos(kx) + \cos(kx - 2kL_1 - \Delta\varphi)] \end{Bmatrix} \left(-F_+ e^{-ky} + F_- e^{ky} \right) \right\rangle \quad (5.68)$$

$$E_{3y}^{s} = \sum_{n} -\frac{k}{2\varepsilon_0 (L_1 + L_2)} \left\langle \begin{Bmatrix} p_x [\sin(kx) - \sin(kx - 2kL_1 - \Delta\varphi)] + \\ p_y [\cos(kx) + \cos(kx - 2kL_1 - \Delta\varphi)] \end{Bmatrix} \left(-G_+ e^{-ky} + G_- e^{ky} \right) \right\rangle \quad (5.69)$$

$$E_{1y}^{m} = \sum_{n} -\frac{k}{2\varepsilon_0 (L_1 + L_2)} \left\langle \begin{Bmatrix} p_x [\sin(kx) - \sin(kx - 2kL_1 - \Delta\varphi)] + \\ p_y [\cos(kx) + \cos(kx - 2kL_1 - \Delta\varphi)] \end{Bmatrix} \left(-C_+ e^{-ky} + C_- e^{ky} \right) \right\rangle \quad (5.70)$$

$$E_{2y}^{m} = \sum_{n} -\frac{k}{2\varepsilon_0 (L_1 + L_2)} \left\langle \begin{Bmatrix} p_x [\sin(kx) - \sin(kx - 2kL_1 - \Delta\varphi)] + \\ p_y [\cos(kx) + \cos(kx - 2kL_1 - \Delta\varphi)] \end{Bmatrix} \left(-D_+ e^{-ky} + D_- e^{ky} \right) \right\rangle \quad (5.71)$$

$$E_{3y}^{m} = \sum_{n} -\frac{k}{2\varepsilon_0 (L_1 + L_2)} \left\langle \begin{Bmatrix} p_x [\sin(kx) - \sin(kx - 2kL_1 - \Delta\varphi)] + \\ p_y [\cos(kx) + \cos(kx - 2kL_1 - \Delta\varphi)] \end{Bmatrix} \left(-E_+ e^{-ky} + E_- e^{ky} \right) \right\rangle \quad (5.72)$$

Based on this, the plasmonic performance of the tripod nanoantenas will be analytically evaluated in terms of F_{nr} calculated with Eq. 5.34 and the above expressions. The results will be compared with numerical simulations using the same boundary conditions and parameters as for the bowtie nanoantennas discussed in the previous section.

5.2.2 Plasmonic response evaluation

First, the tripod nanoantennas are studied considering a fixed air gap and changing the angle *θ'* of the arms. Here, the nano-structure shown in Fig. 5.9(a) is rotated 30º clockwise in order evaluate the symmetric case ($d_1 = d_2$ for the multi-slab geometry case).

The analytical and numerical results of the F_{nr} spectra for values of *θ'* from 5º to 45º are shown in the first and second column of Fig. 5.10, respectively, considering a vertical and horizontal polarization of the nanoemitter. From this figure it is clearly observed the good agreement between the numerical and the analytical values. It is shown that the first LSP mode with $n = 1$ is blue shifted from ~480nm (461 nm) to

~215 nm (214 nm) under vertical (horizontal) polarization of the dipole when θ' is changed from 5º to 45º, respectively. Note that the other peaks of F_{nr} are also blue-shifted when increasing θ', as expected, in agreement with the results of the bowtie nanoantenna discussed in Fig. 5.2. For completeness, the numerical results of the radiative Purcell enhancement spectra $F_{r,}$ are also shown in the third column for each polarization of the dipole. As it is shown, smaller values are obtained, compared with the F_{nr}, as expected.

It is interesting to note that the the tripod nano-structure operates in the UV range, due to the fact that the size of the tripod is smaller than the bowtie nanoantenna. Hence, the peaks of F_{nr} and F_r are expected to be shifted to smaller wavelengths. For the sake of completeness, the results of the analytical and numerical results of the F_{nr} along with the F_r for the case of tripod nanoantennas with θ' = 10º, 20º and 30º under vertical and horizontal polarization of the dipole are shown in Fig. 5.11 where the agreement is more clearly shown.

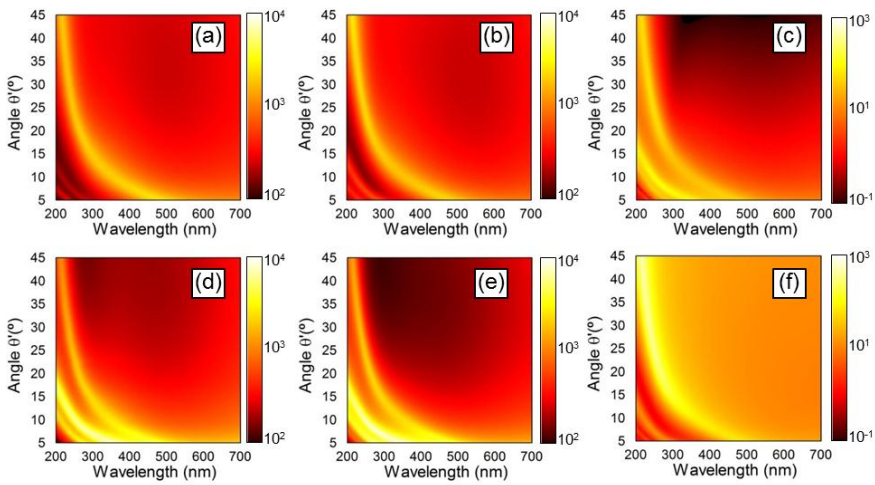

Figure 5.10. Analytical (first column) and simulation (second column) results in log scale of the non-radiative Purcell enhancement along with the radiative Purcell spectra (third column) for tripod nanoantennas with θ' ranging from 5º to 45ºwhen they are illuminated with a vertical (first row) and an horizontal dipole (second row).

All the previous studies in this chapter have been carried out considering only a vertical or a horizontal polarization of the nanoemitter close to the nanoantennas. However, it is also interesting to evaluate the performance when the dipole is polarized for values within these two extreme cases. For this purpose, a tripod nanoantenna with θ' = 10º is used and the results of F_{nr} are shown in Fig. 5.12 when

the polarization of the dipole is changed from vertical (θ'_{pol} = 0º) to horizontal (θ'_{pol} = 90º). By comparing the analytical and numerical results shown in Fig. 5.11(a,b) a very good agreement is observed. For completeness, the numerical results of F_r are also shown in Fig. 5.12(c).

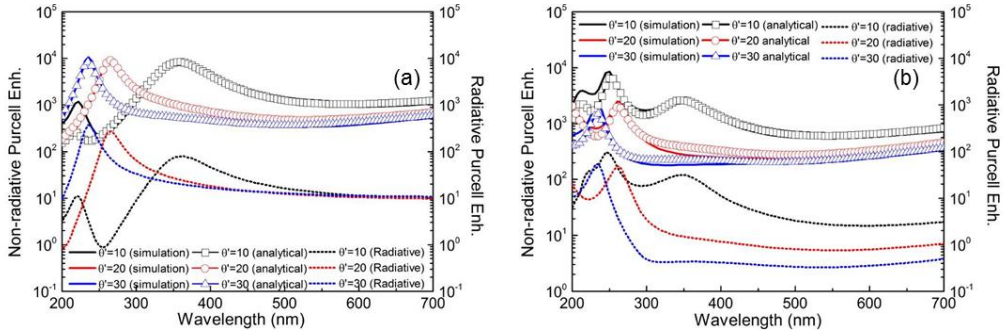

Figure 5.11. Analytical (symbols) and simulation (solid lines) results of the non-radiative Purcell enhancement along with the radiative Purcell spectra (dotted lines) for bowtie antennas with θ' ranging from 10º to 30º with a step of 10º when they are illuminated with a vertical (a) and an horizontal dipole (b).

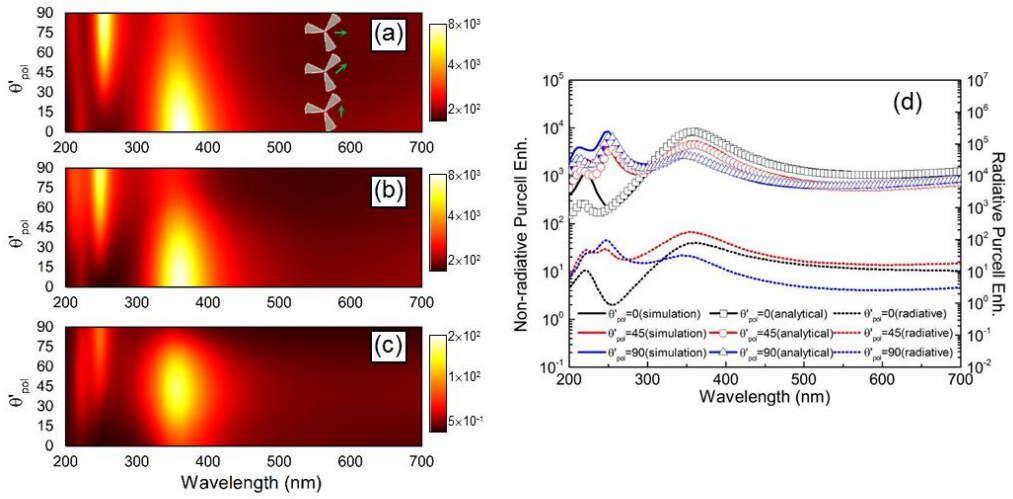

Figure 5.12. Analytical (a) and simulation (b) results of the non-radiative Purcell enhancement along with the radiative Purcell spectra (c) for a bowtie antenna with θ' = 10º when it is illuminated by a dipole with different polarizations ranging from 0º to 90º which correspond to a vertical and horizontal dipole, respectively. (d) Results for three different angles of polarization of the dipole. The contour plots are in linear scale to better appreciate the results.

It can be observed that the peak of F_{nr} related to the LSP mode with n = 1 has higher values when a vertical dipole is used. On the contrary, higher values of F_{nr} are obtained for the other two higher LSP modes when the polarization of the dipole is horizontal. These results demonstrate that the non-radiative Purcell enhancement has a dependence on the polarization of the dipole and there are preferred polarizations when it can be increased, in good agreement with the results shown in Fig. 5.2 for the case of the bowtie nanoantenna. For the sake of completeness, the results for θ'_{pol} = 0º, 45º and 90º are shown in Fig. 5.12(d) where the agreement between the numerical and the analytical results is more evident.

As mentioned before, there are other cases that can be studied using the bowtie and tripod nanoantennas such as different materials of the arms, rotation of the nanoantennas, position of the dipole, asymmetric nano-structures and also going beyond the quasi-static limit. These cases are now under study but they are not included in this thesis because they need a more thorough analysis. The results expected and the future work foreseen will be underlined in Chapter 6.

Chapter 6

Conclusions and future work

This final chapter shows a summary of the main conclusions obtained in this thesis. Furthermore, despite that several studies have been presented for each structure reported on each chapter, there are still many improvements and applications that can be performed which are susceptible for further investigation. Also, as commonly occurs in research, for each solution or proposed designs, several new ideas can emerge which are interesting to be evaluated. Hence, a list of task to be evaluated is presented which hopefully will be further studied and explored in the near future.

6.1 Conclusions

Chapter 2:

- A narrow hollow rectangular waveguide can emulate an effective ENZ medium working near cut-off. This is due to the almost infinite wavelength, almost zero propagation constant and high phase velocity of waves traveling through them.

  Una guía de onda rectangular de agujero estrecho puede emular un medio efectivo ENZ trabajando cerca del corte. Esto se debe a la casi infinita longitud de onda, un valor cercano a de la constante de propagación y alta velocidad de fase de las ondas que viajan a través de ellas.

- The mechanical beam steering performance of a plano-concave ENZ-lens working at the D-band of millimeter waves has been demonstrated experimentally, numerically and analytically using the Huygens-Fresnel approximation.

  La respuesta mecánica de direccionamiento de haz de una lente ENZ plano-cóncava trabajando en la banda D de ondas milimétricas ha sido demostrada experimental, numérica y analíticamente haciendo uso de la aproximación de Huygens-Fresnel.

- A suitable beam steering up to ±15º has been achieved with the proposed plano-concave ENZ-lens considering a gain scan loss below 3dB.

  Un adecuado direccionamiento de haz hasta ±15º ha sido logrado con la lente ENZ plano-cóncava considerando una pérdida de ganancia de escaneo por debajo de 3dB

- The beam shaping capabilities of ENZ media has been demonstrated by using a prism made with stacked narrow hollow rectangular waveguides designed to deflect an incoming planewave to an output angle of 45º at THz frequencies.

  Las capacidades de moldeado de haz de los medios ENZ ha sido demostrada haciendo uso de un prisma hecho de guias de onda rectangulares estrechas apiladas diseñadas para deflectar una onda plana en la entrada a un ángulo de salida de 45º a frecuencias de THz.

- To reduce the volume of the ENZ prism, the GRIN technique has been applied in the design of beam steerers using an array of stacked narrow hollow

waveguides. The dimensions of each waveguide has been designed in order to obtain the required phase delay at their output and achieve impedance matching with free-space.

Con el fin de reducir el volúmen del prisma ENZ, la técnica GRIN ha sido aplicada en el diseño de direccionadores de haz haciendo uso de un arreglo de guias de onda estrechas. Las dimensiones de cada guía de onda han sido diseñadas con el fin de obtener el retardo de fase deseado a la salida y alcanzar adaptación de impedancias con el espacio libre.

- Symmetrical and asymmetrical ENZ-GRIN power splitters have been also proposed with output angles of (±45º) and (−80º, +35º) demonstrating a good agreement between the numerical and the designed output angles.

  Divisores de potencia ENZ-GRIN simétricos y anti-simétricos han sido también propuestos con ángulos de salida de (±45º) y (–80º, +35º) demostrando un buen acuerdo entre los resultados numéricos y los ángulos de salida seleccionados en el diseño.

- The first experimental demonstration of an ENZ-GRIN metalens at THz frequencies has been presented. A high power enhanmcement of 42 times of the incident power at the *FL* has been achieved experimentally at 0.675 THz, with an excellent agreement with numerical simulations.

  Se ha presentado la primera demostración experimental de una lente metálica ENZ-GRIN a frecuencias de terahercio. Una alta mejora de potencia de 42 veces la potencia incidente en la posición de foco ha sido lograda a la frecuencia experimental de 0.675 THz con un acuerdo excelente con simulaciones numéricas.

- An in-depth theoretical study of an ENZ-based sensor has been presented using the transmission line theory. The sensor has been designed using a narrow hollow rectangular waveguide working as an ENZ medium with a high sensitivity (up to 0.04 m/RIU) and *FoM* (about 20).

  Se ha presentado un estudio teórico en profundidad de un sensor ENZ haciendo uso de la teoría de líneas de transmisión. El sensor se ha diseñado usando una guía de onda rectangular estrecha trabajando como un medio ENZ con una alta sensibilidad (hasta 0.04 m/RIU) y FoM (con un valor cercano a 20).

- An excellent performance of the sensing platform has been obtained even with very small analyte sizes (~$0.075\lambda_0$).

Se ha obtenido una excelente respuesta de la plataforma de sensado aún con analitos de tamaños muy pequeños (~0.075λ_0).

- The effective medium approach has been applied to the ENZ sensor by treating the inhomogeneous cross section of the analyte as a transmission line filled with a homogeneous material.

  El enfoque de medio efectivo se ha aplicado al sensor ENZ considerando la sección transversal inhomogénea del analito como una línea de transmisión rellena con un material homogéneo.

- The dispersion of metal-dielectric-metal plasmonic waveguides has been exploited to artificially mimic an ENZ medium at optical wavelengths by working near the cut-off of the TE_1 mode demonstrating that the ENZ performance may be emulated within the whole visible spectrum by simply changing the percentage of dielectric and metal per unit cell.

  La dispersión de guias plasmónicas del tipo metal-dielectrico-metal ha sido explotada para imitar artificialmente un medio ENZ en longitudes de onda del visible trabajando cerca del corte del modo TE_1 demostrando que la respuesta ENZ puede ser emulada dentro de todo el espectro visible simplemente ajustando el porcentaje de dieléctrico y metal por celda uidad

- Several types of focusing metalenses have been designed at λ_0 = 474.9 nm (*f* = 631.67 THz) using arrays of plasmonic waveguides emulating an ENZ medium. The best performance is obtained with GRIN design offering a reduction of volume of ~52% compared with the full concave profiled metalens.

  Varios tipos de lentes de enfoque han sido diseñadas a λ_0 = 474.9 nm (f = 631.67 THz) usando arreglos de guias de onda plasmónicas emulando a un medio ENZ. Los mejores resultados se han obtenido con el diseño GRIN ofreciendo una reducción de volumen de ~52% comparados con la lente cóncava con perfil completo.

Chapter 3:

- The fishnet MTM with double in-plane periodicity used in this thesis has a strongly dispersive effective negative refractive index within a spectral range below the cut-off frequency of the holes.

El metamaterial de tipo red de pesca "fishnet" con doble periodicidad en el plano utilizado en ésta tesis posee una repuesta fuertemente dispersiva con índice de refracción negativo en una banda espectral por debajo del corte de los agujeros.

- It has been demonstrated that the zoning technique can be applied to the fishnet metamaterial in order to design compact focusing devices.

  Se ha demostrado que la técnica de zonado se puede aplicar al metamaterial tipo red de pezca con el fin de diseñar dispositivos de enfoque compactos.

- A zoned cylindrical plano-concave fishnet MTM lens working at millimeter wavelengths has been designed, fabricated and measured with a good agreement between them in terms of the *FL, FWHM* and *DF*.

  Una lente metamaterial de tipo fishnet cilíndrica plano-cóncava ha sido diseñada, fabricada y medida trabajando a ondas milimétricas con un buen acuerdo entre ellos en términos de FL, FWHM y DF.

- The power enhancement at the *FL* achieved with the fishnet MTM lens has been 11.1 dB, which is in good agreement with simulations and also with previous plano-concave and biconcave lenses using this MTM.

  La mejora de potencia en el foco alcanzada con la lente metamaterial tipo fishnet ha sido 11.1 dB, la cual está en buen acuerdo con los resultados de simulación y con lentes plano-cóncavas y bióncavas reportadas previamente.

- The advantage of the zoned lens proposed is the volume reduction of 60% compared with a non-zoned lens made with the fishnet MTM.

  La ventaja de la lente zonada propuesta es la reducción de volumen de 60% comparada con una lente no zonada hecha con el metamaterial tipo fishnet.

- The fishnet MTM lens is an alternative to conventional binary zone plates, which, unlike the zoned fishnet lens, cannot be free-space matched and display dielectric losses arisen from the unavoidable sustaining substrate.

  La lente metamaterial tipo fishnet es una alternativa a las convencionales zonas de placas binarias que, a diferencia de las lentes zonadas fishnet, no pueden ser adaptadas al espacio libre y tienen pérdidas de dieléctrico debido a los inevitables sustratos.

- The steering capabilities in the radiation pattern of the lens have been evaluated experimentally and numerically demonstrating that a suitable beam steering up to 10º can be achieved considering a standard 3 dB scan loss.

  Las capacidades de direccionamiento de haz del patrón de radiación de la lente han sido evaluadas experimental y numéricamente demonstrando un direccionamiento de haz adecuado de hasta 10º considerando el estándar de pérdidas de escaneo de 3 dB.

- The reference phase technique has been applied to the fishnet metalens to improve its performance in terms of the reduction of *SLL*. A general expression of the zoning profile has been shown to include the extra-phase added to the first zone with this technique.

  La técnica de referencia de fase se ha aplicado a la metalente de tipo fishnet con el fin de mejorar su respuesta en términos de una reducción de sus lóbulos laterales. Una expresión general del perfil zonado se ha mostrado para incluir la fase extra añadida a la primera zona con ésta técnica.

- The focusing properties of several zoned fishnet metalenses with different positive reference phase factors have been evaluated demonstrating numerically that the higher power intensity at the *FL* and lower first *SLL* are achieved for the design with $q = 0.35$.

  Las propiedades focales de varias lentes zonadas metamaterials tipo fishnet con diferentes valores positivos de referencia de fase han sido evaluadas demonstrando numéricamente que la mayor intensidad de potencia en el foco y mejores primeros lóbulos laterales son obtenidos para el diseño con q = 0.35.

- Stimulated by these numerical studies, $q = 0$ and $q = 0.35$ have been fabricated demonstrating a better performance for the design wiith $q = 0.35$ in focusing and radiation properties, compared with the case $q = 0$.

  Estimulados por estos resultados numéricos, q = 0 y q = 0.35 han sido fabricados, demostrando mejores resultados para el diseño con q = 0.35 en las propiedades del foco y patrón de radiación, comparadas con el caso q = 0.

- These results have demonstrated that the techniques applied to FZPA can be used to improve the performance of the zoned fishnet metalens.

  Estos resultados han demostrado que las técnicas aplicadas en FZPA pueden ser usadas para mejorar la respuesta de las lentes zonadas metamateriales tipo fishnet.

- Several fishnet metalenses have been designed with a small *FL* of 1.5 λ_0 at the frequency of 55 GHz. Here, positive and negative values of reference phase have been used (q = -0.35, q = 0 and q = 0.35) in order to study its influence. The focusing performance of the three designs has been evaluated both numerically and experimentally, demonstrating a good agreement between them.

  Varias lentes metamaterials tipo fishnet han sido diseñadas con un foco a una distancia pequeña de 1.5 λ_0 a la frecuencia de 55 GHz. Aquí, valores positivos y negativos de referencia de fase han sido usados (q = -0.35, q = 0 y q = 0.35) con el fin de estudiar su influencia. Las propiedades del foco de los tres diseños han sido evaluadas numérica y experimentalmente demonstrando un buen acuerdo entre ambos.

- A clear focus has been obtained for the designs with q = 0 and q = 0.35 while the focus has been strongly deteriorated for the case with a negative reference phase (q = −0.35). This is due to the fact that the metalens in the latter case is only made with one zoned plate. Hence, its profile is almost a single grating which produces a focus with strong *SLL*.

  Un foco claro ha sido obtenido para los diseños q = 0 y q = 0.35 mientras que el foco es fuertemente deteriorado para el caso con un valor negativo de referencia de fase (q = -0.35). Esto se debe a que la lente en el último caso es hecha solamente de una placa zonada. Por tanto, su perfil es aproximado a un simple grating, lo cual produce un foco con elevados lóbulos laterales.

- The profile of the fishnet metalenses with small *FL* has been changed from concave to convex in order to evaluate their performance when the phase distribution inside of them is reversed. From the results of the expectral response, it has been shown that the chromatic dispersion is reduced with these designs compared with the concave profiles.

  El perfil de las lentes metamateriales tipo fishnet con un pequeño FL ha sido cambiado de cóncavo a convexo con el fin de evaluar sus respuestas cuando la distribución de fase dentro de ellas es revertida. A partir de los resultados de la respuesta espectral, se ha mostrado que la aberración cromática es reducida con estos diseños, comparados con los perfiles cóncavos.

- The best performance of the focus in terms of the power enhancement, reduced *FWHM*, *DF* and a *FL* close to the designed value has been achieved with the design q = 0.35 (i.e., when both, reference phase and phase reversal techniques are applied).

La mejor respuesta en el foco en térinos de la mejora en potencia, reducido FWHM, DF y un FL cerca del valor diseñado ha sido lograda con la lente q = 0.35 (es decir cuando ambas técnicas, referencia de fase y fase revertida, son aplicadas.

- It has been shown that spherical aberrations are produced with these designs because of the increased *DF* compared with the concave metalenses. However, the convex profiles can be used in applications where a wideband response is needed due to the reduced chromatic aberration of the focus.

  Se ha mostrado que aberraciones esféricas son producidas con éstos diseños debido al incremento de DF comparados con las lentes cóncavas. Sin embargo, los perfiles convexos pueden ser usados en aplicaciones donde mayor ancho de banda sea requerido debido a la reducida dispersión cromática del foco.

Chapter 4:

- 3D dielectric cuboids working at THz frequencies have been studied numerically with the ability to generate teajets (similar to PNJs at optical frequencies) at its output surface under plane wave illumination.

  Cuboides dieléctricos 3D trabajando a frecuencias de terahercio han sido estudiados numéricamente con la habilidad de generar terajets (similar a PNJs a frecuencias ópticas) a su salida bajo una iluminación de onda plana.

- By changing the refractive index of the 3D cuboids, it has been shown that the focus is moved from inside to outside the structure with a quasi-symmetric terajet and a high intensity of about 10 times the illuminating power when n = 1.41. Moreover, the contrast between the refractive index of the cuboid and the background medium should be less than 2 in order to produce the terajet at the output surface of the cuboid.

  Se ha mostrado que, si se cambia el índice de refracción de los cuboides dieléctricos, el foco se mueve desde dentro hacia fuera de la estructura con un terajet quasi-simétrico y una alta intensidad de cerca de 10 veces la potencia de iluminación cuando n = 1.41. Ademñas, el contraste entre el índice de refracción del cuboide y del medio que lo rodea debe ser menor que 2 con el fin de producir el terajet en la superficie de salida del cuboide.

- It has been demonstrated that 3D dielectric cuboids have the ability to enhance the backscattering perturbation when gold spheres of different sizes are introduced within the terajet region.

  Se ha demostrado que los cuboides dieléctricos 3D tienen la habilidad de mejorar la radiación tracera cuando esferas de oro con diferentes tamaños son introducidas dentro de la región del terajet.

- The capability to generate multifrequency terajets using 3D dielectric cuboids has been studied at THz frequencies. It has been shown that an intensity enhancement of ∼10, ∼18, and ∼14 for the fundamental frequency and the first and second harmonics, respectively, is achieved with a subwavelength focus in all these cases.

  La capacidad de generar terajets multifrecuencia usando cuboides dieléctricos 3D ha sido estudiada a frecuencias de terahercio. Se ha mostrado que una mejora de intensidad de ~10, ~18 y ~14 es obtenida para la frecuencia fundamental y primer y segundo harmónico, respectivamente, con un foco sublambda en todos los casos.

- The terajet performance using 3D dielectric cuboids has been evaluated under oblique incidence demonstrating that the terajet not deteriorated in terms of the intensity at the focus for input angles from 0º - 45º.

  La respuesta del terajet usando cuboides dieléctricos 3D ha sido evaluada bajo incidencia oblícua demostrando el terajet no es deteriodado en términos de la intensidad en el foco para ángulos de entrada de 0º - 45º.

- Experimental results of the terajet generated by a 3D dielectric cuboid made of teflon (n = 1.46) have been presented at sub-THz frequencies demonstrating a good agreement with numerical simulations.

  Se han presentado resultados experimentales de terajets generados por un cuboide dieléctrico 3D hecho de teflón (n = 1.46) trabajando a frecuencias de sub-THz, demostrando un buen acuerdo con los resultados de simulación.

- The capability to design waveguides using an array of 3D dielectric cubes of refractive index n = 1.46 immersed in vacuum (n_0=1) has been studied demonstrating that the optimum distance between the cuboids should be ~2.5λ_0 in order to extend the maximum propagation distance of the EM waves.

Se ha estudiado la capacidad de diseñar guias de onda con un arreglo de cuboides dieléctricos 3D con índice de refracción n = 1.46 inmersos en aire (n_0 = 1), demostrando que la distancia óptima entre los cuboides debe ser de ~2.5 λ_0 con el fin de aumentar la máxima distancia de propagación de las ondas electromagnéticas.

- The influence of dielectric losses has been evaluated in terms of both transversal resolution and exploration range by introducing two overestimated values of loss tangent (tan δ = 0.05 and tan δ = 0.1). It has been shown that, even when higher dielectric losses are introduced, the resolution of the terajets is not strongly deteriorated.

  La influencia de las pérdidas de dieléctrico ha sido evaluada en términos de la resolución transversal y rango de exploración introduciendo dos valores de tangente de pérdidas sobreestimados (tan δ = 0.05 and tan δ = 0.1) Se ha mostrado que, aunque son introducidos valores grandes de pérdidas de dieléctrico, la resolución de los jets no es fuertemente deteriorada.

- The capability to produce PNJs using a 3D dielectric cuboid working in the reflection mode has been studied at the fundamental and first frequency harmonic. Numericla results have demonstrated that the best performance in terms of the *FL* and *FWHM* are obtained when the cuboid has the dimension along the *z* axis of $H = 0.33\lambda_0$ and $H = 0.4\lambda_0$.

  La capacidad de producir PNJs usando cuboides dieléctricos 3D trabajando en reflexión ha sido estudiada a la frecuencia fundamental y primer harmónico. Los resultados numéricos han demostrado que la mejor respuesta en términos del FL y FWHM son obtenidos cuando el cuboide tiene la dimensión a lo largo del eje z de $H = 0.33\lambda_0$ y $H = 0.4\lambda_0$.

- It has been shown that the position of the PNJ can be controlled under oblique incidence by simply extending the width of the cuboid, demonstrating that the PNJ can be parallel to the flat surface of the cuboid.

  Se ha mostrado que la posición del PNJ puede ser controlada bajo incidencia oblicua simplemente extendiendo la anchura del cuboide, demostrando que el PNJ puede estar paralelo a la superficie plane del cuboide.

- The excitation of PNJs in 3D dielectric cuboids by SPPs at telecom wavelengths has been proposed. The analysis has been carried out using the effective refractive index approach. It has been demonstrated that the contrast between the index of the region with and without the cuboid should be less than 2 in order to produce the PNJ at the output of the cuboid.

La excitación de PNJs en cuboides dieléctricos 3D a través de SPPs a longitudes de onda de telecomunicaciones ha sido propuesta. El análisis se ha llevado a cabo usando el enforque de índice de refracción efectivo. Se ha demostrado que el contrate entre índices de la región con y sin el cuboide debe ser menor que 2 con el fin de producir el PNJ a la salida del cuboide.

- The best performance of the PNJ at the wavelength of 1550 nm has been obtained when the height of the cuboids is 160 nm producing a jet just at the output interface with a resolution of 0.68 λ_0 and a high intensity enhancement of 5 times at the focus.

  La mejor respuesta del PNJ a la longitud de onda de 1550 nm ha sido obtenida cuando la altura del cuboide es 160 nm produciendo un jet justo en la interfaz de salida con una resolución de 0.68 λ_0 y una alta mejora de intensidad de 5 veces en el foco.

- The multi-wavelength response has been also studied for the PNJs excited with SPPs demonstrating that it is possible to use the proposed structure at different wavelengths.

  La respuesta de multiple-longitud de onda ha sido estudiada oara los PNJs excitados con SPPs demostrando que es posible usar la estructura propuesta a diferentes longitudes de onda.

- The backscattering enhancement has been numerically evaluated by inserting a metal particle within the PNJ region. The enhancement is below that obtained for the 3D cuboid under plane wave illumination. However, it has been shown that the proposed structure can still be used in sensing applications at telecom wavelengths.

  La mejora en radiación hacia atrás ha sido evaluada numéricamente insertando partículas metálicas dentro de la zona del PNJ. La mejora es menor que la obtenida con el cuboide dieléctrico bajo iluminación con onda plana. Sin embargo, se ha mostrado que la estructura propuesta puede usarse en aplicaciones de sensado a longitudes de onda de telecomunicaciones.

- An array of 3D cuboids producing PNJs excited by SPPs has been proposed at the telecom wavelength of 1550 nm. It has been demonstrated that the SPP propagation distance can be greater than 2 compared with the case without the cuboids, reaching a value of 19λ_0.

Se ha propuesto un arreglo de cuboides 3D produciendo PNJs excitados por SPPs a la longitud de onda de telecomunicación de 1550 nm. Se ha demostrado que la distancia de propagación de SPP puede ser mayor que 2 comparada con el casi sin cuboides, alcanzando un valor de $19\lambda_0$.

Chapter 5:

- The transformation optics concepts have been exploited to explain the dependence of the nonradiative decay spectra of bowtie and tripods nanoantennas on their geometrical parameters under dipole illumination.

  Los conceptos de transformación óptica han sido explotados para explicar la dependencia del decaimiento espectral no-radiativo de nanoantenas de tipo pajarita y trípodes en sus parámetros geométricos bajo una iluminación de un dipolo.

- The analytical solutions for bowtie and tripod nanoantennas have been rigorously derived based on conformal transformation in the quasi-static limit.

  Las soluciones anlíticas para nanoantenas de tipo pajarita y trípodes han sido rigurosamente derivadas basadas en la transformación conformada dentro del limite quasi-estático.

- For situations beyond the quasi-static limit, one could explore the implementation of a radiative correction based on a fictitious absorbing dipole in the transformed space.

  Para situaciones mas allá del límite quasi-estático, se podría explorar la implementación de una corrección radiativa basada en un dipolo absorvente ficticio en el espacio transformado.

- The conformal mapping approach here applied has enabled to describe in detail all the spectral features in the nonradiative Purcell enhancement of a nanoemitter placed in the vicinity of different bowtie and tripod nanoantennas.

  El enfoque del mapeo conformado aquí aplicado ha permitido describir en detalle todas las características espectrales en la mejora no-radiativa Purcell de un nano-emisor localizado en las cercanías de diferentes nanoantenas de tipo pajarita y trípodes.

6.2 Future work

- Experimental demonstration of ENZ-GRIN beam steerers and power splitters at THz frequencies.

  Demostración experimental de direccionadores de haz y divisores de potencia ENZ-GRIN a frecuencias de terahercio.

- Experimental demonstration of the ENZ-based sensor using subwavelength analytes.

  Demostración experimental del sensor ENZ usando analitos sublambda.

- Study of the time response of the ENZ-based sensor and experimental evaluation.

  Estudio de la respuesta temporal del sensor ENZ y evaluación experimental.

- Experimental demonstration of the ENZ lenses at visible frequencies.

  Demostración experimental de las lentes ENZ a frecuencias del visible.

- Design and experimental demonstration of GRIN converging lenses using all dielectric waveguides.

  Diseño y demostración experimental de lentes convergentes GRIN usando guías de ondas completamente dieléctricas.

- Experimental demonstration of PNJs produced by 3D dielectric cuboids in reflection mode at visible frequencies.

  Demostración experimental de PNJs producidos por cuboides dieléctricos 3D en modo de reflexión a frecuencias del visible.

- To combine waveguides and 3D dielectric cuboids with the aim to design millimeter and THz probes.

  Combinar guías de onda y cuboides dieléctricos 3D con el fin de diseñar sondas en el rango de ondas milimétricas y terahercio.

- Design of power dividers and beam steerers using 3D dielectric cuboids illuminated with SPPs.

  Diseño de divisores de potencia y direccionadores de haz usando cuboides dieléctricos 3D iluminados por SPPs.

- Experimental demonstration of PNJs produced by 3D dielectric cuboids excited by SPPs at THz and telecom wavelengths.

  Demostración experimental de PNJs producidos por cuboides dieléctricos 3D excitados por SPPs en terahercios y longitudes de onda de telecomunicaciones.

- To apply the zoning technique in the design of beam steerers using the fishnet MTM.

  Aplicar la técnica de zonado en el diseño de direccionadores de haz usando el metamaterial tipo fishnet.

- Evaluation of the influence of different metals on the nonradiative Purcell enhancement of bowtie and tripod nanoantennas using conformal transformation.

  Evaluación de la influencia de diferentes metales en la mejora Purcell no-radiative de nanoantenas tipo bowtie y trípodes usando transformación conformada.

- Analytical evaluation of bowtie and tripod nanoantennas with connected arms using conformal transformation.

  Evaluación analítica de nanoantenas tipo pajarita y trípodes con brazos conectados usando transformación conformada.

- Systematic study of the maximum diameter that can be evaluated using the quasi-static limit for bowtie and tripod nanoantennas with different metals.

  Estudio sistemático del máximo diámetro que puede ser evaluado bajo el límite quasi-estático para nanoantenas de tipo pajarita y trípodes con diferentes metales.

- Analytical evaluation of bowtie and tripod nanoantennas beyond the quasi-static limit.

  Evaluación analítica de nanoantenas tipo pajarita y trípodes mas allá del límite quasi-estático.

Appendix A

Surface Plasmons polaritons

Here, we will discuss the dispersive performance of SPPs for different configurations of the materials: We will start with the simplest case by studying an insulator-metal interface considering both media as semi-infinite. Then, more complex geometries are considered: insulator-metal-insulator (IMI) and insulator-insulator-metal-insulator (IIMI). This study is carried out using the effective media approach in order to obtain the expression of the effective wave number of SPPs for each case. Finally, a comparison between the single interface and (IMI) structures is presented in order to evaluate the influence of the thickness of the metal on the effective wave number of SPPs. In all the studies the terms A, B, C, D and E are constants.

i. Single interface (IM)

Let us first deduce the expression of the effective propagation constant of surface plasmons for a single interface. The schematic representation of the structure under study is shown in the following figure.

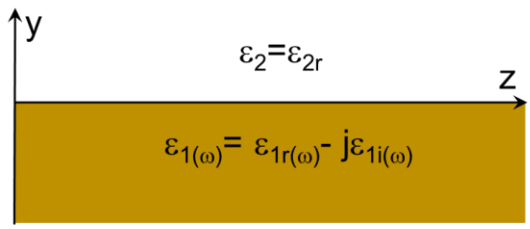

Figure A.1. Schematic representation of the two-layer system under study which consists of two semi-infinite media: dielectric (top) and metal (bottom).

Moreover, we assume media free from external charges and currents, leading to the following Maxwell's equations:

$$\nabla \times E = -\frac{\partial B}{\partial t} \xrightarrow{e^{j\omega t}} -j\omega\mu H \tag{A.1}$$

$$\nabla \times H = \frac{\partial D}{\partial t} \xrightarrow{e^{j\omega t}} j\omega\varepsilon E \tag{A.2}$$

Since we are dealing with a TM wave propagating along the *z*-axis, the electric field has components along both *z* and *y* axes while the magnetic field lies only along the *x*-axis; i.e. $H_z = H_y = E_x = 0$. Therefore, we only need to work with the non-zero components of *H* and *E*. The magnetic field can be expressed as follows:

$$H = H_x = Af(y)e^{-jk_z z} \tag{A.3}$$

where $k_z = k_{zr} - jk_{zi}$ is the wavenumber parallel to the interface shown in Fig.A.1 and *f(y)* defines the magnetic field dependence considering the interface of both media; it is defined as:

$$f(y) = \begin{cases} e^{-k_2 y} = e^{-y\sqrt{k_z^2 - \varepsilon_{2r}k_0^2}}; y > 0 \\ e^{k_1 y} = e^{y\sqrt{k_z^2 - \varepsilon_1 k_0^2}}; y < 0 \end{cases} \tag{A.4}$$

Now that we have defined the *H*-field, the *E*-field components are expressed as follows:

$$E_z = -\frac{j}{\omega\varepsilon}\frac{\partial H_x}{\partial y} = \begin{cases} -\frac{j}{\omega\varepsilon_2}(-k_2)Ae^{-jk_2 y}e^{-jk_z z}; y > 0 \\ -\frac{j}{\omega\varepsilon_1}(k_1)Ae^{jk_1 y}e^{-jk_z z}; y < 0 \end{cases} \tag{A.5}$$

$$E_y = \frac{j}{\omega\varepsilon}\frac{\partial H_y}{\partial z} = \begin{cases} \dfrac{k_z}{\omega\varepsilon_2} A e^{-jk_2 y} e^{-jk_z z}; y > 0 \\ \dfrac{k_z}{\omega\varepsilon_1} A e^{jk_1 y} e^{-jk_z z}; y < 0 \end{cases} \tag{A.6}$$

Note that with this condition we have a discontinuity of the component of the electric field perpendicular to the direction of propagation (E_y). Hence, the surface waves will be coupled to collective electron density oscillations generated by the free-electrons on the surface.

Now we can apply continuity of the tangential components of the electric field $E_{z(1)} = E_{z(2)}$ at the interface of both media ($y = 0$). The resulting dispersion relation is as follows:

$$-k_1\varepsilon_2 = k_2\varepsilon_1 \tag{A.7}$$

Then, we can work with Eqs. A.4-A.7 to calculate the expressions of the three unknown factors k_1, k_2 and k_z. After solving these equations, these factors are as follows:

$$k_1 = \frac{k_0\varepsilon_1}{\sqrt{\varepsilon_1 + \varepsilon_2}} \tag{A.8}$$

$$k_2 = -\frac{k_0\varepsilon_2}{\sqrt{\varepsilon_1 + \varepsilon_2}} \tag{A.9}$$

$$k_z = k_0\sqrt{\frac{\varepsilon_1\varepsilon_2}{\varepsilon_1 + \varepsilon_2}} \tag{A.10}$$

ii. Insulator-Metal-Insulator (IMI)

Now we will evaluate an interesting case when a metal film is in between two semi-infinite dielectrics, as it is shown in Fig.A.2

Following the steps described for the case of a single interface (Eqs. A.1-A.3), we can define the electric and magnetic field components for each region in Fig. A.2 as follows:

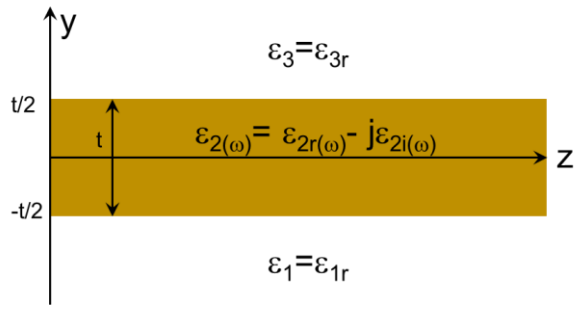

Figure A.2. Schematic representation of the IMI system under study. It consists of a metal film (with complex permittivity ε_2) in between two semi-infinite media with ε_1 and ε_3.

Region I: y > t/2

$$H_x = Ae^{-k_3 y}e^{-jk_z z} = Ae^{-\sqrt{k_z^2-\varepsilon_3 k_0^2}}e^{-jk_z z} \tag{A.11}$$

$$E_z = \frac{j}{\omega\varepsilon_3}k_3 Ae^{-k_3 y}e^{-jk_z z} = \frac{j}{\omega\varepsilon_3}k_3 Ae^{-\sqrt{k_z^2-\varepsilon_3 k_0^2}}e^{-jk_z z} \tag{A.12}$$

$$E_y = \frac{A}{\omega\varepsilon_3}k_z e^{-k_3 y}e^{-jk_z z} = \frac{A}{\omega\varepsilon_3}k_z e^{-\sqrt{k_z^2-\varepsilon_3 k_0^2}}e^{-jk_z z} \tag{A.13}$$

Region II: y < -t/2

$$H_x = Be^{k_1 y}e^{-jk_z z} = Be^{\sqrt{k_z^2-\varepsilon_1 k_0^2}}e^{-jk_z z} \tag{A.14}$$

$$E_z = -\frac{j}{\omega\varepsilon_1}k_3 Be^{k_3 y}e^{-jk_z z} = -\frac{j}{\omega\varepsilon_1}k_1 Be^{\sqrt{k_z^2-\varepsilon_1 k_0^2}}e^{-jk_z z} \tag{A.15}$$

$$E_y = \frac{B}{\omega\varepsilon_1}k_z e^{k_1 y}e^{-jk_z z} = \frac{B}{\omega\varepsilon_1}k_z e^{\sqrt{k_z^2-\varepsilon_1 k_0^2}}e^{-jk_z z} \tag{A.16}$$

Region III: -t/2 < y < t/2

$$H_x = Ce^{k_2 y}e^{-jk_z z} + De^{-k_2 y}e^{-jk_z z} = Ce^{\sqrt{k_z^2-\varepsilon_2 k_0^2}y}e^{-jk_z z} + De^{-\sqrt{k_z^2-\varepsilon_2 k_0^2}y}e^{-jk_z z} \tag{A.17}$$

$$\begin{aligned} E_z &= -\frac{j}{\omega\varepsilon_2}k_2 Ce^{k_2 y}e^{-jk_z z} + \frac{j}{\omega\varepsilon_2}k_2 De^{-k_2 y}e^{-jk_z z} \\ &= -\frac{j}{\omega\varepsilon_2}k_2 Ce^{\sqrt{k_z^2-\varepsilon_2 k_0^2}y}e^{-jk_z z} + \frac{j}{\omega\varepsilon_2}k_2 De^{-\sqrt{k_z^2-\varepsilon_2 k_0^2}y}e^{-jk_z z} \end{aligned} \tag{A.18}$$

$$\begin{aligned} E_x &= \frac{k_z}{\omega\varepsilon_2}Ce^{k_2 y}e^{-jk_z z} + \frac{k_z}{\omega\varepsilon_2}De^{-k_2 y}e^{-jk_z z} \\ &= \frac{k_z}{\omega\varepsilon_2}Ce^{\sqrt{k_z^2-\varepsilon_2 k_0^2}y}e^{-jk_z z} + \frac{k_z}{\omega\varepsilon_2}De^{-\sqrt{k_z^2-\varepsilon_2 k_0^2}y}e^{-jk_z z} \end{aligned} \tag{A.19}$$

Now, if we apply the boundary conditions as for the case of a single interface (i.e., the continuity of the tangential components of the E_z and H_x fields) at $z = -t/2$ and $z = -t/2$, we obtain the following system of equations:

$$Ae^{-\frac{1}{2}k_3 t} = Ce^{\frac{1}{2}k_2 t} + De^{-\frac{1}{2}k_2 t} \tag{A.20}$$

$$\frac{k_3}{\varepsilon_3}Ae^{-\frac{1}{2}k_3 t} = -\frac{k_2}{\varepsilon_2}Ce^{\frac{1}{2}k_2 t} + \frac{k_2}{\varepsilon_2}De^{-\frac{1}{2}k_2 t} \tag{A.21}$$

$$Be^{-\frac{1}{2}k_1 t} = Ce^{-\frac{1}{2}k_2 t} + De^{\frac{1}{2}k_2 t} \tag{A.22}$$

$$-\frac{k_1}{\varepsilon_1}Be^{-\frac{1}{2}k_1 t} = -\frac{k_2}{\varepsilon_2}Ce^{-\frac{1}{2}k_2 t} + \frac{k_2}{\varepsilon_2}De^{\frac{1}{2}k_2 t} \tag{A.23}$$

After applying basic algebra, this system of equations can be solved resulting in the following expression:

$$e^{2k_2 t}\left[\frac{\left(\frac{k_2}{\varepsilon_2}+\frac{k_1}{\varepsilon_1}\right)\left(\frac{k_2}{\varepsilon_2}+\frac{k_3}{\varepsilon_3}\right)}{\left(\frac{k_2}{\varepsilon_2}-\frac{k_1}{\varepsilon_1}\right)\left(\frac{k_2}{\varepsilon_2}-\frac{k_3}{\varepsilon_3}\right)}\right]=1 \tag{A.24}$$

Which can be further simplified resulting in the following transcendental equation for the propagation constant of the coupled SPP mode:

$$\tanh(k_2 t)=-\left(\frac{\varepsilon_1\varepsilon_2 k_2 k_3+\varepsilon_3\varepsilon_2 k_1 k_2}{\varepsilon_1\varepsilon_3 k_2^2+\varepsilon_2^2 k_1 k_3}\right) \tag{A.25}$$

By numerically solving the previous equation, the propagation constant of the SPP mode (k_z) for the IMI structure can be calculated. Note that from equation Eqs. A.24-A.25, when the thickness of the metal film is infinite ($t\to\infty$), the solution is reduced to the single layer system as it has been shown in equation A.7 but now for each interface shown in Fig. A.2:

$$-k_1\varepsilon_2=k_2\varepsilon_1 \tag{A.26a}$$

and

$$-k_3\varepsilon_2=k_2\varepsilon_3 \tag{A.26b}$$

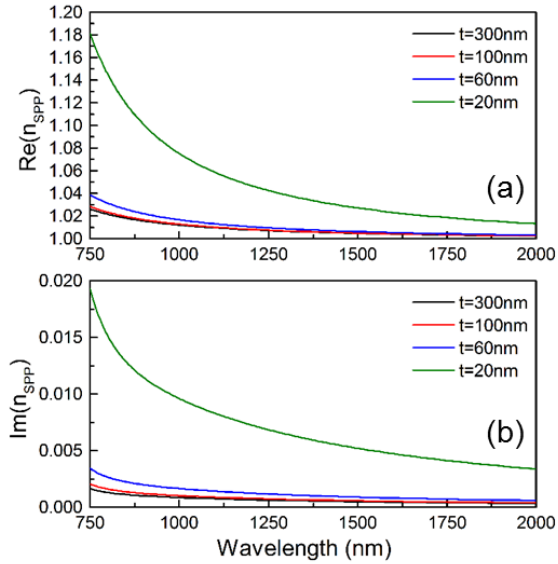

Figure A.3. Analytical results of the real (a) and imaginary (b) values of the complex effective refractive index for the case of an IMI structure with $\varepsilon_1 = \varepsilon_3 = 1$ and several metal thicknesses.

Fig. A.3 shows the analytical results of the complex effective refractive index as a function of wavelength for the case of an IMI structure with different values of metal thickness *t*. Here we simplify the analysis to the case where $\varepsilon_1 = \varepsilon_3 = 1$. A dispersive model of gold is used for the metal according to Johnson and Christy experimental data [JOHN 72]. The effective refractive index is calculated as:

$$n_{eff} = k_z / k_0 \tag{A.27}$$

It can be observed the influence of the metal thickness on the effective refractive index of the SPPs. As it is expected, for very thin metals (such as t = 20nm), the effective n is increased compared with those values obtained with t = 100 nm and t = 300 nm, due to the fact that the top and bottom SPPs are coupled. Moreover, note that the effective index for t = 100 nm and t = 300 nm almost overlap with the whole spectral range. This is because the effective index is approximately equal to the case of a single interface (air-metal).

iii. Insulator-insulator-Metal-Insulator (IIMI)

Now that we have evaluated the IM and IMI structures, we can also evaluate the case of the IIMI multilayer system shown in Fig. A.4.

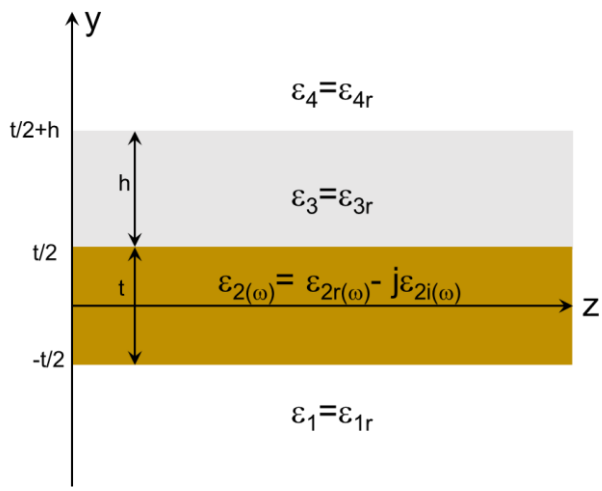

Figure A.4. Schematic representation of the IIMI system under study which consists of a metal film (with complex permittivity ε_2) and a dielectric with thickness h and permittivity ε_3 in between of two semi-infinite dielectric media with ε_1 and ε_4.

Following the same procedure as in the previous cases we can define the electric and magnetic field components for each region in Fig. A.4 as follows:

Region I: y < -t/2

$$H_x = Ae^{k_1 y}e^{-jk_z z} = Ae^{\sqrt{k_z^2-\varepsilon_1 k_0^2}}e^{-jk_z z} \tag{A.28}$$

$$E_z = -\frac{j}{\omega\varepsilon_1}k_1 Ae^{k_1 y}e^{-jk_z z} = -\frac{j}{\omega\varepsilon_1}k_1 Ae^{\sqrt{k_z^2-\varepsilon_1 k_0^2}}e^{-jk_z z} \tag{A.29}$$

$$E_y = \frac{A}{\omega\varepsilon_1}k_z e^{k_1 y}e^{-jk_z z} = \frac{A}{\omega\varepsilon_1}k_z e^{\sqrt{k_z^2-\varepsilon_1 k_0^2}}e^{-jk_z z} \tag{A.30}$$

Region II: -t/2 < y < t/2

$$H_x = Be^{k_2 y}e^{-jk_z z} + Ce^{-k_2 y}e^{-jk_z z} = Be^{\sqrt{k_z^2-\varepsilon_2 k_0^2}}e^{-jk_z z} + Ce^{-\sqrt{k_z^2-\varepsilon_2 k_0^2}}e^{-jk_z z} \quad \text{(A.31)}$$

$$E_z = -\frac{j}{\omega\varepsilon_2}k_2 Be^{k_2 y}e^{-jk_z z} + \frac{j}{\omega\varepsilon_2}k_2 Ce^{-k_2 y}e^{-jk_z z} = -\frac{j}{\omega\varepsilon_2}k_2 Be^{\sqrt{k_z^2-\varepsilon_2 k_0^2}}e^{-jk_z z} + \frac{j}{\omega\varepsilon_2}k_2 Ce^{-\sqrt{k_z^2-\varepsilon_2 k_0^2}}e^{-jk_z z} \quad \text{(A.32)}$$

$$E_y = \frac{k_z}{\omega\varepsilon_2}Be^{k_2 y}e^{-jk_z z} + \frac{k_z}{\omega\varepsilon_2}k_2 Ce^{-k_2 y}e^{-jk_z z} = \frac{k_z}{\omega\varepsilon_2}Be^{\sqrt{k_z^2-\varepsilon_2 k_0^2}}e^{-jk_z z} + \frac{k_z}{\omega\varepsilon_2}Ce^{-\sqrt{k_z^2-\varepsilon_2 k_0^2}}e^{-jk_z z} \quad \text{(A.33)}$$

Region III: t/2 < y < h

$$H_x = De^{k_3 y}e^{-jk_z z} + Ee^{-k_3 y}e^{-jk_z z} = De^{\sqrt{k_z^2-\varepsilon_3 k_0^2}}e^{-jk_z z} + Ee^{-\sqrt{k_z^2-\varepsilon_3 k_0^2}}e^{-jk_z z} \quad \text{(A.34)}$$

$$E_z = -\frac{j}{\omega\varepsilon_3}k_3 De^{k_3 y}e^{-jk_z z} + \frac{j}{\omega\varepsilon_3}k_3 Ee^{-k_3 y}e^{-jk_z z} = -\frac{j}{\omega\varepsilon_3}k_3 De^{\sqrt{k_z^2-\varepsilon_3 k_0^2}}e^{-jk_z z} + \frac{j}{\omega\varepsilon_3}k_3 Ee^{-\sqrt{k_z^2-\varepsilon_3 k_0^2}}e^{-jk_z z} \quad \text{(A.35)}$$

$$E_y = \frac{k_z}{\omega\varepsilon_3}De^{k_3 y}e^{-jk_z z} + \frac{k_z}{\omega\varepsilon_3}k_3 Ee^{-k_3 y}e^{-jk_z z} = \frac{k_z}{\omega\varepsilon_3}De^{\sqrt{k_z^2-\varepsilon_3 k_0^2}}e^{-jk_z z} + \frac{k_z}{\omega\varepsilon_3}Ee^{-\sqrt{k_z^2-\varepsilon_3 k_0^2}}e^{-jk_z z} \quad \text{(A.36)}$$

Applying the continuity of the tangential components of the H_x and E_z fields at $z = -t/2$ we obtain the following set of equations:

$$Ae^{-\frac{1}{2}k_1 t} = Be^{-\frac{1}{2}k_2 t} + Ce^{\frac{1}{2}k_2 t} \quad \text{(A.37)}$$

$$-\frac{k_1}{\varepsilon_1}Ae^{-\frac{1}{2}k_1 t}=-\frac{k_2}{\varepsilon_2}Be^{-\frac{1}{2}k_2 t}+\frac{k_2}{\varepsilon_2}Ce^{\frac{1}{2}k_2 t} \tag{A.38}$$

We can also apply the same boundary conditions at the interface $z = t/2$:

$$Be^{\frac{1}{2}k_2 t}+Ce^{-\frac{1}{2}k_2 t}=De^{\frac{1}{2}k_3 t}+Ee^{-\frac{1}{2}k_3 t} \tag{A.39}$$

$$-\frac{k_2}{\varepsilon_2}Be^{\frac{1}{2}k_2 t}+\frac{k_2}{\varepsilon_2}Ce^{-\frac{1}{2}k_2 t}=-\frac{k_3}{\varepsilon_3}De^{\frac{1}{2}k_3 t}+\frac{k_3}{\varepsilon_3}Ee^{-\frac{1}{2}k_3 t} \tag{A.40}$$

Finally, at the interface $z = t/2+h$:

$$De^{k_3\left(\frac{1}{2}t+h\right)}+Ee^{-k_3\left(\frac{1}{2}t+h\right)}=Fe^{-k_4\left(\frac{1}{2}t+h\right)} \tag{A.41}$$

$$-\frac{k_3}{\varepsilon_3}De^{k_3\left(\frac{1}{2}t+h\right)}+\frac{k_3}{\varepsilon_3}Ee^{-k_3\left(\frac{1}{2}t+h\right)}=\frac{k_4}{\varepsilon_4}Fe^{-k_4\left(\frac{1}{2}t+h\right)} \tag{A.42}$$

Note that we have obtained a set of 6 equations which involve 6 unknown variables. After working with Eqs. A.37-A.38 and Eqs. A.41-A.42 we can reduce these 4 equations into two equations. The results are as follows:

$$Be^{-\frac{1}{2}k_2 t}\left(\frac{k_2}{\varepsilon_2}-\frac{k_1}{\varepsilon_1}\right)-Ce^{\frac{1}{2}k_2 t}\left(\frac{k_2}{\varepsilon_2}+\frac{k_1}{\varepsilon_1}\right)=0 \tag{A.43}$$

$$De^{k_3\left(\frac{1}{2}t+h\right)}\left(\frac{k_4}{\varepsilon_4}+\frac{k_3}{\varepsilon_3}\right)+Ee^{-k_3\left(\frac{1}{2}t+h\right)}\left(\frac{k_4}{\varepsilon_4}-\frac{k_3}{\varepsilon_3}\right)=0 \tag{A.44}$$

Finally, we can rearrange our system of equations (A.39-A.40 and A.43-A.44) in a matrix form, as follows:

$$\begin{bmatrix} e^{\frac{1}{2}k_2 t} & e^{-\frac{1}{2}k_2 t} & -e^{\frac{1}{2}k_3 t} & e^{-\frac{1}{2}k_3 t} \\ -\frac{k_2}{\varepsilon_2}e^{\frac{1}{2}k_2 t} & \frac{k_2}{\varepsilon_2}e^{-\frac{1}{2}k_2 t} & \frac{k_3}{\varepsilon_3}e^{\frac{1}{2}k_3 t} & -\frac{k_3}{\varepsilon_3}e^{-\frac{1}{2}k_3 t} \\ e^{-\frac{1}{2}k_2 t}\left(\frac{k_2}{\varepsilon_2}-\frac{k_1}{\varepsilon_1}\right) & -e^{\frac{1}{2}k_2 t}\left(\frac{k_2}{\varepsilon_2}+\frac{k_1}{\varepsilon_1}\right) & 0 & 0 \\ 0 & 0 & e^{k_3\left(\frac{1}{2}t+h\right)}\left(\frac{k_4}{\varepsilon_4}+\frac{k_3}{\varepsilon_3}\right) & e^{-k_3\left(\frac{1}{2}t+h\right)}\left(\frac{k_4}{\varepsilon_4}-\frac{k_3}{\varepsilon_3}\right) \end{bmatrix} \quad \text{(A.45)}$$

The solution of this set of equations can be calculated by extracting the determinant of the matrix and force it to be equal to zero. After solving and reducing this system, we obtain the next transcendental expression:

$$\tanh(k_3 h) = -\frac{k_3\varepsilon_3\left[k_2\varepsilon_2\left(k_4\varepsilon_1+k_1\varepsilon_4\right)\cosh(k_2 t)+\left(k_1k_4\varepsilon_2^2+k_2^2\varepsilon_1\varepsilon_4\right)\sinh(k_2 t)\right]}{k_2\varepsilon_2\left(k_1k_4\varepsilon_3^2+k_3^2\varepsilon_1\varepsilon_4\right)\cosh(k_2 t)+\left(k_2^2k_4\varepsilon_1\varepsilon_3^2+k_1k_3^2\varepsilon_2^2\varepsilon_4\right)\sinh(k_2 t)} \quad \text{(A.46)}$$

By numerically solving the previous equation, the propagation constant of the SPP mode (k_z) for the IIMI structure can be calculated. Note that from Eq. A.46, when the thickness of the dielectric 3 (ε_3) is zero ($h \to 0$), the solution is reduced to the IMI system as it has been shown in equation A.25.

iv. Comparison between the IM and IMI structures

First we will compare the dispersion of the single interface and IMI structure discussed in A and B in order to obtain the thickness of the metal of the IMI structure at which the dispersion is the same as the single interface.

To begin with, let us evaluate the influence of the metal thickness for the IMI structure. To simplify the problem we will consider that $\varepsilon_1 = \varepsilon_3 = 1$ for the IMI structure shown in Fig. A.2. Based on this, the analytical effective refractive index (n_{eff}, calculated as k_z/k_0) for the semi-infinite metal model (using Eq. A.10) as a function of wavelength is shown in Fig. A.5(a). It can be observed that the effective index approaches 1 in the long wavelength limit. This result can be easily explained

by noting that for long wavelengths the value of k_z approaches the free space wavenumber k_0, leading to a weaker coupling of SPPs to the metal film.

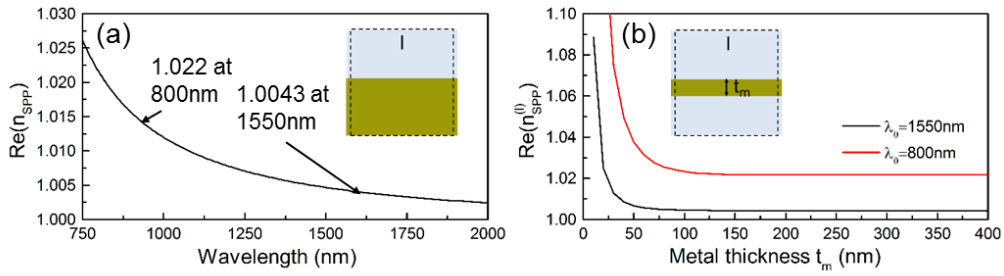

Figure A.5. Analytical results of the effective refractive index for the case of a semi-infinite metal (a) and an IMI structure (b). The results in (b) show the effective index as a function of the metal thickness at two different wavelengths.

We also show in Fig. A.5(b) the analytical results of the effective refractive index as a function of metal thickness (t) for the case of the IMI structure using Eq.A.25 at two different wavelengths (800 and 1550 nm). It is shown that that for very thin films (t < 50 nm) the effective refractive index is different to the semi-infinite metal case shown in panel (a). This is due to the fact that there is a coupling between the top and bottom SPPs. On the other hand, it can be observed that the effective index for the IMI case approaches the case of a semi-infinite metal when the thickness is increased. For example, when t = 100 nm, the effective index is 1.0045 and 1.023 at the wavelength of 1550 nm and 800 nm respectively. From these results we observe that the effective index is exactly as the semi-infinite case when the thickness of the metal is larger than 130 nm with values of 1.0043 and 1.022 at the wavelengths of 1550 nm and 800 nm.

To better observe this performance, the numerical results of the E_y-field along the optical z-axis at the top and bottom surfaces of the metal film for the case of the IMI structure are shown in Fig. A.6. Here three different values of t are evaluated at the wavelength of 1550 nm. In order to clarify if there is a coupling of SPPs between the top and bottom surfaces, we restrict the excitation of SPPs to the top of the structure.

From Fig. A.6, it can be better observed the influence of the metal thickness. When t = 20 nm [panel (a)], it is evident that we have SPP propagation on both, top and bottom, surfaces. This is because the thickness is below the skin depth of the metal at this wavelength. On the other hand, when the thickness is t = 100 nm and t = 300 nm, the SPP propagation at the bottom surface is almost negligible. This is due to the fact that, as it has been discussed in Fig. A.5, the metal behaves as a semi-infinite metal. Hence, there is no SPP excited at the bottom of the metal film and only one SPP is excited (at the top of the structure).

For the sake of completeness, the numerical results of the field distribution for the case of a semi-infinite metal are also shown as green plots in Fig. A.6, demonstrating that for the cases with t = 100 nm and t = 300 nm the performance can be approximated to the case of a semi-infinite metal. Note that these values are in agreement with [KRAS 10] where it is stated that in practice, 100 nm of metal is enough to consider a metal film as a semi-infinite medium. Also, we can find in the literature several works working at the telecommunication wavelength of 1550 nm and 850 nm using this or a thicker metal film as a semi-infinite medium [STEE 06], [FENG 08], [JU 13], [KHAL 14].

Finally, we also plot in Fig. A.6 the numerical results of the E_y-field distribution at the wavelength of 800 nm for the three different values of t under study. Note that a similar performance to the wavelength of 1550 nm is observed.

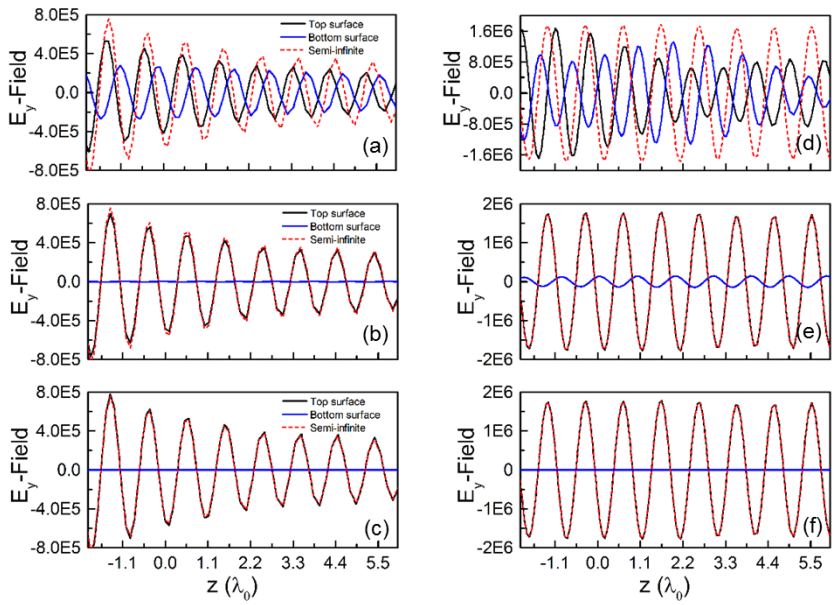

Figure A.6. Numerical results of the E_y-field distribution along the propagation z-axis at the wavelength of 1550 nm (a-c) and 800 nm (d-f) for the case of an IMI structure with a metal thickness of (a,d) t = 20 nm, (b,e) t = 100 nm and (c,f) t = 300 nm.

v. Comparison between the IIM and IIMI structures

Now that we have compared the cases of a single interface (IM) and double dielectric metal cases (IMI), let us evaluate the cases when the multilayers consist on an insulator- insulator -metal (IIM) and IIMI. First, we calculate the effective refractive index for the case of the IIM multilayer as a function of wavelength for several values of dielectric thickness. The analytical results are shown in Fig. A.7.

As it has been demonstrated before, 100 nm is enough to consider a metal film as a semi-infinite metal. Therefore, for the cases shown in Section iv, the IMI model can be approximated to a IM structure for thickness of the metal > 100 nm.

Based on this, we use this thickness of metal as a reference and we calculate the effective refractive index at two different wavelengths:1550 nm and 800 nm as a function of the thickness of the dielectric for the case of the IIMI structure discussed in section iii. The results are shown in Fig. A.8(b).

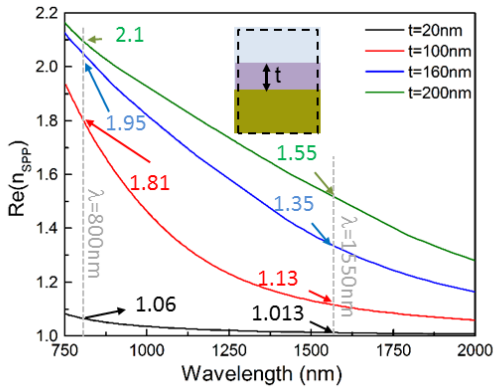

Figure A.7. Analytical results of the effective refractive index for the case of an IIM structure as a function of wavelength for different thickness of the dielectric on top of the semi-infinite metal.

We also calculate the effective refractive index for the case of a metal thickness of 300 nm [see Fig. A.8(a)]. By comparing these results, it can be observed that the same values are obtained for both cases at both wavelengths. This is due to the fact that the metal can be considered as a semi-infinite metal for these metal thicknesses, as it has been demonstrated for the case of the IM and IMI structure discussed in the previous section. This can be also corroborated by comparing these results with those obtained for the case of a semi-infinite metal [see Fig. A.7], demonstrating that we can reduce the structure as an IIM multilayer when the thickness of the metal is > 100 nm.

Finally, the results when the thickness of the metal is 20 nm are also shown as panel c in the same figure. Here it is clearly observed that the effective refractive index is different from those obtained with the other values of *t*, corroborating that this thickness cannot be considered as a semi-infinite metal

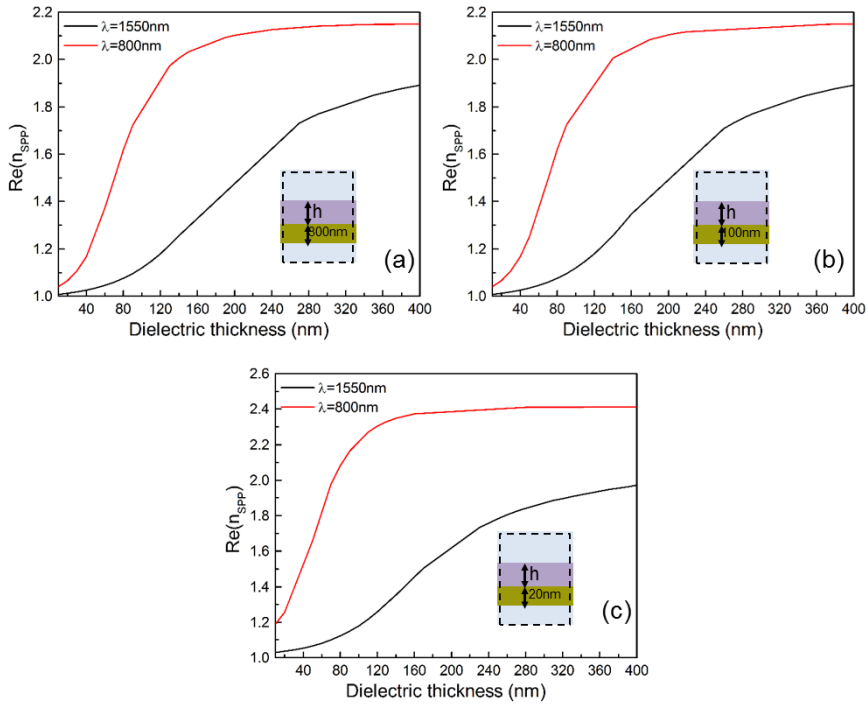

Figure A.8. Analytical results of the effective refractive index for the case of an IIMI structure as a function of the thickness of the dielectric on top of a metal film with thickness (a) 300 nm, (b) 100 nm and (c) 20 nm.

Appendix B

Materials and Methods

i. Simulation tools

Nowadays, there are several commercial simulation tools available for the numerical evaluation of structures within different scenarios. All these EM softwares solve the Maxwell's equations (shown in Chapter 1) either in integral or differential form. In Fig. B.1, different numerical resolution methods is schematically shown. Here, the branches corresponding to the two commercial softwares used in this thesis are highlighted: CST Microwave Studio™ and Comsol Multiphysics®.

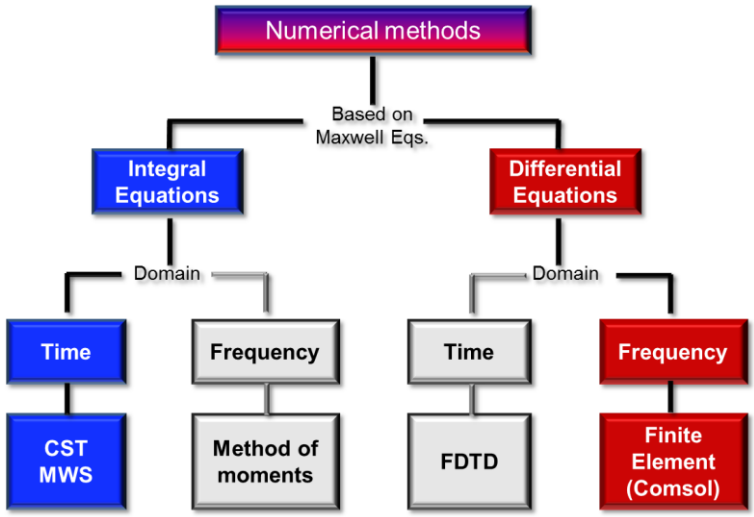

Figure B.1. Conceptual tree of the classification of the different numerical methods.

a. CST Microwave Studio™

This commercial software is the most used in this thesis to evaluate the EM response of the structures analyzed. Examples of the electromagnetic solver products available within this tool are:

- CST MICROWAVE STUDIO® (MWS), covering the high frequency range, both in transient and in time harmonic state. Seven solver types are available with this product: transient, frequency domain, integral equation, eigenmode, resonant, asymptotic and TLM (3D time-domain Transmission-Line Matrix method). A description of the first two solvers will be shown below since they are the most used in this thesis.
- CST EM STUDIO™ (EMS), the low-frequency package, which includes a variety of static and low frequency solvers.
- CST PARTICLE STUDIO® (PS), the particle tracking solver package

In this thesis the only module used is CST Microwave Studio™ [CST 15]. It is based on the Finite-Integration Technique (FIT) [WEIL 77] and is a fully featured software package for electromagnetic analysis and design in the high frequency range. It simplifies the process of creating structures by providing a powerful graphical solid modeling front-end. After the model has been constructed, a fully automatic meshing procedure is applied before a simulation engine is launched. Since no method works equally well for all applications, the software contains several different simulation techniques, as described below, to best suit various applications. Each method in turn supports several meshing schemes suited for each simulation technique.

CST Microwave Studio™ solves Maxwell's equations in the integral form in the time domain:

$$\oint_{\partial A} \mathbf{E}.d\vec{s} = -\int \frac{\partial \mathbf{B}}{\partial t}.d\vec{A} \tag{B.1}$$

$$\oint_{\partial V} \mathbf{D}.d\vec{A} = \int_{V} \rho.dV \tag{B.2}$$

$$\oint_{\partial A} \mathbf{H}.d\vec{s} = \int_{A} \left(\frac{\partial \mathbf{D}}{\partial t} + \mathbf{J} \right).d\vec{A} \tag{B.3}$$

$$\oint_{\partial V} \mathbf{B}.d\vec{A} = 0 \tag{B.4}$$

Before solving these equations numerically, the problem is divided mesh cells. The mesh system used is very important for any software package for electromagnetic analysis and CST Microwave Studio is not an exception. Therefore, a primary mesh is created and can be visualized in the Mesh View of the software. However, the mesh system applies a second mesh orthogonally to the primary mesh. Using these two orthogonal grids, the spatial discretization of Maxwell's equations is performed. Furthermore, the degrees of freedom are introduced as integral values. This software has three mesh types available: hexahedral, tetrahedral and surface mesh. It depends of the solver type used which determines the mesh types that will be available:

- Transient Solver (Time domain solver) → hexahedral mesh.
- Frequency domain solver → hexahedral and tetrahedral mesh.

TRANSIENT SOLVER OVERVIEW

The transient solver is a flexible and powerful time-domain solver. It can obtain the entire broadband frequency behavior of the simulated structure using only one simulation run. The mesh grid type available with this solver is the hexahedral grid (as mentioned above). This solver is remarkably efficient for most high frequency applications such as connectors, transmission lines, filters, antennas, amongst others.

The time domain solver calculates the development of fields through time at discrete locations and at discrete time samples. It calculates the transmission of energy between various ports and/or open space of the investigated structure.

This solver is less efficient for structures that are electrically much smaller than the shortest wavelength. In such cases it is advantageous to solve the problem by using the frequency domain solver. Some application areas for the transient solver are:

- Scattering parameter matrices (S-Parameter).
- Electromagnetic field distributions at various frequencies.
- Antenna radiation patterns and relevant antenna parameters.
- Structure design by using the optimizer or the parameter sweep.
- Time domain reflectometry.
- Radar cross section calculations using farfield/RCS monitors.
- Simulation of dispersive materials.

FREQUENCY DOMAIN SOLVER OVERVIEW

The frequency domain solver of CST Microwave Studio™ is, like the transient solver, a general purpose tool. It delivers electromagnetic near and farfields as well as S-Parameters. As mentioned, this solver is the better choice for electrically small

structures, or devices with a high Q-value. As an unique feature, this solver can be switched from cartesian to tetrahedral meshing. Broadband results are provided quickly with the built-in adaptive frequency sweep. For both mesh types automatic mesh adaptation schemes are implemented. The frequency domain solver also offers a direct and an indirect linear equation system solver. The direct one is preferable if the number of tetrahedrons is not too large. It shows its main strength when the full S-matrix of a structure with multiple excitations is required.

A key application for the Frequency Domain Solver are periodic structures, such as the rectangular waveguides and SSHAs used in Chapters 2-3, FSSs, or phased arrays. CST MWS features a special periodic boundary implementation, which automatically creates the boundaries for arbitrarily shaped unit cells. The ports are equipped with Floquet-mode solvers for highly accurate and fast simulation, and the easy analysis of polarization and mode type.

As an example, a screen shot of a SSHA simulated in CST MWS showing the two mesh types (hexahedral and tetrahedral) is shown in Fig. B.2.

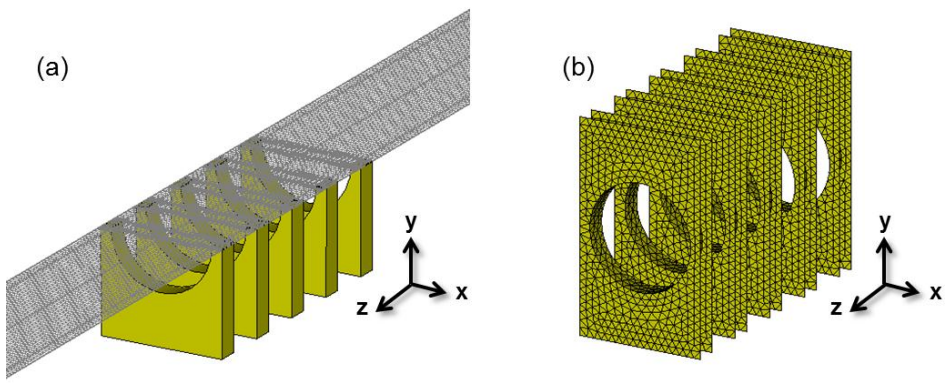

Figure B.2. Screenshots taken from CST MWS of a fishnet metamaterial made with 5 SSHA along the *z* axis showing: (a) Tetrahedral and (b) Hexahedral mesh types.

EIGENMODE SOLVER OVERVIEW

The Eigenmode Solver is dedicated to the simulation of closed resonant structures. Primary results are, besides the field distribution of the modes, the eigenfrequencies of the structures. Typical application areas are the determination of the poles of a highly resonant filter structure, Q-value (also external) calculation, and the design of slow wave structures (like Travelling Wave Tube (TWT) or accelerating cavities). There are two solvers available: The Advanced Krylov Subspace method (AKS), and the Jacobi-Davidson method (JDM). The former solver calculates efficiently a number of

modes with the lowest resonant frequencies in lossfree structures. The JDM solver can also be used to calculate non extremal modes at an arbitrary position inside the spectrum. In addition, the JDM solver can include even highly lossy materials.

In this thesis, the eigenmode solver has been used to calculate the dispersion diagrams of infinitely periodic structures such as the fishnet metamaterial used in Chapter 3. A schematic representation of this structure taken from the commercial software is shown in Fig. B.3. The periodic boundary conditions applied to the structure are also shown in the same figure. A more complete description of the features of this solver can be found in [CST 15].

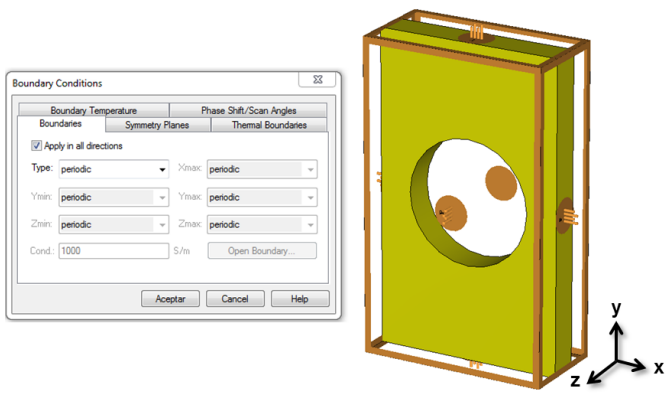

Figure B.3. Screenshots taken from CST MWS of the unit cell of a fishnet metamaterial (right) along with the dialog box showing periodic boundary conditions (left).

b. Comsol Multiphysics®

Comsol Multiphysics® is a general-purpose software platform, based on advanced numerical methods, for modeling and simulating physics-based problems accounting for coupled or multiphysics phenomena. Tha main difference here is that this software deals with the Maxwell equations in differential form (as shown in Chapter 1). Also, the simulation platform can be expanded using dedicated physics interfaces and tools for electrical, mechanical, fluid flow, and chemical applications. It includes a set of core physics interfaces for common physics application areas such as structural analysis, laminar flow, pressure acoustics, electrostatics, electric currents, heat transfer, and Joule heating.

This software has been used to validate the analytical results of the bowtie and tripod nanoantennas shown in Chapter 5. For this case, the electrical physics has been used which has different modules depending of the application or the scenario to be analyzed: AC/DC, RF, Wave Optics, Ray Optics, MEMS, Plasma and Semiconductor module. In this thesis, the RF module has been used. A brief description will be provided to better understand its performance.

RF MODULE OVERVIEW

This module is used by designers of RF and microwave devices to design antennas, waveguides, filters, circuits, cavities, and metamaterials. By quickly and accurately simulating electromagnetic wave propagation and resonant behavior, it is posible to compute electromagnetic field distributions, transmission, reflection, impedance, Q-factors, S-parameters, and power dissipation. Compared to traditional electromagnetic modeling, it also has the capability to include in the model different effects such as temperature rise, structural deformations, and fluid flow. Multiple physical effects can be coupled together and consequently affect all included physics during the simulation of an electromagnetic device. This module includes RF interfaces for frequency-domain and time-domain modeling, microwave heating, electrical circuits and transmission line.

All the simulations in Chapter 5 have been carried out using the first interface which solves a frequency-domain wave equation for the electric field given its sources. The sources can be in the form of point dipoles, line currents or incident fields on boundaries or domains. It is primarily used to model EM wave propagation in different media and structures.

Regarding the mesh type, automatic and semi-automatic meshing tools are available with this software, including free tetrahedral meshing (which can be changed manually) and swept meshing. The default algorithm is automatic tetrahedral meshing for physics defined in solids, and a combination of tetrahedral and boundary-layer meshing for fluids. It is also possible to take full control over the sequence of operations used for creating the mesh by defining a so-called mesh sequence. This allows for a mix of tetrahedral, prismatic, or hexahedral elements and can be made parametrically driven.

As an example, in Fig. B.4 it is shown an example of the model used in Chapter 5 for the case of the bowtie nanoantennas (for a detailed description of the setup see section 5.1).

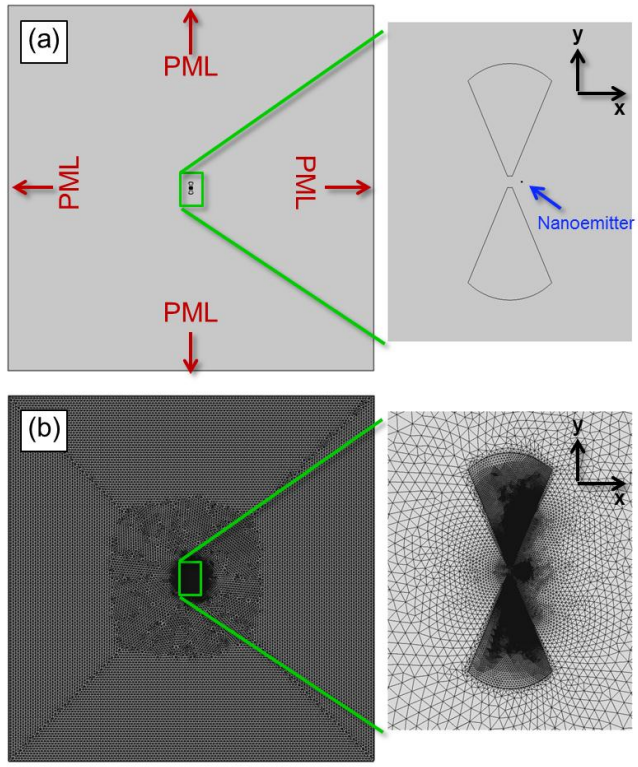

Figure B.4. Schematic representation of the RF module interface showing the bowtie nanoantenna evaluated in Chapter 5 using Comsol Multiphysics. (a) Representation of the whole problem and a zoom-in picture of the bowtie nanoantenna (right). (b) Extremelly refined mesh for the whole system and a zoom-in of the improved mesh for the nanoantenna (right).

ii. Experiment

All the experimental results shown in this thesis have been performed using a millimeter wave quasi-optical VNA AB-millimetre™. Here, an overview of this instrument will be provided showing some of the spectral bands that can be covered with this VNA.

a. Quasi-otpical vector network analyzer (VNA) AB-millimetre™

The VNA MVNA-8-350, which is produced by AB MILLIMETRE™ since 1990, is the only all-solid-state electronics millimeter and submillimeter waves spectrometer/network analyzer, which allows to do vector measurements (simultaneous measurements of both, the amplitude and the phase of transmitted/reflected signal) over very broad frequency range extending from 8 to 1000 GHz (wavelengths from 4 cm to 0.3 mm). It is the state-of-the-art millimeter and submillimeter domain diagnostics and spectroscopy tool, for many applications, from space telecommunications and satellites diagnostics, to physics and chemistry spectroscopy. The version MVNA-8-350-4 that has been used in this thesis was delivered to the Public Univerity of Navarra in 2003 to the Antennas Group-Teralab and covers the frequency range of 41-1000 GHz. It consists of several components and some of them are listed below:

- *MVNA Central unit:*
  It consists on two parts: the Vector Receiver (VR) and the Microwave Part (MP). The former can be a single channel, model VR-8-350-1 (one millimeter wave signal detected at a time only), or (as in our case) dual channel VR-8-350-2 (two millimeter signals detected simultaneously). The MP has two connectors for a harmonic generator (HG) cables, and two connectors for harmonic mixer (HM) cables. A picture showing both parts of the MNVA central unit is shown in Fig. B.5(a).

- *PC computer:*
  A picture is shown in Fig. B.5(b). The logical and operational control of the analyzer is done with this PC computer. The AB Millimetre software provides also many tools for data storage and analysis. This includes Fourier Transform FT analysis, data fitting, averaging and smoothing. The installed software can also drive one or two stepper motors and supply a variable voltage corresponding, for instance, to the independent variable of the experiment like the sweep of frequency, time, angle, temperature or magnetic field.

- *Quasi-optical bench:*
  A picture of the quasi-optical bench in the Public University of Navarra is shown in Fig. B.6. Here, the radiated beam propagates to reach a pair of focusing elliptical mirrors designed to obtain an undistorted beam having its beam waist in the half of the distance of the setup, where the sample is placed.

Then, another pair of mirrors focuses the transmitted beam on a receiving corrugated horn antenna.

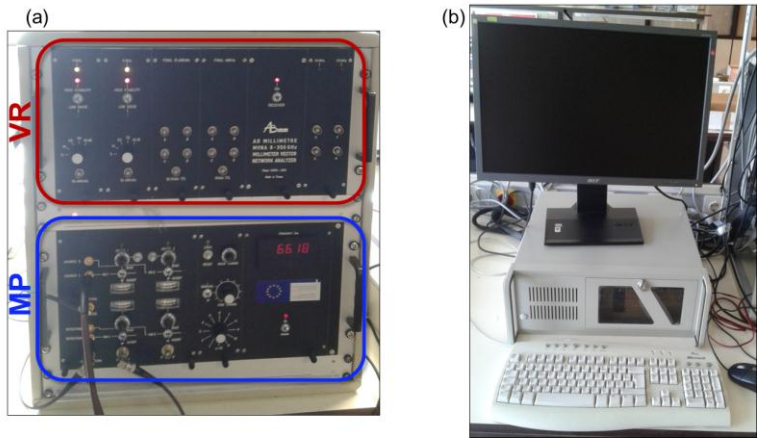

Figure B.5. (a) Vector Receiver, VR, (top) and Microwave Part, MP, (bottom). (b) PC computer.

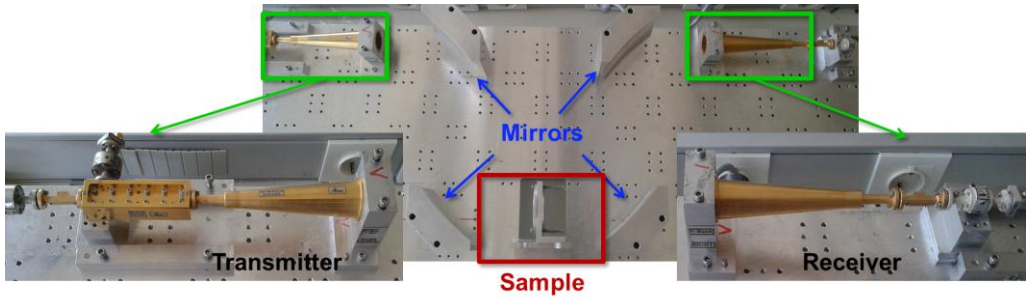

Figure B.6. Quasi-optical bench

Depending of the frequency band used, different components such as antennas, filters, attenuators and directional couplers should be used, which are specifically provided for each frequency band. A brief description of these components is as follows:

- *Attenuators:*
  Fixed value attenuators (40 dB in the K-Ka bands, 30 dB in the Q-V bands, 20 dB in the W band, 6 dB in the D band, etc.) are very useful for direct signal calibration, and also to measure low loss devices, since they damp the standing waves. An appropriate attenuator is attached by default with each HG head between the isolators.

- *Filters:*
  For higher frequencies (> 170 GHz), the use of high-pass filters is required which are supplied by AB MILLIMETRE.

- *Directional couplers:*
  Directional couplers are necessary for reflection measurements, and they are also very useful for the characterization of waveguide structures (sample holders, diplexers, light pipes, etc.). There are separate couplers for each frequency range, corresponding to waveguide standard sizes, up to 336 GHz (WR-3.4).

- *Feed horn, conical transitions:*
  For free space (as used in this thesis), or quasi optical mode of propagation, it is necessary to couple the radiation from the millimeter heads outputs, which are waveguides, to the free space with horn antennas creating Gaussian beams, typically with about 10° half angle aperture (RF field dropping by 1/e), and side lobes below –20 dBc.

As an example, some components for the V, W and D band are shown in Fig. B.7

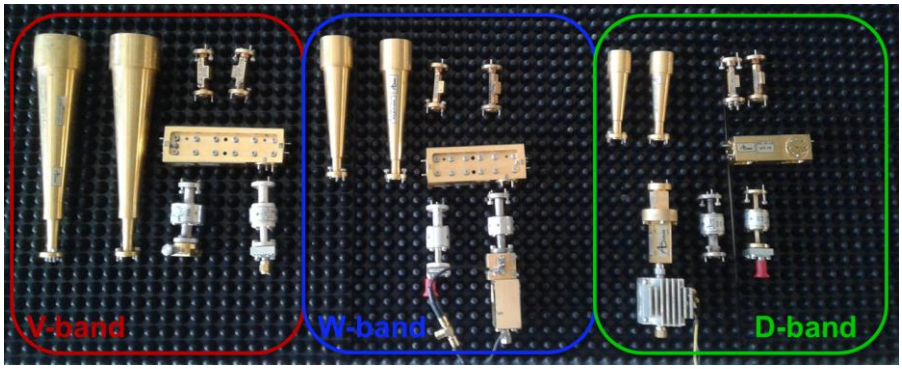

Figure B.7. Different components used in the AB Millimeter™ MVNA-8-350-4 for the spectral bands: V, W and D bands.

Appendix C

Effective propagation constant of an inhomogeneous rectangular waveguide

Here, the effective propagation constant of an inhomogeneous rectangular waveguide is derived. To begin with, let us consider the transversal cross-section of the cavity used in Chapter 2, as shown in Fig. C.1

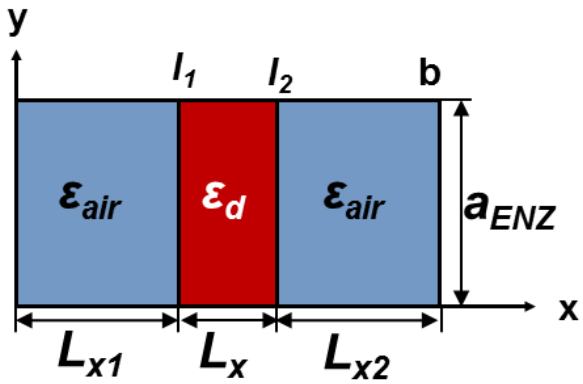

Figure C.1. (a) Schematic representation of the transversal cross-section of an inhomogeneous rectangular waveguide

There are different methods that can be applied to this configuration in order to obtain an expression of the propagation constant of such waveguide cross-section. Here, we will apply a similar process to the one reported in [POZA 04] and extend it for the three region case shown in Fig. C.1.

We can define the wave propagation for each region of the waveguide as follows:

$$\left(\frac{\partial^2}{\partial x^2}+k_{air}^2\right)h_z=0;\ for\ \ 0\le x\le l_1 \tag{C.1}$$

$$\left(\frac{\partial^2}{\partial x^2}+k_{diel}^2\right)h_z=0;\ for\ \ l_1\le x\le l_2 \tag{C.2}$$

$$\left(\frac{\partial^2}{\partial x^2}+k_{air}^2\right)h_z=0;\ for\ \ l_2\le x\le l_b \tag{C.3}$$

where k_{air} and k_{diel} are the wave number of the air and dielectric regions which can be calculated as:

$$k_{diel}=\sqrt{\varepsilon_d k_0^2-\beta^2} \tag{C.4}$$

$$k_{air}=\sqrt{\varepsilon_{air} k_0^2-\beta^2} \tag{C.5}$$

Note that β in both cases should be the same in order to ensure field matching along the interfaces of different materials, i.e., at $x = l_1$ and $x = l_2$. Now, the solution for the z component of the magnetic field from Eqs. C.1-C.3 is the following:

$$h_z=\begin{cases}A\cos\left(k_{air}x\right)+B\sin\left(k_{air}x\right) & For\ \ 0\le x\le l_1\\ C\cos\left[k_{diel}\left(l_2-x\right)\right]+D\sin\left[k_{diel}\left(l_2-x\right)\right] & For\ \ l_1\le x\le l_2\\ E\cos\left[k_{air}\left(b-x\right)\right]+F\sin\left[k_{air}\left(b-x\right)\right] & For\ \ l_2\le x\le b\end{cases} \tag{C.6}$$

Now that the h_z field has been defined, the y component of the electric field (E_y) can be calculated as:

$$E_y=\frac{j\omega\mu}{k^2}\frac{\partial h_z}{\partial x} \tag{C.7}$$

Based on this, the resulting E_y field is as follows:

$$E_y = \begin{cases} \dfrac{j\omega\mu}{k_{air}^2}\left[-k_{air}A\sin\left(k_{air}x\right)+k_{air}B\cos\left(k_{air}x\right)\right] & For \;\; 0 \le x \le l_1 \\ \dfrac{j\omega\mu}{k_{diel}^2}\left\{k_{diel}C\sin\left[k_{diel}\left(l_2-x\right)\right]-k_{diel}D\cos\left[k_{diel}\left(l_2-x\right)\right]\right\} & For \;\; l_1 \le x \le l_2 \\ \dfrac{j\omega\mu}{k_{air}^2}\left\{k_{air}E\sin\left[k_{air}\left(b-x\right)\right]-k_{air}F\cos\left[k_{air}\left(b-x\right)\right]\right\} & For \;\; l_2 \le x \le b \end{cases} \quad (C.8)$$

Since we have metallic walls at $x = 0$ and $x = b$, the tangent electric field component must be zero there. By applying this condition to Eq. C.8, the constants B and F vanish (B = F = 0). Finally, applying the condition of continuity of the tangential components of E and h at $x = l_1$ and $x = l_2$ we obtain:

$$-\frac{A}{k_{air}}\sin\left(k_{air}l_1\right)=\frac{C}{k_{diel}}\sin\left[k_{diel}\left(l_2-l_1\right)\right]-\frac{D}{k_{diel}}\cos\left[k_{diel}\left(l_2-l_1\right)\right] \quad (C.9)$$

$$A\cos\left(k_{air}l_1\right)=C\cos\left[k_{diel}\left(l_2-l_1\right)\right]+D\sin\left[k_{diel}\left(l_2-l_1\right)\right] \quad (C.10)$$

$$-\frac{D}{k_{diel}}=\frac{E}{k_{air}}\sin\left[k_{air}\left(b-l_2\right)\right] \quad (C.11)$$

$$C=E\cos\left[k_{air}\left(b-l_2\right)\right] \quad (C.12)$$

By introducing Eqs. C.11-C.12 into Eqs. C.9-C.10, we get the final system of equations:

$$-\frac{A}{k_{air}}\sin\left(k_{air}l_1\right)=\frac{E}{k_{air}}\sin\left[k_{air}\left(b-l_2\right)\right]\sin\left[k_{diel}\left(l_2-l_1\right)\right]+\frac{E}{k_{air}}\sin\left[k_{air}\left(b-l_2\right)\right]\cos\left[k_{diel}\left(l_2-l_1\right)\right] \quad (C.13)$$

$$A\cos\left(k_{air}l_1\right)=E\cos\left[k_{air}\left(b-l_2\right)\right]\cos\left[k_{diel}\left(l_2-l_1\right)\right]-\frac{k_{diel}}{k_{air}}E\sin\left[k_{air}\left(b-l_2\right)\right]\left[k_{diel}\left(l_2-l_1\right)\right] \quad (C.14)$$

Note that this is a homogeneous system which has a trivial solution when A = E = 0. For a non-trivial, the determinant of the system must vanish:

$$\frac{1}{k_{diel}}\tan\left[k_{diel}\left(l_2-l_1\right)\right]+\frac{1}{k_{air}}\tan\left[k_{air}\left(b-l_2\right)\right]+\frac{1}{k_{air}}\tan\left(k_{air}l_1\right)\ldots$$
$$\ldots-\frac{k_{diel}}{k_{air}^2}\tan\left(k_{air}l_1\right)\tan\left[k_{air}\left(b-l_2\right)\right]\tan\left[k_{diel}\left(l_2-l_1\right)\right]=0 \quad (C.15)$$

Now we can insert the particular dimensions of the waveguide cross-section $L_{x1} = l_1$, l_2-$l_1 = L_x$, $b - l_2 = L_{x2}$ and obtain the final equation that defines the propagation constant:

$$\frac{1}{k_{diel}}\tan\left(k_{diel}L_x\right)+\frac{1}{k_{air}}\left[\tan\left(k_{air}L_{x2}\right)+\tan\left(k_{air}L_{x1}\right)\right]-\frac{k_{diel}}{k_{air}^2}\tan\left(k_{air}L_{x1}\right)\tan\left(k_{air}L_{x2}\right)\tan\left(k_{diel}L_x\right)=0 \quad \text{(C.16)}$$

Acronyms

ε	Permittivity
μ	Permeability
CFZPA	Circular Planar Fresnel Zone Plate Antennas
CSRR	Complementary Split Ring Resonator
DNG	Double Negative
DPS	Double Positive
EM	Electromagnetic
ENG	Negative Permittivity Media
ENZ	Epsilon Near Zero
EOT	Extraordinary Optical Transmission
ET	Extraordinary Transmission
FL	Focal Length
FoM	Figure of Merit
FP	Fabry – Perot
FSS	Frequency Selectrive Surfaces
FT	Fourier Transform
FWHM	Full – Width at Half – Maximum
FZPA	Fresnel Zone Plate Antennas
GRIN	Graded Index
HG	Harmonic Generator
HM	Harmonic Mixer

HPBW	Half – Power Beam – Width
HR	High – Resistivity
IIM	Insulator – Insulator – Metal
IIMI	Insulator – Insulator – Metal – Insulator
IM	Insulator-Metal
IMI	Insulator – Metal – Insulator
LHM	Left-Handed Media
LSP	Localized Surface Plasmons
MIM	Metal – Insulator – Metal
MNG	Negative Permeability Media
MNRP	Maximum Normalized Radiation Power at the Output Angle
MNZ	Permeability Near Zero
MP	Microwave Part
MTM	Metamaterial
NNZ	Refractive Index Near Zero
NRI	Negative Refractive Index
OA	Output Angle
PBG	Photonic Band Gap
PEC	Perfect Electric Conductor
PhC	Photonic Crystals
PMC	Perfect Magnetic Conductor
PMMA	Polymethyl Methacrylate
PNJ	Photonic Nanojets
PPW	Parallel Plates Waveguide

RCS	Radar Cross Section
RHM	Right-Handed Media
RIU	Refractive Index Unit
SHA	Subwavelength Hole Array
SLL	Side Lobe Level
SNG	Single Negative Media
SPP	Surface Plasmons Polaritons
SRR	Split Ring Resonator
SSA	Subwavelength Slit Array
SSHA	Stacked Subwavelength Hole Array
THz	Terahertz
UV	Ultra Violet
VNA	Vector Network Analyzer
VR	Vector Receiver
ZIM	Zero Index Materials

List of Figures

Chapter 1:

Chapter 2:

Chapter 3:

Chapter 4:

Chapter 5:

Appendix:

References

A

[AKAR 04] S. S. Akarca-Biyikli, I. Bulu and E. Ozbay, "Enhanced transmission of microwave radiation in one-dimensional metallic gratings with subwavelength aperture," *Applied Physics Letters*, **85**, 1098 (2004)

[ALAB 13] A. Alabastri, S. Tuccio, A. Giugni, A. Toma, C. Liberale, G. Das, F. De Angelis, E. Di Fabrizio and R. P. Zaccaria, "Molding of plasmonic resonances in metallic nanostructures: dependence of non-linear electric permittivity on system size temperatura," *Materials*, **6**, 4879 (2013)

[ALCA 15] R. Alcaraz de la Osa, J. M. Sanz, A. I. Barreda, J. M. Saiz, F. González, H. O. Everitt and F. Moreno, "Rhodium tripod stars for UV plasmonics," *The Journal of Physical Chemistry C*, **119**, 12572 (2015)

[ALIT 08] P. Alitalo, O. Luukonen, J. Vehmas and S.A. Tretyakov, "Impedance-Matched Microwave Lens," *IEEE Antennas Wireless Propag. Letters*, **7**, 187 (2008)

[ALLE 11] K. W. Allen, A. Darafsheh and V. N. Astratov, "Photonic nanojet-induced modes: from physics to applications," in *International Conference on Transparent Optical Networks*, (2011)

[ALLE 14] K. W. Allen, A. Darafsheh, F. Abolmaali, N. Mojaverian, N. I. Limberopoulos, A. Lupu, and V. N. Astratov, "Microsphere-chain waveguides: Focusing and transport properties," *Applied Physics Letters*, **105**, 021112 (2014)

[ALÙ 05] A. Alù and N. Engheta, "Achieving transparency with plasmonic and metamaterial coatings," *Physical. Review. E.*, **72**, 016623 (2005)

[ALÙ 06] A. Alù and N. Engheta, "Optical nanotransmission lines: synthesis of planar left-handed metamaterials in the infrared and visible regimes," *Journal of Optical Society of America B*, **23**, 3 (2006)

[ALÙ 07a] A. Alù, N. Engheta, A. Erentok and R. W. Ziolkowski, "Single-negative, double-negative, and low-index metamaterials and their electromagnetic applications," *IEEE Antennas and Propagation Magazine*, **49**, 1 (2007)

[ALÙ 07b] A. Alù, M. G. Silveirinha, A. Salandrino and N. Engheta, "Epsilon-near-zero metamaterials and electromagnetic sources: Tailoring the radiation phase pattern," *Physical Review B - Condensed Matter and Materials Physics*, **75**, 15 (2007)

[ALÙ 07c] A. Alù and N. Engheta, "Plasmonic materials in transparency and cloacking problems: mechanism, robustness, and physical insights," *Optics Express*, **15**, 6 (2007)

[ALÙ 08a] A. Alù, M. G. Silveirinha and N. Engheta, "Transmission-line analysis of ε -near-zero-filled narrow channels," *Physical Review E – Statistical, Nonlinear, and Soft Matter Physics*, **78**, 1 (2008)

[ALÙ 08b] A. Alù, and N. Engheta, "Dielectric Sensing in ε-Near-Zero Narrow Waveguide Channels," *Physical Review B*, **78**, 4 (2008)

[ALÙ 08c] A. Alù and N. Engheta, "Light squeezing through arbitrarily shaped plasmonic channels and sharp bends," *Physical Review B.,* **78**, 035440 (2008)

[ALÙ 10] A. Alù and N. Engheta, "Coaxial-to-waveguide matching with ε-Near-Zero ultranarrow channels and bends," *IEEE Transactions on Antennas and Propagation*, **58**, 2 (2010)

[ANKE 08] J. N. Anker, W. P. Hall, O. Lyandres, N. C. Shah, J.Zhao and R. P. Van Duyne, "Biosensing with plasmonic nanosensors", *Nature materials*, **7,** 442 (2008)

[AOUA 12] H. Aouani, M. Navarro-Cia, M. Rahmani, T. P. H. Sidiropoulos, M. Hong, R. F. Oulton and S. A. Maier, "Multiresonant broadband optical antennas as efficient tunable nanosources of second harmonic light," *Nano Letters*, **12**, 4997 (2012)

[AOUA 14] H. Aouani, M. Rahmani, M. Navarro-Cia, S. A. Maier, "Third-harmonic-upconversion enhancement from a single semiconductor nanoparticle coupled to a plasmonic antenna," *Nature Nanotechnology*, **9**, 290 (2014)

[ARGY 12] C. Argyropoulos, P. –Y. Chen, G. D'Aguanno, N. Engheta and A. Alù, "Boosting optical nonlinearities in ε-near-zero plasmonic channels," *Physical Review B – Condensed Matter and Materials*, **85**, 4 (2012)

[ASTR 04] V. N. Astratov, J. P. Franchak and S. P. Ashili, "Optical coupling and transport phenomena in chains of spherical dielectric microresonators with size disorder," *Applied Physics Letters*, **85**, 5508 (2004)

[ATWA 10] H. A. Atwater, A. Polman, "Plasmonics for Improved Photovoltaic Devices," *Nature Materials*, **9**, 205 (2010)

[AUBR 11] A. Aubry, D. Y. Lei, S. A. Maier and J. B. Pendry, "Plasmonic hybridization between nanowires and a metallic surface : A transformation optics approach," *Nano*, **5**, 3293 (2011)

[AUBR 13] A. Aubry and J. B. Pendry, *Transformation Optics for Plasmonics*. In *Active Plasmonics and Tunable Plasmonic Metamaterials*; A. Zayats and S. A. Maier; John Wiley & Sons: Hoboken, New Jersey (2013)

B

[BAEN 05] J. D. Baena, J. Bonache, F. Martin, R. Marques, F. Falcone, T. Lopetegui, M. A. G. Laso, J. García, I. Gil, M. Flores and M. Sorolla, "Equivalent-Circuit Models for Split-Ring Resonators and Complementary Split-Ring Resonators Coupled to Planar Transmision Lines," *IEEE Transactions on Microwave Theory and Techniques*, **53**, 4 (2005)

[BAHL 70] I. J. Bahl and K. C. Gupta, "Measurement of parameters of an artificial dielectric using a partially filled parallel plate waveguide," *Int. J. Electron*, **28**, 2 (1970)

[BALA 05] C. A. Balanis, *Antenna theory: analysis and design*, Hoboken, New Jersey: John Wiley & Sons, (2005)

[BALT 13] J. P. B. Mueller and F. Capasso, "Asymmetric surface plasmon polaritons emission by a dipole emiiter near a metal surface," *Physical Review B*, **88**, 12 (2013)

[BERU 04a] M. Beruete, M. Sorolla, I. Campillo, J. S. Dolado, L. Martín-Moreno, J. Bravo-Abad and F. J. García-Vidal, "Enhanced millimeter-wave transmission through subwavelength hole arrays," *Optics Letters*, **29**, 2500 (2004)

[BERU 04b] M. Beruete, I. Campillo, J. S. Dolado, J. E. Rodríguez-Seco, E. Perea and M. Sorolla, "Enhanced microwave transmission and beaming using subwavelength slot in corrugated plate," *IEEE Microwave Wireless. Components Letters*, **15**, 116 (2005)

[BERU 05a] M. Beruete, M. Sorolla, I. Campillo and J. S. Dolado, "Increase of the transmission in cut-off metallic hole arrays," *IEEE. Microwave Wireless Components Letters* **15**, 116 (2005)

[BERU 05b] M. Beruete, M. Sorolla, I. Campillo, and J. S. Dolado, "Subwavelength slotted corrugated plate with enhanced quasioptical millimeter wave transmission," *IEEE Microw. Wireless Components Letters*, **15**, 286 (2005)

[BERU 05c] M. Beruete, M. Sorolla, I. Campillo, J. S. Dolado, L. Martín-Moreno, J. Bravo-Abad, and F. J. García-Vidal, "Enhanced millimeter wave transmission through quasioptical subwavelength perforated plates," *IEEE Transactions on Antennas and Propagation*, **53**, 1897 (2005)

[BERU 06] M. Beruete, M. Sorolla, and I. Campillo, "Left-handed extraordinary optical transmission through a photonic crystal of subwavelength hole arrays," *Optics Express*, **14**, 5445 (2006)

[BERU 07a] M. Beruete, I. Campillo, M. Navarro-Cía, F. Falcone, and M. S. Ayza, "Molding left-or right-handed metamaterials by stacked cutoff metallic hole arrays," *IEEE Transactions on Antennas and Propagation*, **55**, 1514 (2007)

[BERU 07b] M. Beruete, M. Sorolla, M. Navarro-Cía, F. Falcone, I. Campillo, and V. Lomakin, "Extraordinary transmission and left-handed propagation in miniaturized stacks of doubly periodic subwavelength hole arrays," *Optics Express*, **15**, 1107 (2007)

[BERU 07c] M. Beruete, M. Navarro-Cía, M. Sorolla, and I. Campillo, "Polarized left-handed extraordinary optical transmission of subterahertz waves," *Optics Express*, **15**, 8125 (2007)

[BERU 08] M. Beruete, M. Navarro-Cía, M. Sorolla, and I. Campillo, "Planoconcave lens by negative refraction of stacked subwavelength hole arrays," *Optics Express*, **16**, 9677 (2008)

[BERU 09] M. Beruete, M. Navarro-Cía, M. Sorolla and I. Campillo, "Negative refraction through an extraordinary transmission left-handed metamaterial slab," *Physical Review B.*, **79**, 195107 (2009)

[BERU 11a] M. Beruete, M. Navarro-Cía, and M. Sorolla Ayza, "Understanding anomalous extraordinary transmission from equivalent circuit and grounded slab concepts," *Microwave Theory*, **59**, 2180 (2011)

[BERU 11b] M. Beruete, M. Navarro-Cía, S. A. Kuznetsov and M. Sorolla, "Circuit approach to the minimal configuration of terahertz anomalous

extraordinary transmission," *Applied Physics Letters*, **98**, 014106 (2011)

[BERU 11c] M. Beruete, M. Navarro-Cía, V. Torres, and M. Sorolla, "Redshifting extraordinary transmission by simple inductance addition," *Physical Review B*, **84**, 1 (2011)

[BERU 13] M. Beruete, P. Rodríguez-Ulibarri, V. Pacheco-Peña, M. Navarro-Cía, and A. E. Serebryannikov, "Frozen mode from hybridized extraordinary transmission and Fabry-Perot resonances," *Physical Review B*, **87**, 205128 (2013)

[BETH 44] H. Bethe, "Theory of diffraction by small holes," *Physical Review*, **66**, 163 (1944)

[BETZ 88] R. E. Betzig, *Nondestructive optical imaging of surfaces with 500 angstrom resolution*, Doctoral Thesis, 1988

[BOHR 07] C. F. Bohren and D. R. Huffman, *Apsorption and Scattering of light by small particles*, Wiley-VCH Verlag GmbH: Weinhwim, Germany (2007)

[BOUW 54] C. J. Bouwkamp, "Diffraction theory," *Rep. Prog. Phys.*, **17**, 35 (1954)

[BORN 99] M. Born and E. Wolf, *Principles of optics: electromagnetic theory of propagation, interference and diffraction of light*, Oxford, Cambridge University Press (1999)

[BORN 15] B. Born, J. D. A. Krupa, S. G.-Gagnon and J. F. Holzman, "Integration of photonic nanojets and semiconductor nanoparticles for enhanced all-optical switching," *Nature Communications*, **6**, 1 (2015)

[BORN 16] B. Born, S. G.-Gagnon, J. D. A. Krupa, I. R. Hristovski, C. M. Collier and J. F. Holzman, "Ultrafast all-optical switching via subdiffractional photonic nanojets and select semiconductor nanoparticles," *ACS Photonics*, **3**, 1095 (2016)

[BROW 53] J. Brown, "Artificial dielectrics having refractive indices less than unity," *Proc. Inst. Elec. Eng.* **100**, (1953)

[BURK 86] J. J. Burke, G. I. Stegeman, and T. Tamir, "Surface-polariton-like waves guided by thin, lossy metal films," *Physical Review B*, **33**, 8 (1986)

C

[CARB 10] J. Carbonell, C. Croënne, F. Garet, E. Lheurette, J. L. Coutaz, and D. Lippens, "Lumped elements circuit of terahertz fishnet-like arrays with composite dispersion," *Journal of Applied Physics*, **108**, 014907 (2010)

[CARR 58] R. Carrel, "The characteristic impedance of two infinite cones of arbitrary cross section," *IRE Transactions on Antennas and Propagation*, **6**, 243 (1958)

[CHAN 10a] Ma. Changbao, Liu. Zhaowei, "A super resolution metalens with phase compensation mechanism," *Applied Physics Letters*, **96**, 183101 (2010)

[CHAN 10b] Ma. Changbao, Liu. Zhaowei, "Focusing light into deep subwavelength using metamaterial inmersion lenses," *Optics Express*, **18**, 5 (2010)

[CHAN 10c] Ma. Changbao, Liu. Zhaowei, "Breaking the imaging symmetry in negative refraction lenses," *Optics Express*, **20**, 3 (2010)

[CHEN 03] S. Chen, Z. L. Wang, J. Ballato, S. H. Foulger and D. L. Carroll, "Monopod, Bipod, Tripod and Tetrapod gold nanocrystals," *Journal of the American Chemical Society*, **125**, 16186 (2003)

[CHEN 04] Z. Chen, A. Taflove and V. Backman, "Photonic nanojet enhancement of backscattering of light by nanoparticles: a potential novel visible-light ultramicroscopy technique," *Optics Express*, **12**, 7 (2004)

[CHEN 06] H. –T. Cheng, W. J. Padilla, J. M. O. Zide, A. C. Zide, A. J. Taylor and R. D. Averitt, "Active terahertz metamaterial devices," *Nature*, **444**, 597 (2006)

[CHEN 06b] Z. Chen, A. Taflove, and V. Backman, "Highly efficient optical coupling and transport phenomena in chains of dielectric microspheres.,"*Optics Letters*, **31**, 3, (2006)

[CHEN 09] H. –T. Cheng, W. J. Padilla, M. J. Chich, A. B. Azad and R. D. Averitt, "A metamaterial solid-state terahertz phase modulator," *Nature Photonics*, **3**, 3 (2009)

[CHEN 12] P. –Y. Chen, C. Argyropoulos and A. Alù, "Enhanced nonlinearities using plasmonic nanoantennas," *Nanophotonics*, **1**, 221 (2012)

[CHEN 15] L. Cheng-Yang and H. Kai-Lung, "Direct imaging of optimal photonic nanojets from core-shell microcylinders," *Optics Letters*., **40**, 22, (2015)

[CHEN 71] C. –C. Chen, "Diffraction of electromagnetic waves by a conducting screen perforated periodically with holes," *IEEE Transactions Microwave Theory and Techniques*, **19**, 475 (1971)

[CHEN 73] C. –C. Chen, "Transmission of microwave through perforated flat plates of finite thickness," *IEEE Transactions Microwave Theory and Techniques*, **21**, 1 (1973)

[CHOU 16] B. –T. Chou, Y. –H. Chou, Y. –M. Wu, Y. –C. Chung, W. –J. Hsueh, S. –W. Lin, T. –C. Lu, T. –R. Lin and S. –D. Lin, "Single-crystalline aluminum film for ultraviolet plasmonic nanolasers," *Scientific Reports*, **6**, 19887 (2016)

[COLE 06] R. M. Cole, Y. Sugawara, J. J. Baumberg, S. Mahajan, M. Abdelsalam, and P. N. Bartlett, "Easily coupled whispering gallery plasmons in dielectric nanospheres embedded in gold films," *Physical Review Letters*, **97**, 13, (2006)

[COLE 16] R. J. Coles, D. M. Price, J. E. Dixon, B. Royall, E. Clarke, P. Kok, M. S. Skolnick, A. M. Fox and M. N. Makhonin, "Chirality of nanophotonics waveguide with embedded quantum emitter for unidirectional spin transfer," *Nature Communications*, **7**, 11183 (2016)

[COLL 69] R. E. Colling and F. J. Zucker, *Antenna Theory Pt. 2*, New York, McGraw-Hill, (1969)

[COLL 00] R. E. Colling, *Fundations for Microwave Engineering*, New York, Willey-IEEE Press (2000)

[CST 15] https://www.cst.com/Products/CSTS2

D

[DEME 11] A. Demetriadou and Y. Hao, "A grounded slim luneburg lens Antenna based on transformation electromagnetic," *IEEE Antennas and Wireless Propagation Letters*, **10**, 6111237 (2011)

[DOLL 06] G. Dolling, C. Enkrich, M. Wegener, C. M. Soukoulis, and S. Linden, "Simultaneous negative phase and group velocity of light in a metamaterial," *Science*, **312**, 5775 (2006)

[DRUD 00] P. Drude, "Zur Elektronentheorie der metalle," *Annalen der Physik*, **306**, 566 (1900)

[DRAG 04] D. Dragoman and M. Dragoman, "Terahertz fields and applications," *Progress in quantum electronics,"* **28**, 1 (2004)

[DUHA 57] R. DuHamel and D. Isbell, "Broadband Logarithmically Periodic Antenna Structures," *IRE Int. Conv. Rec.*, **5**, 119 (1957)

E

[EBBE 98] T. W. Ebbesen, H. J. Lezec, H. Ghaemi, T. Thio and P. A. Wolf, "Extraordinary optical transmission through sub-wavelength hole arrays," *Nature*, **391**, 6668 (1998)

[EDWA 08] B. Edwards, A. Alù, M. E. Young, M. Silveirinha and N. Engheta, "Experimental verification of epsilon-near-zero metamaterial coupling and energy squeezing using a microwave waveguide," *Physical Review Letters*, (100), 3 (2008)

[EGGL 15] M. S. Eggleston, K. Meser, L. Zhang, E. Yablonovitch and M. C. Wu, "Optical antenna enhanced spontaneous emission," *Proc. Natl. Acad. Sci*., **112**, 1704 (2015)

[ENGH 06] N. Engheta and R. Ziolkowski, *Metamaterials:Physics and Engineering Explorations*, 1st ed. USA: John Wiley & Sons & IEEE Press, (2006)

[ENGH 07] N. Engheta, "Circuits with light at nanoscales: Optical nanocircuits inspired by metamaterials," *Science*, **317**, 5485 (2007)

[ENOC 02] S. Enoch, G. Tayeb, P. Sabouroux, N. Guérin and P. Vincent, "A metamaterial for directive emission," *Physical Review Letters*, **89**, 21 (2002)

[ETCH 06] P. G. Etchegoin, E. C. Le Ru and M. Meyer, "An analytic model for the optical properties of gold," *The journal of chemical physics*, **125**, 164705 (2006)

F

[FANG 05] N. Fang, H. Lee, C. Sun and X. Zhang, "Sub-diffraction –limited optical imaging with a silver superlens," *Science*, **309**, 5721 (2005)

[FALC 04] F. Falcone, T. Lopetegi, J. D. Baena, R. Marques, F. Martín and M. Sorolla, "Effective Negative-ε Stopband Microstrip Lines Based on Complementary Split Ring Resonators," *IEEE Microwave and Wireless Components Letters*, **14**, 6 (2004)

[FENG 08] L. Feng, K. Tetz, B. Slutsky, V. Lomakin, Y. Fainman, "Fourier plasmonics: diffractive focusing of in-plane surface plasmon polaritons waves," *Applied Physics Letters*, **91**, 081101 (2008)

[FERG 02] B. Ferguson and X. –C. Zhang, "Materials for terahertz science and technology," *Nature Materials*, **1**, 1 (2002)

[FERN 12] A. I. Fernández-Domínguez, Y. Luo, A. Wiener, J. B. Pendry and S. A. Maier, "Theory of three-dimensional nanocrescent light harvesters. *Nano Letters*, **12**, 5946 (2012)

[FILI 93] D. F. Filipovic, S. S. Gearhart and G. M. Rebeiz, "Double-slot antennas on extended hemispherical and elliptical silicon dielectric lenses," *IEEE Transactions on Microwave Theory and Techniques*, **41**, 10 (1993)

[FLEU 13] R. Fleury and A. Alù, "Enhanced superradiance in epsilon-near-zero plasmonc channels," *Physical Review B.*, **87**, 201101(R) (2013)

[FORE 16] C. Forestiere, Y. He, R. Wang, R. M. Kirby and L. Dal Negro, "Inverse design of metal nanoparticles' morphology," *ACS Photonics*, **3**, 1 (2016)

[FRES 66] A. Fresnel, "Calcul de l'intensite de la lumiere au centre de l'ombre d'un ecran et d'une ouverture circulaires eclairee par une point radieux," *Oeuvres d'Agustin Fresnel*, **1**, 365 (1866)

G

[GAO 13] J. Gao, L. Sun, H. Deng, C. J. Mathai, S. Gangopadhyay and X. Yang, "Experimental realization of epsilon-near-zero metamaterial slabs with metal-dielectric multilayers," *Applied Physics Letters*, **103**, 051111 (2013)

[GARC 03] F. J. García-Vidal, H. J. Lezec, T. W. Ebbesen and L. Martín-Moreno, "Multiple paths to enhance optical transmission through a single subwavelength slit," *Physical Review Letters*, **90**, 21 (2003)

[GARC 05] F. J. García de Abajo, R. Gómez-Medina and J. J. Sáenz, "Full transmission through perfect-conductor subwavelength hole arrays," *Physical Review E.*, **72**, 1 (2005)

[GARC 07] F. J. García de Abajo, "Colloquium: Light scattering by particle and hole arrays," *Reviews of Modern Physics,* **79**, 1267 (2007)

[GARC 09] C. García-Meca, R. Ortuño, F. J. Rodríguez-Fortuño, J. Martí, and A. Martínez, "Double-negative polarization-independent fishnet metamaterial in the visible spectrum," *Optics Letters*, **34**, 1603 (2009)

[GARC 10] F. J. García-Vidal, T. W. Ebbesen, and L. Kuipers, "Light passing through subwavelength apertures," *Reviews of Modern Physics*, **82**, 729 (2010)

[GEIN 11] Y. E. Geints, A. A. Zemlyanov and E. K. Panina, "Photonic nanojet calculations in layered radially inhomogeneous micrometer-sized spherical particles," *Journal of the Optical Society of America B*, **28**, 8 (2011)

[GENT 15] A. N. Gentselev, B. G. Goldenberg and S. A. Kuznetsov, "Microstructured elements for electromagnetic radiation selection and the method for their fabrication," *Russian Federation Pattent* (2015, in Russian)

[GIAN 10] V. Giannini, A. I. Fernández-Domínguez, Y. Sonnefraud, T. Roschuk, R. Fernández-García and S. A. Maier, "Controlling light localization and light-matter interactions with nanoplasmonics," *Small*, **6**, 2498 (2010)

[GIAN 10a] V. Giannini, R. Rodríguez-Oliveros, J. A. Sánchez-Gil, "Surface plasmon resonances of metallic nanostars/nanoflowers for surface-enhanced Raman scattering," *Plasmonics*, **5**, 1 (2010)

[GIAN 11] V. Giannini, A. I. Fernández-Domínguez, S. C. Heck and S. Maier, "Plasmonic nanoantennas: fundamentals and their use in controlling the radiative properties of nanoemitters," *Chemical Reviews*, **111**, 6 (2011)

[GOLD 92] P. F. Goldsmith, "Zone plate lens antennas for millimeter and submillimeter wavelengths," *in Third International Symposium on Space Terahertz Technology*, (1992)

[GOLD 97] P.F. Goldsmith, *Quasioptical systems: Gaussian beam, quasioptical propagation and applications*, (IEEE Press, 1998)

[GRBI 02a] A. Grbic and G. V. Eleftheriades, "A backward-wave antenna based on negative refractive index L-C networks," *IEEE Antennas and Propagation Society, AP-S International Symposium (Digest)*, **4**, 340 (2002)

[GRBI 02b] A. Grbic and G. V. Eleftheriades, "Experimental verification of backward-wave radiation from a negative refractive index metamaterial," *Journal of Reviews of Modern Physics*, **92**, 10 (2002)

[GREE 05] R. B. Greegor, C. G. Parazzoli, J. A. Nielsen, M. A. Thompson, M. H. Tanielian, and D. R. Smith, "Simulation and testing of a graded negative index of refraction lens," *Applied Physics Letters*, **87**, (2005)

[GRIS 90] D. Grischkowsky, S. Keiding, M. Van Exter, and C. Fattinger, "Far-infrared time-domain spectroscopy with terahertz beams of dielectrics and semiconductors," *Journal of the Optical Society of America. B*, **7**, 10 (1990)

[GUO 02] Y. J. Guo and S. K. Barton, *Fresnel Zone Antennas*. Dordrecht, The Netherlands: Kluwer Academic Publishers, (2002)

[GUPT 71] K. C. Gupta, "Narrow beam antenna using an artificial dielectric medium with permittivity less than unity," *Electronics Letters*, **7**, 1 (1971)

H

[HAO 11] X. Hao, C. Kuang, X. Liu, H. Zhang and Y. Li, "Microsphere based microscope with optical super-resolution capability," *Applied Physics Letters*, **99**, 203102 (2011)

[HAO 15] Q. Hao, C. Wang, H. Huang, W. Li, D. Du, D. Hang, T. Qiu and P. K. Chu, "Aluminum plasmonic photocatalysis," *Scientific Reports*, **5**, 15288 (2015)

[HATA 10] N. A. Hatab, C. H. Hsueh, A. L. Gaddis, S. T. Retterer, J. H. Li, G. Eres, Z. Zhang and B. Gu, "Free-standing optical gold bowtie nanoantenna with variable gap size for enhanced Raman spectroscopy," *Nano Letters*, **10**, 4952 (2010)

[HEIB 75] M. Heiblum and J. H. Harris, "Analysis of curved optical waveguides by conformal transformation," *IEEE J. Quant. Electron*, **11**, 75 (1975)

[HEIF 06] A. Heifetz, K. Huang, A. V. Sahakian, X. Li, A. Taflove, and V. Backman, "Experimental confirmation of backscattering enhancement induced by a photonic jet," *Applied Physics Letters*, **89**, 22 (2006)

[HEIF 09] A. Heifetz, S.-C. Kong, A. V. Sahakian, A. Taflove and V. Blackman, "Photonic Nanojets," *Journal of computational and theoretical nanoscience*, **6**, 9 (2009)

[HENT 16] M. Hentschel, B. Metzger, B. Knabe, K. Buse and H. Giessen, "Linear and nonlinear optical properties of hybrid metallic-dielectric plasmonic nanoantennas," *Beilstein Journal of Nanotechnology*, **7**, 111 (2016)

[HESS 65] A. Hessel and A. A. Oliner, "A new theory of Wood's anomalies on optical gratings," *Appl. Opt.*, **4**, 1275 (1965)

[HRIS 95] H. D. Hristov and M. H. A. J. Herben, "Millimeter-wave Fresnel-zone plate lens and antenna," *IEEE Transactions Microwave Theory and Techniques*, **43**, 12, (1995)

[HRIS 00] H. D. Hristov, *Fresnel Zones in Wireless Links, Zone Plate Lenses and Antennas*, Inc., Norwood, MA: Artech House (2000)

[HRIS 11] H. D. Hristov, "Terahertz harmonic operation of microwave Fresnel zone plate lens antenna: frequency filtering and space resolution properties," *International Journal of Antennas and Propagation*, **2011**, 541734 (2011)

[HO 08] L. Ho, M. Pepper and P. Taday, "Terahertz spectroscopy: signatures and fingerprints," *Nature photonics*, **2**, 541 (2008)

I

[IEEE 79] *IEEE Standard Test Procedures foe Antennas*, **(149-1979)** (1979)

[ISHI 90] A. Ishimaru, *Electromagnetic wave propagation, radiation, and scattering* (Prentice Hall, 1990)

J

[JACK 98] J. D. Jackson, *Classical Electrodynamics* (Wiley, 1998)

[JIN 06] Y. Jin, G. Kim, and S. Jeon, "Terahertz Dielectric Properties of Polymers," *Journal-Korean Physical Society*, **49**, 2 (2006)

[JOAN 95] J. D. Joannopoulos, S. G. Johnson, J. N. Winn and R. D. Meade, *Photonic Crystals Molding the Flow of Light*, Princeton, NJ: Princeton Univ. Press, 1995

[JOHN 97] S. John, "Frozen-light," *Nature* **390,** 6661, (1997)

[JOHN 72] P. B. Johnson and R. E. Christy, "Optical constants of the noble metals," *Physical Review B*, **6**, 12 (1972)

[JU 13] D. Ju, H. Pei, Y. Jiang and X. Sun, "Controllable and enhanced nanojet effects excited by surface plasmon polaritons," *Applied Physics Letters*, **102**, 171109 (2013)

K

[KAFE 07] M. Kafesaki, I. Tsiapa, N. Katsarakis, T. Koschny, C. M. Soukoulis, and E. N. Economou, "Left-handed metamaterials: The fishnet structure and its variations," *Physical Review B*, **75**, 1 (2007)

[KAIP 10] C. S. R. Kaipa, A. B. Yakovlev, F. Medina, F. Mesa, C. A. M. Butler, and A. P. Hibbins, "Circuit modeling of the transmissivity of stacked two-dimensional metallic meshes," *Optics Express*, **18**, 13309 (2010)

[KARL 15] N. J. Karl, R. W. McKinney, Y. Monnai, R. Mendis and D. M. Mittleman, "Frequency-division multiplexing in the terahertz range using a leaky-wave antenna," *Nature Photonics*, **9**, 717 (2015)

[KHAL 14] A. Khaleque and Z. Li, "Tailoring the properties of photonic nanojets by changing the material and geometry of the concentrator," *Progress in Electromagnetics Research Letters*, **48**, 7 (2014)

[KIM 06] K. Y. Kim, Y. K. Cho and H. –S. Tae, "Light transmission along dispersive plasmonic gap and its subwavelength guidance characteristics," *Optics Express*, **14**, 1 (2006)

[KINK 09] A. Kinkhabwala, Z. Yu, S. Fan, Y. Avlasevich, K. Mullen and W. E. Moerner, "Large single-molecule fluorescence enhancements produced by a bowtie nanoantenna," *Nature Photonics*, **3**, 654 (2009)

[KNIG 11] M. W. Knight, H. Sobhani, P. Nordlander, N. J. Halas, "Photodetection with Active Optical Antennas," *Science*, **332**, 702 (2011)

[KNIG 14] M. W. Knight, N. S. King, L. Liu, H. O. Everitt, P. Nordlander and N. J. Halas, "Aluminum for plasmonics," *ACS Nano*, **8**, 1 (2014)

[KO 11] K.D. Ko, A. Kumar, K. H. Fung, R. Ambekar, G. L. Liu, N. X. Fang, and K. C. Toussaint, "Nonlinear optical response from arrays of Au bowtie nanoantennas," *Nano Letters*, **11**, 61 (2011)

[KOCK 46] W. E. Kock, "Metal-Lens Antennas," *Proceedings of the I.R.E and Waves and Electrons, IRE* **34** (11), (1946)

[KRAS 10] A. V. Krasavin and A. V. Zayats, "Silicon-based plasmonic waveguides," *Optics Express*, **18**, 081101 (2010)

[KUZN] S. A. Kuznetzov, *et.al.*, "High-performance subterahertz high-pass filters and planar focusing structures produced with deep X-ray lithography, *Applied Physics Letters* (2016, submitted)

[KWON 09] D. H. Kwon and D. H. Werner, "Beam scanning using flat transformation electromagnetic focusing lenses," *IEEE Antennas and Wireless Propagation Letters*, **8**, 5276827 (2009)

L

[LAUR 11] B. Lauritzen, J. Minář, H. de Riedmatten, M. Afzelius, and N. Gisin, "Approaches for a quantum memory at telecommunication wavelengths," *Physical Review A*, **83**, 1 (2011)

[LEE 09] Y. –S. Lee, *Principles of Terahertz Science and Technology* (Springer, 2009)

[LEE 09a] J. Y. Lee, B. H. Hong, W. Y. Kim, S. K. Min, Y. Kim, M. V. Jouravlev, R. Bose, K. S. Kim, I.-C. Hwang, L. J. Kaufman, C. W. Wong, P. Kim, and K. S. Kim, "Near-field focusing and magnification through self-assembled nanoscale spherical lenses," *Nature*, **460**, 7254, (2009)

[LEE 15] K. Lee, S.- Y. Lee, J. Jung and B. Lee, "Plasmonic achromatic doublet lens," *Optics Express*, **23**, 5 (2015)

[LEON 06] U. Leonhardt, "Optical conformal mapping," *Science*, **312**, 1777 (2006)

[LERE 12] A. L. Lereu, J. P. Hoogenboom and N. F. van Hulst, "Gap nanoantennas toward molecular plasmonic devices," *International Journal of Optics*, **2012**, 502930 (2012)

[LEZE 02] H. J. Lezec, A. Derigon, E. Deveaux, R. A. Linke, L. Martín-Moreno, F. J. García-Vidal and T. W. Ebbesen, "Beam light from a sub-wavelength apperture," *Science*, **97**, 5582 (2002)

[LI 05] X. Li, Z. Cheng, A. Taflove and V. Backman, "Optical analysis of nanoparticles via enhanced backscattering facilitated by 3-D photonic nanojets," *Optics Express*, **13**, 3 (2005)

[LIN 08] X. Q. Lin, T. J. Cui, J. Y. Chin, X. M. Yang, Q. Cheng and R. Liu, "Controlling electromagnetic waves using tunable gradient dielectric metamaterial lens," *Applied Physics Letters*, **92**, 13, (2008)

[LIN 15] L. Lin and Y. Zheng, "Optimizing plasmonic nanoantennas via coordinated multiple coupling," *Scientific Reports*, **5**, 14788 (2015)

[LIU 07] Z. Liu, H. Lee, Y. Xiong, C. Sun, and X. Zhang, "Far-field optical hyperlens magnifying sub-diffraction-limited objects," *Science*, **315**, 5819, (2007)

[LIU 08] R. Liu, Q. Cheng, T. Hand, J. J. Mock, T. J. Cui, S. A. Cummer and D. R Smith, "Experimental demonstration of electromagnetic tunneling through an epsilon-near-zero metamaterial at microwave frequencies," *Physical Review Letters*, **100**, 2 (2008)

[LIU 09] R. Liu, Q. Cheng, J. Y. Chin, J. J. Mock, T. J. Cui and D. R. Smith, "Broadband gradient index microwave quasi-optical elements based on non-resonant metamaterials," *Optics Express*, **17**, 23 (2009)

[LIU 09a] M. Liu, T. Lee, S. K. Gray, P. Guyot-Sionnest, and M. Pelton, "Excitation of dark plasmons in metal nanoparticles by a localized emitter," *Physical Review Letters*, **102**, 107401 (2009)

[LIU 11] H. Liu and T. Zhou, "Two dimensional invisibility cloaking via transformation optics, *Discrete and Continuous Dynamical Systems*, **31**, 2 (2011)

[LIU 13] C. Liu, "Ultra-elongated photonic nanojets generated by a graded-index microellipsoid," *Progress in Electromagnetic Research Letters*, **37**, 153 (2013)

[LIU 14] C. –Y. Liu, L.- J. Chang and L. –J. Yang, "Photonic nanojet in non-spherical micro-particles," in *9th IEEE International Conference on Nano/Micro Engineered and Molecular Systems*, (2014)

[LIU 15] H. -W. F. –C. Lin, S. –W. Lin, J. –Y. Wu, B. –T. Chou, K. –J. Lai, S. -–D. Lin and J. –S. Huang, "Single-crystalline Aluminum nanostructures on a semiconducting GaAs substrate for ultraviolet to near-infrared plasmonics," *ACS Nano*, **15**, 4 (2015)

[LLOM 12] N. Llombart and A. Neto, "THz time-domain sensing : the antenna dispersion problem and a possible solution," *IEEE Transactions on Terahertz Science and Technology*, **2**, 4 (2012)

[LOMA 04] V. Lomakin and E. Michielssen, "Enhanced transmission through two-period arrays of subwavelength holes," *IEEE Microwave and Wireless Components Letters.*, **14**, 355 (2004)

[LOMA 05] V. Lomakin and E. Michielssen, "Enhanced transmission through metallic plates perforated by arrays of subwavelength holes and sandwiched between dielectric slabs," *Physical Review B.*, **71**, 235117 (2005)

[LOVA 06] G. Lovat, P. Burghignoli, F. Capolino, D. R. Jackson and D. R. Wilton, "Analysis of directive radiation from a line source in a metamaterial slab with low permittivity," *IEEE Transactions on Antennas and Propagation*, **54**, 3 (2006)

[LOVA 07] G. Lovat, P. Burghignoli, F. Capolino, D. R. Jackson, "Combinations of low/high permittivity and/or permeability substrates for highly directive planar metamaterial antennas," *IET Microwaves, Antennas and Propagation*, **1**, 1 (2007)

[LU 00] Y. F. Lu, L. Zhang, W. D. Song, Y. W. Zheng and B. S. Luk'yanchuck, " Laser writing of a subwavelength structure on silicon (100) surfaces with particle-enhanced optical irradiation," *Journal of experimental and theoretical physics letters*, **72**, 9 (2000)

[LUO 10] Y. Luo, J. B. Pendry and A. Aubry, "Surface Plasmons and Singularities," *Nano Letters*, **10**, 4186 (2010)

[LUO 12] Y. Luo, D. Y. Lei, S. A. Maier and J. B. Pendry, "Transformation-optics description of plasmonic nanostructures containing blunt edges/corners: From symmetric to asymmetric edge rounding," *ACS Nano*, **6**, 6492 (2012)

[LUO 12a] Y. Luo, D. Y. Lei, S. A. Maier and J. B. Pendry, "Broadband light harvesting nanostructures robust to edge bluntness," *Physical Review Letters*, **108**, 023901 (2012)

M

[MAAS 13] R. Maas, J. Parsons, N. Engheta and A. Polman, "Experimental realization of an epsilon-near-zero metamaterial at visible frequencies," *Nature Photonics*, **7**, 11 (2013)

[MAIE 04] S. A. Maier, *Plasmonics, Fundamentals and Applications* (Springer, 2004)

[MARQ 08] R. Marques, F. Martin, and M. Sorolla, *Metamaterials with Negative Parameters: Theory, Design, and Microwave Applications*, New York: John Wiley & Sons, 2008

[MARQ 09a] R. Marqués, F. Mesa, L. Jelinek, and F. Medina, "Analytical theory of extraordinary transmission through metallic diffraction screens perforated by small holes," *Optics Express*, **17**, 5571 (2009)

[MARQ 09b] R. Marqués, L. Jelinek, F. Mesa, and F. Medina, "Analytical theory of wave propagation through stacked fishnet metamaterials," *Optics Express*, **17**, 11582 (2009)

[MART 01] L. Martín-Moreno, F. J. García-Vidal, H. J. Lezec, K. M. Pellerin, T. Thio, J. B. Pendry and T. W. Ebbesen, "Theory of extraordinary optical transmission through subwavelength hole arrays," *Physical Review Letters*, **86**, 6 (2001)

[MART 13] J. Martin, J. Proust, D. Gérard and J. Plain, "Localized surface plasmon resonances in the ultraviolet from large scale nanostructured aluminum films," *Optical Materials Express*, **3**, 7 (2013)

[MASS 13] E. Massa, S. A. Maier and V. Giannini, "An analytical approach to light scattering from small cubic and rectangular cuboidal nanoantennas," *New Journal of Physics*, **15**, 063013 (2013)

[MASL 16] A. V. Maslov and V. N. Astratov, "Imaging of sub-wavelength structures radiating coherently near microspheres," *Applied Physics Letters*, **108**, 5, (2016)

[MAYE 11] K. M. Mayer and J. H. Hafner, "Localized surface plasmon resonance sensors," *Chemical Reviews*, **111**, 6 (2001)

[MEDI 08] F. Medina, F. Mesa, and R. Marqués, "Extraordinary transmission through arrays of electrically small holes from a circuit theory perspective," *IEEE Transactions on Microwave Theory and Techniques*, **56**, 3108 (2008)

[MEDI 10] F. Medina, F. Mesa, and D. C. Skigin, "Extraordinary transmission through arrays of slits: a circuit theory model," *IEEE Transactions on Microwave Theory and Techniques*, **58**, 105 (2010)

[MINI 90] I. V. Minin and O. V. Minin, "Control of focusing properties of diffraction elements," *Quantum Electron*, **20**, 2 (1990)

[MINI 04] I. V. Minin and O. V. Minin, *Diffractional Optics of Millimetre Waves*, First. Bristol, UK: The institute of Physics Publishing, (2004)

[MINI 05] I. V. Minin, O. V. Minin, and G. Webb, "Flat and conformal zone plate antennas with new capabilities," *Proceeding Int. Congr. Appl. Electromagn. Commun.*, (2005)

[MINI 06] I. V. Minin, O. V. Minin, N. Gagnon and A. Petosa, "FDTD analysis of a flat diffractive optics with sub-Reyleigh limit resolution in MM/THz waveband," in *Infrared millimeter waves and 14th International Conference on Terahertz and Electronics*, (2006)

[MINI 11] I. V. Minin and O. V. Minin, "Reference Phase in Diffractive Lens Antennas: A Review," *J. Infrared, Millimeter, Terahertz Waves*, **32**, 6 (2011)

[MINI 14] I. V. Minin and O. V. minin, "Experimental verification 3D subwavelength resolution beyond the diffraction limit with zone plate in millimeter wave," *Microwave and Optical Technology Letters*, **58**, 2436 (2014)

[MINI 14b] I. V. Minin and O. V. Minin, "3D diffractive lenses to overcome the 3D Abbe subwavelength diffraction limit," *Chinesse Optics Letters*, **12**, 060014 (2014)

[MINI 15a] I. V. Minin, O. V. Minin and Y. E. Geints, "Localized EM and photonic jets from non-spherical and non-symetrical dielectric mesoscale objects: Brief review," *Annalen der Physik*, **527**, 7 (2015)

[MONT 12] A. Monti, F. Bilotti, A. Toscano, and L. Vegni, "Possible implementation of epsilon-near-zero metamaterials working at optical frequencies," *Optics Communications.*, **285**, 16 (2012)

[MONT 13] F. Monticone and A. Alù, "Do cloacked objects really scatter less?," *Physical Review X*, **3**, 041005 (2013)

[MOSC 12] A. Moscatelli, "Plasmonics: the aluminium rush," *Nature Nanotechnology*, **7**, 778 (2012)

[MUNK 00] B. A. Munk, *Frequency selective surfaces: theory and design*, (Wiley, 2000)

N

[NAVA 08] M. Navarro-Cía, M. Beruete, M. Sorolla, and I. Campillo, "Negative refraction in a prism made of stacked subwavelength hole arrays," *Optics Express*, **16**, 560 (2008)

[NAVA 09a] M. Navarro-Cía, M. Beruete, I. Campillo, and M. Sorolla, "Millimeter-Wave left-handed extraordinary transmission metamaterial demultiplexer," *IEEE Antennas and Wireless Propagation Letters*, **8**, 212 (2009)

[NAVA 09b] M. Navarro-Cía, M. Beruete, M. Sorolla and I. Campillo, "Converging biconcave metallic lens by double-negative extraordinary transmission metamaterial," *Applied Physics Letters*, **94**, 144107 (2009)

[NAVA 10a] M. Navarro-Cía, M. Beruete, I. Campillo and M. Sorolla, "Fresh metamaterials ideas for metallic lenses," *Metamaterials*, **4**, 119 (2010)

[NAVA 10b] M. Navarro-Cía, M. Beruete, M. Sorolla and I. Campillo, "Viability of focusing effect by left-handed stacked subwavelength hole arrays," *Physica B: Condensed Matter*, **405**, 14 (2010)

[NAVA 10c] M. Navarro-Cía, M. Beruete, F. Falcone and M. Sorolla, "Polarization-tunable negative or positive refraction in self-complementariness-based extraordinary transmission prism," *Progress in Electromagnetics Research PIER*, **103**, 101 (2010)

[NAVA 11a] M. Navarro-Cía, V. Torres Landivar, M. Beruete, and M. Sorolla Ayza, "A slow light fishnet-like absorber in the millimeter-wave," *Progress in Electromagnetics Research PIER* **118**, 287 (2011)

[NAVA 11b] M. Navarro-Cía, M. Beruete, I. Campillo and M. Sorolla, "Beamforming by left-handed extraordinary transmission metamaterial bi- and plano-concave lens at millimeter-waves," *IEEE Transactions on Antennas and Propagation*, **59**, 6 (2011)

[NAVA 11c] M. Navarro-Cía, M. Beruete, I. Campillo and M. Sorolla, "Enhanced lens by ε and μ near-zero metamaterial boosted by extraordinary optical transmission," *Physical Review B*, **83**, 115112 (2011)

[NAVA 12] M. Navarro-Cía, M. Beruete, M. Sorolla, N. Engheta, "Lensing System and Fourier Transformation using ε-near-zero (ENZ) metamaterials," *Physical Review B*, **86**, 16 (2012)

[NAVA 12a] M. Navarro-Cia and S. A. Maier, "Broad-band near-infrared plasmonic nanoantennas for higher harmonic generation," *ACS Nano*, **6**, 3537 (2012)

[NEU 10] J. Neu, B. Krolla, O. Paul, B. Reinhard, R. Beigang, and M. Rahm, "Metamaterial-based gradient index lens with strong focusing in the THz frequency range," *Optics Express*, **18**, 26 (2010)

[NEU 13] J. Neu, R. Beigang and Marco Rahm, "Metamaterial-based gradient index beam steerers for terahertz radiation," *Applied Physics Letters*, **103**, 041109 (2013)

[NG 13] B. Ng, J. Wu, S. M. Hanham, A. I. Fernández-Domínguez, N. Klein, Y. F. Liew, M. B. H. Breese, M. Hong and S. A. Maier, "Spoof plasmon resonances: a novel platform for THz sensing," *Advanced Optical Materials*, **1**, 8 (2013)

[NGUY 09] V. N. Nguyen, S. H. Yönak, and D. R. Smith, "Millimeter-wave artificial dielectric gradient index lenses," *in EuCAP 2009 - 3rd European Conference on Antennas and Propagation*, (2009)

[NIE 97] S. Nie, "Probing single molecules and single nanoparticles by surface-enhanced Raman scattering," *Science*, **275**, 1102 (1997)

[NOVO 12] L. Novotny, B. Hecht, *Principles of Nano-Optics*, 2nd Edition, Cambridge University Press: U.K. (2012)

O

[OHAR 12] J. F. O'Hara, W. Withayachumnankul and I. Al-Naib, "A review on thin-film sensing with terahertz waves," *Journal of Infrared, Millimeter, Terahertz waves*, **33,** 245 (2012)

[ORAZ 15a] B. Orazbayev, M. Beruete, V. Pacheco-Peña, G. Crespo, J. teniente and M. Navarro-Cía, "Soret fishnet metalens antenna," *Scientific reports*, **4**, 9988 (2015)

[ORAZ 15b] B. Orazbayev, V. Pacheco-Peña, M. Beruete and M. Navarro-Cía, "Exploiting the dispersion of the double-negative-index fishnet metamaterial to créate a broadband low-profile metallic lens," *Optics Express*, **23**, 7 (2015)

[ORAZ 15c] B. Orazbayev, N. M. Estarkhi, M. Beruete and A. Alù, "Terahertz carpet cloack based on a ring resonator metasurface," *Physical Review B.*, **91**, 195444 (2015)

[ORAZ 15d] B. Orazbayev, M. Beruete and M. Navarro-Cía, "Wood zone plate fishnet metalens," *EPJ Applied Metamaterials*, **2**, 8 (2015)

[OURI 09] A. Ourir and A. De Lustrac, "Metamaterial-based phased array for directional beam steering," *Microwave and Optical Technology Letters*, **51**, 11 (2009)

P

[PACH 13a] V. Pacheco-Peña, V. Torres, M. Navarro-Cía, M. Beruete, M. Sorolla and N. Engheta, "ε-near-zero graded index structure as a bi-concave metallic lens using stacked rectangular near cut-off waveguide," *in 7th European Conference on Antennas and Propagation (EuCAP 2013)*, (2013)

[PACH 14a] V. Pacheco-Peña, V. Torres, B. Orazbayev, M. Beruete, M. Navarro-Cía, M. Sorolla and N. Engheta, "Mechanical 144 GHz beam steering with all-metallic epsilon-near-zero lens antenna," *Applied Physics Letters*, **105**, 243503 (2014)

[PACH 14b] V. Pacheco-Peña, V. Torres, M. Beruete, M. Navarro-Cía and N. Engheta, "ε-near-zero (ENZ) graded index quasi-optical devices: steering and splitting millimeter waves," *Journal of Optics*, **16**, 9 (2014)

[PACH 16a] V. Pacheco-Peña, N. Engheta, S. Kuznetsov and M. Beruete, "Experimental realization of an epsilon-near-zero graded-index metalens at terahertz frequencies," *(Under Review)*, (2016)

[PACH 16b] V. Pacheco-Peña, M. Beruete, P. Rodríguez-Ulibarri and N. Engheta, "Systematic study of an ENZ-based sensor via the transmission line theory and the effective médium approach," *(Under Review)*, (2016)

[PACH 16c] V. Pacheco-Peña, M. Navarro-Cía and M. Beruete, "Focusing optical waves via graded-epsilon-near-zero metalens," *in 10th International Congress on Advanced Electromagnetic materials in Microwaves and Optics (Metamaterials 2016)*, (2016)

[PADI 06] W. J. Padilla, D. N. Basov and D. R. Smith, "Negative refractive index metamaterials," *Materials Today*, **9**, 7 (2006)

[PALI 85] E. D. Palik, *Handbook of optical constants of solids*, Academic, (1985)

[PARA 04] C. G. Parazzoli, R. B. Greegor, J. A. Nielsen, M. A. Thompson, K. Li, A. M. Vetter, M. H. Tanielian, and D. C. Vier, "Performance of a negative index of refraction lens," *Applied Physics Letters*, **84**, 17 (2004)

[PAUL 10] O.Paul, B. Reinhard, B. Krolla, R. Beigang, and M. Rahm, "Graded index metamaterial based on slot elements," *Applied Physics Letters*, **96**, 24 (2010)

[PEND 99] J. B. Pendry, A. J. Robbins and W. J. Stewart, "Magnetism from Conductors and Enhanced Nonlinear Phenomena," *IEEE Transactions on Microwave Theory and Techniques*, **47**, 11 (1999)

[PEND 00] J. B. Pendry, "Negative refraction makes a perfect lens," *Physical Review Letters*, **85**, 3966 (2000)

[PEND 06] J. B. Pendry. D. Schurig and D. R. Smith, "Controlling electromagnetic fields," *Science*, **312**, 1780 (2006)

[PEND 12] J. B. Pendry, A. Aubry, D. R. Smith and S. A. Maier, "Transformation optics and subwavelength control of light," *Science*, **337**, 549 (2012)

[PEND 13] J. B. Pendry, A. I. Fernández-Domínguez, Y. Luo and R. Zhao, "Capturing photons with transformation optics," *Nature Physics*, **9**, 518 (2013)

[PETR 11] E. Petryayeva and U. J. Krull, "Localized surface plasmon resonance: nanostructures, bioassays and biosensing - A review," *Analytica Chimica Acta*, **706**, 1 (2011)

[PIME 07] A. Pimenov, A. Loidl, K. Gehrke, V. Moshnyaga and K. Samwer, "Negative refraction observed in a metallic ferromagnetic in the gigahertz frequency range," *Physical Review Letters*, **98**, 197401 (2007)

[PITA 07] J. M. Pitarke, V. M. Silkin, E. V. Chulkov and P. M. Echenique, "Theory of surface plasmons and surface-plasmons polaritons," *Reports on progress in physics*, **70**, 1 (2007)

[PODD 13] A. Poddubny, I. Iorsh, P. Belov, and Y. Kivshar, "Hyperbolic metamaterials," *Nature Photonics*, **7**, 12 (2013)

[PORT 99] J. A. Porto, F. J. García-Vidal and J. B. Pendry, "Transmission resonances on metallic gratings with very narrow slits," *Physical Review Letters*, **83**, 14 (1999)

[POWE 59a] C. J. Powell and J. B. Swan, "Origin of the characteristic electron energy losses in aluminum," *Physical Review*, **115**, 4 (1959)

[POWE 59b] C. J. Powell and J. B. Swan, "Origin of the characteristic electron energy losses in magnesium," *Physical Review*, **116**, 1 (1959)

[POWE 09] D. A. Powell, A. Alù, B. Edwards, A. Vakil, Y. Kivshar and N. Engheta, "Nonlinear control of tunneling through an epsilon-near-zero channel," *Physical Review B – Condensed Matter and Materials Physics*, **79**, 24 (2009)

[POZA 04] D. Pozar, *Microwave Engineering*, New York: John Wiley & Sons (2004)

Q

R

[RADK 07] I. P. Radko and S. I. Bozhevolnyi, "Surface plasmon polaritons beam focusing with parabolic nanoparticle chains," *Optics Express*, **15**, 11 (2007)

[RAMA 98] S. Raman, N. S. Barker and G. M. Rebeiz, "A W-band dielectric-lens-based integrated monopulse radar receiver," *IEEE Transactions on Microwave Theory and Techniques*, **46,** 12 (1998)

[RAYL 07] Lord Rayleigh, "On the dynamical theory of gratings," *Proceedings of the Royal Society of London A*, **79**, 399 (1907)

[REDO 13] A. Redo-Sanchez, N. Laman, B. Schulkin and T. Tongue, "Review of terahertz technology readiness assessment and applications," *Journal of infrared, millimeter and terahertz waves*, **34**, 9 (2013)

[RAMO 94] S. Ramo, J. R. Whinnery and T. V. Duzer, *Field and waves in communications electronic*, Wiley (1994)

[RITC 57] R. H. Ritchie, "Plasma losses by fast electrons in thin films," *Physical Review*, **106**, 5 (1957)

[RIVA 05] J. G. Rivas, C. Janke, P. Bolivar and H. Kurz, "Transmission of THz radiation through InSb gratings of subwavelength apertures," *Optics Express*, **13**, 3 (2005)

[ROBI 60] L. A. Robinson, "Electrical properties of metal loaded radomes," *Wright air Develop. Div. Rep. WADD-TR-***60-84** (1960)

[RODR 10] R. Rodríguez-Berral, F. Mesa, and F. Medina, "Circuit model for a periodic array of slits sandwiched between two dielectric slabs," *Applied Physics Letters*, **96**, 161104 (2010)

[RODR 13] F. J. Rodríguez-Fortuño, G. Marino, P. Ginzburg, D. O'Connor, A. Martínez, G. A. Wurtz and A. V. Zayats, "Near field interference for the unidirectional excitation of electromagnetic guided modes," *Science*, **340**, 6130 (2013)

[RODR 16] P. Rodríguez-Ulibarri, S. A. Kuznetsov and M. Beruete, "Wide angle terahertz sensing with a cross-dipole frequency selective surface," *Applied Physics Letters*, **108**, 111104 (2016)

[ROGE 12] E. T. F. Rogers, J. Lindberg, T. Roy, S. Savo, J. E. Chad, M. R. Dennis, and N. I. Zheludev, "A super-oscillatory lens optical microscope for subwavelength imaging.," *Nature Materials*, **11**, 5 (2012)

[ROTM 62] W. Rotman, "Plasma Simulation by artificial dielectric and parallel plate media, *IRE Transactions on Antennas and Propagation*, **10**, 82 (1962)

[ROXW 14] B. J. Roxworthy, A. M. Bhuiya, X. Yu, E. K. C. Chow, and K. C. Toussaint, "Reconfigurable nanoantennas using electron-beam manipulation," *Nature Communications*, **5**, 4427 (2014)

S

[SAIL 09] V. Saile, U. Wallrabe, O. Tabata and J. G. Korvink, "LIGA and its applications," *Advanced micro & nanosystems*, **7,** Wiley-VCH Verlag GmbH & Co. KGaA (2009)

[SAVI 12] G. Savini, O. A. R. Ade and J. Zhang, "A new artificial material approach for flat THz frequency lenses," *Optics Express*, **20**, 23 (2012)

[SEED 13] A. J. Seeds, M. J. Fice, K. Balakier, M. Natrella, O. Mitrofanov, M. Lamponi, M. Chtioui, F. van Dijk, M. Pepper, G. Aeppli, a G. Davies, P. Dean, E. Linfield, and C. C. Renaud, "Coherent terahertz photonics.," *Optics Express*, **21**, 19,(2013)

[SHEL 01] R. A. Shelby, D. R. Smith and S. Schultz, "Experimental verification of a negative index of refraction," *Science*, **292,** 5514 (2001)

[SIEG 02] P. H. Siegel, "Terahertz technology," *IEEE Transactions on Microwave Theory and Techniques*, **50**, 3 (2002)

[SIHV 07a] A. Sihvola, "Metamaterials in electromagnetics," *Metamaterials*, **1**, 2 (2007)

[SIHV 07b] A. Sihvola, S. Tretyarov, A. De Baas, "Metamaterials with Extreme Material Parameters," *Journal of Communications Technology and Electronics*, **52,** 9 (2007)

[SILV 06] M. G. Silveirinha and N. Engheta, "Tunneling of electromagnetic energy through subwavelength channels and bends using ε-near-zero materials," *Physical Review Letters*, **97**, 15 (2006)

[SILV 07a] M. G. Silveirinha and N. Engheta, "Theory of supercoupling, squeezing wave energy, and field confinement in narrow channels and tight bends using ε near-zero metamaterials," *Physical Review B - Condensed Matter and Materials Physics*, **76**, 24 (2007)

[SILV 07b] M. Silveirinha and N. Engheta, "Design of matched zero-index metamaterials using nonmagnetic inclusions in epsilon-near-zero media," *Physical Review B - Condensed Matter and Materials Physics*, **75**, 7 (2007)

[SING 14] R. Singh, W. Cao, I. Al-Naib, L. Cong, "Ultrasensitive terahertz sensing with high – Q Fano resonances in metasurfaces." *Applied Physics Letters*, **105**, 17 (2014)

[SIVI 13] M. Sivis, M. Duwe, B. Abel, and C. Ropers, "Extreme-ultraviolet light generation in plasmonic nanostructures," *Nature Physics*, **9**, 304 (2013)

[SMIT 00] D. R. Smith, W. J. Padilla, D. C. Vier, S. C. Nemat-Nasser and Schultz, "Composite medium with simultaneously Negative Permeability and Permittivity," *Physical Review Letters* **84**, 18 (2000)

[SMIT 05a] D. R. Smith, J. J. Mock, A. F. Starr and D. Schuring, "Gradient index metamaterials," *Physical Review E.*, **71**, 036609 (2005)

[SMIT 05b] D. R. Smith, D. C. Vier, Th. Koschny and C. m. Soukoulis, "Electromagnetic parameter retrieval from inhomogeneous materials," *Physical Review E*, **71**, 036617 (2005)

[SMOL 10] V. N. Smolyaninova, I. I. Smolyaninov, A. V Kildishev, and V. M. Shalaev, "Maxwell fish-eye and Eaton lenses emulated by microdroplets.," *Optics Letters*, **35**, 20, (2010)

[SMOL 16] V. N. Smolyaninova, C. Jensen, W. Zimmerman, A. Johnson, D. Schaefer and I. Smolyaninov, "Lithographically fabricated magnifying Maxell fisheye lenses," *Photonics*, **3**, 1 (2016)

[SOLY 09] L. Solymar and E. Shamonina, *Waves in Metamaterials* (Oxford University Press, 2009)

[SOMM 99] A. Sommerfield, "Ueber die Fortpflanzung elektrodynamischer Wellen längs eines Drahtes", *Annalen der Physik und Chemie*, **303**, 233 (1899)

[SOUK 11] C. M. Sooukoulis and M. Wegener, "Past achievements and future challenges in the development of three-dimensional photonic metamaterials," *Nature Photonics*, **5**, 523 (2011)

[STEE 06] J. M. Steele, Z. Liu, Y. Wang and X. Zhang, "Resonant and non-resonant generation and focusing of surface plasmons with circular gratings," *Optics express*, **14**, 5664 (2006)

[STER 60] E. A. Stern and R. A. Ferrel, "Surface plasma oscillations of a degenerate electron gas," *Physical Review*, **120**, 1 (1960)

[STOU 06] S. M. Stout-Grandy, A. Petosa, I. V Minin, O. V Minin, and J. Wight, "A systematic study of varying reference phase in the design of circular fresnel zone plate antennas," *IEEE Trans. Antennas Propag.*, **54**, 12 (2006)

[STRA 16] J. Straubel, R. Filter, C. Rockstuhl and K. Słowik, "Plasmonic nanoantenna based triggered single-photon source," *Physical Review B*, **93**, 195412 (2016)

[SYNG 28] E. H. Synge, "A suggested method for extending microscopic resolution into the ultra-microscopic region," *Philos. Mag. Ser. 7*, **6**, 356 (1928)

[SUBR 12] G. Subramania, A. J. Fisher and T. S. Luk, "Optical properties of metal-dielectric based epsilon near zero metamaterials," *Applied Physics Letters*, **101**, 241107 (2012)

T

[THAC 15] B. D. Thackray, P. a. Thomas, G. H. Auton, F. J. Rodriguez, O. P. Marshall, V. G. Kravets, and A. N. Grigorenko, "Super-Narrow, Extremely High Quality Collective Plasmon Resonances at Telecom Wavelengths and Their Application in a Hybrid Graphene-Plasmonic Modulator," *Nano Letters*, **15**, 3519 (2015)

[THOR] www.thorlab.com

[TORR 12a] V. Torres, V. Pacheco-Peña, P. Rodríguez-Ulibarri, M. Navarro-Cía, M. Beruete, M. Sorolla and N. Engheta, "Terahertz epsilon-near-zero graded-index lens," *Optics Express*, **21**, 7 (2013)

[TORR 12b] V. Torres, P. Rodríguez-Ulibarri, M. Navarro-Cía and M.Beruete, "Fishnet metamaterial from an equivalent circuit perpective," *Applied Physics Letters*, **101**, 244101 (2012)

[TORR 15] V. Torres, B. Orazbayev, V. Pacheco-Peña, J. Teniente, M. Beruete, M. Navarro-Cía, M. Sorolla and N. Engheta, "Experimental demonstration of a millimeter-wave metallic ENZ lens based on the energy squeezing principle," *IEEE Trans. Antennas and Propag.*, **63**, 1 (2015)

[TREA 99] M. M. J. Treacy, "Dynamical diffraction in metallic optical gratings," *Applied Physics Letters*, **75**, 5 (1999)

[TREA 02] M. M. J. Treacy, "Dynamical diffraction explanation of the anomalous transmission of light through metallic gratings," *Physical Review B*, **66**, 66 (2002)

U

[ULRI 67] R. Ulrich, "Far-infrared properties of metallic mesh and its complementary structure," *Infrared Physics*, **7**, 37 (1967)

V

[VAN 94] M. Van Houten and M. H. A. J. Herben, "Analysis of a phase-correcting Fresnel-zone plate antenna with dielectric/transparent zones," *Journal of Electromagnetic Waves and Applications*, **8**, 847 (1994)

[VESE 68] V. G. Veselago, "The electrodynamics of substances with simultaneously negative values of ε and μ," *Sov. Phys. Usp.*, **10**, 509, (1968)

[VIAL 05] A. Vial, A. –S. Grimault, D. Macías, D. Barchiesi and M. L. de la Chapelle, "Improved analytical fit of gold dispersión: application to the modeling of extintion spectra with a finite-difference time-domain method," *Physical Review B.* **71**, 085416 (2015)

W

[WANG 11] Z. Wang, W. Guo, L. Li, B. Luk'yanchuk, A. Khan, Z. Liu, Z. Chen and M. Hong, "Optical virtual imaging at 50nm lateral resolution with a white-light nanoscope," *Nature communications*, **2**, 218 (2011)

[WATS 15] A. M. Watson, X. Zhang, R. Alcaraz de la Osa, J. M. Sanz, F. González, F. Moreno, G. Finkelstein, J. Liu and H. O. Everitt, "Rhodium nanoparticles for ultraviolet plasmonics," *Nano Letters*, **15**, 1095 (2015)

[WEIG 03] W. S. Weiglhofer, A. Lakhtakia, *Introduction to complex mediums for optics and electromagnetics*, SPIE Press, Bellingham, WA, USA 2003

[WEIL 77] T. Weiland, "A discretization method for the solution of Maxwell's equations for six-component fields: Electronics and Communication," (AEÜ), **31**, 116 (1977)

[WILL 07] K. A. Willets and R. P. Van Duyne, "Localized surface plasmons resonance spectroscopy and sensing," *Annual Review of Physical Chemistry*, **58**, 267 (2007)

[WOLF 95] K. B. Wolf and G. Krötzsch, "Geometry and dynamics in refractive systems," *European Journal of Physics*, **16**, 14 (1995)

[WOOD 02] R. D. Wood, "On a remarkable case of uneven distribution of light in a diffraction grating spectrum," *Proc. Phys. Soc. London*, **18**, 269 (1902)

[WOOD 35] R. D. Wood, "Anomalous Diffraction Gratings," *Physical Review*, **48**, 928 (1935)

X

[XU 14] L. Xu and H. Chen, "Conformal transformation optics;" *Nature Photonics*, **9**, 1 (2014)

Y

[YABL 87] E. Yablonovitch, "Inhibited spontaneous emission in solid-state physics and electronics," *Physical Review Letters*, **58**, 2059 (1987)

[YABL 91] E. Yablonovitch, T. J. Gmitter, R. D. Meade, A. M. Rappe, K. D. Brommer, and J. D. Joannopoulos, "Donor and acceptor modes in photonic band-structure," *Physical Review Letters*, **67**, 3380 (1991)

[YANG 11] R. Yang, R. Rodríguez-Berral, F. Medina, and Y. Hao, "Analytical model for the transmission of electromagnetic waves through arrays of slits in perfect conductors and lossy metal screens," *Journal of Applied Physics*, **109**, 103107 (2011)

[YANG 13] X. Yang, C. Hu, H. Deng, D. Rosenmann, D. A. Czaplewski and J. Gao, "Experimental demonstration of near-infrared epsilon-near-zero multilayer metamaterial slabs," *Optics Express*, **21**, 20 (2013)

[YU 07] N. Yu, E. Cubukcu, L. Diehl, D. Bour, S. Corzine, J. Zhu, G. Höfler, K. B. Crozier and F. Capasso, "Bowtie plasmonic quantum cascade laser antenna," *Optics Express*, **15**, 13272 (2007)

[YURD 14] O. Yurduseven, D. Cavallo and A. Neto, “Wideband dielectric lens antenna with stable radiation pattern fed by coherent array of connected leaky slots,” *IEEE Transactions on Antennas and Propagation* **62**, 4 (2014)

Z

[ZELG 16] J. Zelgowski, A. Abdurrochman, F. Mermet, P. Pfeiffer, J. Fontaine and S. Lecler, “Photonic jet subwavelength etching using a shaped optical fiber tip,” *Optics Letters*, **41**, 9 (2016)

[ZENT 11] T. Zentgraf, Y. Liu, M. H. Mikkelsen, J. Valentine and X. Zhang, “Plasmonic Luneburg and Eaton lenses,” *Nature Nanotechnology*, **6**, 3 (2011)

[ZHAN 05] S. Zhang, W. Fan, N. Panoiu, K. Malloy, R. Osgood, and S. Brueck, “Experimental Demonstration of Near-Infrared Negative-Index Metamaterials,” *Physical Review Letters*, **95**, 1 (2005)

[ZHAN 08] X. Zhang and Z. Liu, “Superlenses to overcome the diffraction limit,” *Nature Materials*, **7**, 435 (2008)

[ZIOL 04] R. W. Ziolkowski, “Propagation in and scattering from a matched metamaterial having a zero index of refraction,” *Physical Review E*, **70**, 046608 (2004)

Author merits

FACTS:

- Articles in international Journals: 27 papers (3 invited in special issues)
- International conferences: 31 (2 invited)
- National conferences: 11 (2 nominated for the award "young scientists", winner in 2016)
- *h* index: Google scholar: 9 (220 citations)
  ISI web of knowledge: 7 (107 citations)
  Scopus: 7 (120 citations)

Journal articles

[1] **V. Pacheco-Peña**, N. Engheta, S. Kuznetsov, A. Gentselev and M. Beruete, "Experimental realization of an epsilon-near-zero graded-index metalens at terahertz frequencies", (Under Review) (2016)

[2] **V. Pacheco-Peña**, M. Beruete, P. Rodríguez-Ulibarri and N. Engheta, "On the performance of an ENZ-based sensor using transmission line theory and effective medium approach", (Under Review) (2016)

[3] **V. Pacheco-Peña**, I. V. Minin, O. V. Minin and M. Beruete, "On the performance of the zoned fishnet metamaterial lens with positive and negative reference phase", (Under Review) (2016)

[4] **V. Pacheco-Peña**, I. V. Minin, O. V. Minin and M. Beruete, "Experimental evaluation of zoned fishnet metalenses with phase reversal", (Under Review) (2016)

[5] **V. Pacheco-Peña**, M. Beruete, A. I. Fernández-Domínguez, Y. Luo, M. Navarro-Cía, "Description of Bow-Tie nanoantennas excited by localized emitters using conformal transformation", *ACS Photonics*, **3**, 7 (2016)

[6] I. V. Minin, O. V. Minin, **V. Pacheco-Peña**, M. Beruete, "Subwavelength optical trap in the field of a standing wave on photonic jets", *Quantum Electronics*, **46**, 6 (2016)

[7] **V. Pacheco-Peña**, I. V. Minin, O. V. Minin, M. Beruete, "Comprehensive analysis of photonic nanojets in 3D dielectric cuboids excited by surface plasmons", *Annalen der physik*, **1,** June (2016)

[8] **V. Pacheco-Peña**, I. V. Minin, O. V. Minin, M. Beruete, "Doubling the propagation distance of surface plasmon polaritons", *SPIE* (2016)

[9] *(Invited)* **V. Pacheco-Peña**, I. V. Minin, O. V. Minin, M. Beruete, "Increasing Surface Plasmons Propagation via Photonic Nanojets with Periodically Spaced 3D Dielectric Cuboids", *Photonics*, **3**, 10 (2016)

[10] *(Invited)* **V. Pacheco-Peña**, M. Navarro-Cía, M. Beruete, "Epsilon-near-zero metalenses operating in the visible", *Optics & Laser Technology*, **80**, 162 (2016)

[11] **V. Pacheco-Peña**, V. Torres, B. Orazbayev, M. Beruete, M. Navarro-Cía, N. Engheta, "Advances in ε-Near-Zero Metamaterial Devices", *Optics and Photonics News*, December (2015)

[12] **V. Pacheco-Peña**, M. Navarro-Cía, B. Orazbayev, I. V. Minin, O. V. Minin, M. Beruete, "Zoned fishnet lens antenna with reference phase for side-lobe reduction", *IEEE Transactions on Antennas and Propagation*, **63**, 8 (2015)

[13] I. V. Minin, O. V. Minin, **V. Pacheco-Peña**, M. Beruete, "All-dielectric periodic terajet waveguide using an array of coupled cuboids", *Applied Physics Letters*, **106**, 254102 (2015)

[14] B. Orazbayev, M. Beruete, **V. Pacheco-Peña**, G. Crespo, J. Teniente, M. Navarro-Cía, "Soret Fishnet Metalens Antenna", *Scientific Reports*, **4**, 9988 (2015)

[15] I. V. Minin, O. V. Minin, **V. Pacheco-Peña**, M. Beruete, "Localized photonic jets from flat, three-dimensional dielectric cuboids in the reflection mode", *Optics Letters*, **40**, 10 (2015)

[16] B. Orazbayev, **V. Pacheco-Peña**, M. Beruete, M. Navarro-Cía, "Exploiting the dispersion of the double-negative-index fishnet metamaterial to create a broadband low-profile metallic lens", *Optics Express*, **23**, 7 (2015)

[17] P. Rodríguez-Ulibarri, **V. Pacheco-Peña**, M. Navarro-Cía, A. Serebryannikov, M. Beruete, "Experimental demonstration of deflection angle tuning in unidirectional fishnet metamaterials at millimeter-waves", *Applied Physics Letters*, **106**, 061109 (2015)

[18] U. Beaskoetxea, **V. Pacheco-Peña**, B. Orazbayev, T. Akalin, S. Maci, M. Navarro-Cía, M. Beruete, "77 GHz High Gain Bull's-Eye antenna with sinusoidal profile", *IEEE Antennas and Wireless Propagation Letters*, **14**, 205 (2015)

[19] **V. Pacheco-Peña**, M. Beruete, I.V. Minin, O.V. Minin, "Multifrequency focusing and wide angular scanning of terajets", *Optics Letters*, **40**, 2 (2015)

[20] V. Torres, B. Orazbayev, **V. Pacheco-Peña**, J. Teniente, M. Beruete, M. Navarro-Cía, M. Sorolla, N. Engheta, "Experimental demonstration of a millimeter-wave metallic ENZ lens based on the energy squeezing principle", *IEEE Transactions on Antennas and Propagation*, **63**, 1 (2015)

[21] **V. Pacheco-Peña**, V. Torres, B. Orazbayev, M. Beruete, M. Navarro-Cía, M. Sorolla, N. Engheta, "Mechanical 144 GHz beam steering with all-metallic epsilon-near-zero lens antenna", *Applied Physics Letters*, **105**, 243503 (2014)

[22] *(Invited)* **V. Pacheco-Peña**, V. Torres, M. Beruete, M. Navarro-Cía, N. Engheta, "ε-near-zero (ENZ) graded index quasi-optical devices: steering and splitting millimeter waves", *Journal of Optics*, **16**, 094009 (2014)

[23] **V. Pacheco-Peña**, M. Beruete, I. V. Minin, O. V. Minin, "Terajets produced by dielectric cuboids", *Applied Physics Letters*, **105**, 084102 (2014)

[24] **V. Pacheco-Peña**, B. Orazbayev, U. Beaskoetxea, M. Beruete, M. Navarro-Cía, "Zoned near-zero refractive index fishnet lens antenna: Steering millimeter waves", *Journal of Applied Physics*, **115**, 12 (2014)

[25] **V. Pacheco-Peña**, B. Orazbayev, V. Torres, M. Beruete, M. Navarro-Cía, "Ultra-compact planoconcave zoned metallic lens based on the fishnet metamaterial", *Applied Physics Letters*, **103**, 18 (2013)

[26] M. Beruete, P. Rodríguez-Ulibarri, **V. Pacheco-Peña**, M. Navarro-Cía, A.E. Serebryannikov, "Frozen mode from hybridized

extraordinary transmission and Fabry-Perot resonances", *Physical Review B*, **87**, 20 (2013)

[27] V. Torres, **V. Pacheco-Peña**, P. Rodríguez-Ulibarri, M. Navarro-Cía, M. Beruete, M. Sorolla, N. Engheta, "Terahertz epsilon-near-zero graded-index lens", *Optics Express*, **21**, 7 (2013)

Conferences

i. International

[1] **V. Pacheco-Peña**, M. Navarro-Cía and M. Beruete, "Focusing optical waves via graded-epsilon-near-zero metalens", *10th international congress on advanced electromagnetic materials in Microwave and optics – Metamaterials 2016* (2016)

[2] **V. Pacheco-Peña**, M. Navarro-Cia, M. Beruete, "Optical Focusing via Epsilon-Near-Zero Plasmonic Metalens", *META'16, the 7th International Conference on Metamaterials, Photonic Crystals and Plasmonics* (2016)

[3] **V. Pacheco-Peña**, M. Navarro-Cía, B. Orazbayev, I.V. Minin, O.V. Minin, M. Beruete, "V-Band Reference-Phase-Based Zoned Fishnet Metalens", *IEEE International Symposium on Antennas and Propagation/USNC-URSI National Radio Science meeting* (2016)

[4] **V. Pacheco-Peña**, M. Beruete, A. I. Fernández-Domínguez, Y. Luo, M. Navarro-Cía, "Transformation optics for bowtie nanoantennas and localized emitters", *New horizons in nanophotonics* (2016)

[5] *(Invited)* **V. Pacheco-Peña**, M. Beruete, V. Torres, B. Orazbayev, M. Navarro-Cía, N. Engheta, "Permittivity-Near-Zero (ENZ) Meta-devices at THz Frequencies", *EMN meeting on THz Energy Materials Nanotechnology* (2016)

[6] I. V. Minin, O. V. Minin, I. Nefedov, **V. Pacheco-Peña** and M. Beruete, "Beam compressed system based on dielectric cluster of self-similar three-dimensional dielectric cuboids", *2016 Global Symposium on Millimeter Waves (GSMM) & ESA Workshop on Millimetre-Wave Technology and Applications* (2016)

[7] B. Orazbayev, M. Beruete, **V. Pacheco-Peña**, G. Crespo, J. Teniente, M. Navarro-Cía, "Soret Lens-Antenna based on the Fishnet Metamaterial", *The 10th European Conference on Antennas and Propagation (EuCAP 2016)* (2016)

[8] **V. Pacheco-Peña**, M. Navarro-Cia, B. Orazbayev, I.V. Minin, O.V. Minin, M. Beruete, "Improving the performance of the zoned fishnet metalens using the reference phase technique ", *The 10th European Conference on Antennas and Propagation (EuCAP 2016)* (2016)

[9] **V. Pacheco-Peña**, M. Beruete, A.I. Fernandez-Dominguez, Y. Luo, M. Navarro-Cia, "Localized emitters close to Nano-Bowties: Insight via Conformal Transformation", *9th International Congress on Advanced Electromagnetic Materials in Microwaves and Optics – Metamaterials 2015* (2015)

[10] B. Orazbayev, **V. Pacheco-Peña**, M. Beruete, M. Navarro-Cía, "A self-supporting broadband zoned fishnet metamaterial lens operating at the millimeter-wave V-band", *9th International Congress on Advanced Electromagnetic Materials in Microwaves and Optics – Metamaterials 2015* (2015)

[11] **V. Pacheco-Peña**, N. A. Haritoshin, I. V. Minin, O. V. Minin, M. Beruete, "High resolution Terajets via 3D dielectric cuboids at THz frequencies", *9th International Congress on Advanced Electromagnetic Materials in Microwaves and Optics – Metamaterials 2015* (2015)

[12] V. Torres, **V. Pacheco-Peña**, B. Orazbayev, J. Teniente, M. Beruete, M. Navarro-Cía, M. Sorolla, N. Engheta, "Epsilon-near-zero lens for beamshaping of sub-terahertz waves", *40th International Conference on Infrared, Millimeter and Terahertz Waves, IRMMW-THz 2015* (2015)

[13] B. Orazbayev, **V. Pacheco-Peña**, V. Torres, M. Beruete, M. Navarro-Cía, "Zoning Technique for a Broadband Fishnet Metamaterial Lens", *40th International Conference on Infrared, Millimeter and Terahertz Waves, IRMMW-THz 2015* (2015)

[14] V. Torres, **V. Pacheco-Peña**, B. Orazbayev, J. Teniente, M. Beruete, M. Navarro-Cía, M. Sorolla, N. Engheta, "144 GHz Epsilon-near-zero Lens Antenna", *2015 IEEE International Symposium on Antennas and Propagation and North American Radio Science Meeting* (2015)

[15] P. Rodríguez-Ulibarri, **V. Pacheco-Peña**, F. Falcone, M. Navarro-Cía, A.E. Serebryannikov, M. Beruete, "Experimental Demonstration of Deflection Angle Tuning in Diffraction-Inspired Unidirectional Structures", *2015 IEEE International Symposium on Antennas and Propagation and USNC-URSI National Radio Science Meeting* (2015)

[16] *(Invited)* **V. Pacheco-Peña**, M. Beruete, A.I. Fernandez-Dominguez, Y. Luo, M. Navarro-Cia, "Conformal transformation for nanoantennas", *6th International Conference on Metamaterials, Photonic Crystals and Plasmonics (META'15)* (2015)

[17] B. Orazbayev, **V. Pacheco-Peña**, M. Beruete, M. Navarro-Cía, "A Broadband Zoned Fishnet Metamaterial Lens", *2015 IEEE International Symposium on Antennas and Propagation & USNC/URSI National Radio Science Meeting* (2015)

[18] **V. Pacheco-Peña**, M. Beruete, M. Navarro-Cía, I.V. Minin, O.V. Minin, "High Resolution Terajets Using 3D Dielectric Cuboids", *2015 IEEE International Symposium on Antennas and Propagation and North American Radio Science Meeting* (2015)

[19] P. Rodríguez-Ulibarri, **V. Pacheco-Peña**, M. Beruete, M. Navarro-Cía, A. E. Serebryannikov, "Deflection Angle Tuning in Thin Structures with Diffraction Inspired Unidirectionality", *The 9th European Conference on Antennas and Propagation (EuCAP 2015)* (2015)

[20] V. Torres, B. Orazbayev, **V. Pacheco-Peña**, J. Teniente, M. Beruete, Miguel Navarro- Cía, Mario Sorolla Ayza, Nader Engheta, "144 GHz Epsilon-Near-Zero Metamaterial Lens", *The 9th European Conference on Antennas and Propagation (EuCAP 2015)* (2015)

[21] B. Orazbayev, **V. Pacheco-Peña**, V. Torres, M. Beruete, M. Navarro-Cía, "Zoned fishnet metamaterial lens with millimeter wave dual-band response", *The 9th European Conference on Antennas and Propagation (EuCAP 2015)* (2015)

[22] **V. Pacheco-Peña**, M. Beruete, I.V. Minin, O.V. Minin, "3D dielectric cuboids: an alternative for high-resolution terajets at THz frequencies", *The 9th European Conference on Antennas and Propagation (EuCAP 2015)* (2015)

[23] U. Beaskoetxea, **V. Pacheco-Peña**, B. Orazbayev, T. Akalin, S. Maci, M. Navarro-Cía, M. Beruete, "High Gain Flat 77GHz Sinusoidal

Bull's Eye", *The 9th European Conference on Antennas and Propagation (EuCAP 2015)* (2015)

[24] **V. Pacheco-Peña**, B. Orazbayev, P. Rodríguez-Ulibarri, M. Beruete, M. Navarro-Cía, "Focusing Millimeter Waves Using a Zoned Fishnet Metalens ", *14th Mediterranean Microwave Symposium, MMS 2014* (2014)

[25] B. Orazbayev, V. Torres, **V. Pacheco-Peña**, P. Rodríguez-Ulibarri, J. Teniente, M. Beruete, M. Sorolla, M. Navarro-Cía, N. Engheta, "All-Metallic ε-Near-Zero (ENZ) Lens Based On Ultra-Narrow Hollow Rectangular Waveguides: Experimental Results", *14th Mediterranean Microwave Symposium, MMS 2014* (2014)

[26] **V. Pacheco-Peña**, V. Torres, B. Orazbayev, M. Beruete, M. Navarro-Cía, N. Engheta, "Focusing Millimetre Waves by Means of a Permittivity-Near Zero Narrow-Waveguide Lens", *8th International Congress on Advanced Electromagnetic Materials in Microwaves and Optics, Metamaterials 2014* (2014)

[27] **V. Pacheco-Peña**, B. Orazbayev, U. Beaskoetxea, V. Torres, M. Beruete, M. Navarro-Cía, "All-metallic Zoned Fishnet Metamaterial Lens for the Unlicensed Millimetre-wave V-band", *8th International Congress on Advanced Electromagnetic Materials in Microwaves and Optics, Metamaterials 2014* (2014)

[28] M. Sorolla, M. Beruete, F. Falcone, V. Torres, **V. Pacheco-Peña**, B. Orazbayev, P. Rodríguez-Ulibarri, M. Navarro-Cía, "From the Extraordinary Transmission to the Zoned Fishnet Metamaterial Lens", *2014 IEEE International Symposium on Antennas and Propagation and USNC-URSI National Radio Science Meeting* (2014)

[29] **V. Pacheco-Peña**, B. Orazbayev, V. Torres, M. Beruete, M. Navarro-Cía, "Slimming the Fishnet Metamaterial Lens", *8th European Conference on Antennas and Propagation, EuCAP 2014* (2014)

[30] **V. Pacheco-Peña**, V. Torres, M. Navarro-Cía, M. Beruete, M. Sorolla, N. Engheta, "e-Near-Zero graded index structure as a bi-concave metallic lens using stacked rectangular near cut-off waveguides", *The 7th European Conference on Antennas and Propagation (EuCAP 2013)* (2013)

[31] **V. Pacheco-Peña**, V. Torres, M. Navarro-Cía, M. Beruete, M. Sorolla, N. Engheta, "Plano-Planar lenses using e near-zero stacked waveguides at millimeter waves", *The 6th International Congress on*

Advanced Electromagnetic Materials in Microwaves and Optics (Metamaterials 2012) (2012)

ii. National

[1] *(Winner)* **V. Pacheco-Peña**, M. Beruete, A. I. Fernández-Domínguez, Y. Luo, M. Navarro-Cía, "Transformation electromagnetics for nanoantennas and localized emitters", XXXI Simposium Nacional de la Unión Científica Internacional de Radio, URSI 2016 (2016)

[2] **V. Pacheco-Peña**, I. V. minin, O. V. Minin and M. Beruete, "Nanojets fotónicos excitados por plasmones de superficie a través de cuboides dieléctricos 3D", XXXI Simposium Nacional de la Unión Científica Internacional de Radio, URSI 2016 (2016)

[3] U. Beaskoetxea, **V. Pacheco-Peña**, B. Orazbayev, T. Akalin, S. Maci, M. Navarro-Cía, M. Beruete, "Antena Bull's Eye de Ondas de Fuga de Perfil Senoidal para Aplicaciones Radar", XXX *Simposium Nacional de la Unión Científica Internacional de Radio, URSI 2015* (2015)

[4] B. Orazbayev, M. Beruete, **V. Pacheco-Peña**, G. Crespo, J. Teniente, M. Navarro-Cía, "Lente de Soret Basada en el Metamaterial Fishnet", *XXX Simposium Nacional de la Unión Científica Internacional de Radio, URSI 2015* (2015)

[5] **V. Pacheco-Peña**, M. Beruete, I.V. Minin, O. V. Minin, "Terajets basados en Cuboides Dieléctricos: Propiedades Focales de alta resolución ", *XXX Simposium Nacional de la Unión Científica Internacional de Radio, URSI 2015* (2015)

[6] **V. Pacheco-Peña**, M. Navarro-Cía, B. Orazbayev, I.V. Minin, O.V. Minin, M. Beruete, "Lentes Zonadas con Referencia de Fase Basadas en el Metamaterial Tipo Fishnet ", *XXX Simposium Nacional de la Unión Científica Internacional de Radio, URSI 2015* (2015)

[7] M. Navarro-Cía, M. Beruete, V. Torres, **V. Pacheco-Peña**, B. Orazbayev, M. A. Astafev, S. A. Kuznetsov, "Dispositivos de ondas milimétricas y terahercio basados en medios y superficies artificiales", *XXX Simposium Nacional de la Unión Científica Internacional de Radio, URSI 2015* (2015)

[8] P. Rodríguez-Ulibarri, **V. Pacheco-Peña**, M. Navarro-Cía, A. E. Serebryannikov, M. Beruete, "Control del ángulo de deflexión en estructuras unidireccionales basadas en placas agujereadas en terminadas en una red de difracción dieléctrica", *XXX Simposium Nacional de la Unión Científica Internacional de Radio, URSI 2015* (2015)

[9] B. Orazbayev, **V. Pacheco-Peña**, V. Torres, M. Beruete, M. Navarro-Cía, "Zoning technique application for the fishnet metamaterial lens", *XXIX Simposium Nacional de la Unión Científica Internacional de Radio, URSI 2014* (2014)

[10] *(Nominated)* **V. Pacheco-Peña**, V. Torres, B. Orazbayev, M. Beruete, M. Navarro-Cía, N. Engheta, "Plano-concave lens based on ultra-narrow hollow rectangular waveguides mimicking an effective ENZ medium", *XXIX Simposium Nacional de la Unión Científica Internacional de Radio, URSI 2014* (2014)

[11] **V. Pacheco-Peña**, V. Torres, M. Navarro-Cía, M. Beruete, M. Sorolla, "Lentes ENZ de perfil plano basadas en guías de onda apiladas", *XXVII Simposium Nacional de la Unión Científica Internacional de Radio, URSI 2012*, (2012)

Participation in funded research projects

[1] AVATAR, "Avanzando en Plasmónica y Metamateriales para Sensores y Comunicaciones," TEC2011-28664-C02-01.

[2] CONSOLIDER INGENIO "Engineering Metamaterials," CSD2008-00066

[3] MEMENTO, "Componentes inspirados en metamateriales y plasmónica para sensado avanzado desde los Terahercios hasta el óptico", TEC2014-51902-C2-2-R

Other activities

i. Visiting Scientist

[1] Imperial College London, London, United Kingdom. Optical and Semiconductor Devices Group. Person in charge at the institution: Dr. Miguel Navarro-Cía. (15/07/2014 to 15/09/2014).

[2] University of Pennsylvania, Philadelphia, United States of America. Department of Electrical and Systems Engineering. Person in charge at the institution: H. Nedwill Ramsey Professor Nader Engheta. (08/05/2015 to 08/08/2015).

ii. Membership

[1] IEEE Student membership

[2] IEEE Nanotechnology Council

[3] IEEE Young Professionals

[4] IEEE Antennas and Propagation Society

[5] IEEE Microwave Theory and Techniques Society

iii. Reviewer

[1] IEEE Photonics Journal

[2] Photonics and Nanostructures – Fundamentals and Applications

[3] Journal of Applied Physics

[4] Optics Letters

[5] Optics Express

[6] Applied Physics Letters

[7] Journal of Optics

[8] Applied Physics B

[9] Nanoscale

[10] IEEE Transactions on Microwave Theory and Techniques

iv. Scholarships and Awards

[1] Winner of the award "Young Scientist 2016" by the *International Union of Radio Science URSI* during the national congress "URSI 2016" in Madrid, Spain, for the presentation of the work "Transformation electromagnetics for nanoantennas and localized emitters"

[2] Article "ε-near-zero (ENZ) graded index quasi-optical devices: steering and splitting millimeter waves" included in "Highlights 2014" of *Journal of Optics*

[3] Manuscript "ε-near-zero (ENZ) graded index quasi-optical devices: steering and splitting millimeter waves" selected as cover of the special issue on mid-infrared and THz photonics, *Journal of Optics* 2014.

[4] University Teacher Training Aid (FPU) by the Spanish Ministry of Education, Culture and Sports (2012).

[5] Scholarship holder by the Navarre Government under the program "Becas Navarra Talento Internacional 2011" to study an MRes in the Public University of Navarra, Spain. (2011-2012).

[6] Scholarship Holder by the European Union under the program "Erasmus Mundus Lot20" (2010-2011).

[7] Scholarship holder by the International Telecommunication Union (ITU) as the representative from El Salvador for the congress "ITU Telecom World 2009", Geneve, Switzerland (2009).

[8] MScI in Telecommunications Engineering, CUM LAUDE

[9] Scholarship holder by Kazma Family Foundation to study the MScI in Telecommunications Engineering, El Salvador (2005-2010).

v. Teaching duties

Demonstrating:

[2014-2016] Assistant: “Propagation and Transmission of waves” for the MSci in Telecommunications Engineering, Universidad Pública de Navarra, Spain.

[2013-2014] Assistant: “CAD Tools for High Frequency” for the MRes in Telecommunications Engineering, Universidad Pública de Navarra, Spain.

[2009-2010] Undergraduate Demonstrator: “Electricity and Magnetism” for the MSc in Telecommunications Engineering, Universidad Don Bosco, El Salvador.

[2007-2010] Undergraduate Demonstrator: “Mathematics II” for the MSc in Telecommunications Engineering, Universidad Don Bosco, El Salvador.